

NASA
Contractor Report 4334

AVSCOM
Technical Report 90-C-019

AD-A231 325

Vibration Transmission Through Rolling Element Bearings in Geared Rotor Systems

Rajendra Singh and Teik Chin Lim
*Ohio State University
Columbus, Ohio*

Prepared for
Propulsion Directorate
USAARTA-AVSCOM and
NASA Lewis Research Center
under Grant NAG3-773

NASA
National Aeronautics and
Space Administration
Office of Management
Scientific and Technical
Information Division

1990

DISTRIBUTION STATEMENT A
Approved for public release
Distribution Unlimited

ACKNOWLEDGEMENTS

We are very grateful for the financial support provided throughout this Ph.D. research by the NASA Lewis Research Center, Department of Mechanical Engineering, and Graduate School of the Ohio State University. Appreciation is also extended to J.S. Lin, D.R. Houser, J.J. Zakrajsek and F.B. Oswald for providing some of the experimental results used in Chapters III-V.



Accession For	
NTIS GRA&I	<input checked="" type="checkbox"/>
DTIC TAB	<input type="checkbox"/>
Unannounced	<input type="checkbox"/>
Justification	
By	
Distribution/	
Availability Codes	
Dist A-1	Avail and/or Special

TABLE OF CONTENTS

ACKNOWLEDGEMENTS.....	iii
LIST OF SYMBOLS	ix
CHAPTER	
I INTRODUCTION	1
1.1 Introduction	1
1.2 Literature Review	6
1.3 Scope and Objectives	7
II BEARING STIFFNESS FORMULATION	12
2.1 Introduction	12
2.2 Literature Review	14
2.3 Assumptions and Objectives	16
2.4 Bearing Load-Displacement Relations	18
2.5 Development of Bearing Stiffness Matrix $[K]_{bm}$	24
2.6 Numerical Estimation of $[K]_{bm}$	31
2.7 Validation of Proposed Model	33
2.8 Parametric Studies	36
2.9 Conclusions	46

III BEARING SYSTEM STUDIES	51
3.1 Introduction	51
3.2 Literature Review	53
3.3 Assumptions and Objectives	54
3.4 System Governing Equations	56
3.4.1 Method A: Lumped Parameter Model	56
3.4.2 Method B: Dynamic Finite Element Formulation	57
3.4.3 Other Methods	58
3.5 Bearing System Stability	60
3.6 System Reponse	63
3.7 Example Case I: Rigid Shaft and Plate System	71
3.7.1 Vibration Models	71
3.7.2 Bearing Transmissibility	75
3.8 Example Case II: Rigid Shaft and Plate Supported on Flexible Mounts ...	80
3.8.1 Vibration Models	80
3.8.2 Frequency Reponse	84
3.9 Example Case III: Experimental Study	88
3.9.1 Physical Setup	88
3.9.2 Bearing Analysis	88
3.9.3 System Study	91
3.10 Concluding Remarks	96
IV GEARED ROTOR SYSTEM STUDIES	97
4.1 Introduction	97
4.2 Literature Review	101
4.2.1 Casing and Mount Dynamics	101
4.2.2 Gear Dynamics	102
4.2.3 Rotor Dynamics	102
4.3 Assumptions and Objectives	103
4.4 Theory	105

4.4.1	Method A: Lumped Parameter Model	105
4.4.1.1	Equations of Motion	105
4.4.1.2	System Kinetic Energy	107
4.4.1.3	Shaft Stiffness Matrix	107
4.4.1.4	Gear Mesh Stiffness Matrix	110
4.4.1.5	Flexible Mount Stiffness Matrix	111
4.4.1.6	Bearing Stiffness Matrix	112
4.4.2	Method B: Dynamic Finite Element Formulation	113
4.4.3	Other Methods	113
4.5	Example Case I: Single-stage Rotor System with Rigid Casing and Flexible Mounts	114
4.5.1	Vibration Models	114
4.5.2	Eigensolution	118
4.5.3	Transmissibility	126
4.6	Example Case II: Geared Rotor System with Rigid Casing and Flexible Mounts	131
4.6.1	Bearing Analysis	131
4.6.2	Vibration Models	133
4.6.3	Eigensolution	136
4.6.4	Transmissibility Spectra	140
4.7	Example Case III: Geared Rotor System with Rigidly Mounted Flexible Casing	144
4.7.1	Physical Setup	144
4.7.2	Vibration Models	146
4.7.3	Casing Response	147
4.8	Concluding Remarks	153
V	STATISTICAL ENERGY ANALYSIS	155
5.1	Introduction	155
5.2	Modal Analysis of Gear Casing and Mounts	156
5.2.1	Finite Element Model	156
5.2.2	Experiments and Modal Validation	158

5.2.3 Parametric Studies	160
5.3 Justification for Using SEA Approach	165
5.3.1 Modal Densities	165
5.3.2 Literature Review	166
5.4 Example Case I: Coupling Loss Factor of Plate-Cantilevered Beam System	167
5.5 Example Case II: Coupling Loss Factor of Circular Shaft-Bearing-Plate System	169
5.6 Example Case III: A Circular Shaft-Bearing-Plate System	175
5.6.1 Theory	175
5.6.2 Validation and Parametric Studies	182
5.7 Example Case IV: A Geared Rotor System	188
5.7.1 Assumptions	188
5.7.2 Coupling Loss Factor	190
5.7.3 Vibroacoustic Response	192
5.7.4 Experimental Validation and Parametric Studies	194
5.8 Concluding Remarks	200
 VI CONCLUSIONS AND RECOMMENDATIONS	 201
6.1 Summary	201
6.2 Future Research	205
 LIST OF REFERENCES	 206

LIST OF SYMBOLS

A_0	unloaded distance between the inner and outer raceway groove curvature centers
A_j	loaded distance between the inner and outer raceway groove curvature centers of j-th ball
$A(\omega)$	accelerance transfer function
$\langle A^2 \rangle$	mean square acceleration spectra
A_c	casing plate surface area
A_s	shaft cross sectional area
a_o, a_i	locations of the outer and inner raceway groove curvature centers
$[C]$	system damping matrix
$[C]_b$	bearing damping matrix
c	wave speed
DOF	degree of freedom
d_G	gear diameter
d_p	pinion diameter
d_{bi}	inner raceway diameter of bearing

d_{bm}	bearing pitch diameter
d_{bo}	outer raceway diameter of bearing
d_s	shaft diameter
EI	flexural rigidity of the shaft
E_C	Rayleigh dissipation function
E_T	kinetic energy
E_U	potential energy
E_s, E_c	total vibratory energy level in the internal (s) subsystem and external (c) subsystem (Chapter V)
$e(t)$	static transmission error
\tilde{F}_w	generalized force in Lagrangian formulation
$F_{jba}(t)$	alternating bearing force in the $j = x, y, z$ or r direction
F_{jbm}	mean bearing force in the $j = x, y$ or z direction
$F_{jsa}(t)$	applied alternating force on the shaft, $j = x, y, z$ or r
F_{jsap}	complex Fourier coefficient of $F_{jsa}(t)$, $p = 1, 2, 3, \dots$
F_{jsm}	applied mean force on the shaft, $j = x, y$ or z
$\{f(t)\}_a$	generalized alternating applied load vector
$\{f\}_{ap}$	complex Fourier coefficient of $\{f(t)\}_a$, $p = 1, 2, 3, \dots$
$\{f\}_{bm}$	mean bearing load vector

$\{f(t)\}_{ca}$	alternating casing load vector
$\{f(t)\}_s$	total shaft load vector
$\{f(t)\}_{sa}$	alternating shaft load vector
$\{f\}_{sm}$	mean shaft load vector
G	bearing outer ring geometrical center
H_k	nonlinear functions, $k = 1, 2, 3, \dots, V$, given by equations (2.12a,b) and (2.13)
h	geometrical thickness
I_{jG}	mass moment of inertia of the gear about $j = x, y, z$ axis
I_{zL}	mass moment of inertia of the load about z axis
I_{zM}	mass moment of inertia of the motor about z axis
I_{jP}	mass moment of inertia of the pinion about $j = x, y, z$ axis
I_{jc}	mass moment of inertia of the casing about $j = x, y, z$ axis
I_{js}	mass moment of inertia of the shaft about $j = x, y, z$ axis
$\{I\}$	Lumped inertia row vector
K_n	rolling element load-deflection stiffness constant
$[K]$	system stiffness matrix
$[K]_v$	mount stiffness matrix
$[K]_{bm}$	proposed bearing stiffness matrix of dimension 6

$[K]_{bms}$	a matrix of dimension 5 as a subset of $[K]_{bm}$ with last row and column excluded
$[K]_h$	gear mesh coupling stiffness matrix
$[K]_s$	shaft stiffness matrix
$[K]_s^e$	shaft segment stiffness matrix
k_{TM}	effective torsional stiffness of the driving shaft coupling
k_{TL}	effective torsional stiffness of the driven shaft coupling
k_{biw}	bearing stiffness coefficient, $i, w = x, y, z, \theta_x, \theta_y, \theta_z$
\hat{k}_{biw}	estimated bearing stiffness coefficient, $i, w = x, y, z, \theta_x, \theta_y, \theta_z$
k_s, k_c	shaft (s) or plate (c) wavenumber (Chapter V)
k_h	gear mesh stiffness
k_{vj}	mount stiffness coefficient, $j = x, y, z, \theta_x, \theta_y, \theta_z$
L_A	frequency bandwidth-averaged mean square acceleration in dB re $\langle A^2 \rangle_{ref} = 1.0g^2$
L_V	spatially and frequency bandwidth averaged mean square mobility level (dB re $\langle V^2 \rangle_{ref} = 1.0 \text{ m}^2/\text{N}^2\text{s}^2$)
L_e	shaft segment length
L_s	shaft length
M_{jba}	alternating bearing moment about $j = x$ or y direction
M_{jbm}	mean bearing moment about $j = x$ or y direction

M_{jsa}	alternating shaft bending moment about $j = x$ or y direction
$[M]$	system mass matrix
$[M]_s$	shaft mass matrix
$[M]_c$	casing mass matrix
m_R	rotor mass
m_c	casing mass
m_s	shaft mass
m_{sej}	shaft lumped mass
$\{m\}$	lumped mass row vector
N_g	number of gear teeth
n	rolling element load-deflection exponent
n_c	casing plate modal density (see Chapter V)
n_s	number of shaft segments (Chapter IV) or shaft modal density (Chapter V)
$p(t)$	normalized dynamic transmission error
Q_j	resultant normal load on the j -th rolling element
Q	acoustic source directivity (Chapter V)
q_w	generalized displacement vector in Lagrangian formulation
$\{q(t)\}_a$	generalized alternating displacement vector
$\{q\}_{ap}$	complex Fourier coefficient of $\{q(t)\}_a$, $p = 1, 2, 3, \dots$

$\{q\}_b$	total bearing displacement vector
$\{q\}_{ba}$	alternating bearing displacement vector
$\{q\}_{bm}$	mean bearing displacement vector
$\{q(t)\}_{ca}$	alternating casing displacement vector
$\{q(t)\}_{sa}$	alternating shaft displacement vector
$\{q\}_{sm}$	mean shaft displacement vector
$R(\omega)$	force or moment transmissibility transfer function or room constant (see Chapter V)
Re	real part of a complex number
\vec{R}_j	j-th bearing coordinate vector, $j = 1, n_s+1, n_s+2, 2n_s+2$
r_L	bearing radial clearance
r_j	pitch radius (roller) or radii of inner raceway groove curvature centers (ball)
S	room surface area (Chapter V)
S_c	total surface area of the casing plate in example case III (Chapter III)
$[T]_b$	bearing field transfer matrix
$T_{jsa}(t)$	applied alternating torque on the shaft, $j = x, y$ or z
T_{jsm}	applied mean torque on the shaft, $j = x, y$ or z
t	time
$u_{jca}(t)$	alternating casing translational displacement in the $j = x, y$ or z direction

$u_{jsa}(t)$	alternating shaft translational displacement in the $j = x, y$ or z direction
u_{jsm}	mean shaft translational displacement in the $j = x, y$ or z direction
$\{u(t)\}_{ca}$	casing alternating displacement vector
$\{u(t)\}_{sa}$	shaft alternating displacement vector
$V(\omega)$	mobility transfer function
$\langle V^2 \rangle$	spatially and frequency bandwidth averaged mean square mobility
v_{jsa}, v_{jca}	shaft (s) or plate(c) alternating velocity in the $j=x, y, z$ direction
X	solution to the problem $H_k = 0, k = 1, 2, 3, \dots, V$
Z	total number of rolling element
Z_s	driving point shaft impedance (Chapter V)
Z_c	driving point plate impedance (Chapter V)
z	number of loaded rolling element
z_0	characteristic impedance of the surrounding medium (Chapter V)
α_0	unloaded bearing contact angle
α_j	loaded j -th rolling element contact angle
$\bar{\alpha}$	average absorption coefficient (Chapter V)
β_{ja}	alternating bearing angular displacement about the $j = x$ or y direction
β_{jm}	mean bearing rotational displacement about the $j = x$ or y direction
ΔF_{rbm}	incremental mean radial bearing force

$\Delta\delta_{rm}$	incremental mean radial bearing displacement
$\Delta\omega$	frequency bandwidth
δ_{Bj}	resultant elastic deformation of the j-th ball element
δ_{Rj}	resultant elastic deformation of the j-th roller element
δX	error vector
δ_{jm}	mean bearing translational displacement in the $j = x, y$ or z direction
δ_j	resultant elastic deformation of the j-th rolling element
δ_{ja}	alternating bearing translational displacement in the $j = x, y$ or z direction
$(\delta)_{rj}$	effective j-th rolling element displacement in the radial direction
$(\delta)_{zj}$	effective j-th rolling element displacement in the axial direction
Φ_j	stability functions given by equation (3.6) and Table 3.1
$\{\phi\}_j$	mode shape vector corresponding to the j-th natural frequency
η_s, η_c	dissipation loss factor for the internal (s) or external (c) subsystems
η_{sc}	coupling loss factor
κ	radius of gyration
$\{\mu\}_p$	complex Fourier coefficient of the principal coordinate vector, $p = 1, 2, 3, \dots$
Π_s	external power input to the internal (s) subsystem
Π_{sc}	net power transfer from the internal (s) subsystem to external (c) subsystems
ρ	material density

$\theta_{jca}(t)$	alternating casing angular displacement about the $j = x, y$ or z coordinate
$\theta_{jsa}(t)$	alternating shaft angular displacement about the $j = x, y$ or z coordinate
θ_{jsm}	mean shaft angular displacement about the i -axis; $j = x, y, z$
$\{\theta(t)\}_{Ra}$	rotor alternating angular displacement vector
$\{\theta(t)\}_{ca}$	casing alternating angular displacement vector
$\{\theta(t)\}_{sa}$	shaft alternating angular displacement vector
σ	Rayleigh damping matrix proportionality constant
σ_c	casing plate radiation efficiency (Chapter V)
Ω_z	mean rotational speed of the shaft
Ω_{zM}	mean rotational speed of the driving shaft
Ω_{zL}	mean rotational speed of the driven shaft
ω	bandwidth center frequency (Chapter V)
ω_h	gear mesh frequency
ω_j	undamped natural frequency, $j = 1, 2, 3, \dots$
ω_{jd}	damped natural frequency, $j = 1, 2, 3, \dots$
ω_o	fundamental frequency
ω_p	excitation frequency, $p = 1, 2, 3, \dots$
ψ_l	bearing load angle
ψ_j	angular distance of j -th rolling element from the x -axis

ζ_j	modal damping ratio
$[]^T$	transpose of a matrix or vector
$ $	magnitude or determinant
$(\dot{})$	first time derivative
$(\ddot{})$	second time derivative
$()^*$	complex conjugate
$(\hat{})$	estimation based on simple models

CHAPTER I

INTRODUCTION

1.1 INTRODUCTION

Noise and vibration generated by the rotating mechanical equipment including geared drives have always been a problem in the implementation of new technology in automobiles, rotorcrafts and industrial machines [1-6]. Recently, the need for reliable vibration/noise prediction methods have been found to be crucial as faster and lighter machines are being designed [6-8]. In most of these rotating systems, structure-borne noise paths through bearings, which support the rotating shafts on flexible or rigid casings, are dominant [5,6,9]. Hence, in order to obtain reliable mathematical prediction of the overall dynamic system, a complete understanding of the vibration transmission mechanism through bearings, and the role of bearings as a dynamic coupler between the shaft and casing, is critical.

Current bearing models, based on ideal boundary condition or purely translational stiffness element description, cannot explain how the vibratory motion may be transmitted from the rotating shaft to the flexible casing and other connecting structures in rotating mechanical equipment [10-15]. These simple models are only adequate for the free and forced vibration analyses of the rotor dynamic system enclosed in a rigid casing. For example, a vibrational model of a rotating system based upon the existing bearing models can only predict purely in-plane type motion on the flexible casing plate,

given only the bending motion on the shaft. However, experimental results have shown that the casing plate motion is primarily flexural or out-of-plane type [9,16,17]. This paradox is essentially due to an incomplete understanding of the bearing as vibratory motion transmitter in rotating mechanical equipment.

The main focus of this research is to clarify this issue quantitatively and qualitatively by developing a new mathematical model for the precision rolling element bearings, and extend the proposed bearing formulation to examine vibration transmissibility in rotating mechanical equipment through several example cases of bearing systems and geared drives. The superiority of the proposed model compared to simple models is also demonstrated in these example cases. A typical shaft-bearing-casing-mount system is shown in Figure 1.1. The rigid or flexible shaft may be subjected to forces and/or torques and supported by a bearing on a flexibly or rigidly mounted casing. Here, the vibration transmission is from the shaft to the casing and mount through the bearing system. Figure 1.2 shows a typical rolling element bearing subjected to forces and moments due to the rolling element deformation. The bearing is free to rotate about the axis perpendicular to the bearing plane, and hence does not transmit any dynamic moment about this axis. However, dynamic moments about the other two orthogonal axis exist which have not been considered in simple bearing models. Finally, a generic geared rotor system consists of a motor, spur gear pair, flexible shafts, load, flexible couplings, rolling element bearings, flexible casing and mounts as shown in Figure 1.3a is also considered. The system is excited by the gear kinematic transmission error at gear mesh frequency. A single-stage rotor system with rotating mass unbalance excitation as shown in Figure 1.3b is treated as a special case of Figure 1.3a. Further description of each system will be presented in later chapters.

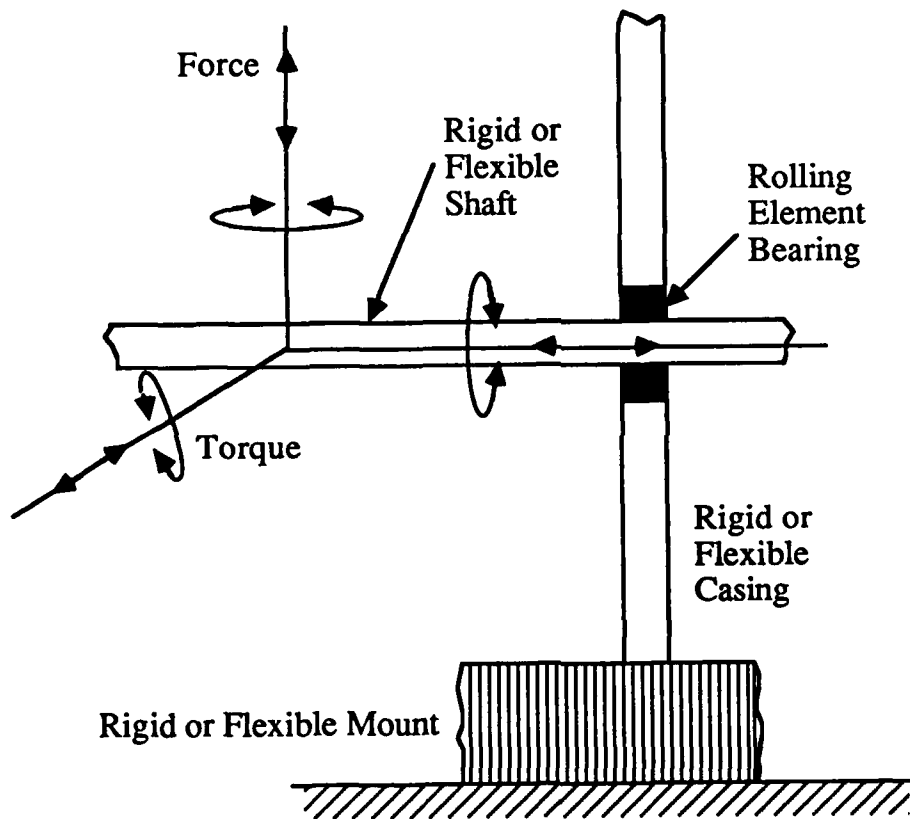


Figure 1.1 Schematic of a typical shaft-bearing-plate-mount system

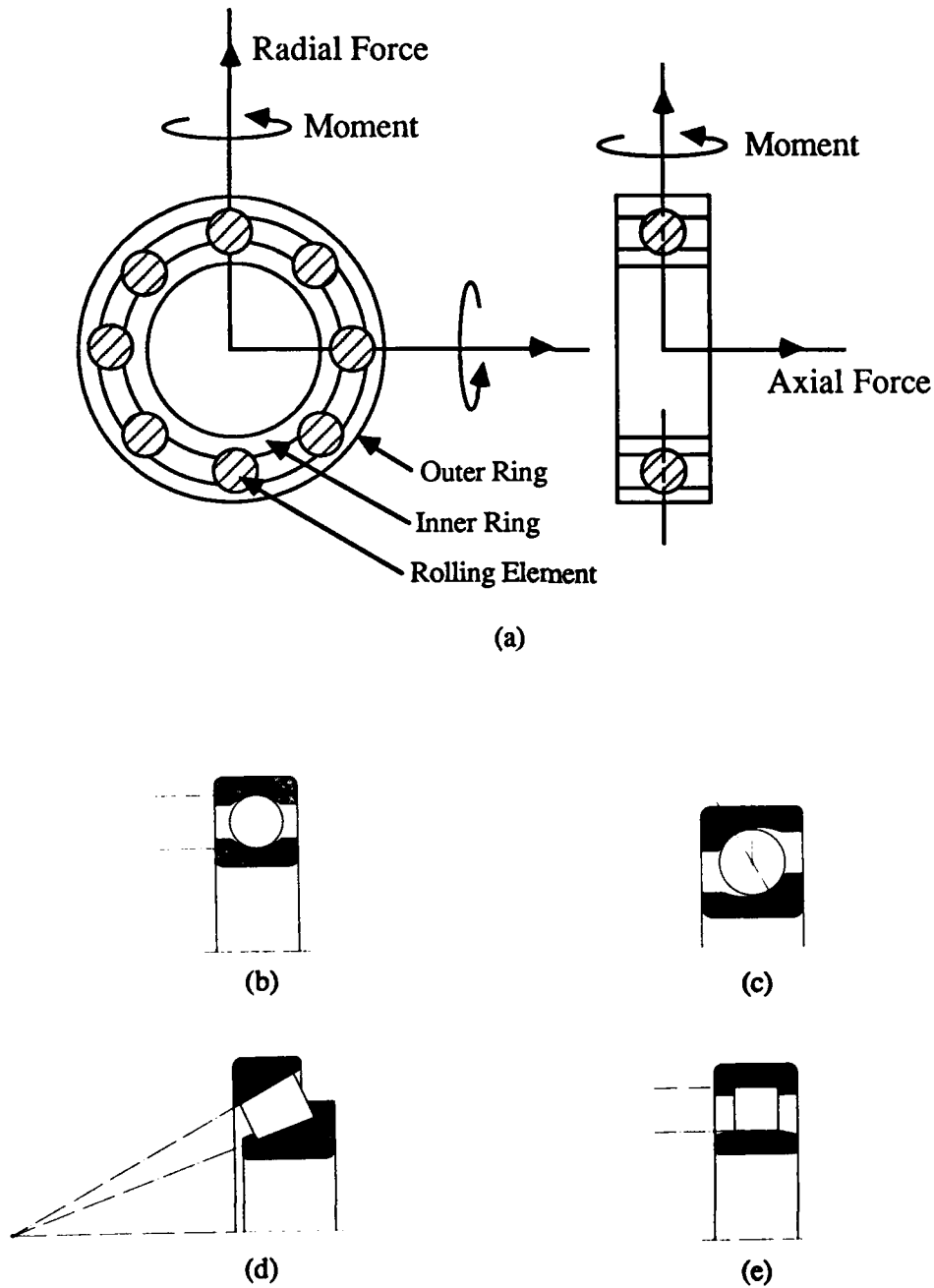
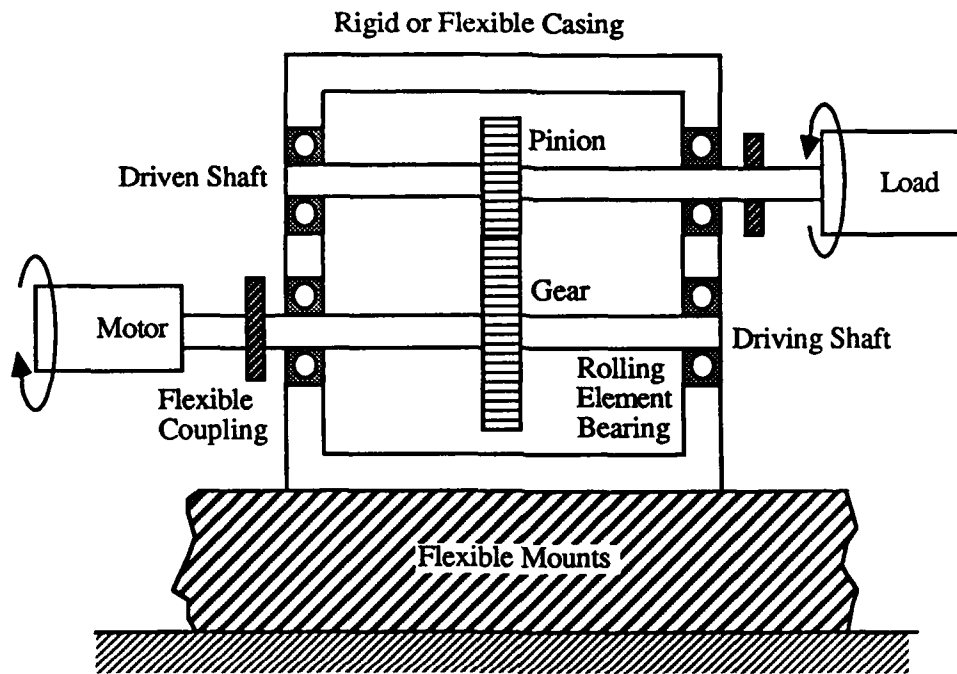
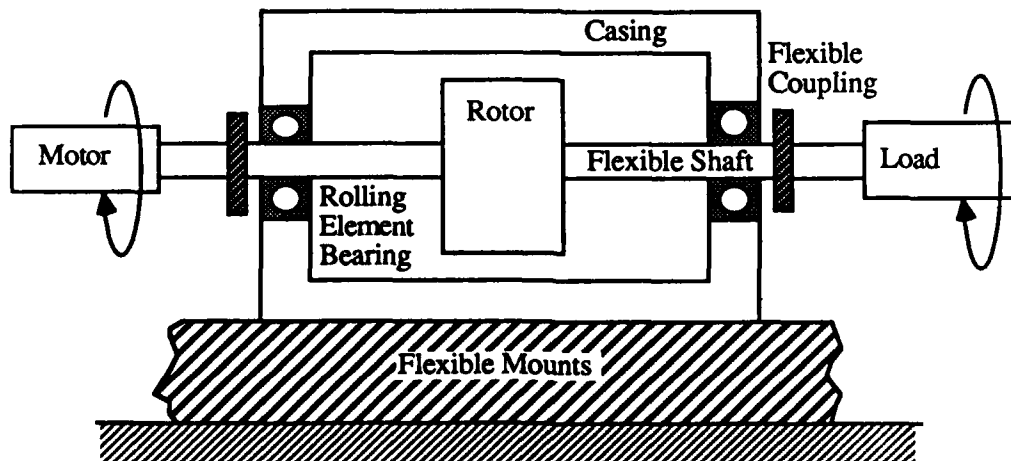


Figure 1.2 Schematic of typical rolling element bearings. (a) Bearing forces and moments. (b) Deep groove ball bearing. (c) Angular contact ball bearing. (d) Taper roller bearing. (e) Cylindrical roller bearing.



(a)



(b)

Figure 1.3 Generic rotating mechanical systems. (a) A geared rotor system. (b) A single-stage rotor system

1.2 LITERATURE REVIEW

Simple bearing models either assume ideal boundary conditions for the shaft or time-invariant translational springs in the axial and radial directions [10-15]. The ideal boundary conditions for the shaft are typically simply-supported for short bearings, clamped for long bearings or free (for torsional motion only) [10-12]. Formulas for the stiffness coefficients derived from the force-displacement relation commonly used by bearing designers [18,19] are given by Harris [18], Gargiulo [14] and White [20]. In 1982 Rajab [21,22] realized the limitations of the simple models and philosophically proposed two additional stiffness coefficients which couple the radial and rotational bearing degrees of freedom, given radial and moment about the axis transverse to the radial line of action. In 1988, Young [23] extended Rajab's [21] analyses to include mean axial force while retaining other features of Rajab's model. This resulted in bearing stiffness matrix of dimension 3.

Simple bearing models are widely used in vibration models of rotor dynamic systems which typically exclude casing and mount dynamics, to calculate critical speeds, dynamic stability, and responses due to shaft excitations such as mass unbalance and gear transmission error [10-15]. In most cases, the vibration transmission through bearings is not the primary issue, and thus the bearing models tend to be simplified. None of the current models studied [20-22,24] can fully explain vibration transmission through bearings in systems similar to Figure 1.1.

Publications on the modal analyses of geared drives and single or multiple stage rotor systems indicate that very little has been reported directly on the force transmissibility through bearings, and the dynamic effects of bearing, casing and mounts on the internal rotating system [10-13,15,25-29]. A comprehensive review of the available vibration studies of casing and mounts has been given by Lim and Singh in 1989 [6]. In these studies, the dynamic interaction between the casing-mount system and the internal rotating system is often not incorporated, and in few instances when this interaction is modeled, only purely radial and/or axial force on the bearings are included. Such models still do not explain how the vibration is transmitted from the shaft to the casing. A more comprehensive review of the relevant studies will be given in each chapter.

1.3 SCOPE AND OBJECTIVES

A new mathematical model for the precision rolling element bearing in Figure 1.2 is developed and incorporated in linear time-invariant discrete and broad band vibration models of Figures 1.1 and 1.3. This study proposes a comprehensive bearing stiffness matrix of dimension 6 which explains the vibratory motion transmission through the bearings and allows for the study of overall geared rotor system dynamics. The lumped parameter and dynamic finite element techniques are used to develop the discrete vibration models while statistical energy analysis method is used for the broad band vibration models. Experimental validation is also included in each chapter, where the driving point and cross point accelerance and mobility levels predicted by theory are compared to experiments.

The specific objectives of this research are grouped as follows: bearing stiffness formulation, bearing system studies, geared rotor system studies, and statistical energy analysis. Each chapter is self sufficient since it is written in a journal paper style. Accordingly, a detailed problem statement is also included in each chapter.

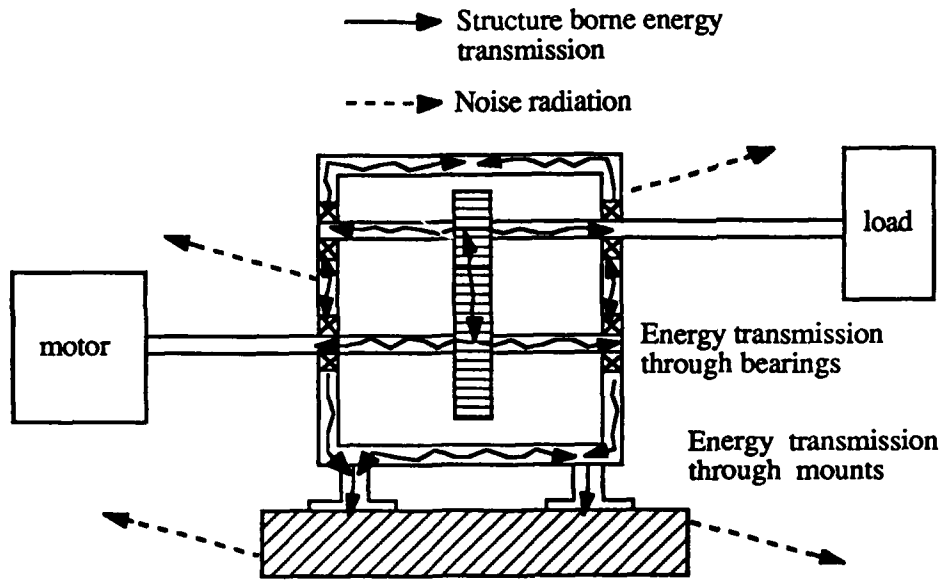
a. Bearing stiffness formulation: Since simple bearing models used in rotor dynamic analyses are inadequate in explaining the role of bearing as a vibratory motion transmitter, this study resolves this issue by proposing and developing a new rolling element bearing stiffness matrix which is suitable for the analysis of the vibration transmission through either ball or roller bearing. A numerical scheme is also developed to compute the stiffness coefficients and indicate the existence of solutions to the nonlinear algebraic bearing equations describing the bearing load-displacement relationships. The proposed bearing model is partially verified by comparing with published analytical and experimental results. In addition, the character of the bearing stiffness matrix and its sensitivity to various bearing parameters will be discussed. (Chapter II)

b. Bearing system studies: The specific objectives of this chapter are to incorporate the proposed bearing matrix developed in Chapter II in linear discrete vibration models of the bearing system as shown in Figure 1.1 using lumped parameter and dynamic finite element methods to compute the eigensolution and forced harmonic response, and to evaluate the dynamic stability. The vibration transmission through bearing is also predicted for several example cases considered previously [14,20,24] and an experimental setup [17]. The advantages of the proposed formulation compared to the

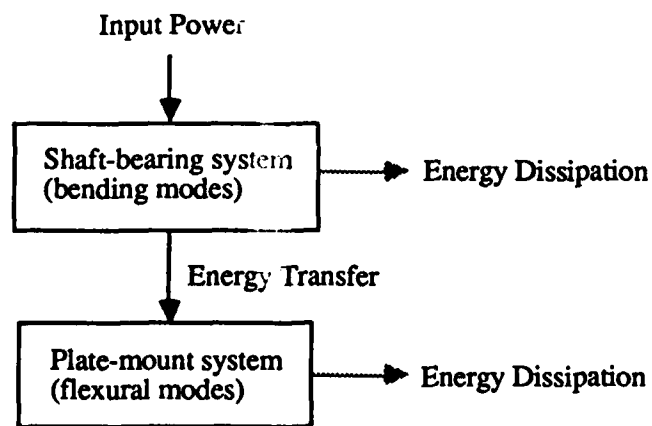
simple models is demonstrated by comparing their predicted transfer functions. The theory is also validated by comparing analytical predictions with experimental data on a shaft-bearing-plate system. (Chapter III)

c. Geared rotor system studies: Current geared rotor system vibration models exclude the effects of casing and mounts, and do not address the overall system behavior. The objectives of this chapter are to incorporate the proposed bearing matrix in the discrete vibration model of the generic geared rotor system of Figure 1.3 and conduct overall system studies by calculating eigensolutions and forced harmonic responses with emphasis on the prediction of vibration transmission through rolling element bearings. *The effects of casing and mount dynamics on the internal rotating system is also evaluated.* Example cases which include a single-stage rotor system with flexible shafts supported by two identical rolling element bearings on rigid casing and flexible mounts, and a spur gear pair with motor and load inertias attached to two flexible shafts supported by four rolling element bearings on rigid or flexible casing and compliant or massive mounts will be studied analytically and/or experimentally. Also, the advantages of the proposed formulation as compared to simple models of geared drives will be demonstrated. (Chapter IV)

d. Statistical energy analysis: At very high frequencies, the narrow band approach using the lumped parameter or dynamic finite element model may not be adequate due to the high structural modal density. To overcome this problem, statistical energy analysis method is used to predict the vibratory energy transmission in and noise radiation from a geared rotor system as illustrated in Figure 1.4a. The proposed bearing matrix is again



(a)



(b)

Figure 1.4 Vibration energy transmission in a geared rotor system. (a) Structure-borne noise paths. (b) Statistical energy analysis model.

incorporated in the vibratory energy model. In this method, only the mean-square spatially averaged response over one third octave frequency bandwidths are predicted which involves solution to a set of algebraic equations obtained through the vibratory energy balance of each subsystem shown in Figure 1.4b. Several example cases including a plate-cantilevered rectangular beam, circular shaft-bearing-plate system and a geared rotor system are chosen to demonstrate the salient features of this technique.

(Chapter V)

CHAPTER 2

BEARING STIFFNESS FORMULATION

2.1 INTRODUCTION

Current rotor dynamic models describe precision rolling element bearings either as ideal boundary conditions for the shafts [10-12], or as purely translational stiffness elements [13-15]. Such simple bearing models may be adequate for the free and forced vibration analyses of the rotor dynamic system enclosed in a rigid casing. But these mathematical models cannot explain how the vibratory motion may be transmitted from the rotating shaft to the flexible or rigid casing and other connecting structures. For example, a vibration model of a system similar to Figure 2.1, based upon the existing bearing models, can only predict purely in-plane type motion on the flexible casing plate given only the bending motion on the shaft. However, experimental results have shown that the casing plate motion is primarily flexural or out-of-plane type [9,16,17]. This paradox is essentially due to an incomplete understanding of the bearing as vibratory motion transmitter in rotating mechanical equipment including geared drives where structure-borne noise paths through bearings are often dominant.

This chapter clarifies this issue qualitatively and quantitatively by developing a new mathematical model for precision rolling element bearings. A schematic of a generic system with a flexible shaft rotating at speed Ω_z and subjected to mean load vector $\{f\}_{sm} = \{F_{wsm}, T_{wsm}\}$, $w = x, y, z$, flexible casing and mount is shown in Figure

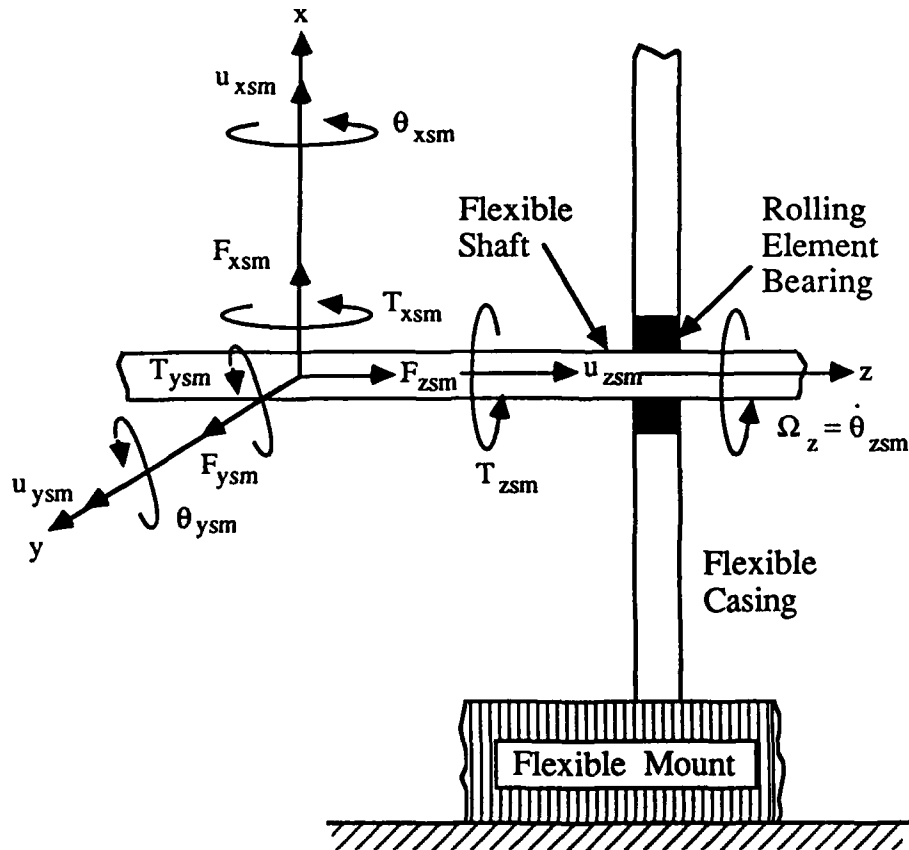


Figure 2.1 Schematic representation of the vibration transmission problem. Here the flexible shaft is subjected to mean forces F_{wsm} and torques T_{wsm} where $w = x, y$ or z , is the direction and subscript m and s implies mean and shaft respectively. Also, θ is the angular displacement and u is the translational displacement.

2.1; the shaft is supported on one of the following bearings: deep groove ball bearing, angular contact ball bearing, thrust ball bearing, straight roller bearing or taper roller bearing. A new bearing stiffness matrix $[K]_{bm}$ will be proposed which is expected to demonstrate a coupling between the shaft bending motion and the flexural motion of the casing plate. It will be shown that the translational bearing stiffness coefficients currently used in rotor dynamic models are a small subset of the proposed $[K]_{bm}$. Several example cases are employed to validate our theory. Our bearing model can be easily incorporated in analytical or numerical models typically used for the dynamic analyses - this will be the basis of Chapters III and IV of this report.

2.2 LITERATURE REVIEW

The ideal boundary conditions for the shaft have typically been assumed to be simply-supported for short bearings, clamped for long bearings or free (in the torsional mode only) [10-12]. In other cases, researchers describe the bearing as time-invariant translational springs with stiffness coefficients k_{brr} and/or k_{bzz} in the radial and axial directions, respectively [13-15,20]. Formulas for such nonlinear stiffness coefficients are given by Harris [18] and Gargiulo [14]; these are derived from the radial or axial mean force-displacement equation commonly used by the precision rolling element bearing designers [18,19]. Their derivations neglect the effects of radial clearance and mean bearing force vector $\{f\}_{bm}$ on the load distribution and hence are applicable only for constant load angle ψ_l of 180 degrees. White refined these formulations by using a finite difference approximation for the computation of stiffness coefficients for radial ball and roller bearings, and by including the effects of radial clearance and force on the

load angle ψ_l [20]. Even with these refinements the mathematical model is still incapable of predicting the total vibration transmission across bearings.

In 1982 Rajab [21], realized the limitations of the current simple theory and philosophically proposed two additional stiffness terms $k_{br\theta}$ and $k_{b\theta\theta}$ which couple the relative radial and rotational bearing displacements between the inner and outer rings, given the mean radial load and moment about the axis transverse to the radial line of action. In 1988 Young [23] extended Rajab's [21] analyses to include the mean axial force F_{zbm} , and then used a discrete summation over all of the loaded rolling elements to obtain bearing forces and moment instead of the integral form while still retaining other features of Rajab's model. This resulted in a 3x3 bearing stiffness matrix. Some of the salient features of Rajab's [21] and Young's [23] models are summarized in Reference [22].

Experimental determination of the bearing stiffness coefficients has been strictly limited to the translational coefficients k_{brr} and k_{bzz} . A method for the measurement of in situ bearing stiffness under oscillating loading conditions has been given by Walford and Stone [30]. Recently, Kraus et al. [24] designed an in situ measurement test stand to determine the translational bearing stiffness from measured vibration spectra, in conjunction with the single degree of freedom system theory. They determined the effect of preload, bearing release and rotational speed Ω_z on k_{brr} and k_{bzz} . Their results show that k_{brr} and k_{bzz} are essentially linear and the effect of Ω_z is negligible when a high preload is applied on the bearing.

2.3 ASSUMPTIONS AND OBJECTIVES

Due to the following key differences, a separate formulation of $[K]_{bm}$ for both ball and roller type rolling element bearings is required: (i) ball bearings have elliptical contacts and roller types have rectangular contacts between the inner race, rolling elements and outer race when loaded, and (ii) the loaded contact angles α_j of the ball types may change but α_j in the roller type remains relatively constant [31]. Each bearing is characterized by its kinematic and design parameters such as unloaded contact angle α_0 , radial clearance r_L , effective stiffness coefficient K_n for inner ring-single rolling element-outer ring contacts, angular misalignment, preloads, radius of inner raceway groove curvature center for ball type and bearing pitch radius for roller type [18,19,31]. It is expected that $[K]_{bm}$ is given in terms of these parameters.

The mean bearing displacements $\{q\}_{bm}$ as shown in Figure 2.2 are given by the relative rigid body motions between the inner and outer rings. The total bearing displacement vector is given as $\{q\}_b = \{q\}_{bm} + \{q(t)\}_{ba}$ where $\{q(t)\}_{ba}$ is the fluctuation about the mean point $\{q\}_{bm}$ during the steady state rotation. Accordingly one must consider time varying bearing stiffness coefficients. However in our analysis, such time varying bearing stiffness coefficients are neglected by assuming very small vibratory motions i.e. $\{q\}_{ba} \ll \{q\}_{bm}$, and high bearing preloads. Consequently, only the mean bearing loads and displacements are included in the derivation of $[K]_{bm}$. The basic load-deflection relation for each elastic rolling element is defined by the Hertzian contact stress theory [18,19,32], and the load experienced by each rolling element is described by its relative location in the bearing raceway. Further it is assumed that the angular position of each rolling element relative to one another is always maintained due to the rigid cages and pin retainers. Secondary effects such as centrifugal forces and

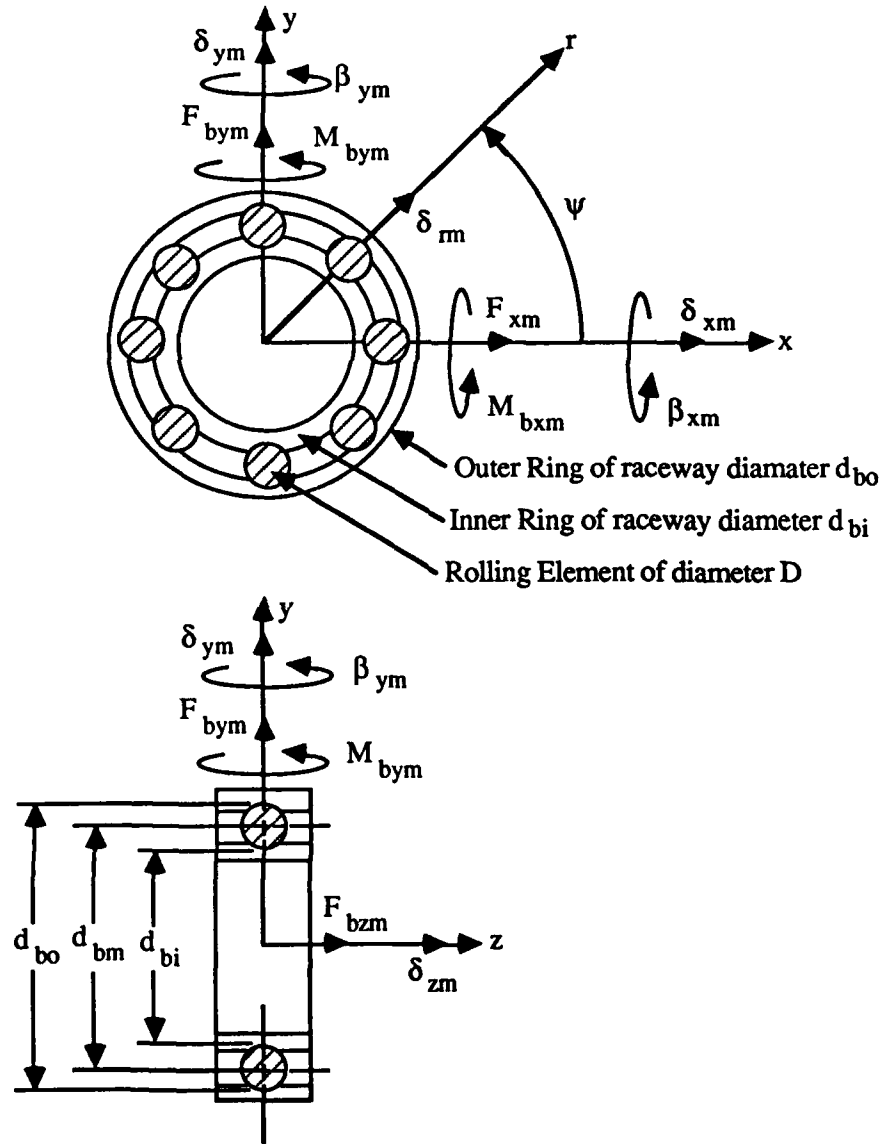


Figure 2.2 Rolling element bearing kinematics and coordinate system. Here the following nomenclature is used: d_{bo} is the outer raceway diameter, d_{bm} is the bearing pitch diameter, d_{bi} is the inner raceway diameter, ψ is the angular position of rolling element, δ_{wm} is the mean translational displacement, β_{pm} is the mean angular displacement, F_{wbm} is the mean bearing force, and M_{pbm} is the mean bearing moment where $w = x, y, z$, and $p = x, y$, are the directions.

gyroscopic moments on the bearing are ignored as these effects are evident only at extremely high rotational speeds. Tribological issues [32,33] are beyond the scope of this study and hence our analysis assumes bearings to be unlubricated.

The specific objectives of this chapter are to: (i) propose and develop a new rolling element bearing stiffness matrix $[K]_{bm}$ which is suitable for the analysis of the vibration transmission through either ball or roller bearing, (ii) develop a numerical scheme to compute $[K]_{bm}$ and discuss the existence of solutions to the nonlinear algebraic bearing equations describing load-displacement relationships, (iii) verify our proposed model by comparing its predictions with published analytical and experimental results [14,20,24] for the translational stiffness coefficients k_{bxx} , k_{byy} and k_{bzz} , (iv) relate $[K]_{bm}$ to various kinematic and design parameters, and perform parametric studies to investigate the effect of unloaded contact angle α_0 and preloads, and (v) characterize the nature of $[K]_{bm}$ and recommend its usage. Finally it should be noted that dimensionless parameters will not be used here as the metric units are invariably employed to specify bearings [32].

2.4 BEARING LOAD-DISPLACEMENT RELATIONS

In this section, the relationships between the bearing forces $\{F_{xbm}, F_{ybm}, F_{zbm}\}$ and moments $\{M_{xbm}, M_{ybm}\}$ transmitted through the rolling element bearing, and the bearing displacements $\{q\}_{bm}$ as given in Figure 2.2 will be derived for both ball and roller bearings. The mean applied loads $\{f\}_{sm}$ at the shaft as given in Figure 2.1 and bearing preloads generate the mean bearing displacements $\{q\}_{bm}$ and loads $\{f\}_{bm}$. These displacements $\{q\}_{bm}$ are used to derive the resultant elastic deformation $\delta(\psi_j)$ of

the j -th rolling element located at angle ψ_j from the x -axis. From the ball bearing kinematics shown in Figure 2.3, $\delta_B(\psi_j)$ is

$$\delta_B(\psi_j) = \begin{cases} A(\psi_j) - A_o & , \quad \delta_{Bj} > 0 \\ 0 & , \quad \delta_{Bj} \leq 0 \end{cases} \quad (2.1a)$$

$$A(\psi_j) = \sqrt{(\delta^*)_{zj}^2 + (\delta^*)_{rj}^2} \quad (2.1b)$$

$$(\delta^*)_{zj} = A_o \sin \alpha_o + (\delta)_{zj}; \quad (\delta^*)_{rj} = A_o \cos \alpha_o + (\delta)_{rj} \quad (2.1c)$$

where A_o and A are the unloaded and loaded relative distances between the inner a_i and outer a_o raceway groove curvature centers. Similarly for the roller bearing kinematics shown in Figure 2.4 for $\alpha_j = \alpha_o$, $\delta_R(\psi_j)$ is

$$\delta_R(\psi_j) = \begin{cases} (\delta)_{rj} \cos \alpha_j + (\delta)_{zj} \sin \alpha_j & , \quad \delta_{Rj} > 0 \\ 0 & , \quad \delta_{Rj} \leq 0 \end{cases} \quad (2.2)$$

Note that in equations (2.1) and (2.2) $\delta_{Bj} \leq 0$ or $\delta_{Rj} \leq 0$ implies that the j -th rolling element is stress free. In both equations (2.1) and (2.2), the effective j -th rolling element displacements in the axial $(\delta)_{zj}$ and radial $(\delta)_{rj}$ directions are given in Figure 2.5 in terms of the bearing displacements $\{q\}_{bm}$.

$$(\delta)_{zj} = \delta_{zm} + r_j \{ \beta_{xm} \sin(\psi_j) - \beta_{ym} \cos(\psi_j) \} \quad (2.3a)$$

$$(\delta)_{rj} = \delta_{xm} \cos \psi_j + \delta_{ym} \sin \psi_j - r_L \quad (2.3b)$$

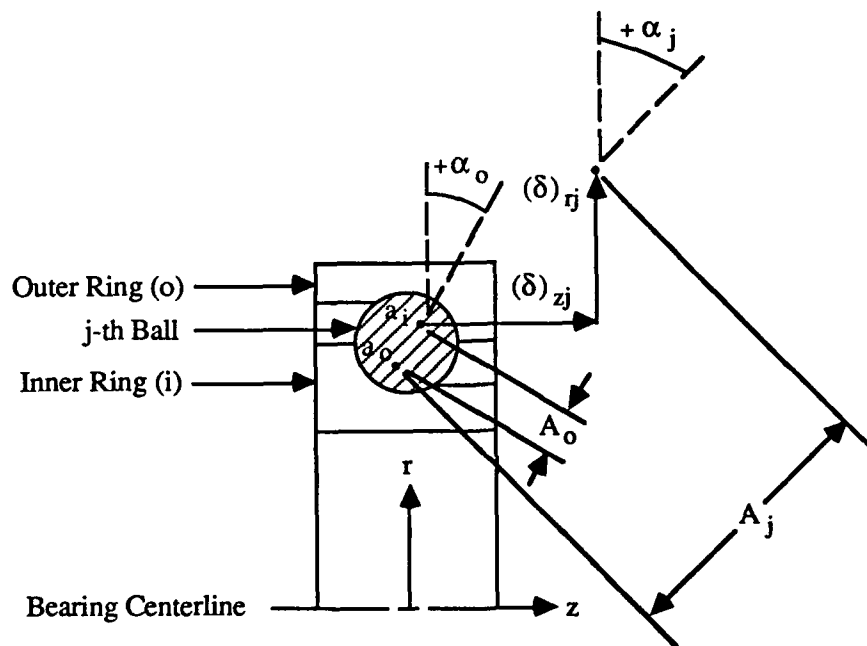


Figure 2.3 Elastic deformation of rolling element for non-constant contact angle α_j given by the change in the distance between the inner a_i and outer a_o raceway groove radius curvature centers due to the mean bearing loads or displacements.

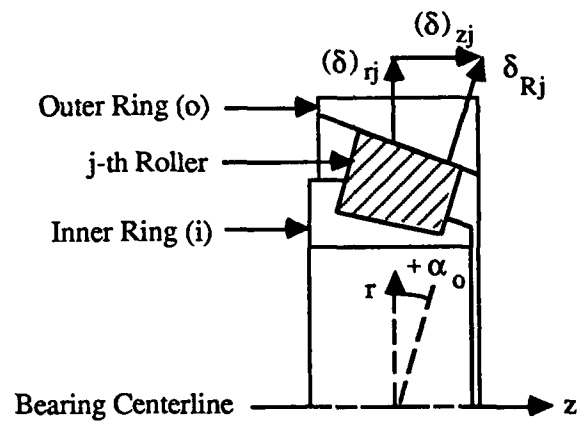


Figure 2.4 Elastic deformation of rolling element for constant contact angle $\alpha_j = \alpha_o$ given by the change in the relative position of the inner and outer raceways due to the mean bearing loads or displacements.

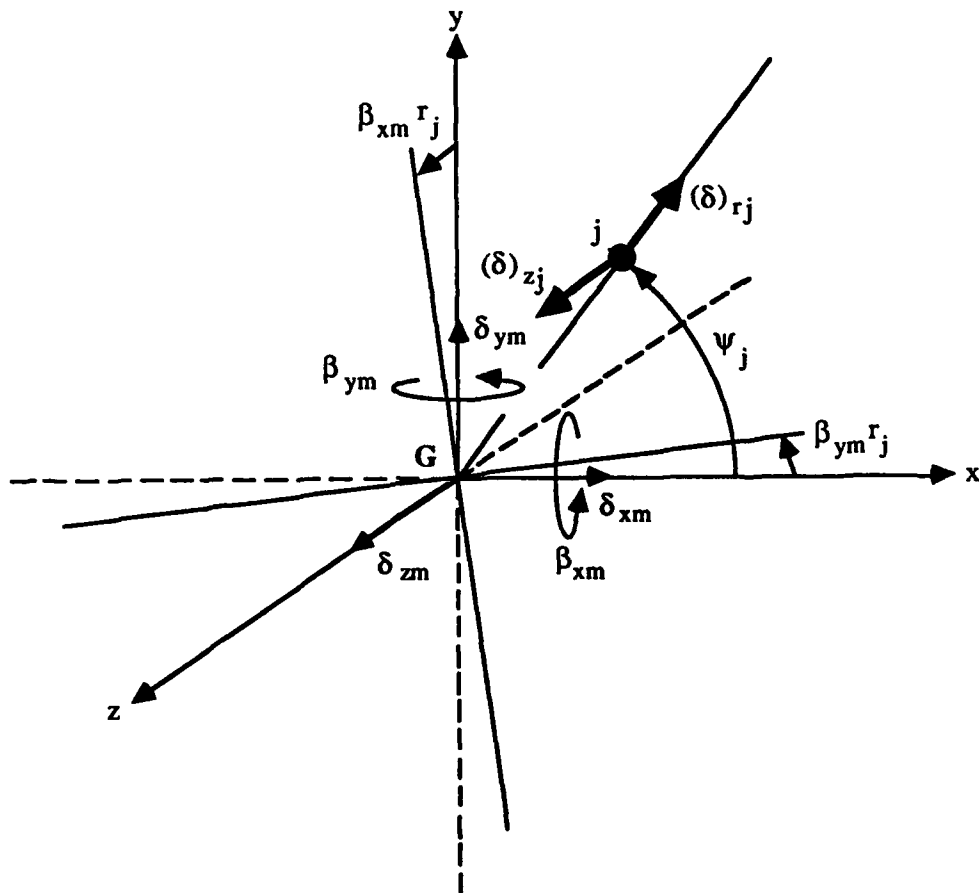


Figure 2.5 Decomposition of the effective radial $(\delta)_{rj}$ and axial $(\delta)_{zj}$ deformations of the j -th rolling element in terms of the mean bearing displacements $\{q\}_{bm}$. Here G is the bearing outer ring geometrical center.

where r_j is the radial distance of the inner raceway groove curvature center for the ball type or is the pitch bearing radius for roller type. Equations (2.1)–(2.3) in conjunction with the Hertzian contact stress principle [18,19,32] stated as follows yield the load-deflection relationships for a single rolling element .

$$Q_j = K_n \delta_j^n \quad (2.4)$$

where Q_j is the resultant normal load on the rolling element, and K_n is the effective stiffness constant for the inner race-rolling element-outer race contacts and it is a function of the bearing geometry and material properties [18,19,31]. Note that the exponent n is equal to $3/2$ for ball type with elliptical contacts and $10/9$ for roller type with rectangular contacts. Previously, we have mentioned that the loaded contact angle α_j for the roller bearing remains unchanged from the unloaded position α_o , but on the other hand α_j may alter in the ball bearing case. The sign convention is such that α_j is positive when measured from the bearing x-y plane towards the axial z-axis as shown in Figures 2.3 and 2.4, and negative otherwise. For the ball bearing of Figure 2.3, the loaded contact angle α_j is

$$\tan(\alpha_j) = \frac{A_o \sin \alpha_o + (\delta)_{zj}}{A_o \cos \alpha_o + (\delta)_{rj}} \quad (2.5)$$

where $(\delta)_{zj}$ and $(\delta)_{rj}$ are given by equations (2.3a) and (2.3b). It is appropriate here to note that Rajab [21,22] and Young [22,23] in their derivation of the bearing stiffness model used an expression similar to equation (2.2) but with $\delta_{xm} = \beta_{ym} = \delta_{zm} = r_L = 0$ in

Rajab's analysis and $\delta_{xm}=\beta_{ym}=r_L=0$ in Young's analysis for both ball and roller bearings. Since always α_j is given by equation (2.5) irrespective of the formulation and since equation (2.2) is valid only if $\alpha_j=\alpha_0$, their ball and roller bearings analyses are in error. Expressions similar to equation (2.1)-(2.5) with minor differences have also been used by Eschmann et al. [31], Jones [34] and Davis [35], but their intentions were to calculate static bearing forces rather than to derive the bearing stiffness models for vibration transmission analysis.

2.5 DEVELOPMENT OF BEARING STIFFNESS MATRIX $[K]_{bm}$

Our proposed bearing stiffness matrix $[K]_{bm}$ is a global representation of the bearing kinematic and elastic characteristics as it combines the effects of z number of loaded rolling element stiffnesses in parallel given by $\delta_j > 0$. First, we need to relate the resultant bearing mean load vector $\{f\}_{bm}$ to the bearing displacement vector $\{q\}_{bm}$. This can be achieved through vectorial sums $Q_j(\delta_{wm}, \beta_{pm}; w = x, y, z \text{ and } p = x, y)$ in equation (2.4) for all of the loaded rolling elements which lead to the following bearing moments $\{M_{wbm}\}$ and forces $\{F_{wbm}\}$ as follows

$$\begin{Bmatrix} M_{xbm} \\ M_{ybm} \\ M_{zbm} \end{Bmatrix} = \sum_j^z r_j Q_j \sin \alpha_j \begin{Bmatrix} \sin \psi_j \\ -\cos \psi_j \\ 0 \end{Bmatrix} \quad (2.6a)$$

$$\begin{Bmatrix} F_{xbm} \\ F_{ybm} \\ F_{zbm} \end{Bmatrix} = \sum_j^z Q_j \begin{Bmatrix} \cos \alpha_j \cos \psi_j \\ \cos \alpha_j \sin \psi_j \\ \sin \alpha_j \end{Bmatrix} \quad (2.6b)$$

Replacing Q_j and α_j in equation (2.6) in terms of $(\delta_{wm}, \beta_{pm})$ yields the following explicit relationships between $\{f\}_{bm}$ and $\{q\}_{bm}$ for ball bearings

$$\begin{Bmatrix} M_{x_{bm}} \\ M_{y_{bm}} \\ M_{z_{bm}} \end{Bmatrix} = K_n \sum_j^z \frac{\left\{ \sqrt{[A_o \sin \alpha_o + (\delta)_{zj}]^2 + [A_o \cos \alpha_o + (\delta)_{rj}]^2} - A_o \right\}^n}{\sqrt{[A_o \sin \alpha_o + (\delta)_{zj}]^2 + [A_o \cos \alpha_o + (\delta)_{rj}]^2}} \begin{Bmatrix} \sin \psi_j \\ -\cos \psi_j \\ 0 \end{Bmatrix} \quad (2.7a)$$

$$\begin{Bmatrix} F_{x_{bm}} \\ F_{y_{bm}} \\ F_{z_{bm}} \end{Bmatrix} = K_n \sum_j^z \frac{\left\{ \sqrt{[A_o \sin \alpha_o + (\delta)_{zj}]^2 + [A_o \cos \alpha_o + (\delta)_{rj}]^2} - A_o \right\}^n}{\sqrt{[A_o \sin \alpha_o + (\delta)_{zj}]^2 + [A_o \cos \alpha_o + (\delta)_{rj}]^2}} \begin{Bmatrix} [A_o \cos \alpha_o + (\delta)_{rj}] \cos \psi_j \\ [A_o \cos \alpha_o + (\delta)_{rj}] \sin \psi_j \\ [A_o \sin \alpha_o + (\delta)_{zj}] \end{Bmatrix} \quad (2.7b)$$

and similarly for roller bearings

$$\begin{Bmatrix} M_{x_{bm}} \\ M_{y_{bm}} \\ M_{z_{bm}} \end{Bmatrix} = K_n \sin \alpha_o \sum_j^z r_j \{ (\delta)_{rj} \cos \alpha_o + (\delta)_{zj} \sin \alpha_o \}^n \begin{Bmatrix} \sin \psi_j \\ -\cos \psi_j \\ 0 \end{Bmatrix} \quad (2.8a)$$

$$\begin{Bmatrix} F_{x_{bm}} \\ F_{y_{bm}} \\ F_{z_{bm}} \end{Bmatrix} = K_n \sum_j^z \{ (\delta)_{rj} \cos \alpha_o + (\delta)_{zj} \sin \alpha_o \}^n \begin{Bmatrix} \cos \alpha_o \cos \psi_j \\ \cos \alpha_o \sin \psi_j \\ \sin \alpha_o \end{Bmatrix} \quad (2.8b)$$

where $(\delta)_{rj}$ and $(\delta)_{zj}$ are functions of $\{\delta_{wm}, \beta_{pm}\}$ as defined by equation (2.3). Approximate integral forms of equations (2.7a,b) and (2.8a,b) are often used instead of the summation forms to eliminate explicit dependence on ψ_j , especially in the case of only one or two degrees of freedom bearings [18,32]. For instance Rajab [21,22] chose the integral form representation but made a mathematical error in constructing the integrand.

Now we define a symmetric bearing stiffness matrix $[K]_{bm}$ of dimension 6 from equations (2.7a,b) and (2.8a,b) and by assuming that $\{q\}_{ba} \ll \{q\}_{bm}$

$$[K]_{bm} = \begin{bmatrix} \frac{\partial F_{wbm}}{\partial \delta_{im}} & \frac{\partial F_{wbm}}{\partial \beta_{im}} \\ \frac{\partial M_{wbm}}{\partial \delta_{im}} & \frac{\partial M_{wbm}}{\partial \beta_{im}} \end{bmatrix} \{q\}_{bm} \quad ; \quad w, i = x, y, z \quad (2.9)$$

Here each stiffness coefficient must be evaluated at the mean point $\{q\}_{bm}$. Explicit expressions for the ball bearing stiffness are as follows; note that $[K]_{bm}$ is symmetric i.e. $k_{biw} = k_{bwi}$.

$$k_{bxx} = K_n \sum_j^z \frac{(A_j - A_o)^n \cos^2 \psi_j \left\{ \frac{n A_j (\delta^*)_{rj}^2}{A_j - A_o} + A_j^2 - (\delta^*)_{rj}^2 \right\}}{A_j^3} \quad (2.10a)$$

$$k_{bxy} = K_n \sum_j \frac{(A_j - A_o)^n \sin \psi_j \cos \psi_j \left\{ \frac{n A_j (\delta^*)_{rj}^2}{A_j - A_o} + A_j^2 - (\delta^*)_{rj}^2 \right\}}{A_j^3} \quad (2.10b)$$

$$k_{bxz} = K_n \sum_j \frac{(A_j - A_o)^n (\delta^*)_{rj} (\delta^*)_{zj} \cos \psi_j \left\{ \frac{n A_j}{A_j - A_o} - 1 \right\}}{A_j^3} \quad (2.10c)$$

$$k_{bx\theta_x} = K_n \sum_j \frac{r_j (A_j - A_o)^n (\delta^*)_{rj} (\delta^*)_{zj} \sin \psi_j \cos \psi_j \left\{ \frac{n A_j}{A_j - A_o} - 1 \right\}}{A_j^3} \quad (2.10d)$$

$$k_{bx\theta_y} = K_n \sum_j \frac{r_j (A_j - A_o)^n (\delta^*)_{rj} (\delta^*)_{zj} \cos^2 \psi_j \left\{ 1 - \frac{n A_j}{A_j - A_o} \right\}}{A_j^3} \quad (2.10e)$$

$$k_{byy} = K_n \sum_j \frac{(A_j - A_o)^n \sin^2 \psi_j \left\{ \frac{n A_j (\delta^*)_{rj}^2}{A_j - A_o} + A_j^2 - (\delta^*)_{rj}^2 \right\}}{A_j^3} \quad (2.10f)$$

$$k_{byz} = K_n \sum_j \frac{(A_j - A_o)^n (\delta^*)_{rj} (\delta^*)_{zj} \sin \psi_j \left\{ \frac{n A_j}{A_j - A_o} - 1 \right\}}{A_j^3} \quad (2.10g)$$

$$k_{by\theta_x} = K_n \sum_j \frac{r_j (A_j - A_o)^n (\delta^*)_{rj} (\delta^*)_{zj} \sin^2 \psi_j \left\{ \frac{n A_j}{A_j - A_o} - 1 \right\}}{A_j^3} \quad (2.10h)$$

$$k_{by\theta_y} = K_n \sum_j^z \frac{r_j (A_j - A_o)^n (\delta^*)_{rj} (\delta^*)_{zj} \sin \psi_j \cos \psi_j \left\{ 1 - \frac{n A_j}{A_j - A_o} \right\}}{A_j^3} \quad (2.10i)$$

$$k_{bzz} = K_n \sum_j^z \frac{(A_j - A_o)^n \left\{ \frac{n A_j (\delta^*)_{zj}^2}{A_j - A_o} + A_j^2 - (\delta^*)_{zj}^2 \right\}}{A_j^3} \quad (2.10j)$$

$$k_{bz\theta_x} = K_n \sum_j^z \frac{r_j (A_j - A_o)^n \sin \psi_j \left\{ \frac{n A_j (\delta^*)_{zj}^2}{A_j - A_o} + A_j^2 - (\delta^*)_{zj}^2 \right\}}{A_j^3} \quad (2.10k)$$

$$k_{bz\theta_y} = K_n \sum_j^z \frac{r_j (A_j - A_o)^n \cos \psi_j \left\{ (\delta^*)_{zj}^2 - \frac{n A_j (\delta^*)_{zj}^2}{A_j - A_o} - A_j^2 \right\}}{A_j^3} \quad (2.10l)$$

$$k_{b\theta_x\theta_x} = K_n \sum_j^z \frac{r_j^2 (A_j - A_o)^n \sin^2 \psi_j \left\{ \frac{n A_j (\delta^*)_{zj}^2}{A_j - A_o} + A_j^2 - (\delta^*)_{zj}^2 \right\}}{A_j^3} \quad (2.10m)$$

$$k_{b\theta_x\theta_y} = K_n \sum_j^z \frac{r_j^2 (A_j - A_o)^n \sin \psi_j \cos \psi_j \left\{ (\delta^*)_{zj}^2 - \frac{n A_j (\delta^*)_{zj}^2}{A_j - A_o} - A_j^2 \right\}}{A_j^3} \quad (2.10n)$$

$$k_{b\theta_y\theta_y} = K_n \sum_j \frac{r_j^2 (A_j - A_o)^n \cos^2 \psi_j \left\{ \frac{n A_j (\delta^*)_{zj}^2}{A_j - A_o} + A_j^2 - (\delta^*)_{zj}^2 \right\}}{A_j^3} \quad (2.10o)$$

$$k_{bi\theta_z} = k_{b\theta_i\theta_z} = 0 \quad ; \quad i = x, y, z \quad (2.10p)$$

where $(\delta^*)_{zj}$, $(\delta^*)_{rj}$ and A_j are defined by equation (2.1). And the roller bearing stiffness coefficients $k_{biw} = k_{bwi}$ are given explicitly as

$$k_{bxx} = n K_n \cos^2 \alpha_o \sum_j \delta_{Rj}^{n-1} \cos^2 \psi_j \quad (2.11a)$$

$$k_{bxy} = \frac{n}{2} K_n \cos^2 \alpha_o \sum_j \delta_{Rj}^{n-1} \sin 2\psi_j \quad (2.11b)$$

$$k_{bxz} = \frac{n}{2} K_n \sin 2\alpha_o \sum_j \delta_{Rj}^{n-1} \cos \psi_j \quad (2.11c)$$

$$k_{bx\theta_x} = \frac{n}{4} K_n \sin 2\alpha_o \sum_j r_j \delta_{Rj}^{n-1} \sin 2\psi_j \quad (2.11d)$$

$$k_{bx\theta_y} = -\frac{n}{2} K_n \sin 2\alpha_o \sum_j r_j \delta_{Rj}^{n-1} \cos^2 \psi_j \quad (2.11e)$$

$$k_{byy} = n K_n \cos^2 \alpha_o \sum_j \delta_{Rj}^{n-1} \sin^2 \psi_j \quad (2.11f)$$

$$k_{byz} = \frac{n}{2} K_n \sin 2\alpha_o \sum_j \delta_{Rj}^{n-1} \sin \psi_j \quad (2.11g)$$

$$k_{by\theta_x} = \frac{n}{2} K_n \sin 2\alpha_o \sum_j^z r_j \delta_{Rj}^{n-1} \sin^2 \psi_j \quad (2.11h)$$

$$k_{by\theta_y} = -\frac{n}{4} K_n \sin 2\alpha_o \sum_j^z r_j \delta_{Rj}^{n-1} \sin 2\psi_j \quad (2.11i)$$

$$k_{bzz} = n K_n \sin^2 \alpha_o \sum_j^z \delta_{Rj}^{n-1} \quad (2.11j)$$

$$k_{bz\theta_x} = n K_n \sin^2 \alpha_o \sum_j^z r_j \delta_{Rj}^{n-1} \sin \psi_j \quad (2.11k)$$

$$k_{bz\theta_y} = -n K_n \sin^2 \alpha_o \sum_j^z r_j \delta_{Rj}^{n-1} \cos \psi_j \quad (2.11l)$$

$$k_{b\theta_x\theta_x} = n K_n \sin^2 \alpha_o \sum_j^z r_j^2 \delta_{Rj}^{n-1} \sin^2 \psi_j \quad (2.11m)$$

$$k_{b\theta_x\theta_y} = -\frac{n}{2} K_n \sin^2 \alpha_o \sum_j^z r_j^2 \delta_{Rj}^{n-1} \sin 2\psi_j \quad (2.11n)$$

$$k_{b\theta_y\theta_y} = n K_n \sin^2 \alpha_o \sum_j^z r_j^2 \delta_{Rj}^{n-1} \cos^2 \psi_j \quad (2.11o)$$

$$k_{bi\theta_z} = k_{b\theta_i\theta_z} = 0 \quad ; \quad i=x,y,z \quad (2.11p)$$

where δ_{Rj} is defined in equation (2.2). It should be noted that all stiffness terms associated with the torsional degree of freedom β_{zm} are zero due to the fact that an ideal bearing allows free rotation about the z-direction. Also, the translational stiffness coefficients k_{bij} , $i=x,y,z$ for $\delta_{ym}=\delta_{zm}=\beta_{xm}=\beta_{ym}=0$, $\delta_{xm}=\delta_{zm}=\beta_{xm}=\beta_{ym}=0$ or $\delta_{xm}=\delta_{ym}=\beta_{xm}=\beta_{ym}=0$ are equivalent to the bearing stiffness coefficients commonly

used by investigators [14,15,20]. The nature of these and other features of $[K]_{bm}$ will be discussed later in Section 2.9.

2.6 NUMERICAL ESTIMATION OF $[K]_{bm}$

The coefficients k_{biw} can be computed by one of the following two methods: I. directly compute k_{biw} given mean bearing displacement vector $\{q\}_{bm}$ employing equations (2.10a-p) and (2.11a-p), or II. numerically solve the nonlinear algebraic equations described by equations (2.7a,b) and (2.8a,b) to obtain $\{q\}_{bm}$ from $\{f\}_{bm}$, and then evaluate k_{biw} per method I. Note that $\{f\}_{bm}$ may be functions of the mean shaft loads, bearing preloads, and shaft and casing compliances depending on the configuration and flexibility of the rotating mechanical system. If the bearing system is statically determinate, then $\{f\}_{bm}$ may be computed explicitly in terms of $\{f\}_{sm}$ and preloads using the force and moment equilibrium equations. Conversely for an indeterminate system, appropriate field equations for the shaft and casing plate are needed in addition to the equilibrium equations to obtain $\{f\}_{bm}$ which must also include shaft and casing compliances. Calculations of $\{f\}_{bm}$ and $\{q\}_{bm}$ in this case are simultaneous, which may be extensive especially when the system is very flexible, and may even require discretization using finite element or lumped mass technique. However, in many real machines the in-plane stiffness of the casing plate which supports most of the mean bearing load is much higher than the bending stiffness of the shaft. Hence the casing in-plane stiffness term may be neglected without contributing any large error to $\{f\}_{bm}$ [18,31]. And only the Euler's beam equation for a statically indeterminate shaft is used along with the nonlinear bearing load-displacement equations (2.7a,b) and (2.8a,b).

Method I is computationally direct and needs no discussion. But method II deals with as many as 10 N nonlinear algebraic equations for N bearings if the casing flexibility is neglected. One must choose an appropriate numerical method as the nonlinear algebraic equations must be solved iteratively [36,37]. In addition, the available numerical methods need a prior knowledge of the approximate location of the solution vector being sought and hence one must be careful in interpreting the numerical results. In this study, we adopted the Newton-Raphson method for its good convergence characteristic [36,37]. To implement this method, equation (2.6) for each bearing is rearranged as

$$\begin{Bmatrix} H_1 \\ H_2 \end{Bmatrix} = \begin{Bmatrix} M_{x\text{bm}} \\ M_{y\text{bm}} \end{Bmatrix} - \sum_j^z r_j Q_j \sin \alpha_j \begin{Bmatrix} \sin \psi_j \\ -\cos \psi_j \end{Bmatrix} = \begin{Bmatrix} 0 \\ 0 \end{Bmatrix} \quad (2.12a)$$

$$\begin{Bmatrix} H_3 \\ H_4 \\ H_5 \end{Bmatrix} = \begin{Bmatrix} F_{x\text{bm}} \\ F_{y\text{bm}} \\ F_{z\text{bm}} \end{Bmatrix} - \sum_j^z Q_j \begin{Bmatrix} \cos \alpha_j \cos \psi_j \\ \cos \alpha_j \sin \psi_j \\ \sin \alpha_j \end{Bmatrix} = \begin{Bmatrix} 0 \\ 0 \\ 0 \end{Bmatrix} \quad (2.12b)$$

where H_1, H_2, \dots, H_5 are functions defined for computational reasons. For an indeterminate system, there are additional functions H_6, H_7, \dots, H_v from the field equations. Using Taylor's series, any function H_k in equations (2.12a,b) can be expanded about the solution vector $X = \{q\}_{\text{bm}}$ for a statically determinate system and $X = [\{q\}_{\text{bm}}^T, \{f\}_{\text{bm}}^T]^T$ for a statically indeterminate system as follows by neglecting second and higher order terms.

$$H_k(X+\delta X) \approx H_k(X) + \sum_j^V \frac{\partial H_k}{\partial X_j} \delta X_j \quad ; \quad k=1,2,3,\dots,V \quad (2.13)$$

The solution for the incremental vector δX can be obtained by setting $H_k(X+\delta X) = 0$ per equations (2.12) and (2.13) which yields a set of linear algebraic equations. This vector δX is added to the previously computed vector X given by $H_k(X) = 0$ for the next iteration until the convergence criterion, say that δX is within a specified tolerance, is satisfied. Our proposed numerical scheme can be summarized as follows: (i) guess bearing displacement vector $\{q\}_{bm}$ and/or load vector $\{f\}_{bm}$, (ii) compute δX and check against a specified tolerance, (iii) add δX to the previous solution vector X and repeat steps (i) and (ii) until the convergence criterion is satisfied. We have found that a few initial guess trials are required in most cases to obtain reasonable results.

2.7 VALIDATION OF PROPOSED MODEL

In order to validate our theory we compare the translational stiffness coefficients of the proposed bearing matrix $[K]_{bm}$ with published analytical and experimental results [14,20,24]. First we apply our theory to predict the nonlinear axial $k_{bzz} = k_{bzz}(\delta_{zm})$ and radial $k_{brr} = k_{brr}(\delta_{rm})$ stiffnesses as shown in Figure 2.6. Our predictions are found to be within 2% of Gargiulo's [14] formulas which are commonly used for both ball and roller bearings.

For the second example case, we consider the ball bearings used by Kraus et al.[24] for an in-situ determination of the bearing stiffness. Using their bearing design parameters, we compute radial stiffness coefficient k_{brr} as a function of the axial preload F_{zbm} . Excellent comparison between theory and experiment is seen in Figure 2.7.

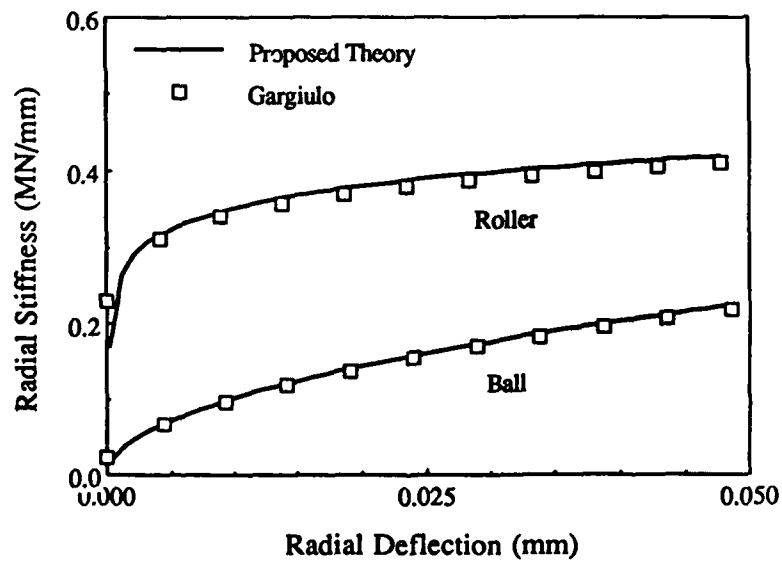
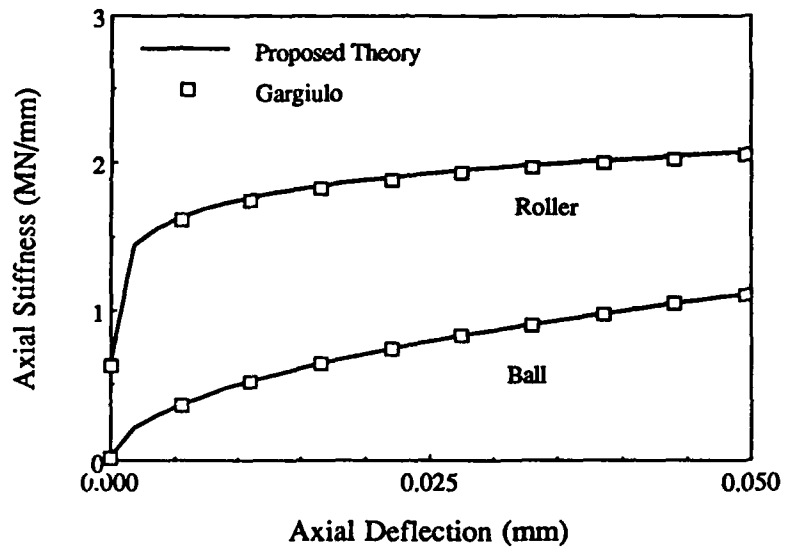


Figure 2.6 Comparison between the proposed theory and Gargiulo's formulas [14] for axial k_{bzz} and radial k_{brr} stiffness coefficients of ball and roller bearings.

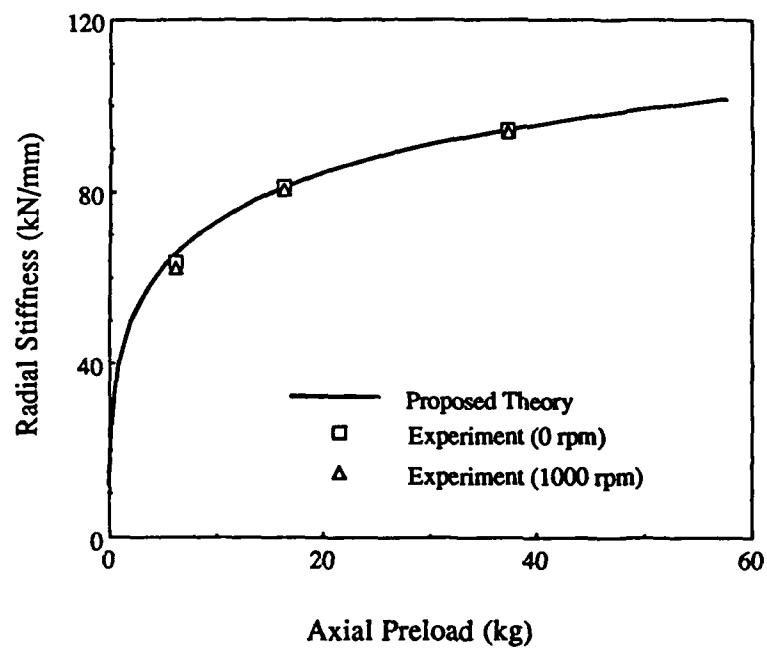


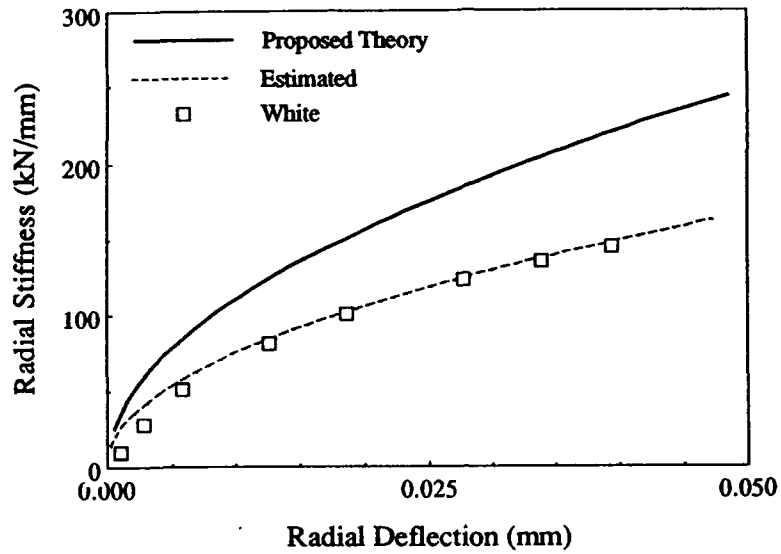
Figure 2.7 Comparison between the proposed theory and the experimental results of Kraus et al.[24] for k_{br} as a function of the mean axial preload.

Finally, we compare our results for the nonlinear radial stiffness k_{br} with those reported earlier by White [20] for both ball and roller bearings. We note discrepancies in Figure 2.8 between our theory and White's results. In order to explain these we now define \hat{k}_{br} using the finite difference approximation which was also used by White: $\hat{k}_{br} \approx \Delta F_{brm} / \Delta \delta_{rm} \approx F_{brm} / (\delta_{rm} - r_L)$. Now a good match is evident in Figure 2.8 between our \hat{k}_{br} values and the data given by White. However, the correct formulation is obviously given by our proposed theory which is based on the analytical partial derivatives $k_{br} = \partial F_{brm} / \partial \delta_{rm}$ as the displacement δ_{rm} may be large.

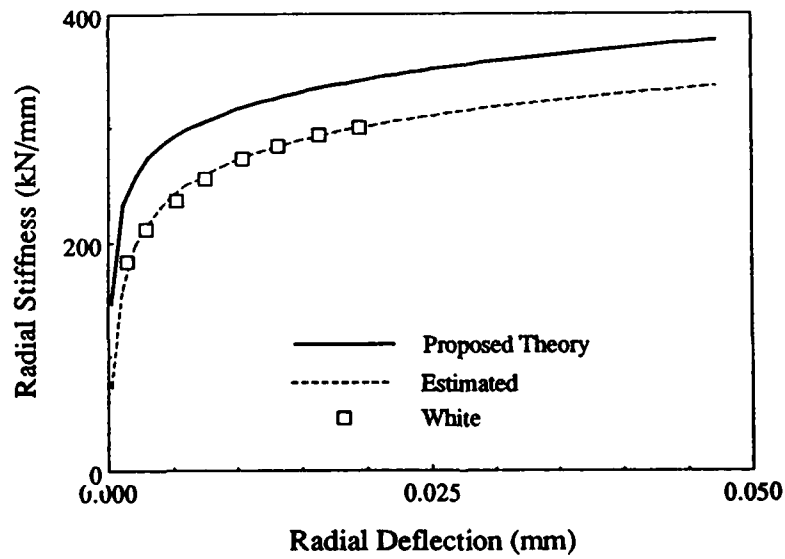
2.8 PARAMETRIC STUDIES

The proposed matrix $[K]_{bm}$ includes a coupling between the casing flexural motion and shaft bending motion which is reflected by some of the dominant off-diagonal, $k_{bx\theta_y}$, $k_{by\theta_x}$, $k_{bz\theta_x}$ and $k_{bz\theta_y}$, and rotational diagonal, $k_{b\theta_x\theta_x}$ and $k_{b\theta_y\theta_y}$, stiffness coefficients; these are labeled as 'coupling coefficients' for discussion purposes. Such stiffness coefficients are investigated further by varying preloading conditions and unloaded contact angle α_0 for both ball (set A) and roller (set B) bearings whose design data are listed in Table 2.1.

The coupling coefficients given a constant mean radial displacement δ_{rm} (radial preload), as shown in Figures 2.9 and 2.10 for both ball and roller bearings respectively, are found to increase as α_0 increases and reach a maximum when α_0 is near 90° . On the other hand, the radial translational stiffness coefficients in the x and y directions are found to decrease as α_0 increases. These observations imply that for deep groove ball type or straight roller type bearing ($\alpha_0 \approx 0^\circ$) the radial stiffness coefficients k_{br} are dominant, but for angular contact ball type or taper roller type bearing ($\alpha_0 > 0^\circ$)



(a)



(b)

Figure 2.8 Comparison between the proposed theory k_{brr} , estimated \hat{k}_{brr} , and White's analytical results [20]. a. Ball bearing. b. Roller bearing.

Table 2.1 Design parameters for typical ball and roller bearings used for parametric studies

Parameters	Set A (ball type)	Set B (roller type)
Load-deflection exponent n	$3/2$	$10/9$
Load-deflection constant K_n (N/m^n)	$8.5 \text{ E}9$	$3.0 \text{ E}8$
Number of rolling element Z	12	14
Radial clearance r_L (mm)	0.00005	0.00175
Pitch radius †† (mm)	19.65	21.25
A_o (mm) †	0.05	—

† Unloaded distance between inner and outer raceway groove curvature centers (see Figure 2.3)

†† Equivalent to r_j for roller bearings and $r_j - A_o/2$ for ball bearings given in equation (2.3)

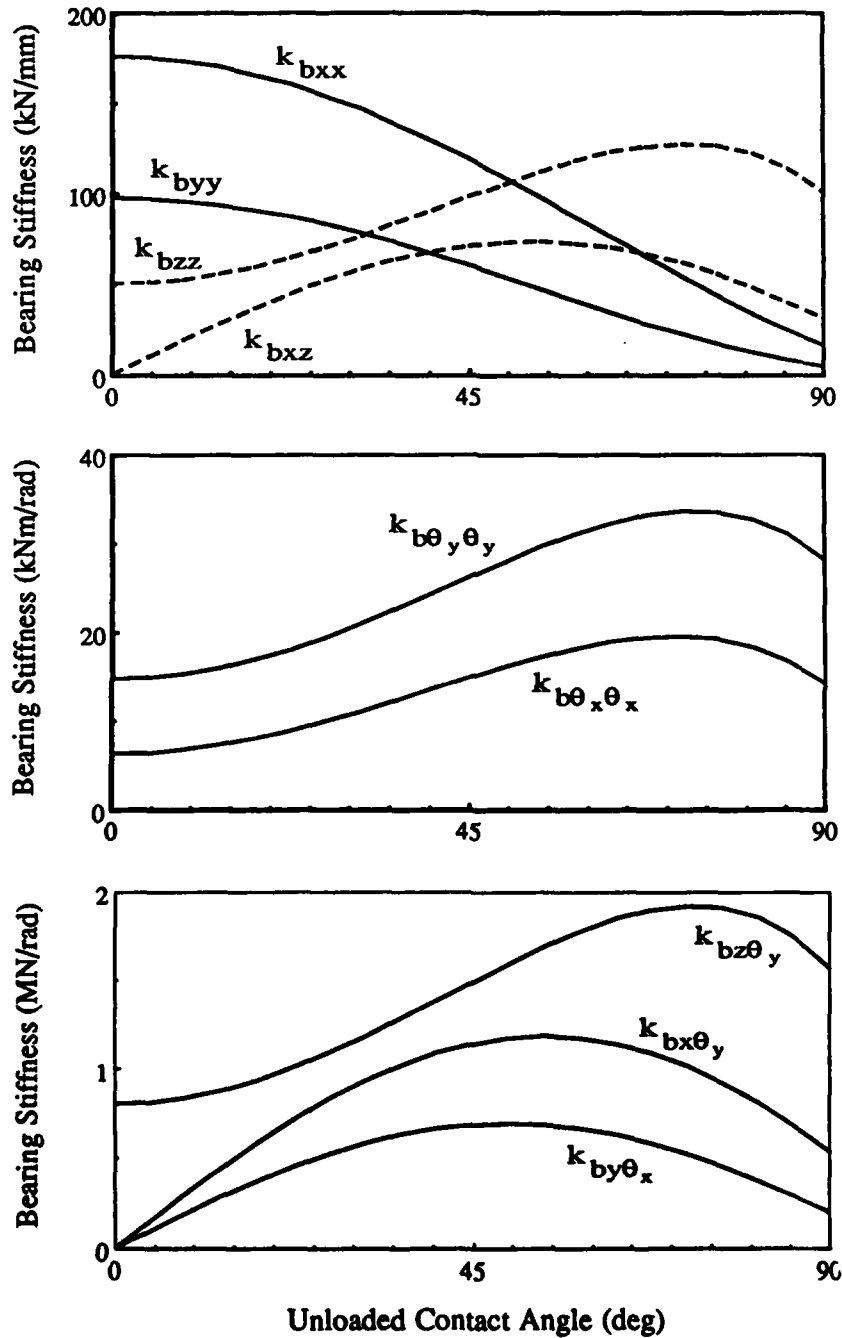


Figure 2.9 Dominant stiffness coefficients of ball bearing set A for $0^\circ \leq \alpha_0 \leq 90^\circ$ and given a constant mean radial bearing displacement $\delta_{xm} = 0.025$ mm.

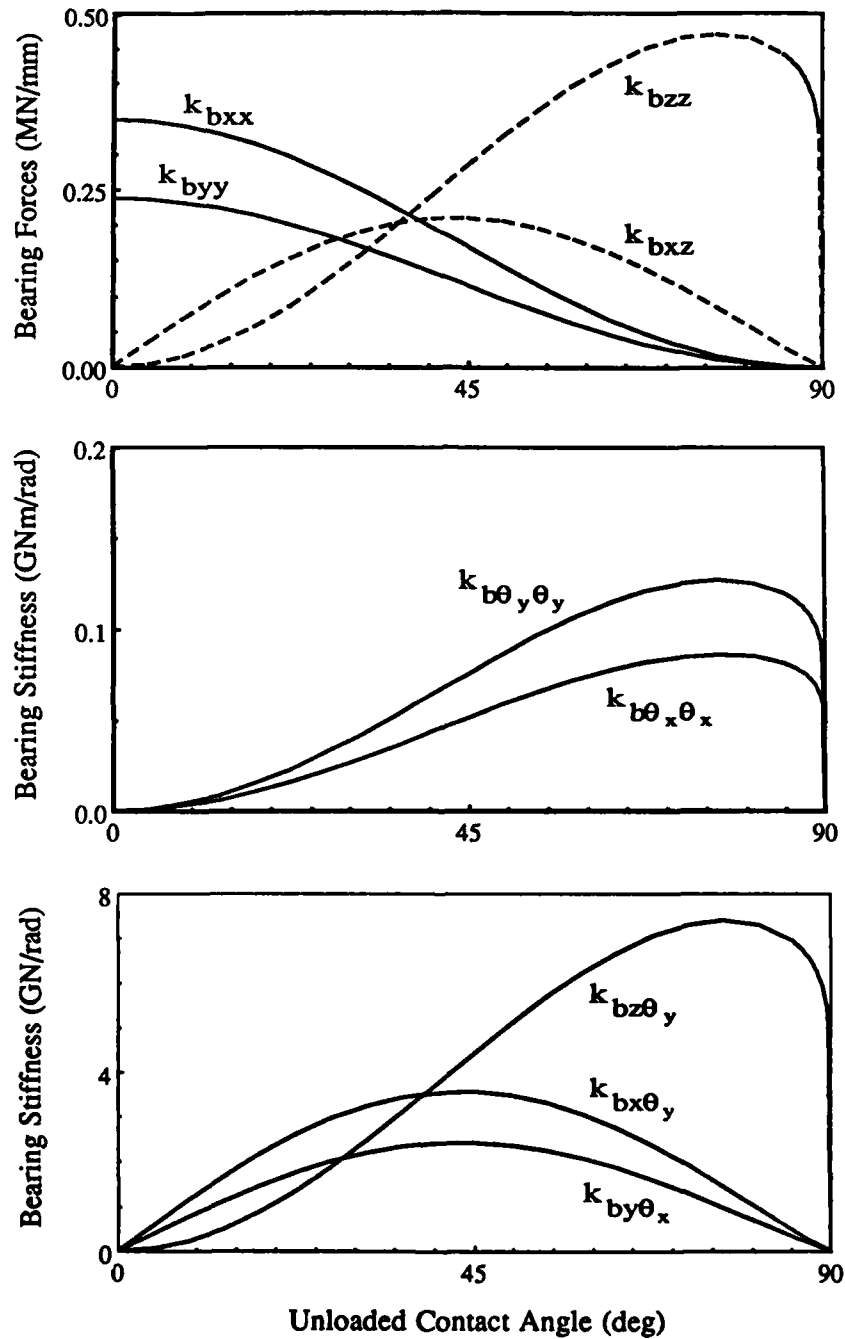


Figure 2.10 Dominant stiffness coefficients of roller bearing set B for $0^\circ \leq \alpha_0 \leq 90^\circ$ and given a constant mean radial bearing displacement $\delta_{xm} = 0.025$ mm.

the coupling terms are more significant. Note that in Figure 2.10, all the stiffness coefficients are zero at $\alpha_0 = 90^\circ$ for the roller type. This is due to the fact that in the thrust roller bearing, radial flanges are included to resist the roller motion in this direction which is not modeled here, and hence these stiffness coefficients must vanish. In addition, thrust roller bearings are designed to carry axial loads [18,31]. On the other hand, ball bearings have finite stiffness coefficients at $\alpha_0 = 90^\circ$ due to the curvature of the raceway which provide some resistance to the radial preloads. In general, the trends in both ball and roller bearing stiffness properties are similar when each is subjected to mean radial displacement or preload.

In the case when the bearings are subjected to mean axial displacement (axial preload), as shown in Figure 2.11 for the ball type and Figure 2.12 for the roller type, the number of nonzero stiffness coefficients are less than those seen for the radial preload only. Again, it is observed that both ball and roller bearings display similar trends. Over mid to high α_0 values, the coupling coefficients are found to be significant. The translational stiffness coefficients are relatively constant except for the axial stiffness which increases as α_0 increases. This is expected due to the inclination of the rolling element line of contact from the x-y plane which increases elastic support in the z-direction. At $\alpha_0 = 0^\circ$, all the stiffness coefficients for roller bearings are zero as there is no constraint in the axial direction. In real bearings such a constraint is provided by the axial flanges [18,31], however this bearing is not designed to carry any axial preload.

Results for the misalignment in ball and roller bearings simulated by specifying a mean bearing angular displacement β_{ym} are shown in Figures 2.13 and 2.14 respectively. The dominant stiffness coefficients are the same as those seen for the

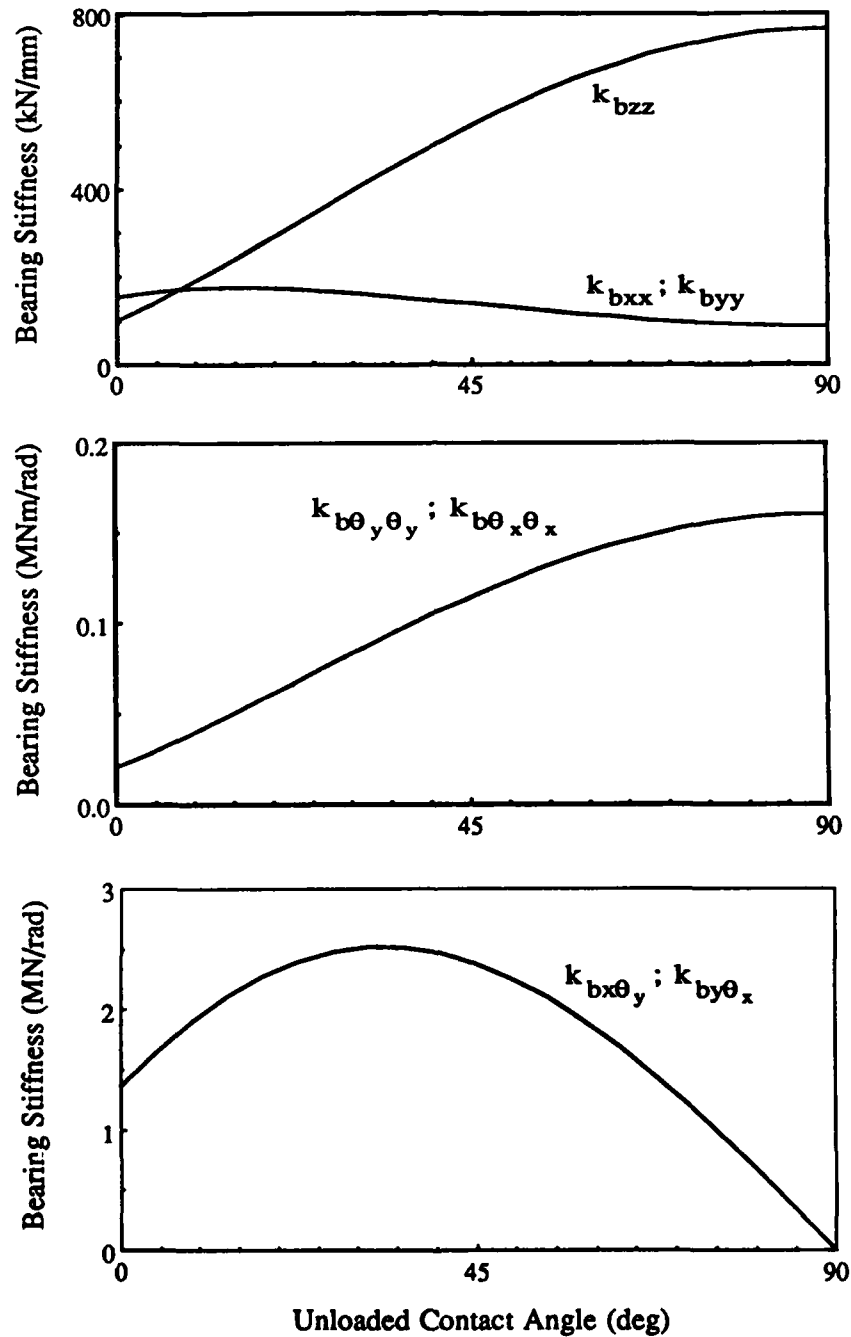


Figure 2.11 Dominant stiffness coefficients of ball bearing set A for $0^\circ \leq \alpha_0 \leq 90^\circ$ and given a constant mean axial bearing displacement $\delta_{zm} = 0.025$ mm.

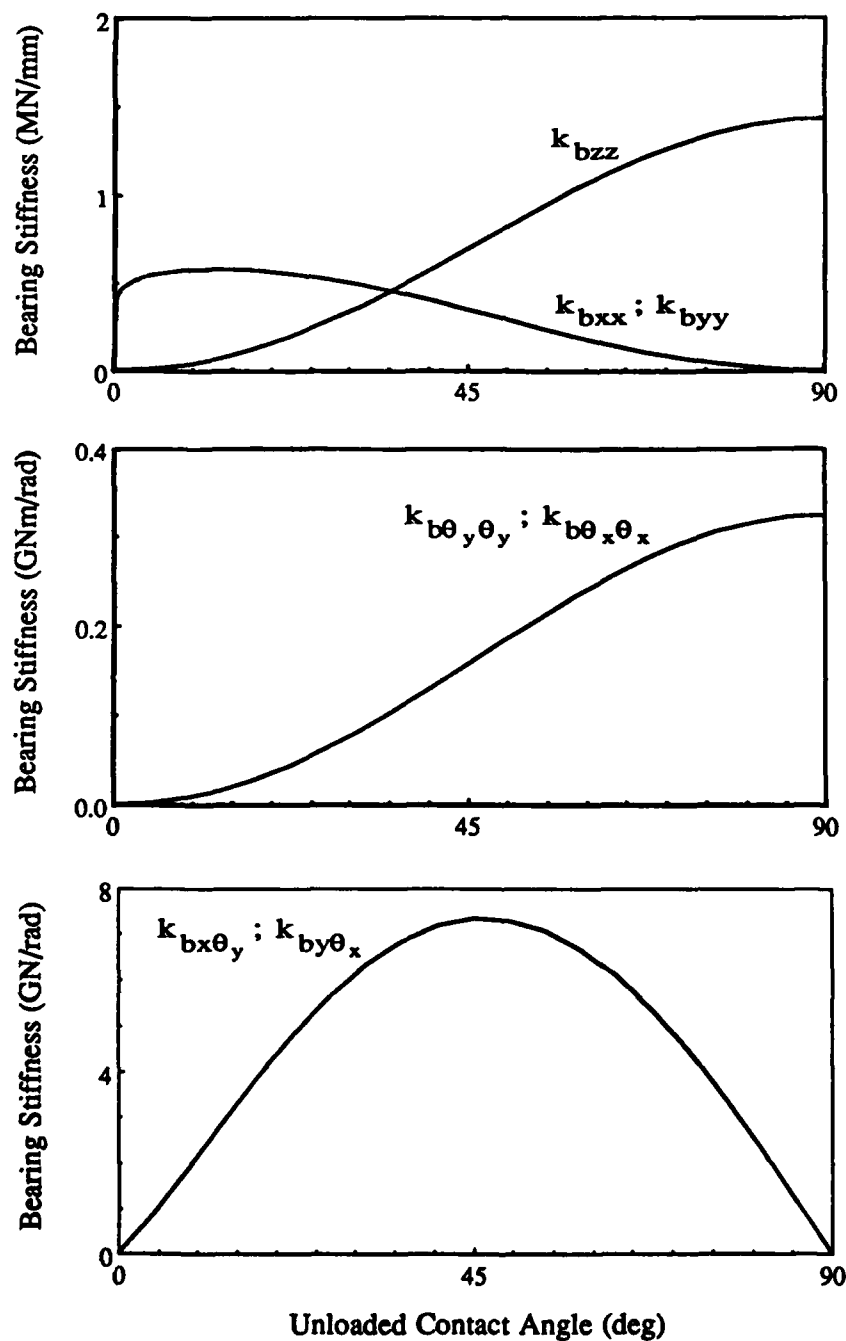


Figure 2.12 Dominant stiffness coefficients of roller bearing set B for $0^\circ \leq \alpha_0 \leq 90^\circ$ and given a constant mean axial bearing displacement $\delta_{zm} = 0.025$ mm.

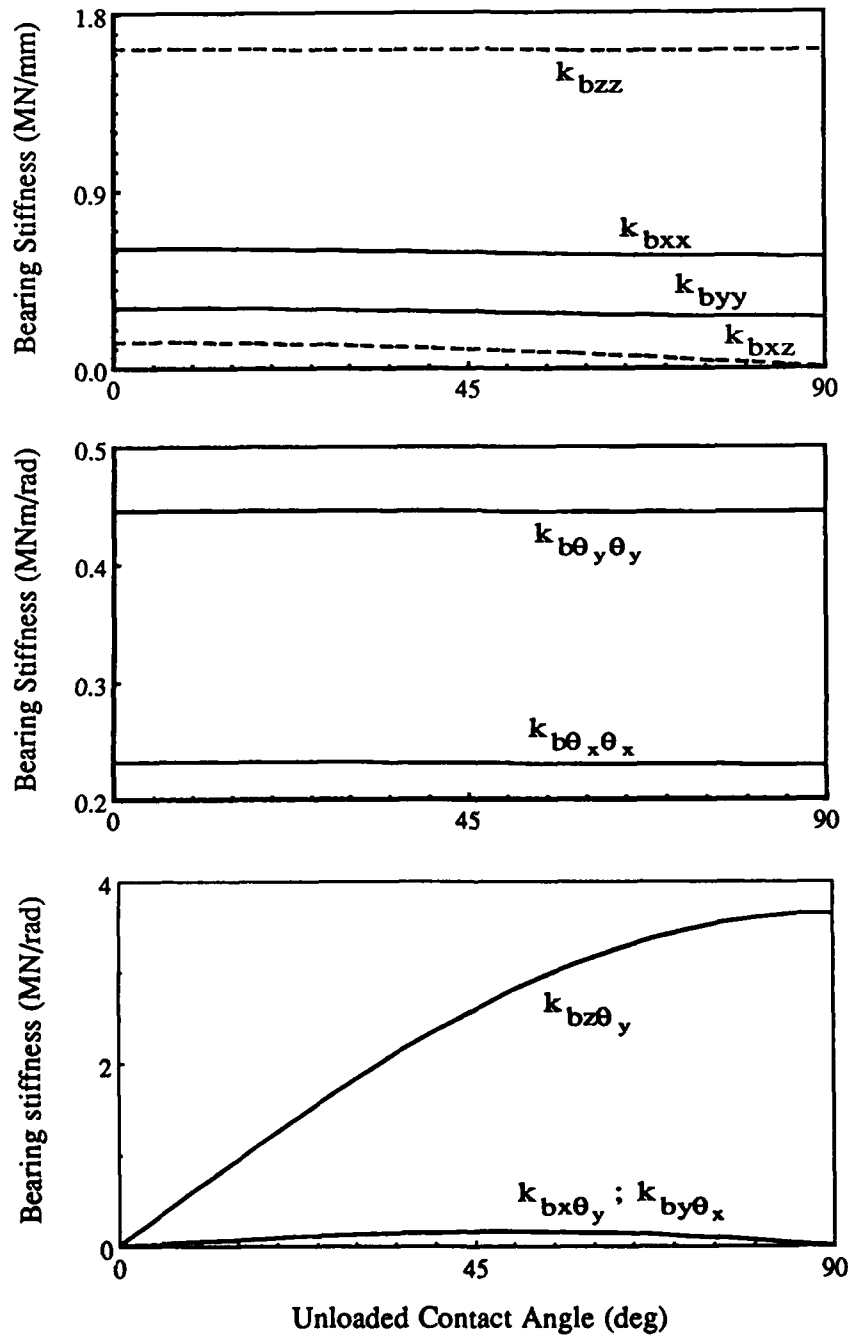


Figure 2.13 Dominant stiffness coefficients of ball bearing set A for $0^\circ \leq \alpha_0 \leq 90^\circ$ and given a constant misalignment $\beta_{ym} = 0.015$ rad.

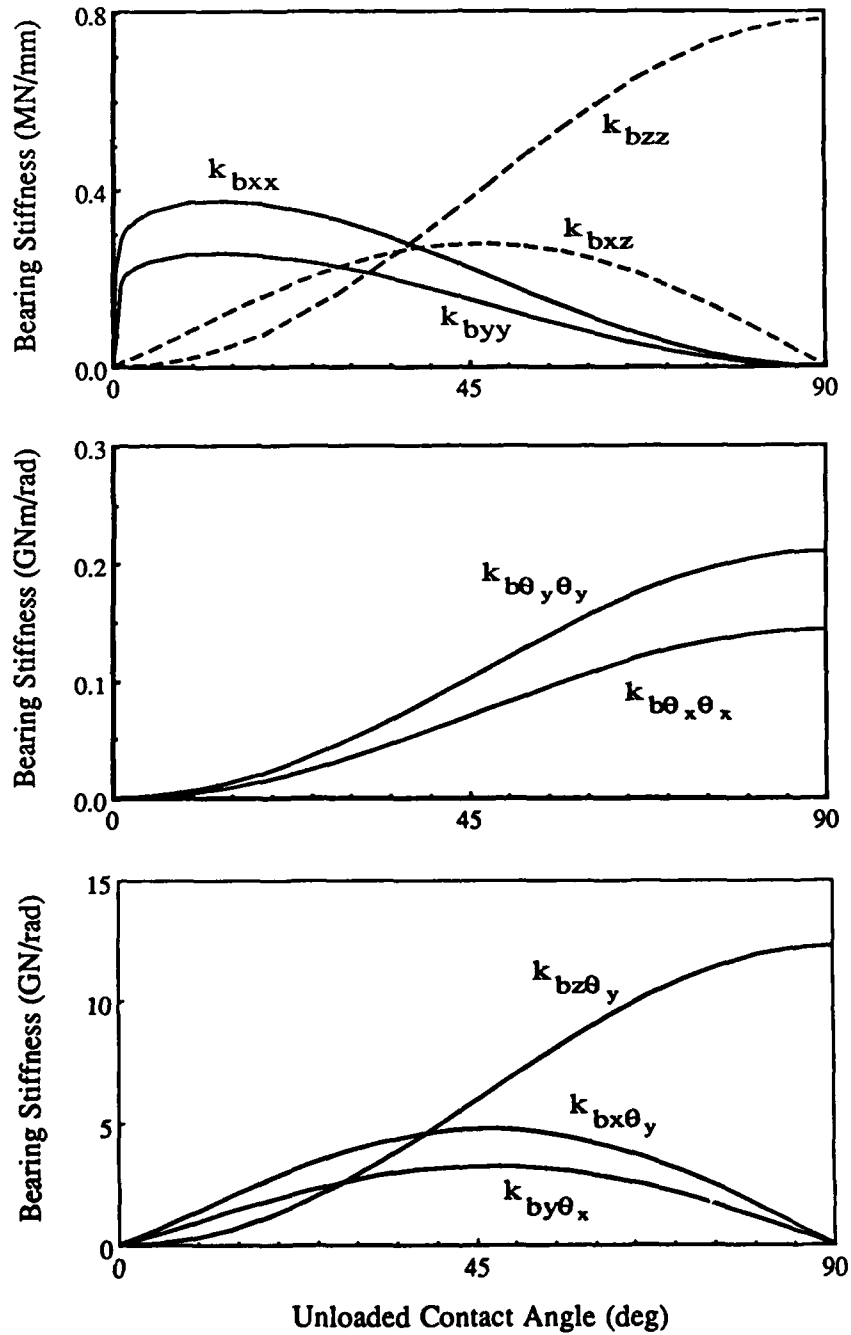


Figure 2.14 Dominant stiffness coefficients of roller bearing set B for $0^\circ \leq \alpha_o \leq 90^\circ$ and given a constant misalignment $\beta_{ym} = 0.015$ rad.

radial preload case. For ball bearings, most of the stiffness coefficients remain constant for $0^\circ \leq \alpha_0 \leq 90^\circ$. On the other hand, the stiffness coefficients for roller bearing have trends similar to those found for the radial preload cases.

From the detailed parametric studies, it is concluded that the nature of $[K]_{bm}$ is dictated by the bearing type, α_0 and preloads. Also, the coupling coefficients are not negligible in most cases as assumed previously by many investigators.

2.9 CONCLUSIONS

Results of Section 2.8, which show similar trends for some of the cases, imply that there may be a systematic approach to characterize the proposed bearing stiffness matrix $[K]_{bm}$. From the kinematic and geometrical considerations, it is always possible to impose any bearing displacement vector $\{q\}_{bm}$ which denotes relative rigid body motions between the inner and outer rings as long as the rolling element is still within the elastic deformation regime. On the other hand, an arbitrary application of $\{f\}_{bm}$ may not produce a singular displacement response from the bearing due to its kinematic and geometrical constraints. Hence, we compute $[K]_{bm}$ and $\{f\}_{bm}$ by systematically varying $\{q\}_{bm}$. The results of all possible forms of $[K]_{bm}$ are listed in Table 2.2 and 2.3 for ball and roller bearings respectively. Also included here are the current bearing models which are based on the translational spring descriptions; these models do not show any coupling. Note that the exact values of the stiffness coefficients are not given as these depend on specific parameters; therefore only the dominant k_{bij} terms are listed for all possible bearing load configurations along with the corresponding $\{q\}_{bm}$ and α_0 . Also, note that not all combinations of the bearing loads are possible which complicates bearing stiffness calculations further, especially for the numerical method II. Tables 2.2

Table 2.2 Comparison between the proposed and current ball bearing stiffness coefficients. (p = x, y; i = x, y but i ≠ p)

Mean bearing ^{††} loads	Mean bearing displacement			Dominant stiffness coefficients	
	$\alpha_0 \approx 0^\circ$	$0^\circ < \alpha_0 < 90^\circ$	$\alpha_0 \approx 90^\circ$	current [†]	proposed ^{†††}
F_{pm}	δ_{pm}	—	—	k_{pp}	$k_{xx}, k_{yy}, k_{zz}, k_{\theta_x \theta_x}, k_{\theta_y \theta_y}, k_{z \theta_i}$
F_{zm}	δ_{zm}	δ_{zm}	—	k_{pp}, k_{zz}	$k_{xx}, k_{yy}, k_{zz}, k_{\theta_x \theta_x}, k_{\theta_y \theta_y}, k_{x \theta_y}, k_{y \theta_x}$
F_{zm}	—	—	δ_{zm}	k_{zz}	$k_{xx}, k_{yy}, k_{zz}, k_{\theta_x \theta_x}, k_{\theta_y \theta_y}$
M_{pm}	β_{pm}	—	—	—	$k_{xx}, k_{yy}, k_{zz}, k_{\theta_x \theta_x}, k_{\theta_y \theta_y}, k_{iz}$
F_{zm}, M_{pm}	—	—	δ_{zm}, β_{pm}	k_{zz}	$k_{xx}, k_{yy}, k_{zz}, k_{\theta_x \theta_x}, k_{\theta_y \theta_y}, k_{z \theta_p}$
F_{xm}, F_{ym}	δ_{xm}, δ_{ym}	—	—	k_{pp}	$k_{xx}, k_{yy}, k_{zz}, k_{\theta_x \theta_x}, k_{\theta_y \theta_y}, k_{xy}, k_{\theta_x \theta_y}, k_{z \theta_x}, k_{z \theta_y}$
F_{pm}, M_{pm}	δ_{pm}, β_{pm}	—	—	k_{pp}	$k_{xx}, k_{yy}, k_{zz}, k_{\theta_x \theta_x}, k_{\theta_y \theta_y}, k_{x \theta_x}, k_{y \theta_y}, k_{pz}, k_{z \theta_i}$
M_{xm}, M_{ym}	δ_{pm}, β_{pm}	—	—	—	$k_{xx}, k_{yy}, k_{zz}, k_{\theta_x \theta_x}, k_{\theta_y \theta_y}, k_{xy}, k_{xz}, k_{yz}, k_{\theta_x \theta_y}$
F_{pm}, F_{zm}, M_{im}	$\delta_{pm}, \delta_{zm}, \beta_{im}$	$\delta_{pm}, \delta_{zm}, \beta_{im}$	$\delta_{pm}, \delta_{zm}, \beta_{im}$	k_{pp}, k_{zz}	$k_{xx}, k_{yy}, k_{zz}, k_{\theta_x \theta_x}, k_{\theta_y \theta_y}, k_{x \theta_y}, k_{y \theta_x}, k_{pz}, k_{z \theta_i}$
F_{zm}, M_{xm}, M_{ym}	$\delta_{zm}, \beta_{xm}, \beta_{ym}$	$\delta_{zm}, \beta_{xm}, \beta_{ym}$	$\delta_{zm}, \beta_{xm}, \beta_{ym}$	k_{pp}, k_{zz}	$k_{xx}, k_{yy}, k_{zz}, k_{\theta_x \theta_x}, k_{\theta_y \theta_y}, k_{xy}, k_{\theta_x \theta_y}, k_{z \theta_x}, k_{z \theta_y}$
$\{f\}_m$	combinations of $\{q\}_m$			k_{pp}, k_{zz}	all non-zero except θ_z terms

† Ideal boundary condition models used to describe the bearing are not tabulated.

†† Here the subscript b which implies bearing has been omitted for brevity.

††† All terms associated with θ_z are zero because of the free rotation about the z axis.

Table 2.3 Comparison between the proposed and current roller bearing stiffness coefficients. ($p = x, y$; $i = x, y$ but $i \neq p$)

Mean bearing ^{††} loads	Mean bearing displacement			Dominant stiffness coefficients	
	$\alpha_o \approx 0^\circ$	$0^\circ < \alpha_o < 90^\circ$	$\alpha_o \approx 90^\circ$	current [†]	proposed ^{†††}
F_{pm}	δ_{pm}	—	—	k_{pp}	k_{bpp}
F_{zm}	—	δ_{zm}	—	$k_{pp}k_{zz}$	$k_{xx}, k_{yy}, k_{zz}, k_{\theta_x\theta_x}, k_{\theta_y\theta_y}, k_{x\theta_y}, k_{y\theta_x}$
F_{zm}	—	—	δ_{zm}	k_{zz}	$k_{zz}, k_{\theta_x\theta_x}, k_{\theta_y\theta_y}$
F_{zm}, M_{pm}	—	—	δ_{zm}, β_{pm}	k_{zz}	$k_{zz}, k_{\theta_x\theta_x}, k_{\theta_y\theta_y}, k_{z\theta_p}$
F_{xm}, F_{ym}	δ_{xm}, δ_{ym}	—	—	k_{pp}	k_{xx}, k_{yy}, k_{xy}
F_{pm}, F_{zm} M_{im}	—	δ_{pm}, δ_{zm} β_{im}	—	k_{pp}, k_{zz}	$k_{xx}, k_{yy}, k_{zz}, k_{\theta_x\theta_x}, k_{\theta_y\theta_y}, k_{x\theta_y}, k_{y\theta_x}, k_{pz}, k_{z\theta_i}$
F_{zm}, M_{xm}, M_{ym}	—	—	$\delta_{zm}, \beta_{xm}, \beta_{ym}$	k_{zz}	$k_{zz}, k_{\theta_x\theta_x}, k_{\theta_y\theta_y}, k_{\theta_x\theta_y}, k_{z\theta_x}, k_{z\theta_y}$
$\{f\}_m$	combinations of $\{q\}_m$			k_{pp}, k_{zz}	all non-zero except θ_z terms

† Ideal boundary condition models used to describe the bearing are not tabulated.

†† Here the subscript b which implies bearing has been omitted for brevity.

††† All terms associated with θ_z are zero because of the free rotation about the z axis.

and 2.3 should provide some insight to the solution of the nonlinear algebraic bearing load-deflection equations which requires a prior knowledge of the type of solution being sought as outlined earlier. In most practical problems, mean bearing loads are typically known. This knowledge can be combined with Table 2.2 or 2.3 to formulate the nonlinear load-deflection equations in the simplest form by deleting all of the zero displacement terms.

Tables 2.2 and 2.3 show that the coupling coefficients $k_{bx\theta_y}$, $k_{by\theta_x}$, $k_{bz\theta_x}$, $k_{bz\theta_y}$, $k_{b\theta_x\theta_x}$ and $k_{b\theta_y\theta_y}$ are found to be dominant in most of the ball bearing cases, and only in some of the roller bearing cases. This is essentially due to the curvature of the raceway in ball bearing which invariably causes the rolling element to orient itself such that $0^\circ < \alpha_j < 90^\circ$ which generates ball loads in the z direction as well. However, in the roller bearing case where $\alpha_j = \alpha_0$, the same phenomenon does not occur when $\alpha_0 = 0^\circ$ or 90° , and the coupling coefficients are seen only when $\alpha_0 \neq 0^\circ$ or 90° . In fact for the 0° and 90° unloaded contact angle cases, the stiffness coefficients associated with x and y directions and those associated with the z , θ_x , and θ_y directions do not exist simultaneously; the former is dominant when $\alpha_0 = 0$ and the latter prevails when $\alpha_0 = 90^\circ$. Another case of interest here is the case when bearing loads are complex as given by the last row in Tables 2.2 and 2.3 where all of the bearing stiffness coefficients unrelated to the rotational degree of freedom θ_z exist. Solution to these cases may require a large number of iterations.

In summary, we have developed a comprehensive bearing stiffness matrix from the basic principles which includes all possible rigid body degrees of freedom of a bearing system. This matrix has been validated partially using several analytical and experimental examples. Further validation of $[K]_{bm}$ is not possible as coupling

coefficients are never measured [24,30]. Nonetheless, our theory is general in nature and is applicable to even those configurations which may be different from the generic case shown in Figure 2.1. Further research is required to incorporate tribological issues [32,33] in this formulation. However the proposed stiffness matrix in its present form, unlike the current models, is clearly capable of explaining the nature of vibration transmission through bearings – this is the subject of Chapters III and IV of this report, which will also include further comparisons between theory and experiment.

CHAPTER III

BEARING SYSTEM STUDIES

3.1 INTRODUCTION

Current bearing models [10-15] can not explain how the vibratory motion may be transmitted from the rotating shaft to the casing and other connecting structures in rotating mechanical equipment. For instance, experimental results [9,16,17] have shown that casing plate motion for a system similar to Figure 3.1 is primarily flexural or out-of-plane type given only the bending motion on the shaft. Using existing vibration models, only in-plane type motions on the casing plate are obtained. Such limitations associated with current bearing models have been discussed thoroughly in Chapter II of this report. Also in Chapter II, a new mathematical model for the precision rolling element bearings has been developed in order to clarify this issue qualitatively and quantitatively.

This study extends the proposed bearing formulation and demonstrates its superiority over the existing models in vibration transmission analyses. A schematic of a generic system with a flexible shaft rotating at constant speed Ω_z , flexible casing and mount is shown in Figure 3.1. The shaft is supported by a rolling element bearing which is modeled by a stiffness matrix $[K]_{bm}$ of dimension 6 as proposed in Chapter II. The excitations at the rotating shaft are given in terms of an alternating load vector $\{f(t)\}_{sa} = \{F_{jsa}(t), T_{jsa}(t)\}^T = \{f(t)\}_s - \{f\}_{sm}; j=x,y,z$, where $F_{jsa}(t)$ and $T_{jsa}(t)$ are the

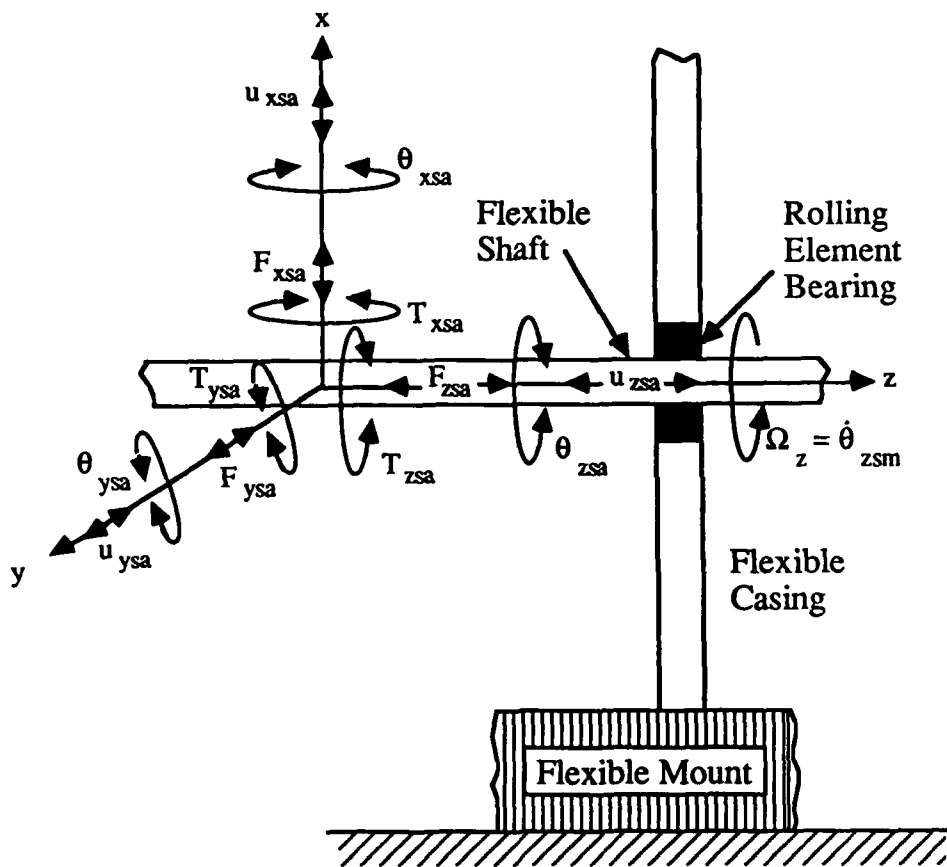


Figure 3.1 Schematic representation of the vibration transmission problem. Here the flexible shaft is subjected to alternating forces $F_{jsa}(t)$ and torques $T_{jsa}(t)$ where $j = x, y$ or z , is the direction and subscript a implies alternating. Also, θ is the angular displacement and u is the translational displacement.

alternating force and torque respectively, $\{f(t)\}_s$ is the total load vector of dimension 6, $\{f\}_{sm}$ represents the mean load vector, and superscript T implies the transpose. In the vibration analysis, $\{f\}_{sm}$ and bearing preloads are not included as they do not appear in the governing equations of the linear vibration model but are used for computing $[K]_{bm}$. The effect of bearing coupling coefficients, which are off-diagonal and rotational diagonal terms of $[K]_{bm}$ as described in Chapter II, on the eigensolution, forced vibration, and vibration transmission through bearings is evaluated. Our theory will be illustrated and validated through 3 physical system example cases; experimental verification is also included.

3.2 LITERATURE REVIEW

The existing bearing models which assume either ideal boundary conditions [10-12] for the shaft or translational stiffness elements [13-15] have already been discussed in Chapter II. Various formulas for estimating translational stiffness coefficients commonly used by researchers have been compared with our proposed $[K]_{bm}$ formulation. These simple bearing models are widely used in vibration models of the rotor dynamic systems, which typically exclude casing and mount dynamics, to calculate critical speeds, responses due to shaft excitations such as mass unbalance and gear transmission error, and dynamic stability [10-15]. In most of these cases, the vibration transmission through bearings is never or not the primary issue, and thus the bearing models tend to be simplified. None of the current models studied [20-22,24] can fully explain vibration transmission through bearings in systems similar to Figure 3.1. In 1979 White [20] evaluated the rolling element bearing vibration transfer

characteristics using a two degrees of freedom (DOF) vibration model of the system shown in Figure 3.1. His formulation is based on only the radial bearing stiffness coefficient k_{brr} . He concluded that an increase in preload increases k_{brr} and system natural frequencies. He also found that the effect of bearing nonlinearity is negligible at higher preloads. In 1987 Kraus et al. [24] proposed a single degree of freedom model for a similar physical system (with a very compliant mount) to estimate k_{brr} from measured vibration transmission spectra. In both of these studies, the coupling coefficients of $[K]_{bm}$ are not included.

In 1982 Rajab [21] philosophically proposed a bearing stiffness matrix which consists of k_{brr} , $k_{br\theta}$ and $k_{b\theta\theta}$ coefficients. Some of the key features of his model are also summarized in Reference [22]. This model is in fact a subset of our $[K]_{bm}$ as shown in Chapter II of this report. He incorporated his bearing model in a system study using a commercial structural synthesis program [38]. However, based on our study we have inferred that he incorrectly synthesized the system model given the plate experimental modal data, shaft finite element model and analytical bearing model. Moreover, an error was found when he converted $k_{br\theta}$ and $k_{b\theta\theta}$ coefficients to "effective stiffness coefficients" which he claimed to couple the shaft bending motion to the plate out-of-plane motion. Also, this method excludes the bearing rotational degree of freedom, which from our study was found to be important.

3.3 ASSUMPTIONS AND OBJECTIVES

Linear discrete vibration models of the generic system shown in Figure 3.1 are used to incorporate $[K]_{bm}$ and to characterize the vibration transmission through rolling

element bearings. The stiffness coefficients of $[K]_{bm}$ are evaluated using the analytical expressions presented in Chapter II of this report. Effect of the gyroscopic moment on the shaft dynamics is not included. Since the bearing system is statically indeterminate, the direct stiffness formulation technique is used to obtain the system governing equations as opposed to the flexibility formulation. The governing equations for the system vibration model can be given in the matrix form as

$$[M]\{\ddot{q}(t)\}_a + [C]\{\dot{q}(t)\}_a + [K]\{q(t)\}_a = \{f(t)\}_a \quad (3.1)$$

where $[M]$, $[C]$ and $[K]$ are the system mass, damping and stiffness matrices respectively, and $\{q(t)\}_a$ and $\{f(t)\}_a$ are defined as the generalized alternating displacement and applied load vectors respectively. Due to the linearity of the vibrating system, mean shaft loads $\{f\}_{bm}$ and preloads do not directly affect the dynamic response of the rotating system and hence are excluded from equation (3.1). However, $\{f\}_{bm}$ and bearing preloads are assumed to be constant to ensure a time-invariant $[K]_{bm}$ matrix which depends only on these mean loads or on the mean deflection operating points. Accordingly, only the alternating shaft loads $\{f(t)\}_{sa}$ in Figure 3.1 which represent typical machine excitation due to the kinematic errors, mass unbalances and torque fluctuations are included in the forced vibration problem. The energy dissipation associated with the rolling element bearings is assumed to be an energy equivalent viscous damping matrix $[C]_b = \sigma [K]_{bm}$ where σ is the Rayleigh damping matrix proportionality constant. Dynamic instabilities due to the oil whirl phenomenon and asymmetry of rotating elements [11,12] are clearly beyond the scope of this study and hence are not considered here.

The specific objectives of this chapter are to: (i) incorporate the proposed bearing matrix $[K]_{bm}$, developed in Chapter II of this report, in the linear discrete vibration model of the rotating mechanical equipment as described by equation (3.1) using both the lumped parameter and dynamic finite element methods, (ii) evaluate the dynamic stability of the proposed bearing system model using the Liapunov's second method, (iii) calculate eigensolution and forced harmonic responses, and predict vibration transmission through rolling element bearings for three example cases, (iv) demonstrate the advantages of our formulation over the existing models by Kraus et al. [24] and White [20], and (v) validate the proposed theory by comparing analytical prediction with experimental data on an analogous system.

3.4 SYSTEM GOVERNING EQUATIONS

3.4.1 Method A: Lumped Parameter Model

The proposed bearing matrix $[K]_{bm}$ can be easily implemented in equation (3.1). Note that, the coupling coefficients of $[K]_{bm}$ provide the capability to predict casing rigid body angular $\theta_{jca}(t)$, $j=x,y,z$, and translational $u_{jca}(t)$ motions given only the unidirectional transverse shaft forces. Hence we can couple the shaft motions to the motions of a casing of a system similar to Figure 3.1 but with rigid shaft and rigid casing using a lumped parameter model. The bearing preloads can now be included in the mean shaft load vector $\{f\}_{bm}$ by a direct vector addition as the rigid shaft can be assumed to be a single lumped mass for this purpose. An alternating displacement vector $\{q(t)\}_a = \{ \{q(t)\}_{sa}^T, \{q(t)\}_{ca}^T \}^T$, is defined where $\{q(t)\}_{sa} = \{u_{jsa}(t), \theta_{jsa}(t)\}^T$ and $\{q(t)\}_{ca} = \{u_{jca}(t), \theta_{jca}(t)\}^T$, $j=x,y,z$, are the shaft and casing alternating

displacement vectors respectively. The governing equations of motion for this generic vibration model with DOF = 12 are given by equation (3.1) with

$$[M] = \begin{bmatrix} [M]_s & [0] \\ [0] & [M]_c \end{bmatrix} ; \quad [K] = \begin{bmatrix} [K]_{bm} & -[K]_{bm} \\ -[K]_{bm} & [K]_{bm} + [K]_v \end{bmatrix} \quad (3.2a,b)$$

$$[C] = \sigma [K] ; \quad \{f(t)\}_a = \begin{Bmatrix} \{f(t)\}_{sa} \\ \{0\} \end{Bmatrix} \quad (3.2c,d)$$

$$[K]_{bm} = \begin{bmatrix} k_{bxx} & k_{bxy} & k_{bxz} & k_{bx\theta_x} & k_{bx\theta_y} & 0 \\ & k_{byy} & k_{byz} & k_{by\theta_x} & k_{by\theta_y} & 0 \\ & & k_{bzz} & k_{bz\theta_x} & k_{bz\theta_y} & 0 \\ & & & k_{b\theta_x\theta_x} & k_{b\theta_x\theta_y} & 0 \\ & \text{symmetric} & & & k_{b\theta_y\theta_y} & 0 \\ & & & & & 0 \end{bmatrix} \quad (3.2e)$$

where the stiffness matrices $[K]_{bm}$ and $[K]_v$ pertain to the bearing and mount respectively, and the matrices $[M]_s$ and $[M]_c$ are diagonal shaft and casing mass matrices respectively; each matrix of dimension 6. Specific examples of this method along with the eigensolution and forced response studies will be presented in Sections 3.7 and 3.8.

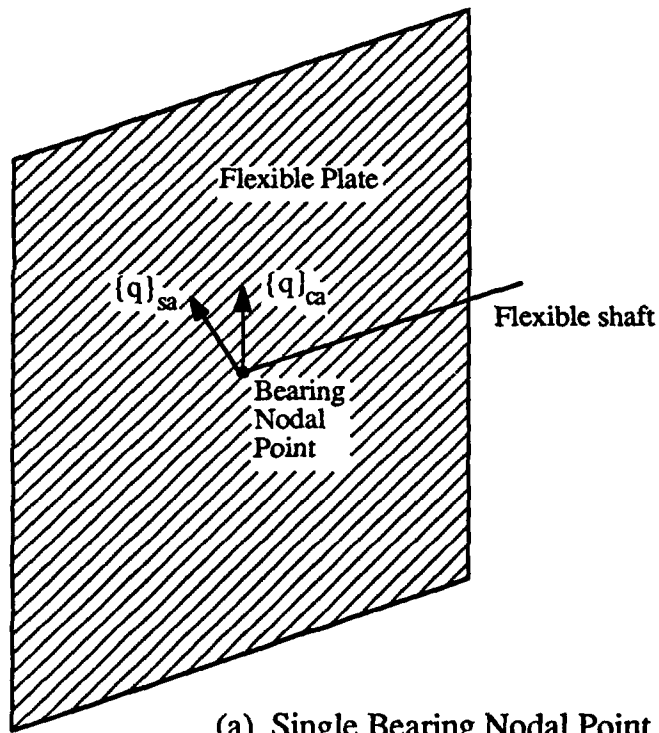
3.4.2 Method B: Dynamic Finite Element Formulation

Consider the dynamic finite element method of incorporating $[K]_{bm}$ in equation (3.1) especially when shaft and casing plate are elastically deformable over the frequency range of interest. This method is different from the lumped parameter formulation of Section 3.4.1 which assumes non-compliant shaft and casing. For

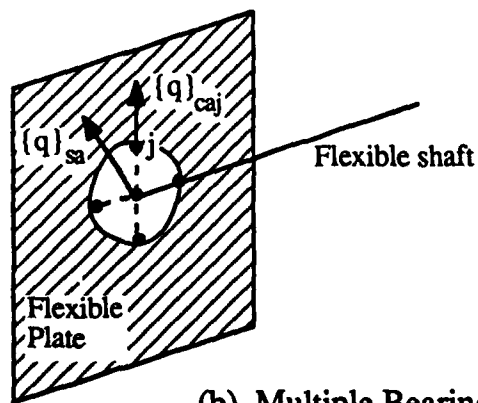
example, if the flexible casing plate is considered to be very large compared to the bearing dimensions, then the bearing nodal point on the shaft can be coupled to only one bearing nodal point on the plate as shown in Figure 3.2a. Accordingly, the present form of $[K]_{bm}$ is implemented in the finite element model as a generalized stiffness matrix like the lumped parameter model. On the other hand, when the flexible casing plate dimensions are finite and of the order of bearing dimensions, then several bearing nodal points are considered as shown in Figure 3.2b. The discretization philosophy here assumes that a relative displacement vector, given by the difference between the averaged displacement vector of bearing nodal points on the plate and the displacement vector of a bearing nodal point on the shaft, is equivalent to the actual rigid body bearing motion. Accordingly, we divide the bearing stiffness coefficients equally among all the generalized stiffness elements connecting the bearing nodal points on the plate to a single bearing nodal point on the shaft. In the limit, where all the bearing nodal points on the plate are collapsed to a single nodal point, $[K]_{bm}$ is recovered as in the first method. Our finite element formulation uses conventional structural elements typically available in commercial software programs [39] – this will be illustrated in Section 3.9. Other features of this method are similar to those discussed earlier in Section 3.4.1.

3.4.3 Other Methods

Alternate methods of incorporating $[K]_{bm}$ in equation (3.1) such as finite difference which is similar to method B, flexibility, component mode synthesis and transfer matrix formulations are also possible. In the flexibility formulation, the bearing flexibility matrix can be obtained by inverting a subset of the bearing stiffness matrix $[K]_{bms}$ which excludes zeroes corresponding to θ_z angular direction from $[K]_{bm}$. In the



(a) Single Bearing Nodal Point on the Plate



(b) Multiple Bearing Nodal Points on the Plate

Figure 3.2 Discretization method for implementation of $[K]_{bm}$ in finite element model of a system similar to Figure 3.1. Here $\{q(t)\}_{sa}$ and $\{q(t)\}_{ca}$ are the alternating shaft and plate displacement vectors at bearing location respectively. Subscript a implies alternating component.

transfer matrix method, the field matrix $[T]_b$ for a bearing can be easily related to $[K]_{bms}$.

$$\begin{Bmatrix} \{q(t)\}_{sa} \\ \{f(t)\}_{sa} \end{Bmatrix} = [T]_b \begin{Bmatrix} \{q(t)\}_{ca} \\ \{f(t)\}_{ca} \end{Bmatrix} \quad ; \quad [T]_b = \begin{bmatrix} [I] & [K]_{bms}^{-1} \\ [0] & [I] \end{bmatrix} \quad (3.3a,b)$$

where $\{ \{q(t)\}_{sa}^T, \{f(t)\}_{sa}^T \}^T$ and $\{ \{q(t)\}_{ca}^T, \{f(t)\}_{ca}^T \}^T$ are now the state vectors at bearing locations on the shaft and casing plate respectively. Equation (3.3) can now be integrated with transfer matrices of the shaft and plate which are well documented in References [40,41]. Direct application of these alternate methods [40-43] are beyond the scope of this paper and are left for further research.

3.5 BEARING SYSTEM STABILITY

The stability of the proposed linear, non-gyroscopic model of a bearing system similar to Figure 3.1, which is governed by equation (3.1) with $\{f(t)\}_a = \{0\}$, can be determined using several techniques such as Liapunov's stability method, Routh-Hurwitz criteria, or from the direct evaluation of system eigenvalues. Here the Liapunov's second method is used for its simplicity when applied to such a vibration model [44,45]. If the system matrices $[M]$, $[C]$ and $[K]$ of equation (3.1) are always symmetric and positive definite, then the system is asymptotically stable per Liapunov. The first condition is directly satisfied since $[M]$, $[C]$ and $[K]$ are symmetric. Further, since $[M]$ is diagonal and consists of only positive entries, it is clearly positive definite. For $[K]$, the positive definite test can be performed by evaluating its principal minor

determinants which is demonstrated here for the generic lumped parameter model. Consider the decomposition of $[K]$ given by equation (3.2) into a product of 3 matrices

$$[K] = \begin{bmatrix} [I] & [0] \\ -[I] & [I] \end{bmatrix} \begin{bmatrix} [K]_{bm} & [0] \\ [0] & [K]_v \end{bmatrix} \begin{bmatrix} [I] & -[I] \\ [0] & [I] \end{bmatrix} \quad (3.4)$$

where the square submatrix $[0]$ of the appropriate dimension consists of only zero entries, $[I]$ is an identity matrix of the same dimension, and $[K]_{bm}$ and $[K]_v$ have been defined in Section 3.4.1. The determinant of $[K]$ is the product of the determinants of the three matrices on the right hand side of equation (3.4)

$$|K| = |[K]_v| |[K]_{bm}| \quad (3.5)$$

If $|[K]_{wj}| > 0$, $w, j = 1, 2, \dots, P$ and $P = 1, 2, \dots, 12$, $[K]$ is positive definite. Other principal minor determinant with $P < 12$ can be obtained by excluding the stiffness coefficients which are not entries in the principal submatrix of equation (3.5). Since $|[K]_v| = k_{vx} \cdot k_{vy} \cdot k_{vz} \cdot k_{v\theta_x} \cdot k_{v\theta_y} \cdot k_{v\theta_z} > 0$, it implies that equation (3.5) is positive only if $|[K]_{bm}|$ is positive. We may recall that $[K]_{bm}$ has zero entries in the last row and in the last column corresponding to torsional θ_z angular direction which forces the bearing system to be semidefinite. Now define a new matrix $[K]_{bms}$ of dimension 5 as a subset of $[K]_{bm}$ with these zeroes excluded. If $[K]_{bms}$ has positive principal minor determinants, then this system is dynamically stable because it will consist of stable oscillations superimposed on the mean shaft rotational motion $\Omega_z \neq \Omega_z(t)$. Further, it follows that $[C]_{bms}$ which is proportional to $[K]_{bms}$ is also positive definite if $[K]_{bms}$ is

positive definite. The resulting equation obtained from the expansion of the determinant of $[K]_{bms}$ in terms of its entries k_{bwj} , $w_j=1,2,3,4,5$, is given as follows in terms of the stability functions Φ_j , $j = 1,2,3,4$.

$$\begin{aligned}
 |[K]_{bms}| = & 2 \Phi_4(55,34,45,35) \{k_{b24} \Phi_4(11,23,12,13)+k_{b14} \Phi_4(22,13,12,23)\}+ \\
 & 2 \Phi_4(44,35,45,34) \{k_{b25} \Phi_4(11,23,12,13)+k_{b15} \Phi_4(22,13,12,23)\}+ \\
 & 2 \Phi_4(24,35,25,34) \{k_{b14} \Phi_4(25,13,23,35)+k_{b15} \Phi_4(12,34,24,13)\} - \\
 & k_{b15} k_{b22} k_{b34} \Phi_3(14,35,15,34) + k_{b24} k_{b15} k_{b14} \Phi_3(23,35,33,25) + \\
 & 2 k_{b14} \Phi_4(25,45,24,55) \Phi_4(13,23,12,33) + \{k_{b14} k_{b25}\}^2 k_{b33} + \\
 & \Phi_1(1,2) \Phi_2(45,34,35,44,55) + \Phi_1(1,3) \Phi_2(45,24,25,44,55) + \\
 & k_{b15} \Phi_1(2,3) \Phi_3(14,45,15,44) + k_{b11} \{ \Phi_4(24,35,25,34) \}^2 + \\
 & \{k_{b14}\}^2 \{ k_{b23} \Phi_3(23,55,35,25) - k_{b22} \Phi_1(3,5) \} + \\
 & \Phi_1(4,5) \{ k_{b11} \Phi_1(2,3) + \Phi_2(23,13,12,33,22) \} + \\
 & 2 k_{b15} \Phi_4(24,45,25,44) \Phi_4(23,13,12,33) + \\
 & 2 k_{b15} \Phi_4(14,25,15,24) \Phi_4(23,34,24,33)
 \end{aligned} \tag{3.6a}$$

$$\Phi_1(w_I, w_{II}) = k_{bw_I w_I} k_{bw_{II} w_{II}} - \{k_{bw_I w_{II}}\}^2 \tag{3.6b}$$

$$\Phi_2(w_I, w_{II}, w_{III}, w_{IV}, w_V) = 2k_{bw_I} k_{bw_{II}} k_{bw_{III}} - k_{bw_{IV}} \{k_{bw_{III}}\}^2 - k_{bw_V} \{k_{bw_{II}}\}^2 \tag{3.6c}$$

$$\Phi_3(w_I, w_{II}, w_{III}, w_{IV}) = 2k_{bw_I} k_{bw_{II}} - k_{bw_{III}} k_{bw_{IV}} \tag{3.6d}$$

$$\Phi_4(w_I, w_{II}, w_{III}, w_{IV}) = k_{bw_I} k_{bw_{II}} - k_{bw_{III}} k_{bw_{IV}} \tag{3.6e}$$

where w_j , $j = I, II, III, IV, V$, are the dummy variables and each w_j may represent either a single number or a set of two numbers in equation (3.6a). The principal minor determinants of $[K]_{bms}$ can also be derived from equation (3.6) by excluding the

appropriate stiffness coefficients which are not entries of the particular principal submatrix. Hence, the bearing system is stable if each principal minor determinants derived from equation (3.6) is positive. The stability of the proposed bearing model given in Chapter II of this report can now be verified using these conditions. Inequalities associated with the stability criteria for these models are summarized in Tables 3.1 and 3.2 for ball and roller bearings respectively. These inequalities arise due to the fact that we are yet to impose any restrictions on these stiffness coefficients. In Chapter II of this report, these stiffness coefficients are given as functions of bearing kinematic and design parameters, and hence any coefficient can not assume an arbitrary value as it is related uniquely to other coefficients through these parameters. Extensive numerical studies performed over a wide range of these parameters have indicated that the bearing models proposed in Chapter II are indeed stable provided the preloads are sufficiently large to avoid the clearance non-linearity. Figures 3.3-3.5 illustrate examples of these bearing system stability studies for precision rolling element bearings whose design data are given in Table 3.3. In all of these figures, the stability functions Φ_j given in Tables 3.1 and 3.2 are found to lie within the stable region.

3.6 SYSTEM RESPONSE

The eigensolution of the linear, non-gyroscopic undamped system, formulated by setting $\{f(t)\}_a = \{0\}$ and $[C] = [0]$ in equation (3.1) given by method A or B, yields real valued natural frequencies ω_j , $j=1,2,3,\dots$, and the modal matrix $[U] = [\{\phi\}_1, \{\phi\}_2, \dots, \{\phi\}_j, \dots]$ for the stable system. Since the system is proportionally damped, the modal damping ratio is $\zeta_j = \sigma \omega_j^2/2$ and the damped natural frequency is

Table 3.1 Bearing system stability criteria for the proposed ball bearing model
(j = x or 1, y or 2; p = x or 1, y or 2 but p ≠ j)

Proposed bearing model [†] see Table 2.2	Stability criteria ^{††}
$k_{xx}, k_{yy}, k_{zz}, k_{\theta_x \theta_x}, k_{\theta_y \theta_y}, k_{z \theta_p}$	$\Phi_1(3, p+3) > 0$
$k_{xx}, k_{yy}, k_{zz}, k_{\theta_x \theta_x}, k_{\theta_y \theta_y}, k_{x \theta_y}, k_{y \theta_x}$	$\Phi_1(1, 5) > 0; \Phi_1(2, 4) > 0$
$k_{xx}, k_{yy}, k_{zz}, k_{\theta_x \theta_x}, k_{\theta_y \theta_y}$	always stable
$k_{xx}, k_{yy}, k_{zz}, k_{\theta_x \theta_x}, k_{\theta_y \theta_y}, k_{pz}$	$\Phi_1(p, 3) > 0$
$k_{xx}, k_{yy}, k_{zz}, k_{\theta_x \theta_x}, k_{\theta_y \theta_y}, k_{xy},$ $k_{\theta_x \theta_y}, k_{z \theta_x}, k_{z \theta_y}$	$\Phi_1(1, 2) > 0; \Phi_1(3, 4) > 0;$ $k_{33} \Phi_1(4, 5) + \Phi_2(4 \ 5, 3 \ 4, 3 \ 5, 4 \ 4, 5 \ 5) > 0$
$k_{xx}, k_{yy}, k_{zz}, k_{\theta_x \theta_x}, k_{\theta_y \theta_y}, k_{x \theta_x},$ $k_{y \theta_y}, k_{jz}, k_{z \theta_p}$	$k_{11} k_{22} \Phi_1(3, 4) + k_{j3}^2 k_{pp} k_{44} + k_{14}^2 k_{22} k_{33} > 0;$ $\Phi_1(j, 3) > 0;$ $\{k_{33} \Phi_1(1, 4) \Phi_1(2, 5) \Phi_5(p \ p+3, j+3 \ j+3, p \ p, 4 \ 4, 5 \ 5)\} \cdot$ $\{k_{j3} k_{3 \ p+3}\}^2 \cdot \{\Phi_5(j \ j+3, p \ p, 1 \ 1, 2 \ 2, j+3 \ j+3)\} > 0$
$k_{xx}, k_{yy}, k_{zz}, k_{\theta_x \theta_x}, k_{\theta_y \theta_y}, k_{xy},$ $k_{xz}, k_{yz}, k_{\theta_x \theta_y}$	$\Phi_1(4, 5) > 0; \Phi_1(1, 2) > 0;$ $k_{11} \Phi_1(1, 2) + \Phi_2(2 \ 3, 1 \ 2, 1 \ 3, 2 \ 2, 3 \ 3) > 0$
$k_{xx}, k_{yy}, k_{zz}, k_{\theta_x \theta_x}, k_{\theta_y \theta_y}, k_{x \theta_y},$ $k_{y \theta_x}, k_{jz}, k_{z \theta_p}$	$\Phi_1(p, j+3) > 0; \Phi_1(j, 3) > 0;$ $k_{jj} \Phi_1(3, p+3) + \Phi_2(3 \ p+3, j \ 3, j \ p+3, 3 \ 3, p+3 \ p+3) > 0$
all non-zero except θ_z terms	$ [K]_{bms} > 0$

[†] Here the subscript b which implies bearing has been omitted for brevity.

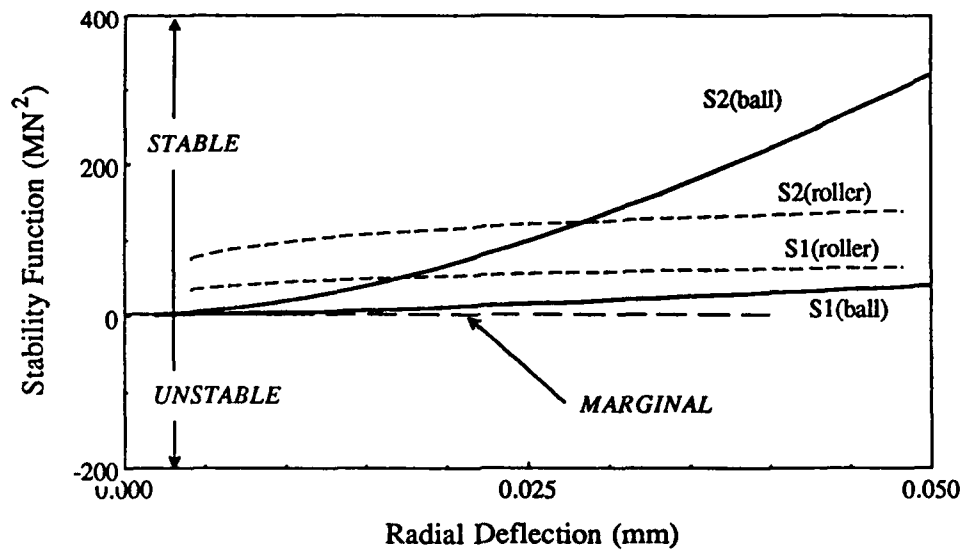
^{††} Stability functions Φ_1 and Φ_2 are defined by equations (3.6b) and (3.6c) and Φ_5 is given by $\Phi_5(w_I, w_{II}, w_{III}, w_{IV}, w_V) = \{k_{bw_I}\}^2 k_{bw_{II}} - k_{bw_{III}} k_{bw_{IV}} k_{bw_V}$

Table 3.2 Bearing system stability criteria for the proposed roller bearing model
($j = x$ or 1, y or 2; $p = x$ or 1, y or 2 but $p \neq j$)

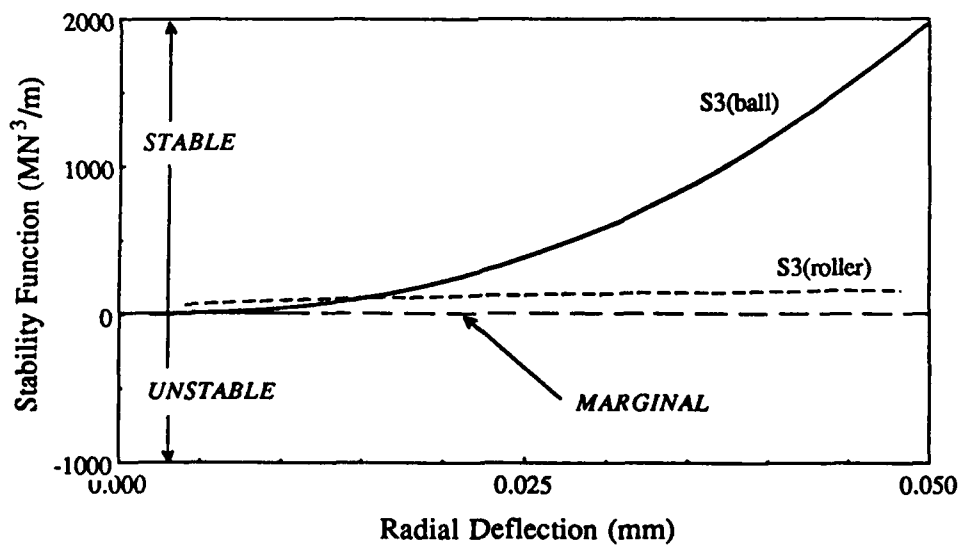
Proposed bearing model [†] see Table 2.3	Stability criteria ^{††}
k_{jj}	always stable
$k_{xx}, k_{yy}, k_{zz}, k_{\theta_x \theta_x}, k_{\theta_y \theta_y}, k_{x \theta_y}, k_{y \theta_x}$	$\Phi_1(1,5) > 0$; $\Phi_1(2,4) > 0$
$k_{zz}, k_{\theta_x \theta_x}, k_{\theta_y \theta_y}$	always stable
$k_{zz}, k_{\theta_x \theta_x}, k_{\theta_y \theta_y}, k_{z \theta_j}$	$\Phi_1(3j+3) > 0$
k_{xx}, k_{yy}, k_{xy}	$\Phi_1(1,2) > 0$
$k_{xx}, k_{yy}, k_{zz}, k_{\theta_x \theta_x}, k_{\theta_y \theta_y}, k_{x \theta_y}, k_{y \theta_x}, k_{jz}, k_{z \theta_p}$	$\Phi_1(pj+3) > 0$; $\Phi_1(j,3) > 0$; $k_{jj} \Phi_1(3,p+3) + \Phi_2(3 \ p+3, j \ 3, j \ p+3, 3 \ 3, p+3 \ p+3) > 0$
$k_{zz}, k_{\theta_x \theta_x}, k_{\theta_y \theta_y}, k_{\theta_x \theta_y}, k_{z \theta_x}, k_{z \theta_y}$	$\Phi_1(3,4) > 0$; $k_{33} \Phi_1(4,5) + \Phi_2(4 \ 5, 3 \ 4, 3 \ 5, 4 \ 4, 5 \ 5) > 0$
all non-zero except θ_z terms	$ [K]_{bms} > 0$

[†] Here the subscript b which implies bearing has been omitted for brevity.

^{††} Functions Φ_1 and Φ_2 are defined by equations (3.6b) and (3.6c)



(a)



(b)

Figure 3.3 Plot of stability criteria functions for ball and roller bearings subjected to mean bearing radial deflection δ_{xm} . (a) $S1 = \Phi_1(2,4)$ and $S2 = \Phi_1(1,3)$. (b) $S3 = k_{b11} \Phi_1(3,5) + \Phi_2(35,13,15,33,44)$.

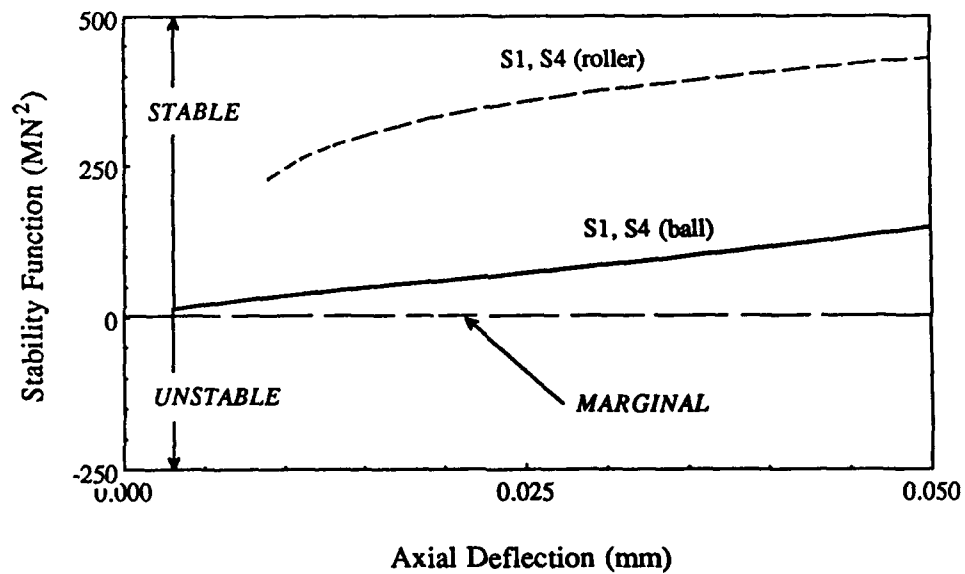
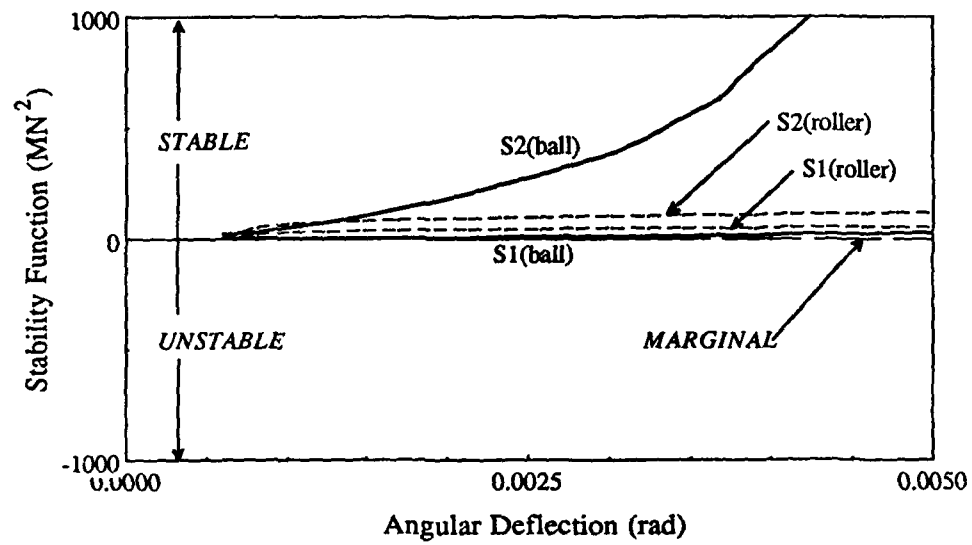
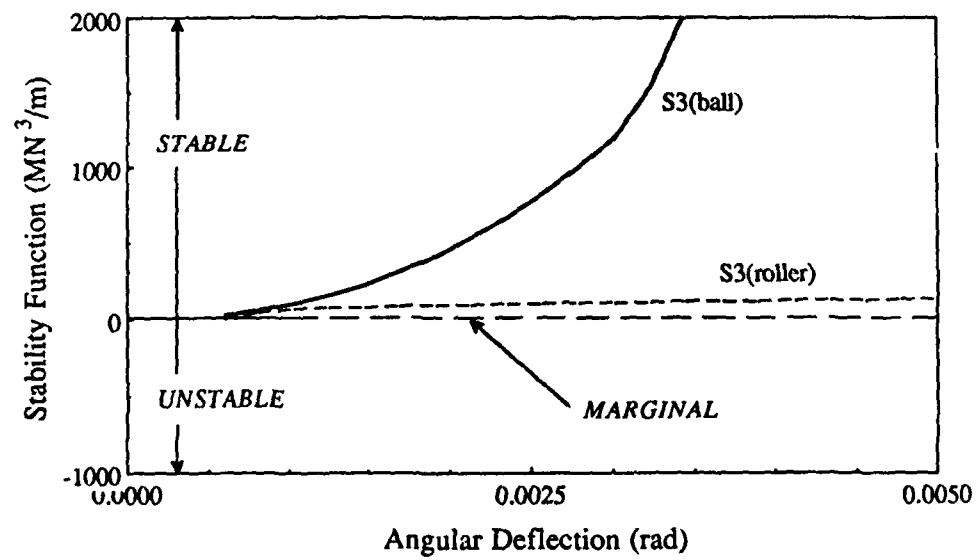


Figure 3.4 Plot of stability criteria functions for ball and roller bearings subjected to mean bearing axial deflection δ_{zm} . Here, $S1 = \Phi_1(2,4)$ and $S4 = \Phi_1(1,5)$.



(a)



(b)

Figure 3.5 Plot of stability criteria functions for ball and roller bearings subjected to mean angular misalignment β_{ym} . (a) $S1 = \Phi_1(2,4)$ and $S2 = \Phi_1(1,3)$. (b) $S3 = k_{b11} \Phi_1(3,5) + \Phi_2(35,13,15,33,44)$

Table 3.3 Design parameters for typical ball and roller bearings used for system studies

Parameters	Ball type	Roller type
Load-deflection exponent n	3/2	10/9
Load-deflection constant K_n (N/m ⁿ)	1.0 E9	1.0 E8
Number of rolling element Z	12	14
Radial clearance r_L (mm)	0.00005	0.00175
Pitch diameter (mm)	40.05	38.00
A_o (mm) [†]	0.05	—
Unloaded contact angle α_o	40°	15°

[†] Unloaded distance between inner and outer raceway groove curvature centers

given by $\omega_{jd} = \omega_j \sqrt{1 - \zeta_j^2}$. Free vibration response due to the initial conditions is not considered as only the steady-state particular solution corresponding to sinusoidal or periodic load vector $\{f(t)\}_a$ is of primary interest. Define excitation by the Fourier series expansion as $\{f(t)\}_a = \sum_p \{f\}_{ap} e^{i\omega_p t}$ where $\omega_p = p\omega_0$, ω_0 is the fundamental frequency, and $\{f\}_{ap}$ is the complex Fourier coefficient load vector. The steady-state particular solution $\{q(t)\}_a$ is given by the normal mode expansion technique [40,42,43] as

$$\{q(t)\}_a = [U] \left(\sum_p \{\mu\}_p e^{i\omega_p t} \right); \mu_{jp} = \frac{\{\phi\}_j^T \{f\}_{ap}}{\omega_j^2 - \omega_p^2 + i 2\zeta_j \omega_j \omega_p}; p=1,2,\dots \quad (3.7a,b)$$

An alternate approach would be to assume the harmonic solution for the alternating displacement as $\{q(t)\}_a = \sum_p \{q\}_{ap} e^{i\omega_p t}$. Substituting this and $\{f(t)\}_a$ definition into equation (3.1), we get

$$\{q\}_{ap} = \frac{\text{Adj} [-\omega_p^2 [M] + \lambda [K]]}{\left| [-\omega_p^2 [M] + \lambda [K]] \right|} \{f\}_{ap}; \quad \lambda = 1 + i\sigma\omega_p \quad (3.8a,b)$$

where the operator Adj refers to the adjoint of the dynamic stiffness matrix. Features of this method are summarized in References [40,42,43]. Since the vibration transmission across the bearing is the primary issue, we now define sinusoidal load transmissibility $R(p\omega)$ terms between two arbitrary locations I and II as

$$R_{f_{wIa}, f_{jIIa}}(\omega_p) = \frac{|f_{wIa}(\omega_p)|}{|f_{jIIa}(\omega_p)|} \quad ; \quad w, j = 1, 2, \dots, 6 \quad (3.9)$$

where f_{wIa} and f_{jIIa} are components of the dynamic load vectors at two arbitrary locations I and II respectively. The accelerance $A(\omega_p)$ and mobility $V(\omega_p)$ transfer functions with motion at location I due to an alternating force or torque f_{jIIa} applied at location II on the shaft are

$$A_{q_{wIa}, f_{jIIa}}(\omega_p) = \frac{|\ddot{q}_{wIa}(\omega_p)|}{|f_{jIIa}(\omega_p)|} \quad (3.10a)$$

$$V(\omega_p) = \frac{1}{i\omega_p} A(\omega_p) \quad ; \quad w, j = 1, 2, \dots, 6 \quad (3.10b)$$

where \ddot{q}_{wIa} is a component of the acceleration vector at location I. Other frequency response functions can also be defined in a similar manner [40,42,43].

3.7 EXAMPLE CASE I: RIGID SHAFT AND PLATE SYSTEM

3.7.1 Vibration Models

Consider the mechanical system shown in Figure 3.6a which is assumed to be freely suspended or softly mounted such that $[K]_v \approx [0]$. A ball bearings (see Table 3.3) with constant axial preload is supporting a short rigid shaft subjected to a mean torque $T_{zsm} \neq T_{zsm}(t)$ and a sinusoidal radial force $F_{rsa}(t) = F_{rsa1} e^{i\omega_0 t}$ applied very close to the bearing. A lumped parameter model with $DOF = 12$ is proposed in Figure 3.6b. Conversely, the same system has also been analyzed by Kraus et al. [24] using a simple vibration model with $DOF = 1$ as shown in Figure 3.6c with only k_{brr}

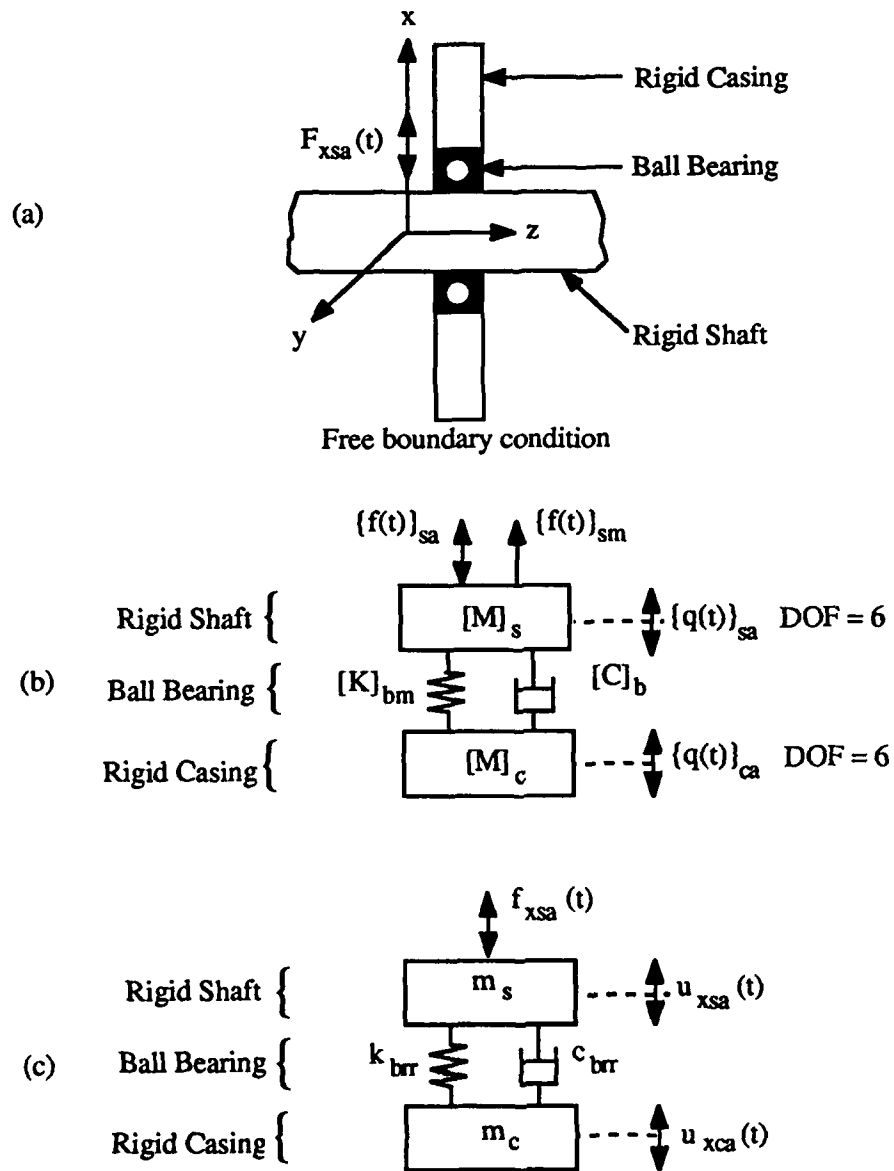


Figure 3.6 Example case I: freely suspended rigid shaft, ball bearing and rigid plate system subjected to alternating radial force $F_{rsa}(t)$ applied at the shaft. (a) Physical system. (b) Proposed multi-degree of freedom vibration model with $\text{DOF} = 12$. (c) Simple model by Kraus et al. [24] with $\text{DOF} = 1$.

coefficient. The bearing stiffness matrix for an axially preloaded ball bearing in Figure 3.6b has non-negligible stiffness coefficients k_{bxx} , k_{byy} , k_{bzz} , $k_{b\theta_x\theta_x}$, $k_{b\theta_y\theta_y}$, $k_{b\theta_x\theta_y}$ and $k_{b\theta_y\theta_x}$ which are functions of the mean axial preload as given in Chapter II of this report. The system matrices of equation (3.2) can be modified for this case by suppressing other bearing stiffness coefficients and $[K]_v$. It can be easily observed from equations (3.1) and (3.2) that 5 sets of uncoupled differential equations exist. The simplest three sets are homogeneous and pertain to the rigid body torsional motions $\theta_{za}(t)$ of the shaft and casing, and axial vibration $u_{za}(t)$ of the shaft-casing system which are of no interest here. The remaining two sets are almost identical and associated with either $\{u_{xa}(t), \theta_{ya}(t)\}^T$ or $\{u_{ya}(t), \theta_{xa}(t)\}^T$ degrees of freedom for rigid shaft and casing. If the coordinate system is chosen such that $F_{rsa}(t)$ line of action coincides with the x-axis, then the steady-state solution to the set of differential equations in terms of $\{u_{ya}(t), \theta_{xa}(t)\}^T$ is trivial. Hence, the problem reduces to a semi-definite vibration system with $\text{DOF} = 4$. Accordingly, rewrite $[M]_s$, $[M]_c$ and $[K]_{bm}$ in equation (3.2) in terms of the displacement vector $\{q(t)\}_a = \{u_{xsa}(t), \theta_{ysa}(t), u_{xca}(t), \theta_{yca}(t)\}^T$ as

$$[M]_s = \begin{bmatrix} m_s & 0 \\ 0 & I_s \end{bmatrix}; [M]_c = \begin{bmatrix} m_c & 0 \\ 0 & I_c \end{bmatrix}; [K]_{bm} = \begin{bmatrix} k_{bxx} & k_{b\theta_x\theta_y} \\ k_{b\theta_x\theta_y} & k_{b\theta_y\theta_y} \end{bmatrix} \quad (3.11)$$

First two eigenvalues corresponding to the rigid body motions in x and θ_y directions are zero. The dimension of equation (3.11) is further reduced to $\text{DOF} = 2$ by defining relative motions $\delta_{xa}(t) = u_{xsa}(t) - u_{xca}(t)$ and $\beta_{ya}(t) = \theta_{ysa}(t) - \theta_{yca}(t)$ which turn out to be the bearing rigid body motions.

$$\begin{bmatrix} \gamma_m m_s & 0 \\ 0 & \gamma_I I_s \end{bmatrix} \begin{Bmatrix} \ddot{\delta}_{xa} \\ \ddot{\beta}_{ya} \end{Bmatrix} + [C] \begin{Bmatrix} \dot{\delta}_{xa} \\ \dot{\beta}_{ya} \end{Bmatrix} + [K]_{bm} \begin{Bmatrix} \delta_{xa} \\ \beta_{ya} \end{Bmatrix} = \begin{Bmatrix} \gamma_m F_{xsa}(t) \\ 0 \end{Bmatrix} \quad (3.12a)$$

$$\gamma_m = \frac{m_c}{m_s + m_c} \quad ; \quad \gamma_I = \frac{I_c}{I_s + I_c} \quad ; \quad [C] = \sigma [K]_{bm} \quad (3.12b)$$

It may be noted that purely translational $\delta_{xa}(t)$ model by Kraus et al. [24] shown in Figure 3.6c constitutes a subset of equation (3.12) with $k_{bx\theta_y} = 0$. Eigensolution of equation (3.12) with $[C]=[0]$ yields the following natural frequencies ω_j and modes $\{\phi\}_j$

$$\omega_{1,2} = \sqrt{\frac{B_1 \pm B_2}{2\gamma_m m_s \gamma_I I_s}} \quad ; \quad B_1 = \gamma_m m_s k_{b\theta_y \theta_y} + \gamma_I I_s k_{bxx} \quad (3.13a,b)$$

$$B_2 = \sqrt{(\gamma_m m_s k_{b\theta_y \theta_y} - \gamma_I I_s k_{bxx})^2 + 4\gamma_m m_s \gamma_I I_s k_{bx\theta_y}^2} \quad (3.13c)$$

$$\{\phi\}_{1,2}^T = \frac{1}{\sqrt{\gamma_m m_s + \gamma_I I_s B_3}} \{ 1, B_3 \} \quad (3.14a)$$

$$B_3 = \frac{\gamma_m m_s k_{b\theta_y \theta_y} - \gamma_I I_s k_{bxx} \pm B_2}{2\gamma_I k_{bx\theta_y}} \quad (3.14b)$$

On the other hand, the eigensolution of the single degree of freedom system is given by

$$\hat{\omega}_2 = \sqrt{\frac{k_{bxx}}{\gamma_m m_s}} \quad \text{and} \quad \{\hat{\phi}\}_1^T = \left\{ \frac{1}{\sqrt{\gamma_m m_s}} \right\} \quad \text{where subscript 2 and superscript } ^\wedge \text{ are}$$

chosen to indicate that this solution essentially estimates ω_2 and $\{\phi\}_2$ in equations

(3.13) and (3.14). Since $\hat{\omega}_2$ does not include $k_{bx\theta_y}$ and $k_{b\theta_y\theta_y}$, $\hat{\omega}_2 < \omega_2$ as evident from Table 3.4 for 3 different axial preloads. This natural mode is dominated by $\delta_{xa}(t)$ as indicated by equation (3.14). And, the first mode $\{\phi\}_1$ which is predominantly $\beta_{ya}(t)$ is also affected by the axial preload.

Table 3.4 Bearing stiffness coefficients and undamped natural frequencies (Hz) of example case I[†]

Axial preload	Bearing stiffness coefficients			Proposed model (DOF = 2)		Simple model (DOF=1)
	k_{bxx} (N/m)	$k_{bx\theta_y}$ (N)	$k_{b\theta_y\theta_y}$ (Nm)	ω_1	ω_2	$\hat{\omega}_2$
F_{zbm} (N)						
115	1.84 E7	-3.05 E6	1.36 E4	156	372	341
190	2.13 E7	-3.12 E6	1.70 E5	191	395	367
285	2.43 E7	-3.09 E6	2.02 E5	221	416	392

† Other system parameters are: $m_s=10.0\text{kg}$, $I_s=0.025\text{kgm}^2$, $\gamma_m=0.4$, $\gamma_s=0.3$, $\sigma=1\text{E-6s}$.

3.7.2 Bearing Transmissibility

The forced harmonic response of equation (3.12) can be obtained using the dynamic stiffness approach given by equation (3.8)

$$\delta_{xa}(t) = \frac{(k_{b\theta_y\theta_y} \lambda - \omega_o^2 \gamma_I I_s) \gamma_m F_{xsa1} e^{i\omega_o t}}{(k_{b\theta_y\theta_y} \lambda - \omega_o^2 \gamma_I I_s)(k_{bxx} \lambda - \omega_o^2 \gamma_m m_s) - (k_{bx\theta_y} \lambda)^2} \quad (3.15a)$$

$$\beta_{ya}(t) = \frac{-k_{bx\theta_y} \lambda \gamma_m F_{xsa1} e^{i\omega_o t}}{(k_{b\theta_y\theta_y} \lambda - \omega_o^2 \gamma_I I_s)(k_{bxx} \lambda - \omega_o^2 \gamma_m m_s) - (k_{bx\theta_y} \lambda)^2} \quad (3.15b)$$

It can be seen from equation (3.15) that $F_{xsa}(t)$ not only excites $\delta_{xa}(t)$ but $\beta_{ya}(t)$ as well, which is not predicted by Kraus et al. [24]. The steady-state solution for this simple model is given by the following; compare it with equation (3.15a).

$$\hat{\delta}_{xa}(t) = \frac{\gamma_m F_{xsa1} e^{i\omega_o t}}{(k_{bxx} \lambda - \omega_o^2 \gamma_m m_s)} \quad (3.16)$$

Both models are used to determine the load transmissibility magnitude terms $R(\omega_o)$ which are computed using $\{\delta_{xa}(t), \beta_{ya}(t)\}^T$, $[K]$ and $[C]$. Dynamic bearing force $F_{xba}(t)$ and moment $M_{yba}(t)$ magnitudes excited by the shaft force $F_{xsa}(t)$ are given by force transmissibility $R_{F_{xba}, F_{xsa}}(\omega_o)$ and moment transmissibility $R_{M_{yba}, F_{xsa}}(\omega_o)$ respectively.

$$R_{F_{xba}, F_{xsa}}(\omega_o) = \frac{\gamma_m \sqrt{(1 + \sigma^2 \omega_o^2)^2 B_4 + (1 + \sigma^2 \omega_o^2) B_5}}{\sqrt{(1 + \sigma^2 \omega_o^2)^2 B_4 + (1 + \sigma^2 \omega_o^2)(B_5 + B_6) + B_7}} \quad (3.17a)$$

$$R_{M_{yba}, F_{xsa}}(\omega_o) = \frac{\gamma_m \gamma_I I_s \omega_o^2 \sqrt{(1 + \sigma^2 \omega_o^2) k_{bxx}^2}}{\sqrt{(1 + \sigma^2 \omega_o^2)^2 B_4 + (1 + \sigma^2 \omega_o^2)(B_5 + B_6) + B_7}} \quad (3.17b)$$

$$B_4 = \left(k_{b\theta_y \theta_y} k_{bxx} - k_{bxx}^2 \right)^2 \quad (3.17c)$$

$$B_5 = \omega_o^2 \gamma_I I_s k_{bxx} \left(k_{bxx} \gamma_I I_s \omega_o^2 + 2k_{bxx}^2 - 2k_{bxx} k_{b\theta_y \theta_y} \right) \quad (3.17d)$$

$$B_6 = \omega_o^2 \gamma_m m_s k_{b\theta_y \theta_y} \left(k_{b\theta_y \theta_y} \gamma_m m_s \omega_o^2 + 2k_{bxx}^2 - 2k_{bxx} k_{b\theta_y \theta_y} \right) \quad (3.17e)$$

$$B_7 = 2\omega_o^4 \gamma_m m_s \gamma_I I_s \left\{ 2k_{bxx} k_{b\theta_y \theta_y} - \omega_o^2 (\gamma_I I_s k_{bxx} + \gamma_m m_s k_{b\theta_y \theta_y}) \right\} + \omega_o^4 \gamma_m m_s \gamma_I I_s \left\{ \gamma_m m_s \gamma_I I_s \omega_o^4 - 2k_{bxx} (1 - \sigma^2 \omega_o^2) \right\} \quad (3.17f)$$

Only the force transmissibility, as given below, is predicted by the simple model [24]; compare it with equation (3.17a).

$$\hat{R}_{F_{xba}, F_{xsa}}(\omega_o) = \frac{k_{bxx} \gamma_m \sqrt{(1 + \sigma^2 \omega_o^2)}}{\sqrt{(k_{bxx} - \omega_o^2 \gamma_m m_s)^2 + (k_{bxx} \omega_o \sigma)^2}} \quad (3.18)$$

Figure 3.7 compares equations (3.17) and (3.18). Our model predicts higher $R_{F_{xba}, F_{xsa}}(\omega_o)$ and ω_2 than the simple model due to the additional constraints imposed by $[K]_{bm}$. Also, it is clear that the simple model can not predict dynamic moment transfer through the bearing. The bearing transmissibility functions $R(\omega_o)$ predicted by our model for 3 different axial preloads are shown in Figure 3.8. Note that the resonant

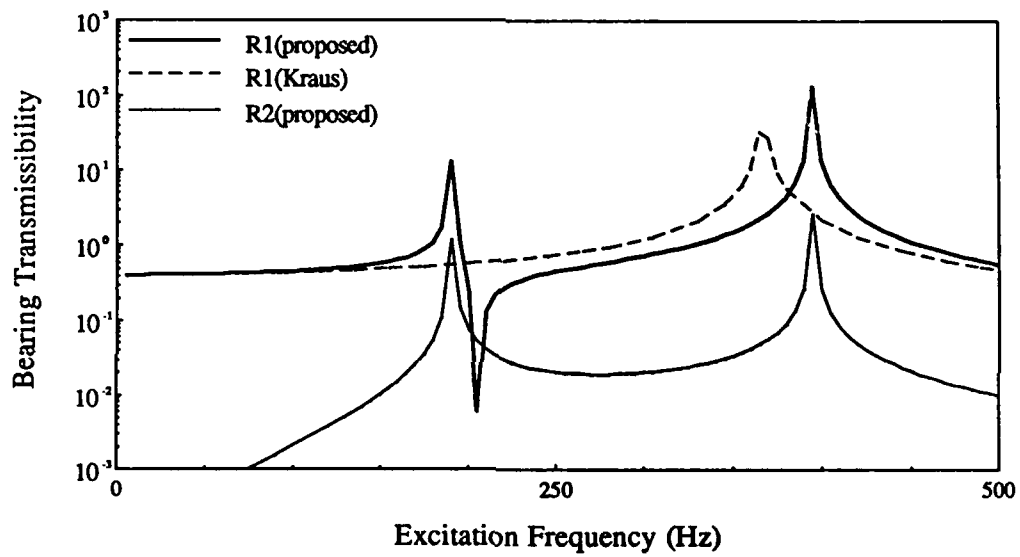
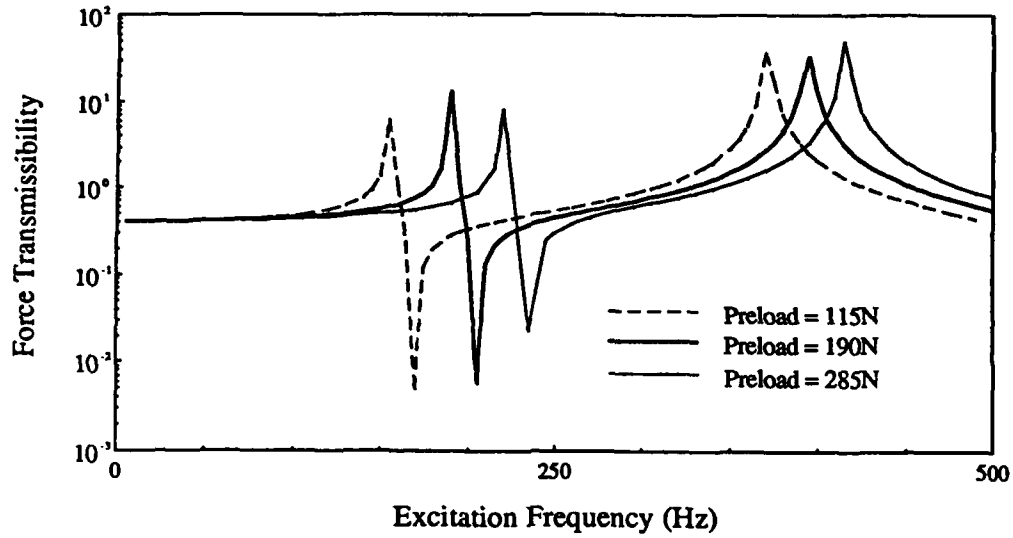
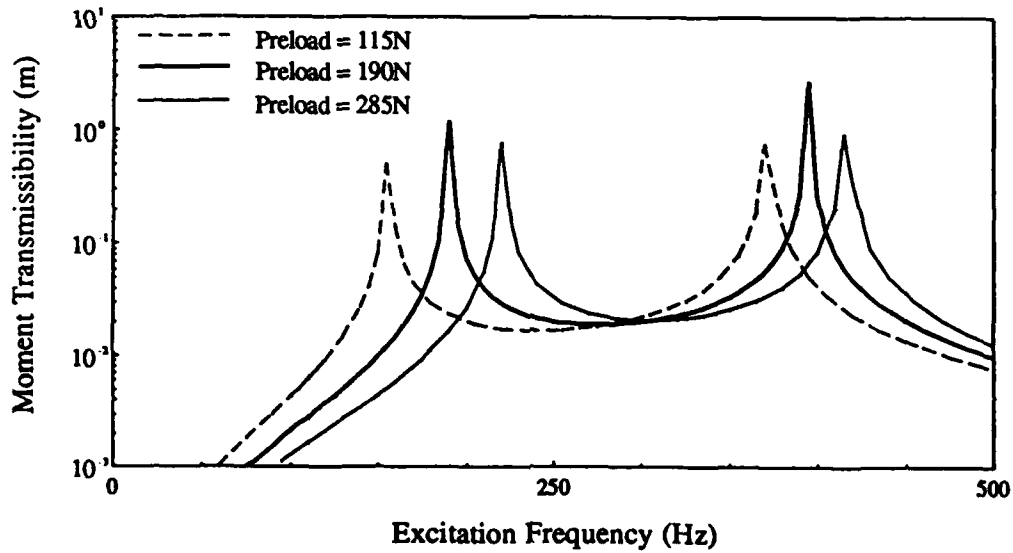


Figure 3.7 Bearing transmissibility spectra $R_{f_{wba}, F_{xsa}}(\omega_0)$ for example case I. Here, R1: force transmissibility with $f_{wba} = F_{xba}$ and R2: moment transmissibility with $f_{wba} = M_{yba}$, as predicted by our model with DOF = 2 and the simple model by Kraus et al. [24] with DOF = 1.



(a)



(b)

Figure 3.8 Effect of mean axial preload on the bearing transmissibility spectra $R_{f_{wba}, F_{xsa}}(\omega_0)$ defined by equation (3.17) for example case I. (a) Force transmissibility with $f_{wba} = F_{xsa}$. (b) Moment transmissibility with $f_{wba} = M_{yba}$.

amplitudes vary depending on the amount of axial preload and the resonant frequencies increase with increasing preloads as expected.

3.8 EXAMPLE CASE II: RIGID SHAFT AND PLATE SUPPORTED ON FLEXIBLE MOUNTS

3.8.1 Vibration Models

The physical system of example case I is modified to include flexible mounts, $[K]_v \neq [0]$, and mean radial shaft force $F_{rsm} \neq F_{rsm}(t)$ and $F_{rsa}(t) = F_{rsa1}e^{i\omega_0 t}$ as shown in Figure 3.9a. The ball bearing (see Table 3.3) is also preloaded in the axial direction. This is modeled using lumped parameter theory with finite mount stiffness coefficients k_{vj} , $j = x, y, z, \theta_x, \theta_y$ or θ_z as illustrated in Figure 3.9b. Since the rigid shaft assumption still holds, $F_{rsm} = F_{rbm}$ is applied directly on the bearing in a manner similar to the axial preload. The bearing matrix $[K]_{bm}$ in Figure 3.9b has non-negligible stiffness coefficients $k_{bxx}, k_{byy}, k_{bzz}, k_{b\theta_x\theta_x}, k_{b\theta_y\theta_y}, k_{b\theta_x\theta_y}, k_{b\theta_y\theta_x}, k_{b\theta_xz}$ and $k_{b\theta_z\theta_x}$ which are functions of the mean bearing load vector $\{f\}_{bm} = \{f\}_{sm}$ or the mean bearing displacement vector $\{q\}_{bm} = \{q\}_{sm} - \{q\}_{cm}$ as given by Chapter II of this report. Conversely, White [20] has investigated this problem using a simple model with $DOF = 2$ as shown in Figure 3.9c. It may be noted that his bearing system model did not include the effect of axial preload.

Like example case I, the governing equations (3.1) and (3.2) can be modified and reduced to 4 uncoupled sets of differential equations. The first two sets associated with $\theta_{ysa}(t)$ and $\theta_{yca}(t)$ are homogeneous. The third set is similar to equation (3.11) but with x and y subscripts interchanged, and two mount stiffness coefficients k_{vy} and $k_{v\theta_x}$ included. However, it is still homogeneous and therefore has only trivial steady-state

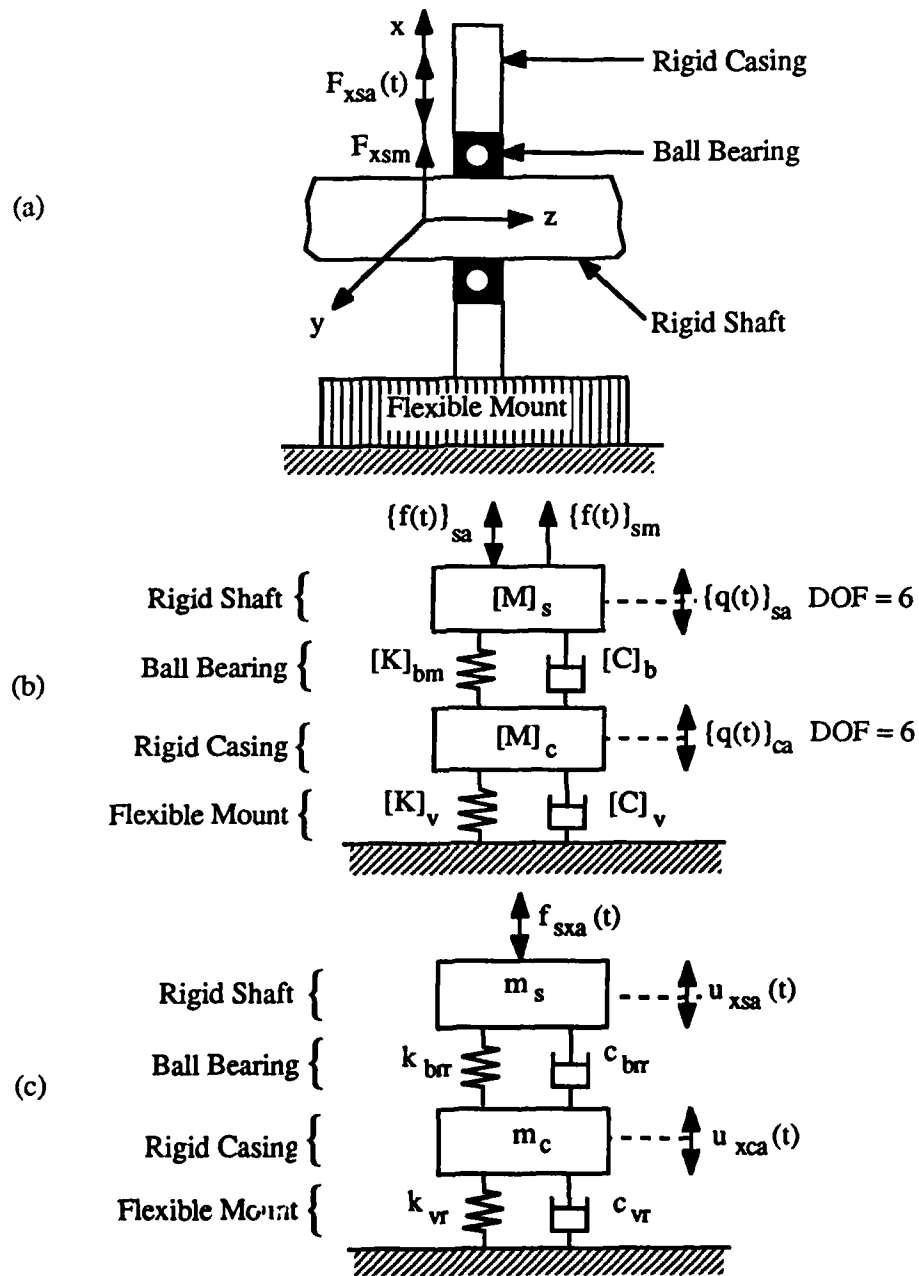


Figure 3.9 Example case II: rigid shaft, ball bearing and rigid plate system supported by flexible mounts and subjected to alternating radial force $F_{xsa}(t)$ applied at the shaft. (a) Physical system. (b) Proposed multi-degree of freedom vibration model with $\text{DOF} = 12$. (c) White's vibration model [20] with $\text{DOF} = 2$.

solution. The final set corresponds to $\{q\}_a(t) = \{u_{xsa}(t), u_{zsa}(t), \theta_{ysa}(t), u_{xca}(t), u_{zca}(t), \theta_{yca}(t)\}^T$ with $[M]_s$, $[M]_c$, $[K]_{bm}$ and $[K]_v$ of equation (3.2) reduced to

$$[M]_s = \begin{bmatrix} m_s & 0 & 0 \\ 0 & m_s & 0 \\ 0 & 0 & I_s \end{bmatrix} ; \quad [M]_c = \begin{bmatrix} m_c & 0 & 0 \\ 0 & m_c & 0 \\ 0 & 0 & I_c \end{bmatrix} \quad (3.19a,b)$$

$$[K]_{bm} = \begin{bmatrix} k_{bxx} & k_{bxz} & k_{bx\theta_y} \\ k_{bxz} & k_{bzz} & k_{bz\theta_y} \\ k_{bx\theta_y} & k_{bz\theta_y} & k_{b\theta_y\theta_y} \end{bmatrix} ; \quad [K]_v = \begin{bmatrix} k_{vx} & 0 & 0 \\ 0 & k_{vz} & 0 \\ 0 & 0 & k_{v\theta_y} \end{bmatrix} \quad (3.19c,d)$$

The vibration model by White [20] may be formulated by retaining only two equations corresponding to $u_{xsa}(t)$ and $u_{xca}(t)$ and excluding all bearing and mount stiffness coefficients except for k_{bxx} and k_{vx} .

Analytical eigensolution of the undamped system is not possible since it requires solving for the zeroes of a 6-th order polynomial in ω^2 . Therefore, this problem is solved numerically using an eigenvalue routine [42]. Using the same system parameters as in example case I with 3 different F_{xsm} , natural frequencies and modes are found as given in Tables 3.5b and 3.5c for both our and White's models. Corresponding bearing mean loads $\{F_{xbm}, F_{zbm}, M_{ybm}\}^T$ and relevant bearing stiffness coefficients computed using the method derived in Chapter II are listed in Table 3.5a. Tables 3.5b and 3.5c indicate that only the first and fifth modes of our model are predicted by White's model; here superscript \wedge is again used to denote estimation based on the simple model. The first natural frequency ω_1 predictions by both models are very similar. But ω_5 prediction, whose mode is similar to the second mode of example case I, indicates a few discrepancies. White's model also underestimates this natural frequency due to the

Table 3.5 Results of example case II [†]

(a) Computed bearing mean loads and stiffness coefficients

Shaft mean load	Bearing loads ^{††}		Bearing stiffness coefficients						
	F _{xsm} (N)	F _{zbm} (N)	M _{ybm} (Nm)	k _{bxx} (N/m)	k _{bxz} (N/m)	k _{bxθ_y} (N)	k _{bzz} (N/m)	k _{bzθ_y} (N)	k _{bθ_yθ_y} (Nm)
44		198	0.62	2.26E7	5.84E7	-2.90E5	8.50E7	-3.10E3	1.71E4
94		216	1.16	2.64E7	1.14E7	-2.33E5	8.55E7	-1.36E4	1.72E4
122		229	1.38	2.93E7	1.40E7	-1.98E5	8.60E7	-2.19E4	1.74E4

(b) Undamped natural frequencies (Hz)

Mean shaft load	Proposed model (DOF=6)						Simple model (DOF=2)		
	F_{xbm} (N)	ω_1	ω_2	ω_3	ω_4	ω_5	ω_6	$\hat{\omega}_1$	$\hat{\omega}_5$
44	93	100	111	287	350	607		97	321
94	96	100	115	300	351	614		97	345
122	97	100	117	308	364	620		98	362

(b) Modes of vibration ^{†††}

Proposed model (DOF=6)						Simple model (DOF=2)	
$\{\phi\}_1$	$\{\phi\}_2$	$\{\phi\}_3$	$\{\phi\}_4$	$\{\phi\}_5$	$\{\phi\}_6$	$\{\hat{\phi}\}_1$	$\{\hat{\phi}\}_5$
0.217	0.031	-0.030	-0.130	0.180	0.044	0.218	0.229
-0.035	0.203	0.003	0.022	-0.036	0.236		
1.648	0.084	5.966	-0.354	-1.245	-0.068		
0.171	0.084	-0.071	0.107	-0.139	-0.031	0.187	-0.178
-0.027	0.194	0.008	-0.018	0.028	-0.165		
0.167	0.009	0.917	4.648	3.295	0.073		

[†] Other system parameters are: $m_s=10.0$ kg, $I_s=0.025$ kgm², $m_c=15.0$ kg,
 $I_c=0.03$ kgm², $\sigma=1E-6$ s, $k_{vx}=1E7$ N/m, $k_{vz}=1E7$ N/m, $k_{x\theta_y}=1$ E5 Nm.

^{††} $F_{xbm} = F_{xsm}$

^{†††} These are for mean shaft load $F_{xsm} = F_{xbm} = 94$ N.

incomplete bearing stiffness model employed. Here again our predicted modes include δ_{xa} , δ_{za} and β_{ya} displacements of shaft and casing components which are not considered by White's model.

3.8.2 Frequency Response

The forced harmonic response solution is also determined numerically using the dynamic stiffness approach outlined in Section 3.6. Driving point (with $j = s$) and cross point (with $j = c$) accelerance spectra $A_{q_{wja}F_{xsa}}(\omega_0)$ are given in Figure 3.10 with $q_{wja} = u_{xja}$, u_{zja} or θ_{yja} for both models. Here, we observe that White's [20] model overestimates the magnitudes of the accelerance and can not predict, unlike our model, axial $u_{za}(t)$ and $\theta_{ya}(t)$ angular motions on the shaft and casing. Figure 3.11 shows the bearing transmissibility spectra $R_{f_{wba},F_{xsa}}(\omega_0)$ for $f_{wba} = F_{xba}$, F_{zxa} or M_{yba} which indicate that transmissibilities corresponding to F_{zxa} and M_{yba} are not predicted using White's model. Such loads also serve as mechanisms for vibration transmission through the bearing to the casing, in addition to F_{xba} . The mount transmissibility spectra $R_{f_{wva},F_{xsa}}(\omega_0)$ as shown in Figure 3.11 indicate that F_{zva} and M_{yva} are also transmitted to the mounts in addition to F_{xva} due to casing motions in x , z and θ_y directions. The effect of mean radial bearing force F_{xbm} on the load transmissibilities $R(\omega_0)$ through the bearing is shown in Figure 3.12 for 3 different mean loads. We again observe that the resonant amplitudes and frequencies are mean load dependent through $[K]_{bm}$. Similar trends show that an increase in mean load raises the resonant frequencies although the effects are not as pronounced as those found in example case I.

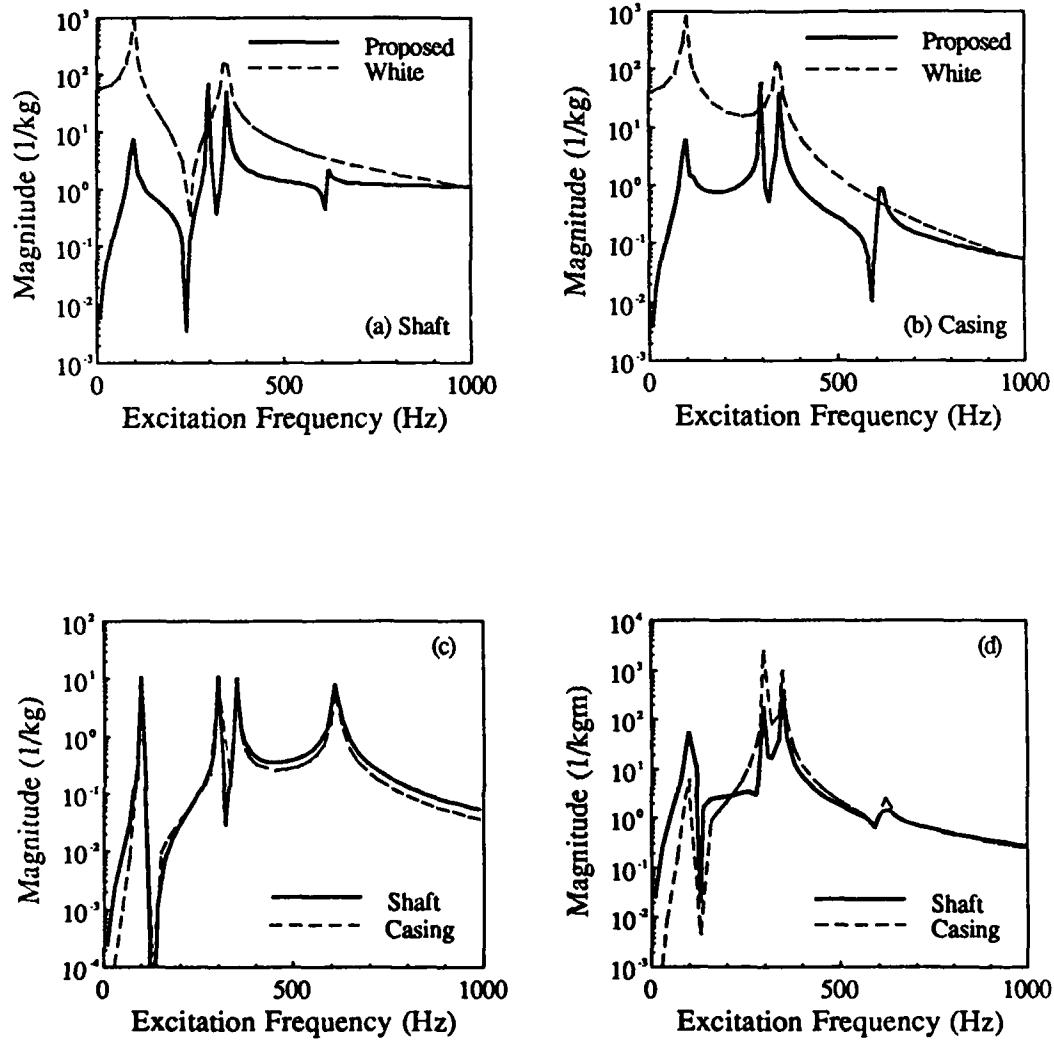


Figure 3.10 Accelerance spectra $A_{q_{wja}, F_{xsa}}(\omega_o)$ for example case II as predicted by our formulation and White's model [20]. (a) Driving point accelerance with $q_{wja} = u_{xsa}$. (b) Cross point accelerance with $q_{wja} = u_{xca}$. (c) Accelerance with $q_{wja} = u_{zsa}$ for shaft and $q_{wja} = u_{zca}$ for casing. (d) Accelerance with $q_{wja} = \theta_{ysa}$ for shaft and $q_{wja} = \theta_{yca}$ for casing.

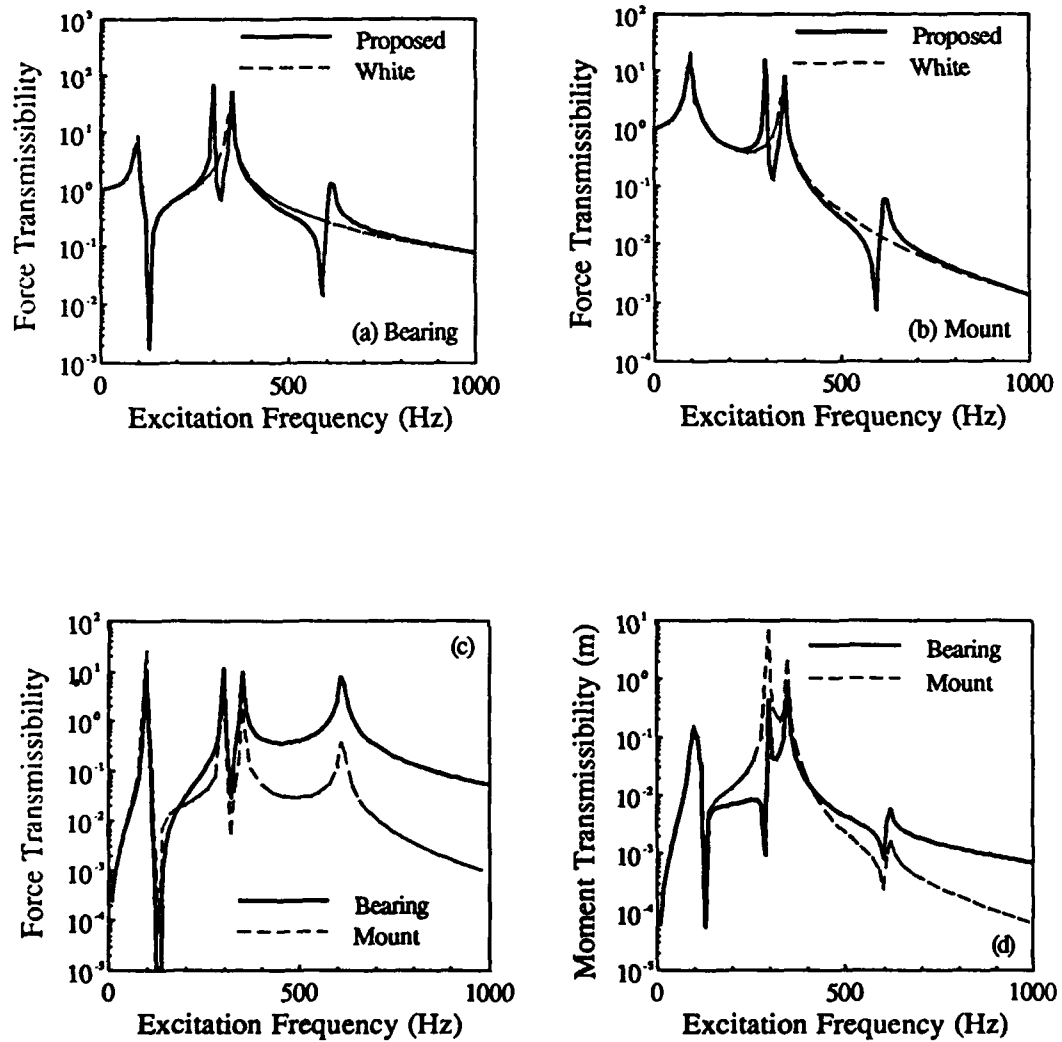


Figure 3.11 Bearing $R_{f_{wba}, F_{xsa}}(\omega_0)$ and mount $R_{f_{wva}, F_{xsa}}(\omega_0)$ transmissibility spectra for example case II as predicted by our formulation and White's model [20]. (a) Bearing force transmissibility with $f_{wba} = F_{xba}$. (b) Mount force transmissibility with $f_{wva} = F_{xva}$. (c) Force transmissibility with $f_{wba} = F_{zba}$ for bearing and $f_{wva} = F_{zva}$ for mount. (d) Moment transmissibility with $f_{wba} = M_{yba}$ for bearing and $f_{wva} = M_{yva}$ for mount.

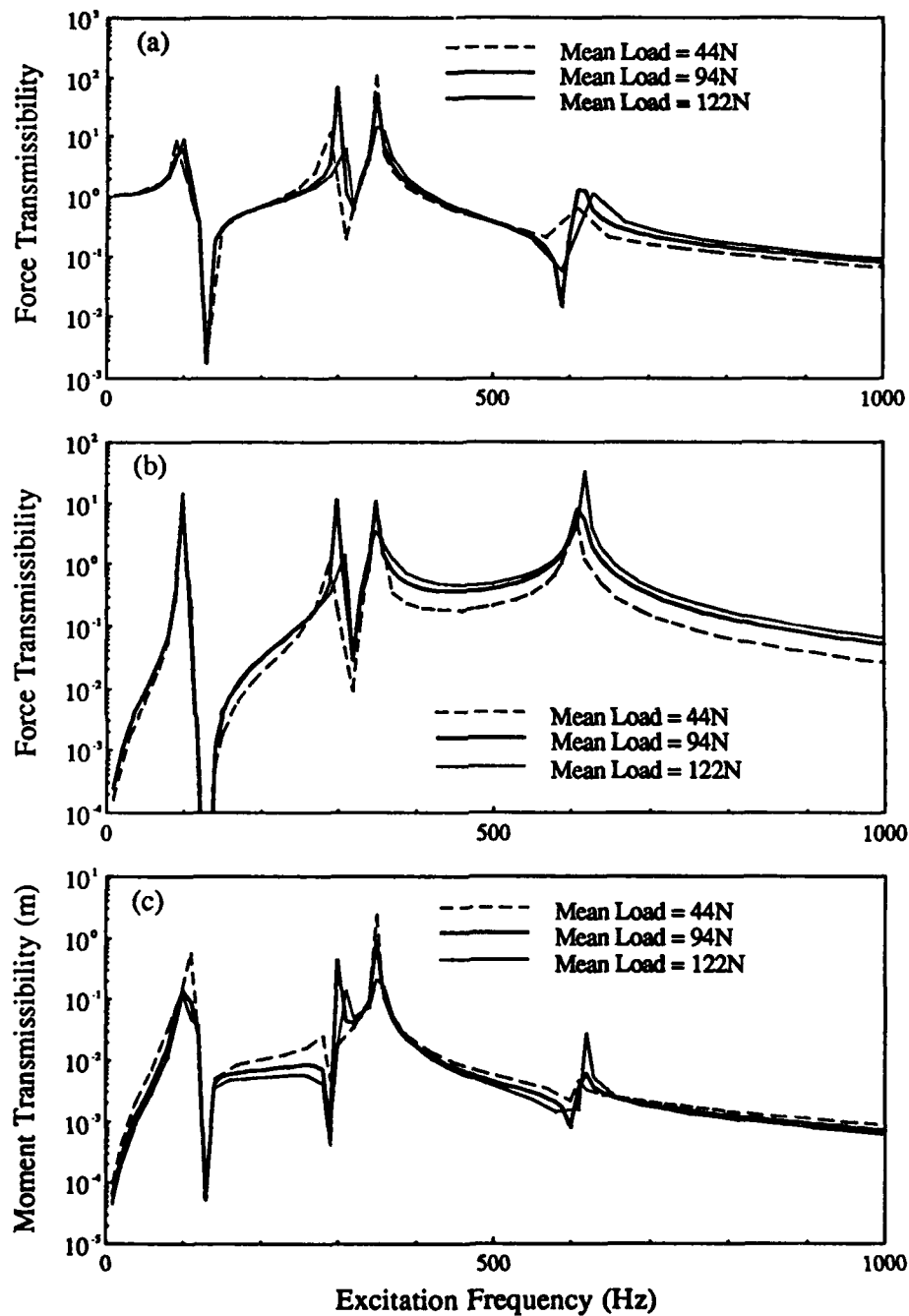


Figure 3.12 Effect of the mean radial bearing force F_{xbm} on the bearing transmissibility spectra $R_{f_{wba}, F_{xsa}}(\omega_0)$ for example case II. (a) Force transmissibility with $f_{wba} = F_{xba}$. (b) Force transmissibility with $f_{wba} = F_{zba}$. (c) Moment transmissibility with $f_{wba} = M_{yba}$.

3.9 EXAMPLE CASE III: EXPERIMENTAL STUDY

3.9.1 Physical setup

The final example case examines the experimental setup of Lin [17] as shown in Figure 3.13a. This system is similar to Figure 3.1 and consists of a 159mm long x 25mm diameter non-rotating shaft supported by two rolling element bearings of 25mm bore x 51mm outer diameter. One is supported on a rectangular plate of approximate dimensions 762mm x 457mm x 9mm and the second is rigidly connected to the base. The plate is also bolted to a massive base structure. Excitation force F_{ys} which consists of a mean $F_{ysm} = 445\text{N}$ via a preloaded spring and an alternating $F_{ysa}(t)$ component applied transversely at the free end of the shaft using a vibrating shaker. Driving and cross point accelerance spectra are measured at the shaft and on the plate respectively. Further details of this experiment are summarized in Reference [17].

3.9.2 Bearing Analysis

Initially, only the static analysis is performed to obtain $[K]_{bm}$ for this experimental system using the method proposed in Chapter II of this report. The static analysis neglects plate flexibility; this assumption is valid since the bearing mean loads are sufficiently low and do not deflect the plate. The shaft-bearing system is statically indeterminate as shown in Figure 3.13b. The mean force F_{ysm} on the shaft produces mean bearing load vector $\{f\}_{bm} = (0, F_{ybm}, F_{zbm}, M_{xbm}, 0)^T$ which depends on the mean bearing displacement vector $\{q\}_{bm} = (0, \delta_{ym}, \delta_{zm}, \beta_{xm}, 0)^T$. The proposed bearing matrix $[K]_{bm}$ includes stiffness coefficients k_{bxx} , k_{byy} , k_{bzz} , $k_{b\theta_x\theta_x}$, $k_{b\theta_y\theta_y}$, $k_{b\theta_z\theta_z}$, $k_{b\theta_x\theta_y}$, $k_{b\theta_y\theta_x}$, $k_{b\theta_x\theta_z}$ and $k_{b\theta_z\theta_x}$ which are direct functions of $\{q\}_{bm}$. In contrast, the

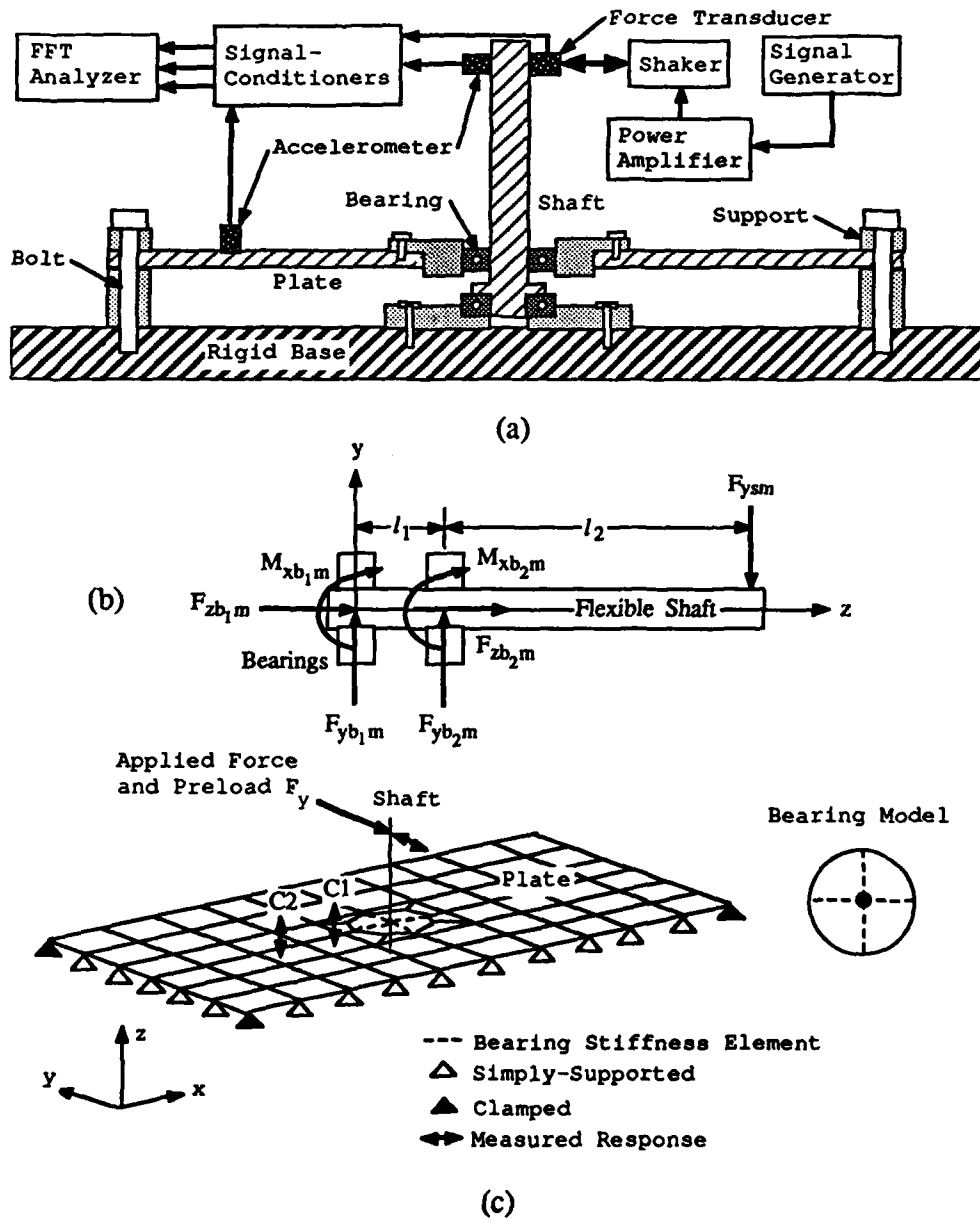


Figure 3.13 Example case III. (a) Schematic of the experimental setup consisting of an overhung shaft, 2 ball bearings and a rectangular plate [17]. (b) Static model of shaft and bearings used for computing $[K]_{bm}$. (c) Finite element model of the experimental system shown in (a). The generalized stiffness matrix elements for the bearing model are shown by dashed lines, connecting 1 node on the shaft to 4 nodes on the plate.

conventional bearing models include only k_{bxx} , k_{byy} and k_{bzz} coefficients. From Figure 3.13b, the force and moment equilibrium equations for this system are

$$F_{yb1m} + F_{yb2m} - F_{ysm} = 0 \quad (3.20a)$$

$$M_{yb1m} + M_{yb2m} - F_{yb2m}l_1 + F_{ysm}(l_1 + l_2) = 0 \quad (3.20b)$$

$$F_{zb1m} + F_{zb2m} = 0 \quad (3.20c)$$

Since the shaft-bearing system is statically indeterminate, bending theory for the shaft and rigid body motion constraint in the z direction are used to estimate stiffness coefficients

$$EI \delta_{y2m} - EI \delta_{y1m} + F_{yb1m}(l_1^3/6) + M_{yb1m}(l_1^2/2) = 0 \quad (3.21a)$$

$$EI \beta_{x2m} - EI \beta_{x1m} + F_{yb1m}(l_1^2/2) + M_{yb1m}l_1 = 0 \quad (3.21b)$$

$$\delta_{z1m} - \delta_{z2m} = 0 \quad (3.21c)$$

Additionally, 6 nonlinear algebraic equations defined by the mean bearing load-displacement relations as given in Chapter II are required. These nonlinear algebraic equations are solved using Newton-Raphson method [36,37]. Since mean loads on each bearing are sufficiently large, the bearing stiffness coefficients for both bearings are almost identical, as listed in Table 3.6 along with other system parameters.

Table 3.6 Design and estimated parameters for two identical rolling element bearings used in example case III

Load-deflection exponent $n=3/2$	$A_o^\dagger=0.05$ mm	$k_{bzz}=1.72E8$ N/m
Load-deflection constant $K_n=6.92E9$ N/m ⁿ	$l_1=41$ mm	$k_{bx\theta_y}=-2.56E5$ N
Number of rolling element $Z=10$	$l_2=84$ mm	$k_{by\theta_x}=3.52E5$ N
Radial clearance $r_L=5.0E-5$ mm	$k_{bxx}=1.44E8$ N/m	$k_{bz\theta_x}=4.02E5$ N
Pitch diameter=38.1 mm	$k_{byy}=3.69E8$ N/m	$k_{b\theta_x\theta_x}=4.19E4$ Nm
Unloaded contact angle $\alpha_o=0^\circ$	$k_{byz}=2.04E8$ N/m	$k_{b\theta_y\theta_y}=1.02E4$ Nm

† Unloaded distance between inner and outer raceway groove curvature centers

3.9.3 System Study

We incorporate the proposed rolling element bearing stiffness matrix $[K]_{bm}$ in a finite element model which includes shaft and plate dynamics, using the formulation given in Section 3.4.2. The finite element model shown in Figure 3.13c is implemented with a commercial software [39]. The shaft component is modeled using 2 noded Timoshenko beam elements with axial degrees of freedom in addition to the bending motion. The plate model is constructed using 4 noded quadrilateral plate elements with shear deformation and rotary inertia effects. Each node has 3 translational and 3 rotational degrees of freedom. Four generalized stiffness matrices corresponding to the first bearing, each matrix being equivalent to $1/4 [K]_{bm}$, are used to couple the single shaft node to 4 plate nodes. The second bearing connects one end of the shaft to a grounded node. The boundary conditions for the plate along the perimeter are chosen to

be a combination of ideal clamps, $u_{xa}(t) = u_{ya}(t) = u_{za}(t) = \theta_{xa}(t) = \theta_{ya}(t) = \theta_{za}(t) = 0$, and simple-supports $u_{za}(t) = 0$ as shown in Figure 3.13c in order to represent the physical model as much as possible. Here, the energy dissipation is assumed to be given by the modal damping ratio $\zeta = 0.03$. A sinusoidal force $F_{ysa}(t) = F_{ysa1}e^{i\omega_0 t}$ is applied at one end of the shaft to simulate the experiment.

Over the frequency range of 400Hz to 2000Hz, Figure 3.14 compares the driving point accelerance spectra $A_{u_{ysa}, F_{ysa}}(\omega_0) = \ddot{u}_{ysa}/F_{ysa}$. The simple theory shown here represents the conventional way of modeling bearings while the other features are exactly the same as in proposed model. Our predictions match measured spectra very well. Conversely, the simple model predicts slightly higher accelerance amplitude and lower resonant frequency in the vicinity of 800Hz due to the incomplete bearing model used. Cross point accelerance spectra $A_{u_{zca}, F_{ysa}}(\omega_0) = \ddot{u}_{zca}/F_{ysa}$ are shown in Figures 3.15a and 3.15b where \ddot{u}_{zca} is measured for 2 different locations on the plate as shown in Figure 3.13c, and excitation $F_{ysa}(t)$ is once again applied transversely at the shaft. Here, each predicted accelerance spectrum has been averaged over 4 points in the immediate vicinity of the measured location. Reasonable comparisons between the proposed model and experiment are seen. Here, the discrepancies are primarily due to physical setup complexities and the limitations associated with the finite element model in describing some of these. In Figure 3.15, the simple model is not included because it predicts exactly zero out-of-plane or flexural motion of the plate. Next, the cross point mobility level L_V is defined by averaging mean square mobility spatially over the entire plate and over a frequency bandwidth $\Delta\omega$. This level is directly related to the structure-borne noise or vibratory energy transmitted through the bearing.

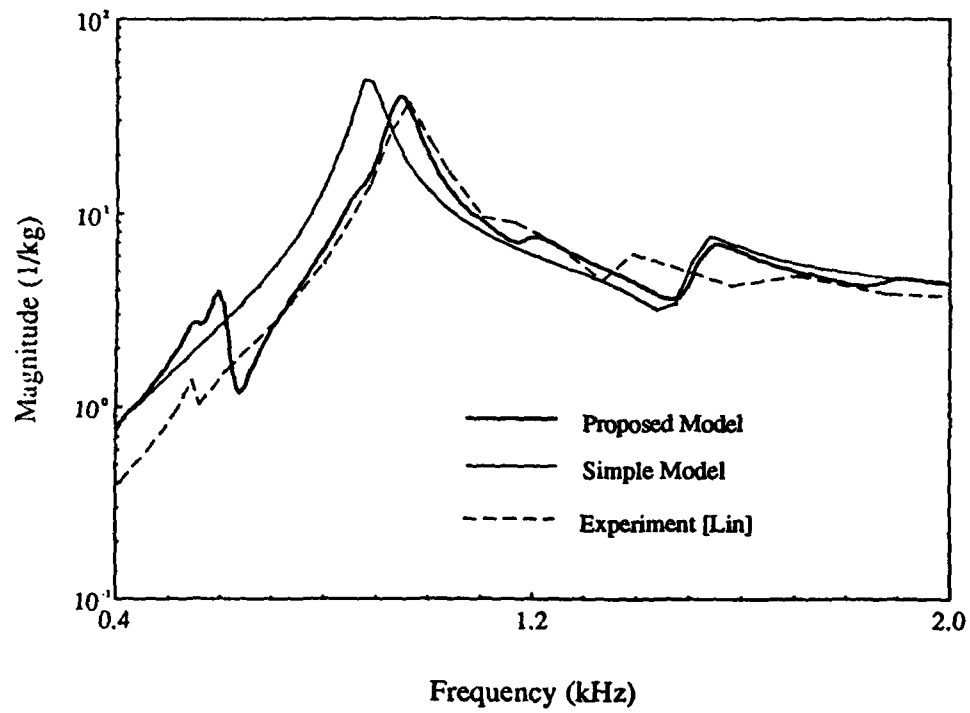
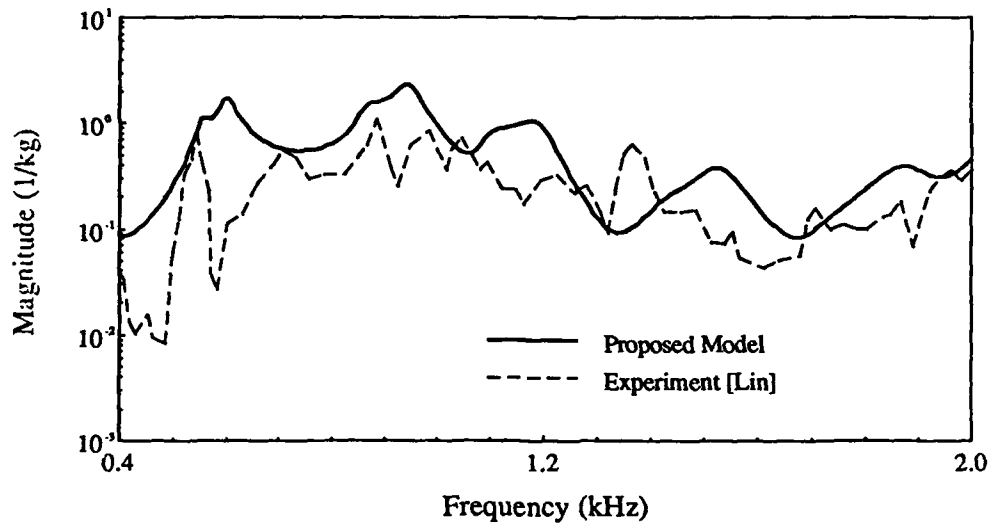
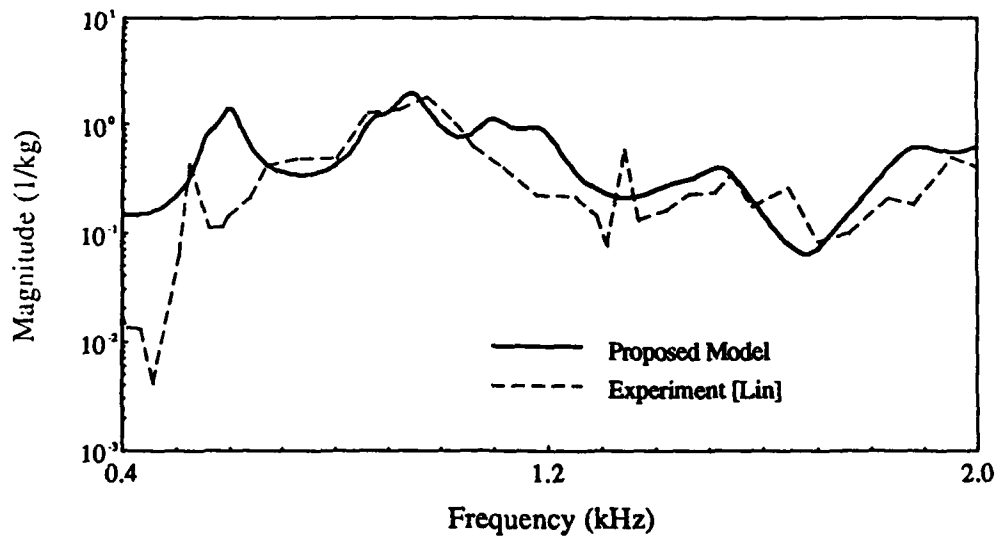


Figure 3.14 Driving point accelerance spectra $A_{u_{ysa}, F_{ysa}}(\omega_o)$ yielded by the proposed model, simple model and experiment by Lin [17] for example case III.



(a)



(b)

Figure 3.15 Cross point accelerance spectra $A_{u_{zca}, F_{ysa}}(\omega_0)$ yielded by the proposed model and experiment by Lin [17] for example case III. In this case, the simple model predicts zero response \ddot{u}_{zca} at the plate. (a) Point C1 (see Figure 3.13c). (b) Point C2 (see Figure 3.13c).

$$L_V = 10 \log_{10} \{ \langle V_{zca}^2 \rangle \} = 10 \log_{10} \left\{ \frac{1}{2 S_c \Delta \omega} \sum_{\Delta \omega} \sum_{S_c} \operatorname{Re} \left(\frac{\dot{u}_{zca} \dot{u}_{zca}^*}{F_{xsa} F_{xsa}^*} \right) \right\}$$

$$\text{dB re } \langle V^2 \rangle_{\text{ref}} = 1.0 \text{ m}^2 / \text{N}^2 \text{ s}^2 \quad (3.22)$$

where (*) implies the complex conjugate, S_c is the plate surface area and $\operatorname{Re}\{ \}$ implies the real part of the complex number. Table 3.7 compares L_V predictions by proposed and simple models with experimental data. It can be seen from this table that the proposed model predicts the experiment quite well and the simple model fails to predict any plate vibration. We can therefore conclude that our model is indeed valid for vibration transmission analyses.

Table 3.7 Predicted and measured cross point mobility level L_V as defined by equation (3.22)

1/3 Octave band center frequency (Hz)	Experiment (dB) [Lin]	Proposed model (dB)	Simple model (dB)
400	-102	-105	$-\infty$
500	-92	-96	$-\infty$
630	-95	-94	$-\infty$
800	-88	-97	$-\infty$
1000	-87	-95	$-\infty$
1250	-97	-108	$-\infty$
1600	-108	-115	$-\infty$
2000	-106	-107	$-\infty$

3.10 CONCLUDING REMARKS

A new mathematical model for precision rolling element bearing has been developed and incorporated in linear system dynamic models using lumped parameter and finite element modeling techniques for the vibration transmission studies of a generic single shaft-bearing-plate system. Stability studies indicate that the bearing system is dynamically stable for most of the practical designs. Through 3 example cases including one experimental study, we have shown that our proposed vibration model is clearly superior to the models currently available in the literature. The current models tend to underestimate the resonant frequencies and force/moment transmissibilities, and overestimate the acceleration amplitudes as compared to our models. The proposed model also predicts how the vibratory bending motion on the shaft is transmitted to the casing, illustrated through coupling coefficients of the proposed bearing stiffness matrix $[K]_{bm}$. Finally, the forced response trends indicated that increase in the mean bearing loads increases system resonant frequencies. We are extending this model to predict vibration transmission in rotating equipment with multiple shafts, bearings and gears. Other applications are evident as our theory is general in nature. However, it is restricted to linear systems. Bearing non-linearities are being examined in a parallel study [46].

CHAPTER IV

GEARED ROTOR SYSTEM STUDIES

4.1 INTRODUCTION

The focus of this chapter is on the dynamic analysis of geared rotor system shown in Figure 4.1 which includes a spur gear pair, shafts, rolling element bearings, motor, load, casing and flexible or rigid mounts. For this purpose, discrete vibration models are developed and used to predict vibration transmission through bearings. Also, the effects of bearing, casing and mount dynamics on the internal rotating system dynamic characteristics are investigated. Traditional analysis approaches [15,25-29] in the gear dynamics area concentrate on the internal rotating system and exclude dynamic effects of casing and flexible mounts. Moreover, simple bearing models are typically used which assume either ideal boundary conditions on the shaft or translational spring elements. Some of the limitations associated with current bearing models have been discussed thoroughly in Chapters II and III of this report. For instance, simple bearing formulations can not explain how the vibratory motion may be transmitted from the rotating shafts to casing and support structures, and moreover can not predict the effects of bearing, casing and mount dynamics on the internal rotating system adequately. Chapter II of this report also presents a new mathematical model for the precision rolling element bearings to clarify this issue qualitatively and quantitatively, and Chapter III utilizes the proposed bearing stiffness matrix $[K]_{bm}$ formulation to analyze the

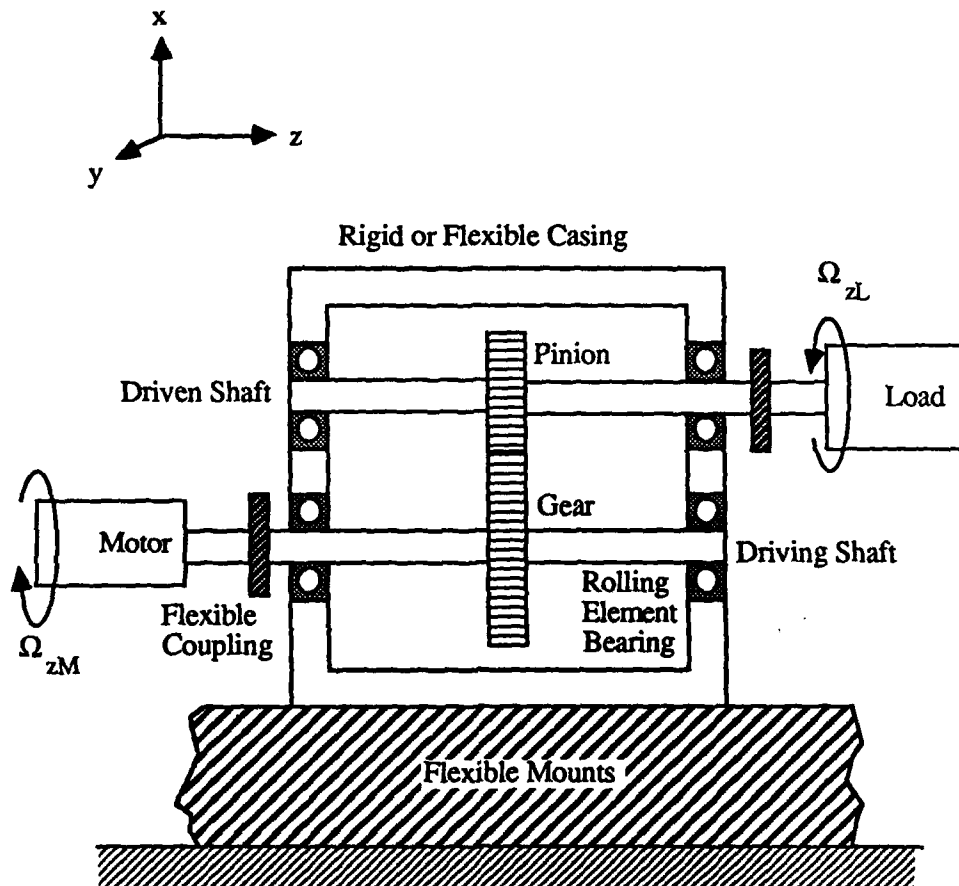


Figure 4.1 Schematic of a geared rotor system with flexible shafts and rigid spur gear and pinion, and supported by 4 rolling element bearings on a flexibly mounted casing. The shaft at the motor end is driven at mean speed Ω_{zM} which in turns drives the load at mean speed Ω_{zL} . This physical system is symmetric about a plane intersecting both the driving and driven shafts. The y axis is assumed parallel to the gear mesh line of action in the pressure angle direction at mesh point. This schematic is used for example case II and III.

vibration transmission problem in a generic shaft-bearing-casing-mount system. Our bearing formulation has already been validated through several example cases.

This study extends the proposed bearing formulation of Chapters II and III to examine vibration transmissibility in rotating mechanical equipment through two generic systems which are a spur gear pair drive and a single-stage rotor system with rolling element bearings as shown in Figures 4.1 and 4.2 respectively. It should be noted that Figure 4.2 can be treated as a special case of Figure 4.1 - this will be illustrated later. The physical systems are assumed to be driven at mean speed $\Omega_z = \Omega_{zM}$ in Figure 4.1 and Ω_z in Figure 4.2; subscript M refers to the motor end. Each shaft is supported by two identical rolling element bearings which are modeled as stiffness matrices $[K]_{bm}$ of dimension 6 as proposed in Chapter II of this report. These generic systems may be excited by motor and/or load torque fluctuations, rotating mass unbalances or gear kinematic transmission error $e(t)$ [29,47]; here $e(t)$ is defined as the deviation of the relative gear-pinion angular position from its relative ideal location. Typical excitation at the shaft is defined by an alternating load vector $\{f(t)\}_{sa} = \{F_{jsa}(t), T_{jsa}(t)\}^T = \{f(t)\}_s - \{f\}_{sm}$; $j=x,y,z$, where $F_{jsa}(t)$ and $T_{jsa}(t)$ are the alternating force and torque respectively, $\{f(t)\}_s$ is the total load vector of dimension 6, $\{f\}_{sm}$ represents the mean load vector, and superscript T implies the transpose. In the case of the geared drive, $\{f(t)\}_{sa}$ consists of $e(t)$ at the mesh point. Additionally, in the case of the single-stage rotor system, transverse forces $F_{xsa}(t)$ and $F_{ysa}(t)$ due to mass unbalances are of interest. Note that in the dynamic analysis $\{f\}_{sm}$ and bearing preloads are not included as they do not appear in the governing equations of the linear vibration model but are used for computing $[K]_{bm}$. Other effects such as bearing coupling coefficients, motor and load inertia, and

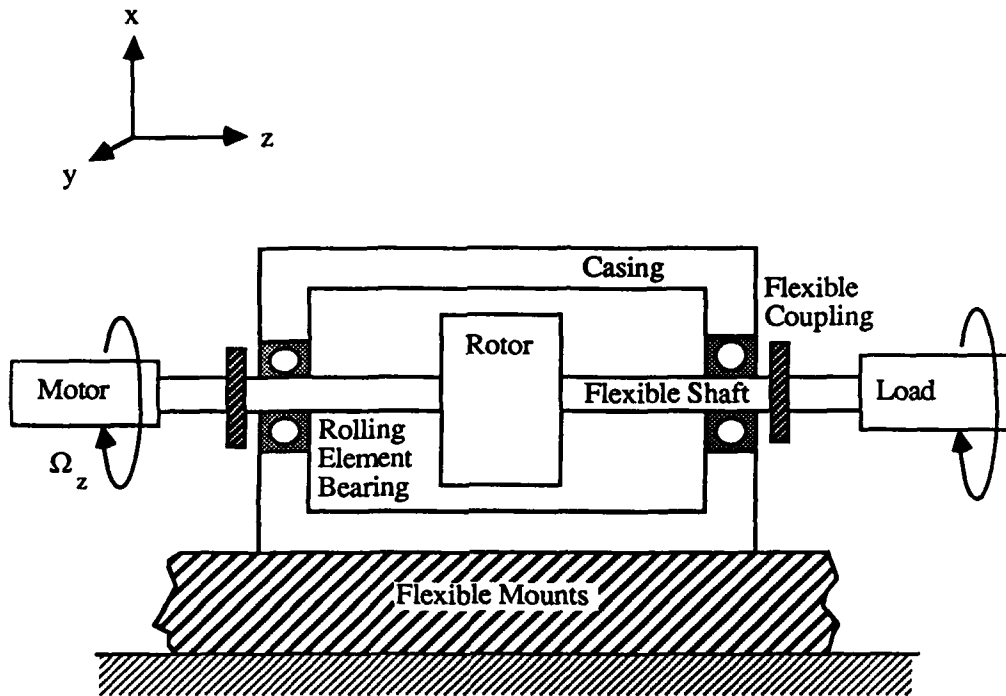


Figure 4.2 Schematic of the single stage rotor system with flexible shaft rotating at mean speed Ω_z and supported by 2 identical rolling element bearings on a flexibly mounted rigid casing. This physical system is symmetric about a plane intersecting the shaft axial axis and parallel to the x-z plane. This schematic is used for example case I.

casing and mount dynamics are considered as the emphasis is on the overall system behavior.

4.2 LITERATURE REVIEW

The available literature on bearing models commonly used for internal rotor and gear dynamic analyses has already been discussed in Chapters II and III of this report. Although there are numerous publications [10-13,15,25-29] on the modal analyses of geared drives and single or multiple-stage rotor systems, very little has been reported directly on the force transmissibility through bearings, and the dynamic effects of bearing, casing and mounts on the internal rotating system.

4.2.1 Casing and Mount Dynamics

A comprehensive review of the available vibration studies of casing and mounts, without the internal rotating system, has been given by Lim and Singh in 1987 [6]. Other related publication not included in Reference [6] are by Gaul and Mahrenholtz [48] in 1984, and Smith [49] in 1988 who have developed lumped parameter models of flexible machine foundations, excluding the internal rotating system dynamics. Their studies report rigid body translational and rotational vibration responses of the casing when excited by forces and/or moments. However, these studies are not specifically directed towards geared rotor systems, and dynamic interactions between internal rotating system and casing-mount system are not incorporated. In addition, Lim et al. [50] in 1989 have also performed a dynamic finite element analysis of a helicopter gearbox excluding the internal rotating system. Results again show that casing rigid

body vibration modes are dominant over the lower frequencies for a flexibly mounted casing, but numerous casing plate elastic modes are observed at higher frequencies.

4.2.2 Gear Dynamics

Current gear dynamic models include only the internal rotating system and simple bearing models, and typically exclude casing and mount flexibilities [15,25-29]. In few instances casing and mounts have also been included, but restricted to cases where only purely radial and/or axial force on the bearing, and unidirectional vertical/horizontal rigid body motion on the casing are modeled, as summarized in Reference [6]. Such models still do not explain how the vibration is transmitted from the gear mesh to the casing and into the machine foundation as witnessed in previous experiments [9,16,17].

4.2.3 Rotor Dynamics

Similar to the geared rotor models, most of the existing rotor dynamic models concentrate on the internal rotating system and address issues related to stability, critical speeds and rotating mass unbalance response [10-13]. But a few investigators have included support flexibility models [51-53]. For instance Lund and Wang [51] in 1986 proposed an impedance matching approach to reduce the large degrees of freedom (DOF) required in such models. Using one example case, they reported that support foundation has little influence on the internal rotor resonances, but then cautioned that this might not be true for other systems. Vance et al. [52] in 1987 incorporated measured support foundation parameters in a transfer matrix model of the rotor dynamic system, and concluded that the omission of support flexibility may miss some of the

rotor critical speeds of interest. Earles et al. [53] in 1988 reported, based on a finite element model of the support foundation, that the rotor critical speeds shift by including support flexibility. In all of the above mentioned studies, the overall dynamic behavior of the rotor system is only investigated partially. Moreover, only a subset of journal bearing $[K]_{bm}$ coefficients is included which can not predict completely the vibration transmission through bearings.

4.3 ASSUMPTIONS AND OBJECTIVES

Linear discrete vibration models of the geared and single-stage rotor systems shown in Figures 4.1 and 4.2 are used to incorporate $[K]_{bm}$ similar to Chapter III. The stiffness coefficients of $[K]_{bm}$ are evaluated using the analytical expressions presented in Chapter II. Each rotating shaft is modeled as an Euler beam in the lumped parameter model and as a Timoshenko beam in the dynamic finite element model but the effect of the gyroscopic moment on the shaft dynamics is not included. The casing is assumed to be rigid in the lumped parameter model and flexible in the dynamic finite element model. The rigid casing assumption is valid for many practical designs as it may be massive and the rotating speeds may be sufficiently low to avoid significant elastic deformation. The governing equations for both discrete vibration models can be given in the general matrix form as

$$[M]\{\ddot{q}(t)\}_a + [C]\{\dot{q}(t)\}_a + [K]\{q(t)\}_a = \{f(t)\}_a \quad (4.1)$$

where $[M]$, $[C]$ and $[K]$ are the system mass, damping and stiffness matrices respectively, and $\{q(t)\}_a$ and $\{f(t)\}_a$ are defined as the generalized alternating

displacement and applied load vectors respectively. Like Chapter III of this report, $\{f\}_{bm}$ and bearing preloads are also assumed constant to ensure a time-invariant $[K]_{bm}$ matrix. Energy equivalent viscous damping matrix $[C]_b = \sigma [K]_{bm}$ is assumed for the energy dissipation mechanism in the bearing where σ is the Rayleigh damping proportionality constant. Other features of the proposed theory given in Chapter III of this report are retained.

The specific objectives of this study are to: (i) incorporate the proposed bearing matrix $[K]_{bm}$, developed in Chapter II, in discrete vibration models of generic geared system of Figure 4.1 as described by equation (4.1) using lumped parameter and/or dynamic finite element method, (ii) conduct overall system studies by calculating eigensolutions and forced harmonic responses, (iii) evaluate the effects of casing and mount dynamics on the internal rotating system, and predict vibration transmission through bearings, (iv) examine the following 3 example cases: I. single-stage rotor system with flexible shaft supported by two identical rolling element bearings on rigid casing and flexible mounts as shown in Figure 4.2, II. spur gear pair system with motor and load inertias attached to two flexible shafts supported by four rolling element bearings on flexibly and rigidly mounted rigid casing as shown in Figure 4.1, and III. case II with flexible casing and rigid mounts, and (v) demonstrate the advantages of our formulation over the existing vibration models.

4.4 THEORY

4.4.1 Method A: Lumped Parameter Model

4.4.1.1 Equations of Motion

Both physical systems shown in Figures 4.1 and 4.2 are discretized using lumped parameter technique to yield equation (4.1) through the Lagrange's equations of motion [45].

$$\frac{d}{dt} \left(\frac{\partial E_T}{\partial \dot{q}_w} - \frac{\partial E_U}{\partial \dot{q}_w} \right) - \frac{\partial E_T}{\partial q_w} + \frac{\partial E_U}{\partial q_w} + \frac{\partial E_C}{\partial \dot{q}_w} = \tilde{F}_w \quad ; \quad w = 1, 2, 3, \dots \quad (4.2)$$

where E_T and E_U is the kinetic and potential energies respectively, $E_C = \frac{1}{2} \{\dot{q}\}^T [C] \{\dot{q}\}$ is the Rayleigh's dissipation function and \tilde{F}_w is the generalized force. The total system potential energy E_U and kinetic energy E_T are obtained by adding the energy of each system component which are derived in subsequent sections. Equation (4.2) when applied to Figure 4.1 will lead to equation (4.1). It is then rearranged in terms of the following $\{q\}$ to obtain the partitioned system matrices

$$\{q(t)\}_a = \left\{ \{u(t)\}_{sa}^T \{u(t)\}_{ca}^T \mid \{\theta(t)\}_{Ra}^T \{\theta(t)\}_{ca}^T \mid \{\theta(t)\}_{sa}^T \right\}^T \quad (4.3a)$$

$$[M] = \text{DIAG} \left\{ \{m\}_s^T \{m\}_c^T \mid \{I\}_R^T \{I\}_c^T \mid \{I\}_s^T \right\} \quad (4.3b)$$

$$[K] = \begin{bmatrix} [K]_{11} & [K]_{12} & [K]_{13} \\ [K]_{21} & [K]_{22} & [K]_{23} \\ [K]_{31} & [K]_{32} & [K]_{33} \end{bmatrix} \quad ; \quad [C] = \sigma [K] \quad (4.3c)$$

where $\{\theta(t)\}_{Ra}$ (subscript R indicates rotor) consists of the alternating angular displacement of all rotors including gears, motor and load; $\{m\}^T$ and $\{I\}^T$ are the lumped mass and inertia row vectors respectively; and the operator $\text{DIAG}\{ \}$ transform the row vector into a diagonal matrix with components of the vector corresponding to the diagonal elements. The stiffness sub-matrices $[K]_{wj} = [K]_{jw}^T$, $w, j = 1, 2, 3$, consist of the appropriate terms corresponding to the partitioned $\{q(t)\}_a$. For example, $[K]_{11}$ couples $\{\{u(t)\}_{sa}^T \{u(t)\}_{ca}^T\}^T$ degrees of freedom to itself, and $[K]_{12}$ provides a coupling between $\{\{u(t)\}_{sa}^T \{u(t)\}_{ca}^T\}^T$ and $\{\{\theta(t)\}_{Ra}^T \{\theta(t)\}_{ca}^T\}^T$ degrees of freedom.

Now assume that the rotary inertia of each shaft lumped mass is negligible. The system matrices given in equation (4.3) are therefore simplified by eliminating $\{\theta(t)\}_{sa}$ degrees of freedom from $\{q(t)\}_a$ in equation (4.3a). The resulting mass and stiffness matrices are

$$[M] = \text{DIAG} \left\{ \{m\}_s^T \{m\}_c^T \mid \{I\}_R^T \{I\}_c^T \right\} \quad (4.4a)$$

$$[K] = \begin{bmatrix} [K]_{11} - [K]_{13}[K]_{33}^{-1}[K]_{31} & [K]_{12} - [K]_{13}[K]_{33}^{-1}[K]_{32} \\ [K]_{21} - [K]_{23}[K]_{33}^{-1}[K]_{31} & [K]_{22} - [K]_{23}[K]_{33}^{-1}[K]_{32} \end{bmatrix} \quad (4.4b)$$

This analytical lumped parameter formulation will be used for example cases I and II. It may be noted that if the effect of the rotary inertias is required, equation (4.3) can be used instead.

4.4.1.2 System Kinetic Energy

A flexible shaft of length L_s with rigid rotor of mass m_R is subdivided into n_s number of segments of equal length $L_e = L_s/n_s$ with lumped masses at both ends of each segment as shown in Figures 4.3a and 4.3b for a single-spur gear mesh geared drive and single-stage rotor system respectively. Each lumped mass has 3 translational and 3 rotational degrees of freedom as illustrated in Figure 4.3c. The total system kinetic energy E_T is given by $\frac{1}{2} \{\dot{q}\}^T [M] \{\dot{q}\}$. The mass matrix $[M]$ is diagonal and consists of the lumped masses and inertias.

4.4.1.3 Shaft Stiffness Matrix

Using the direct stiffness approach, the stiffness matrix $[K]_s^e$ of dimension 12 corresponding to the alternating displacement vector $\{q(t)\}_{sa}^e = \{u_{xj}(t), u_{xj+1}(t), u_{yj}(t), u_{yj+1}(t), u_{zj}(t), u_{zj+1}(t), \theta_{yj}(t), \theta_{yj+1}(t), \theta_{xj}(t), \theta_{xj+1}(t), \theta_{zj}(t), \theta_{zj+1}(t)\}^T$, of a generic shaft segment is given by

$$[K]_s^e = \begin{bmatrix} [K_{uu}]_s^e & [K_{u\theta}]_s^e \\ [K_{\theta u}]_s^e & [K_{\theta\theta}]_s^e \end{bmatrix} \quad (4.5)$$

and the non-zero elements of $[K_{uu}]_s^e$, $[K_{u\theta}]_s^e = [K_{\theta u}]_s^{eT}$ and $[K_{\theta\theta}]_s^e$ of dimension 6 are given by the following equations (4.6), (4.7) and (4.8) respectively.

$$\begin{aligned} k_{11} = k_{22} = k_{33} = k_{44} = -k_{12} = -k_{21} = -k_{34} = -k_{43} &= 12 EI/L_e^3 ; \\ k_{55} = k_{66} = -k_{56} = -k_{65} &= AE/L_e \end{aligned} \quad (4.6)$$

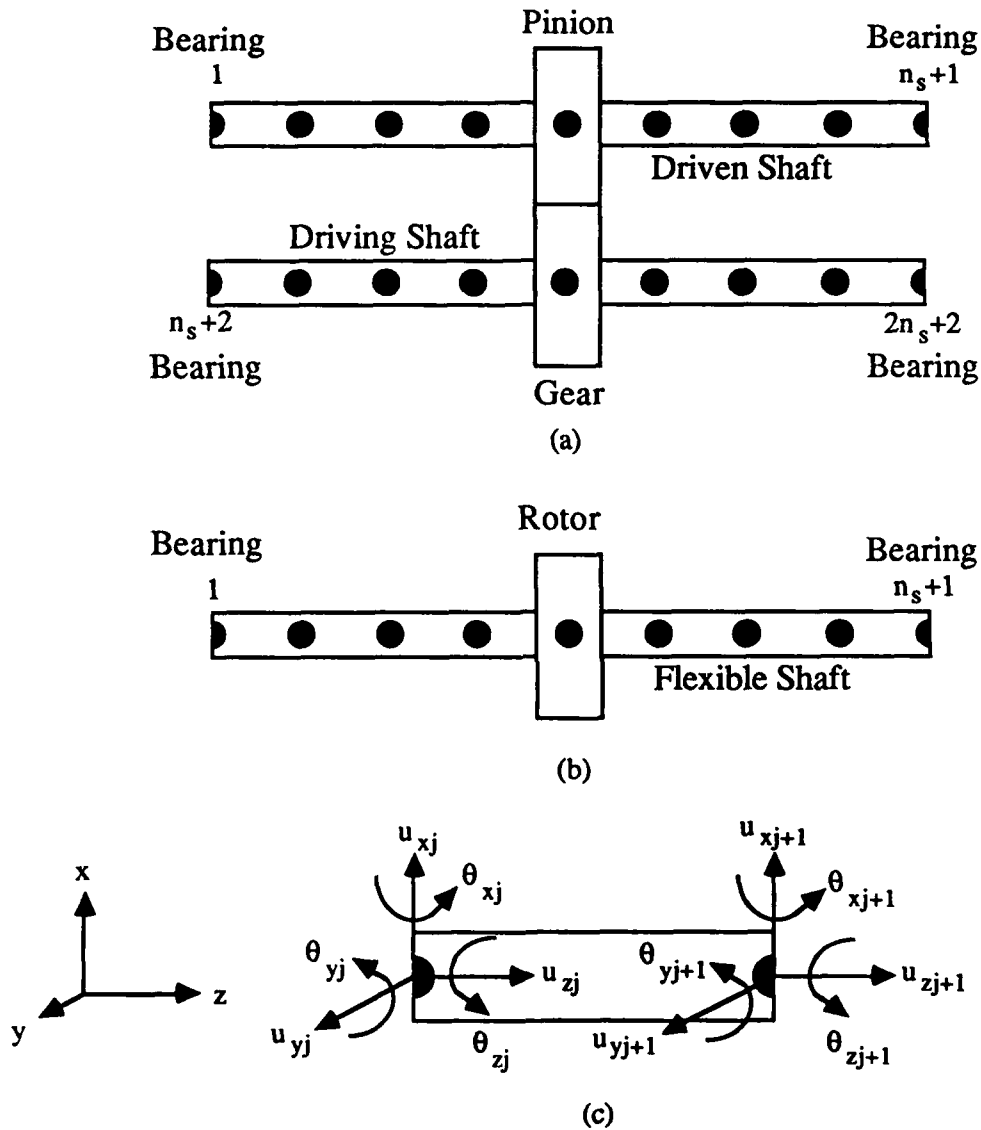


Figure 4.3 Lumped parameter model of the flexible shafts with rigid rotors. Each shaft is supported by 2 identical bearings on both ends. (a) Internal rotating system of a typical geared rotor system of Figure 4.1. (b) Internal rotating system of a typical single-stage rotor system of Figure 4.2. (c) Discretization of a shaft segment and the degrees of freedom associated with each lumped mass.

$$k_{11} = -k_{22} = k_{33} = -k_{44} = k_{12} = -k_{21} = k_{34} = -k_{43} = 6EI/L_e^2 \quad (4.7)$$

$$\begin{aligned} k_{11} &= k_{22} = k_{33} = k_{44} = 4EI/L_e ; \\ k_{12} &= k_{21} = k_{34} = k_{43} = 2EI/L_e ; \\ k_{55} &= k_{66} = -k_{56} = -k_{65} = GJ/L_e \end{aligned} \quad (4.8)$$

where E is the modulus of elasticity, G is the shear modulus of elasticity, I is the moment of inertia, and J is the polar moment of inertia of the shaft. The lumped stiffness matrix $[K]_s$ corresponding to $\{q(t)\}_{sa} = \{u_{xj}(t), u_{yj}(t), u_{zj}(t), \theta_{yj}(t), \theta_{xj}(t), \theta_{zj}(t)\}^T$, $j = 1, 2, 3, \dots$ for the shaft is constructed by the superposition of all $[K]_s^e$ matrices and merging terms associated with each degree of freedom.

$$[K]_s = \begin{bmatrix} [K_{uu}]_s & [K_{u\theta}]_s \\ [K_{\theta u}]_s & [K_{\theta\theta}]_s \end{bmatrix} \quad (4.9)$$

The non-zero elements of $[K_{uu}]_s$, $[K_{u\theta}]_s = [K_{\theta u}]_s^T$ and $[K_{\theta\theta}]_s$ of dimension $3(n_s+1)$ are similarly given by the following equations (4.10), (4.11) and (4.12) respectively.

$$\begin{aligned} k_{11} &= k_{22} = k_{3n_s+1, 3n_s+1} = k_{3n_s+2, 3n_s+2} = 12EI/L_e^3 ; \\ k_{33} &= k_{3n_s+1, 3n_s+1} = AE/L_e \end{aligned} \quad (4.10a)$$

$$k_{w_I+3, w_I} = k_{w_I, w_I+3} = -12EI/L_e^3 ; \quad w_I = 1, 2, 4, 5, 7, 8, \dots, 3n_s-1 \quad (4.10b)$$

$$k_{w_{II}, w_{II}} = 24EI/L_e^3 ; \quad w_{II} = 4, 5, 7, 8, 10, 11, \dots, 3n_s-1 \quad (4.10c)$$

$$k_{w_{III}+3, w_{III}} = k_{w_{III}, w_{III}+3} = -AE/L_e ; \quad w_{III} = 3, 6, 9, \dots, 3n_s \quad (4.10d)$$

$$k_{w_{IV}, w_{IV}} = 2AE/L_e ; \quad w_{IV} = 6, 8, 12, \dots, 3n_s \quad (4.10e)$$

$$k_{11} = k_{22} = -k_{3n_s+1, 3n_s+1} = -k_{3n_s+2, 3n_s+2} = 6 EI/L_e^2 \quad (4.11a)$$

$$-k_{w_I+3, w_I} = k_{w_I, w_I+3} = 6 EI/L_e^2 \quad ; \quad w_I = 1, 2, 4, 5, 7, 8, \dots, 3n_s-1 \quad (4.11b)$$

$$k_{11} = k_{22} = k_{3n_s+1, 3n_s+1} = k_{3n_s+2, 3n_s+2} = 4 EI/L_e \quad ;$$

$$k_{33} = k_{3n_s+1, 3n_s+1} = GJ/L_e \quad (4.12a)$$

$$k_{w_I+3, w_I} = k_{w_I, w_I+3} = 2 EI/L_e \quad ; \quad w_I = 1, 2, 4, 5, 7, 8, \dots, 3n_s-1 \quad (4.12b)$$

$$k_{w_{II}, w_{II}} = 8 EI/L_e \quad ; \quad w_{II} = 4, 5, 7, 8, 10, 11, \dots, 3n_s-1 \quad (4.12c)$$

$$k_{w_{III}+3, w_{III}} = k_{w_{III}, w_{III}+3} = -GJ/L_e \quad ; \quad w_{III} = 3, 6, 9, \dots, 3n_s \quad (4.12d)$$

$$k_{w_{IV}, w_{IV}} = 2 GJ/L_e \quad ; \quad w_{IV} = 6, 8, 12, \dots, 3n_s \quad (4.12e)$$

Note that here $[K]_s$ is only for a shaft, of dimension $6(n_s+1)$. The same formulation should be applicable to a geared system with multiple shafts where each shaft stiffness matrix is still given by $[K]_s$. Accordingly, the shaft potential energy E_{Us} is given as

$$E_{Us} = \frac{1}{2} \{q\}_{sa}^T [K]_s \{q\}_{sa} \quad (4.13)$$

Formulations for the motor and load rotary inertias, and flexible coupling torsional stiffness will be given in the later sections on example cases.

4.4.1.4 Gear Mesh Stiffness Matrix

For the generic geared rotor system with a spur gear pair, the driving and driven shafts are coupled via a linear, time-invariant spur gear mesh stiffness $k_h \neq k_h(t)$. Now we define the gear mesh coupling stiffness matrix $[K]_h$ as follows where coupled

torsional and translational motions of the gear and pinion are defined by $\{u_{yGa}(t), u_{yPa}(t), \theta_{zGa}(t), \theta_{zPa}(t)\}^T$

$$[K]_h = \begin{bmatrix} k_h & -k_h & \frac{k_h d_G}{2} & -\frac{k_h d_P}{2} \\ -k_h & k_h & -\frac{k_h d_G}{2} & \frac{k_h d_P}{2} \\ \frac{k_h d_G}{2} & -\frac{k_h d_G}{2} & \frac{k_h d_G^2}{4} & -\frac{k_h d_P d_G}{4} \\ -\frac{k_h d_P}{2} & \frac{k_h d_P}{2} & -\frac{k_h d_P d_G}{4} & \frac{k_h d_P^2}{4} \end{bmatrix} \quad (4.14)$$

where d_G and d_P are the gear and pinion diameters respectively; subscript G and P refer to gear and pinion respectively. Here, the y axis is taken to be parallel to the gear mesh force which is along the pressure angle direction at the mesh point. The potential energy E_{Uh} in this case is

$$E_{Uh} = \frac{1}{2} \{u_{yGa}, u_{yPa}, \theta_{zGa}, \theta_{zPa}\} [K]_h \begin{Bmatrix} u_{yGa} \\ u_{yPa} \\ \theta_{zGa} \\ \theta_{zPa} \end{Bmatrix} \quad (4.15)$$

4.4.1.5 Flexible Mount Stiffness Matrix

The flexible mounts are represented by a diagonal stiffness matrix $[K]_v$ corresponding to $\{q(t)\}_{ca}$ which consist of effective stiffness coefficients k_{vw} , $w = x, y, z, \theta_x, \theta_y, \theta_z$. This modeling procedure assumes that no coupling exists between the

casing rigid body degrees of freedom due to the flexibility of the mounts. Accordingly, one has

$$E_{Uv} = \frac{1}{2} \{q\}_{ca}^T [K]_v \{q\}_{ca} \quad (4.16)$$

4.4.1.6 Bearing Stiffness Matrix

The proposed bearing stiffness matrix $[K]_{bm}$ corresponding to the bearing degrees of freedom $\{\delta_{wa}(t), \beta_{wa}(t)\}^T$, $w = x, y, z$, has been formulated in Chapter II. The corresponding potential energy E_{Ub} is

$$E_{Ub} = \frac{1}{2} \left\{ \delta_{waj}, \beta_{waj} \right\} [K]_{bm} \begin{Bmatrix} \delta_{waj} \\ \beta_{waj} \end{Bmatrix} \quad (4.17)$$

Here, $\{\delta_{waj}(t), \beta_{waj}(t)\}^T$ may be expressed in terms of $\{q(t)\}_{saj}$ and $\{q(t)\}_{ca}$ through a coordinate transformation for the j -th bearing located at $\vec{R}_j = \{x_j, y_j, z_j\}$ from the casing center of mass. For the geared rotor system, four bearings are denoted by $j = 1, n_s+1, n_s+2$ and $2n_s+2$ as shown in Figure 4.3a, while for the single-stage rotor system two bearings are denoted by $j = 1$ and n_s+1 as shown in Figure 4.3b. Assuming the small angle approximation, $\{\delta_{waj}(t), \beta_{waj}(t)\}^T$ for the j -th bearing is

$$\begin{Bmatrix} \delta_{waj} \\ \beta_{waj} \end{Bmatrix} = \begin{bmatrix} -1 & 0 & 0 & 0 & 0 & 0 & 1 & 0 & 0 & 0 & z_j & -y_j \\ 0 & -1 & 0 & 0 & 0 & 0 & 0 & 1 & 0 & -z_j & 0 & x_j \\ 0 & 0 & -1 & 0 & 0 & 0 & 0 & 0 & 1 & y_j & -x_j & 0 \\ 0 & 0 & 0 & -1 & 0 & 0 & 0 & 0 & 0 & 1 & 0 & 0 \\ 0 & 0 & 0 & 0 & -1 & 0 & 0 & 0 & 0 & 0 & 1 & 0 \\ 0 & 0 & 0 & 0 & 0 & -1 & 0 & 0 & 0 & 0 & 0 & 1 \end{bmatrix} \begin{Bmatrix} \{q\}_{saj} \\ \{q\}_{ca} \end{Bmatrix} \quad (4.18)$$

4.4.2 Method B: Dynamic Finite Element Formulation

The dynamic finite element technique of incorporating $[K]_{bm}$ in equation (4.1) is employed especially when the casing plate is elastically deformable over the frequency range of interest, as discussed previously in Chapter III. In this method, $[K]_{bm}$ is implemented in the dynamic finite element model as a generalized stiffness matrix. This stiffness element provides the only coupling between the flexible shaft and casing at the appropriate nodal points on both components corresponding to the bearing locations. Additionally, the gear mesh stiffness k_h in Figure 4.1 behaves like a linear translational spring. Since the coupling between torsional and transverse shaft vibrations is due to k_h only, the corresponding portion of the stiffness matrix is also given by equation (4.14). Our finite element formulation uses conventional structural elements typically available in commercial software programs [39] for the shaft, casing plate and mounts – this will be illustrated for example cases I, II and III. Other features of this method are similar to those discussed earlier in Section 4.4.1.

4.4.3 Other Methods

Alternate techniques of formulating the geared rotor system dynamic problems such as finite difference (which is similar to method B), flexibility, component mode synthesis and transfer matrix formulations are also possible. It may be noted that Berman [54] has philosophically proposed application of the component mode synthesis to geared problems. Other researchers [40,41] have utilized the transfer matrix method in the rotor dynamic problems. However, such models need to be modified or extended in order to solve the overall dynamic problems discussed in this research. Direct

application of these alternate methods [40-43,54] are beyond the scope of this report and are left for further research.

4.5 EXAMPLE CASE I: SINGLE-STAGE ROTOR SYSTEM WITH RIGID CASING AND FLEXIBLE MOUNTS

4.5.1 Vibration Models

Consider the single-stage rotor system shown in Figure 4.2 where two axially preloaded identical deep groove ball bearings support a flexible rotating shaft; see Table 4.1 for bearing parameters. The shaft is assumed to be subjected to a mean torque $T_{zsm} \neq T_{zsm}(t)$ and harmonic excitation forces $\{F_{xsa}(t) = F_{xsa1}(\Omega_z) e^{i\Omega_z t}, F_{ysa}(t) = F_{ysa1}(\Omega_z) e^{i(\Omega_z t - \pi/2)}\}^T$ due to the rotating rotor mass unbalance. The rotor is fixed to the center of the shaft which coincides with the rigid casing centroid. The shaft is assumed to be transversely decoupled from the motor and load due to the flexible torsional couplings.

A lumped parameter model with $n_s + 2$ lumped masses is developed according to the theory given in Section 4.4.1. The bearing stiffness matrix for an axially preloaded ball bearing has significant stiffness coefficients $k_{bxx}, k_{byy}, k_{bzz}, k_{b\theta_x\theta_x}, k_{b\theta_y\theta_y}, k_{b\theta_x\theta_y}$ and $k_{b\theta_y\theta_x}$ which depend on the mean axial preload. Since there is no external $F_{za}(t)$ force on the system and no coupling between the torsional and transverse motions of the shaft, the dynamics associated with $\{u_{zsa_j}(t), u_{zca}(t), \theta_{zRa}(t)\}^T$ degrees of freedom (here subscript j is a dummy index to identify the shaft lumped masses) are decoupled from the others and have trivial steady-state particular solution. The system matrices of equation (4) can now be simplified by suppressing such degrees of freedom. Also, it can be easily observed from equations (1) and (4) that 2 sets of uncoupled differential equations exist. One set has $\{q(t)\}_a = \{u_{xsa_j}(t), u_{xca}(t), \theta_{yRa}(t), \theta_{yca}(t)\}^T$ which are excited by $F_{xsa}(t)$ and the other set consists of $\{q(t)\}_a = \{u_{ysa_j}(t), u_{yca}(t), \theta_{xRa}(t),$

Table 4.1 Design parameters for deep groove ball bearings used for example cases [†]

Load-deflection exponent n	3/2
Load-deflection constant K_n (N/m ⁿ)	7.5 E9
Number of rolling element Z	12
Radial clearance r_L (mm)	0.005 – 0.02
Pitch diameter (mm)	38.5
A_o (mm) ^{††}	0.0625
Unloaded contact angle α_o	23° – 47°

[†] These bearings are currently being used in a NASA gear test facility [55]. Also see example cases II and III.

^{††} Unloaded distance between inner and outer raceway groove curvature centers.

$\theta_{xca}(t)\}^T$ with $F_{ysa}(t)$. The steady-state solution to these two sets will always result in the synchronous whirling motion of the internal rotating shaft. However, since the two sets of equations are similar and independent, only one set is considered in the following analysis. Hence, the problem reduces to a 2 dimensional vibration system with $\text{DOF} = n_s + 4$ which consists of a flexible shaft with rigid rotor vibrating transversely and coupled to a rigid casing and a flexible mounts through two bearings. Accordingly, $[M]$ in equation (4.4) is rewritten in terms of the alternating displacement vector $\{q(t)\}_a = \{u_{xsaj}(t), u_{xca}(t), \theta_{yRa}(t), \theta_{yca}(t)\}^T$ as

$$[M] = \text{DIAG} \{m_{sej}, m_c, I_{yR}, I_{yc}\} \quad (4.19)$$

where m and I_y are the lumped mass and inertia about the y axis respectively, and the subscript e refers to the shaft segment. To define $[K]$ in equation (4.4), the nonzero elements of $[K]_{11}$, $[K]_{12}$, $[K]_{22}$, $[K]_{23}$, $[K]_{13}$ and $[K]_{33}$ are given by equations (4.20), (4.21), (4.22), (4.23) and (4.25) respectively.

$$k_{11} = k_{n_s+1, n_s+1} = 12 EI/L_e^3 + k_{bxx} ; \quad k_{n_s+2, n_s+2} = k_{vx} + 2 k_{bxx} ;$$

$$k_{n_s+2, 1} = k_{n_s+2, n_s+1} = k_{1, n_s+2} = k_{n_s+1, n_s+2} = -k_{bxx} \quad (4.20a)$$

$$k_{w_I+1, w_I} = k_{w_I, w_I+1} = -12 EI/L_e^3 ; \quad w_I = 1, 2, 3, \dots, n_s \quad (4.20b)$$

$$k_{w_{II}, w_{II}} = 24 EI/L_e^3 ; \quad w_{II} = 2, 3, \dots, n_s \quad (4.20c)$$

$$k_{n_s/2, 1} = -k_{n_s/2+2, 1} = 6 EI/L_e^2 ; \quad k_{n_s+2, 2} = (z_1 + z_{n_s+1}) k_{bxx} + 2 k_{bx\theta_y} ;$$

$$k_{12} = -z_1 k_{bxx} - k_{bx\theta_y} ; \quad k_{n_s+1, 2} = -z_{n_s+1} k_{bxx} - k_{bx\theta_y} \quad (4.21)$$

$$k_{11} = 8 EI/L_e ; k_{22} = k_{v\theta_y} + 2 k_{b\theta_y\theta_y} + (z_1^2 + z_{n_s+1}^2) k_{bxx} + (z_1 + z_{n_s+1}) k_{bx\theta_y} \quad (4.22)$$

$$k_{1,n_s/2} = k_{1,n_s/2+1} = 2 EI/L_e ;$$

$$k_{21} = -z_1 k_{bx\theta_y} - k_{b\theta_y\theta_y} ; k_{2,n_s} = -z_{n_s+1} k_{bx\theta_y} - k_{b\theta_y\theta_y} \quad (4.23)$$

$$k_{11} = -k_{n_s+1,n_s} = 6 EI/L_e^2 + k_{bx\theta_y} ; k_{n_s+2,1} = k_{n_s+2,n_s} = -k_{bx\theta_y} ;$$

$$k_{n_s/2+1,n_s/2+1} = -k_{n_s/2+1,n_s/2} = 6 EI/L_e^2 \quad (4.24a)$$

$$k_{12} = -k_{n_s+1,n_s-1} = -k_{n_s/2,n_s/2-1} = k_{n_s/2+2,n_s/2+2} = 6 EI/L_e^2 ; n_s > 2 \quad (4.24b)$$

$$k_{w_{III}-1,w_{III}} = -k_{w_{III}-1,w_{III}-2} = -k_{w_{III}+n_s/2,w_{III}-2+n_s/2} = k_{w_{III}+n_s/2,w_{III}+n_s/2} = 6 EI/L_e^2 ;$$

$$n_s \geq 6, w_{III} = 3, 4, \dots, n_s/2 \quad (4.24c)$$

$$k_{11} = k_{n_s,n_s} = 4 EI/L_e + k_{b\theta_y\theta_y} \quad (4.25a)$$

$$k_{w_{IV},w_{IV}} = 8 EI/L_e ; n_s > 2, w_{IV} = 2, 3, \dots, n_s-1 \quad (4.25b)$$

$$k_{w_V,w_V-1} = 2 EI/L_e ; k_{w_V-1,w_V} = 2 EI/L_e ;$$

$$n_s > 2, w_V = 2, 3, \dots, n_s (w_V \neq n_s/2+1) \quad (4.25c)$$

Due to the symmetric nature of $[K]$, $[K]_{wj} = [K]_{jw}^T$. The generalized load vector $\{f(t)\}_a = \{0, \dots, F_{xsa}(t), 0, \dots\}$ consists of only the x component of the rotor mass unbalance force. The other set of linear governing equation may be obtained by interchanging subscripts x and y in the above formulation. Our proposed vibration model can also be readily reduced to the conventional rotor dynamic models, excluding the gyroscopic moment, internal structural damping, dissimilar bearings and other secondary effects, by retaining only k_{bxx} , k_{byy} and k_{bzz} in our bearing formulation.

4.5.2 Eigensolution

The natural frequencies ω_j and modes ϕ_j of Figure 4.2 with system parameters given in Table 4.2 are obtained numerically. Initially, we check for ω_j convergence rate as shown in Figure 4.4. through ω_4 and ω_5 by varying the number of shaft segments n_s ; it may be noted that ω_1 , ω_2 and ω_3 behave like ω_4 , and ω_6 trend is very similar to ω_5 . Beyond $n_s = 4$, there are no noticeable changes in the natural frequencies. These predictions are now compared with two simple lumped parameter vibration models and a dynamic finite element model (FEM) in Table 4.3. One of the simple models excludes the effect of casing and flexible mounts, and both employ a conventional bearing model with only k_{bxx} incorporated as described earlier in Section 4.5.1. The dynamic finite element formulation models the flexible casing constructed with four noded quadrilateral plate elements – a description of the methodology will be presented later in example case III. Our proposed theory and FEM are in excellent agreement with each other as the deviations are within $\pm 4\%$ for first 6 natural frequencies. The corresponding mode shapes ϕ_j are shown in Figure 4.5. Note that for each mode in the x-z plane given here, there is a complementary mode in the y-z plane which will have the same natural frequency if $k_{vy}=k_{vx}$, $k_{v\theta_x}=k_{v\theta_y}$ and $I_{xc}=I_{yc}$. Using the exactly same parameters, results obtained from two simple models are also compared in Table 4.3. The simple model with casing and mount dynamics included predicts lower natural frequencies as compared to our prediction except for $\hat{\omega}_5$; here the symbol $\hat{\omega}$ implies estimation using a simple formulation. This model gives a rough approximation for most of the modes, as evident from Table 4.3. Further, the simple model without casing and mounts can not predict all the modes below 2 kHz. In addition, $\hat{\omega}_3$ shifts while other modes remain

Table 4.2 System parameters of example case I: single-stage rotor system shown in Figure 4.2

Rotor mass m_R (kg) and inertia I_{yR} (kgm ²)	5.0, 1.24E-2
Shaft mass m_s (kg) and length L_s (m)	1.03, 4.2E-1
Casing mass m_c (kg) and inertia I_{yc} (kgm ²)	148, 4.27
Shaft flexural rigidity EI (Nm ²)	1.626E3
Bearing axial preload F_{zbm} (N)	238
$k_{bxx}, k_{bx\theta_y}, k_{b\theta_y\theta_y}$ †	1.37E8, -1.96E6, 4.27E4
$k_{vx}, k_{v\theta_y}$	4.0E8, 1.8E7

† Computed k_{bwj} as proposed in Chapter II. Only relevant bearing coefficients are listed.

Table 4.3 Comparison of natural frequencies in Hz for example case I

Mode	Proposed Theory	FEM	$\Delta_1\%$	Simple Models		$\Delta_2\%$
				without casing	with casing	
1	97.2	97.2	0.0	69.5	69.4	28.6
2	262	262	0.0	not predicted	262	0.0
3	309	309	0.0	297	294	4.9
4	332	334	0.6	not predicted	329	1.5
5	1405	1365	-2.9	1442	1443	-5.7
6	1755	1690	-3.8	1452	1453	14.0

$$\Delta_1\% = 100 \times (\text{FEM} - \text{Proposed Theory}) / \text{FEM}$$

$$\Delta_2\% = 100 \times (\text{FEM} - \text{Simple Model}) / \text{FEM}$$

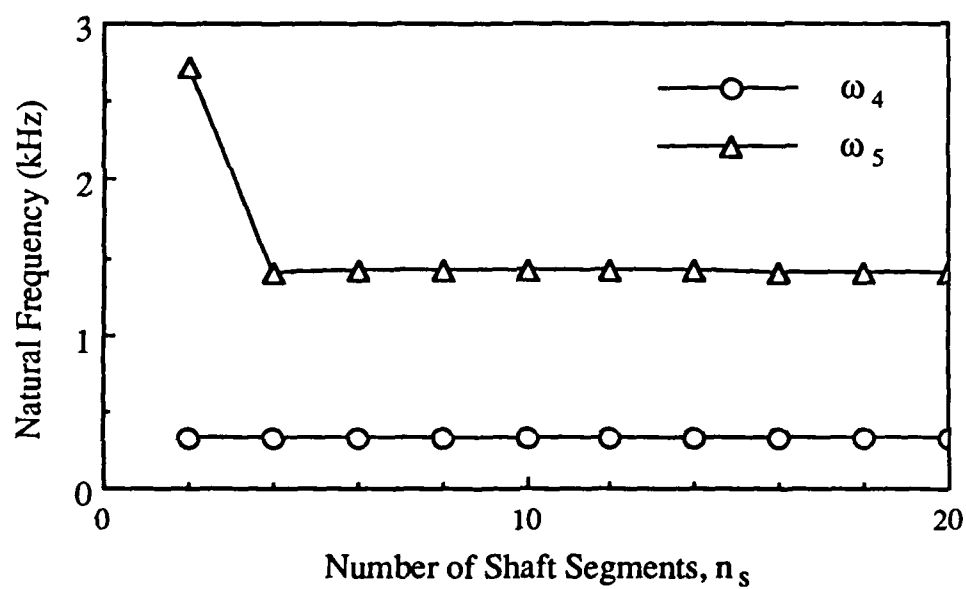


Figure 4.4 Natural frequencies ω_4 and ω_5 versus the number of shaft segments, n_s for example case I.

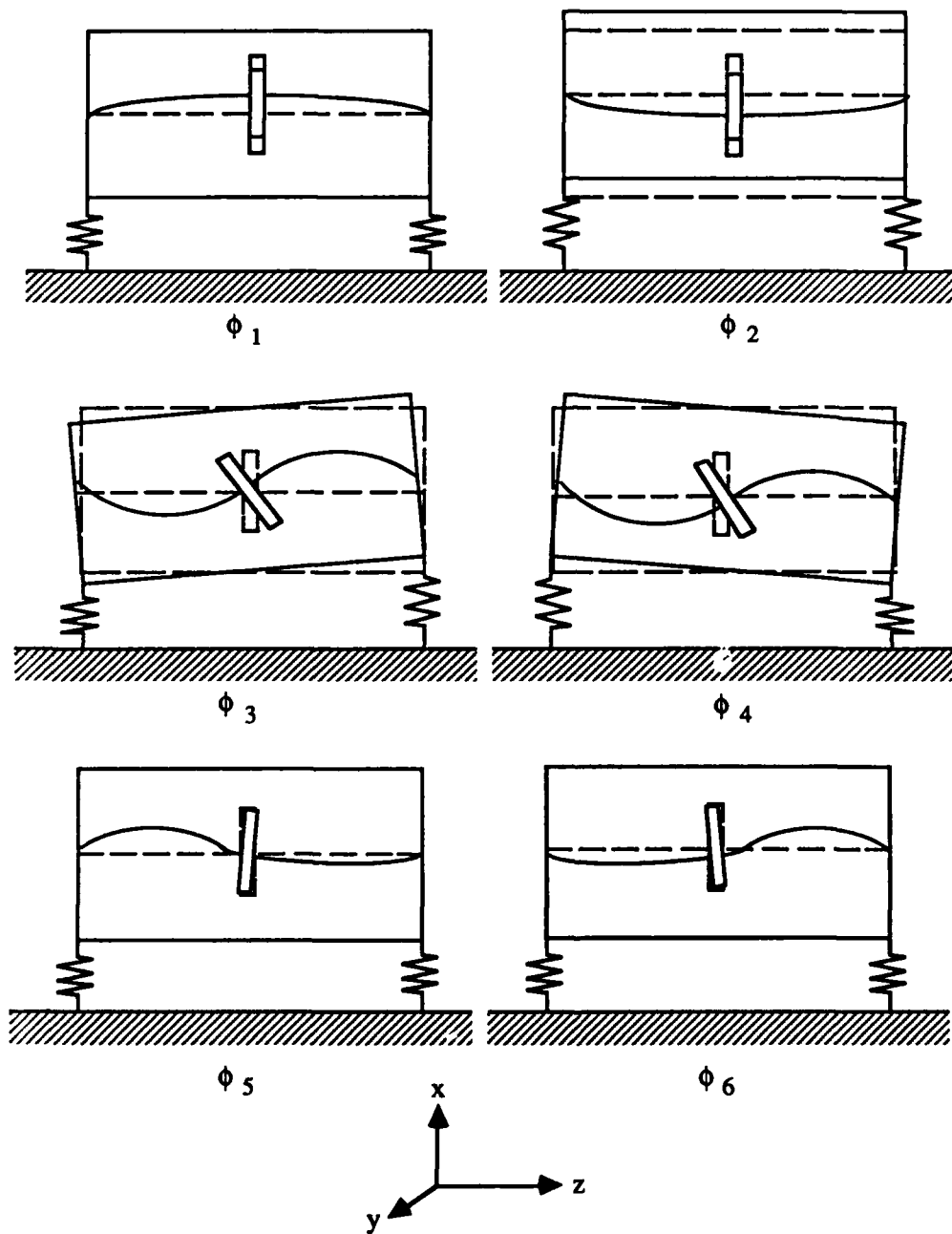


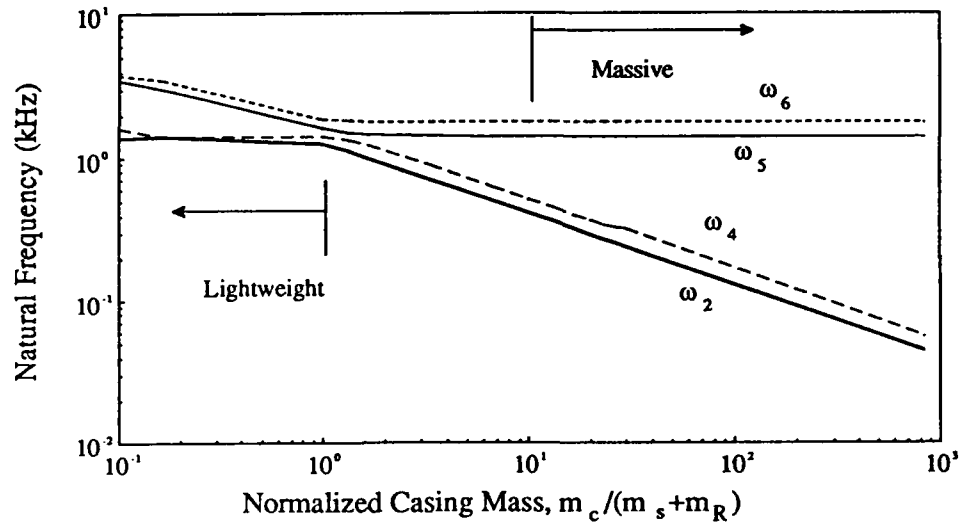
Figure 4.5 First 6 mode shapes of example case I: single-stage rotor system including rigid casing and flexible mounts.

nearly the same. These observations are consistent with the findings reported earlier [51-53].

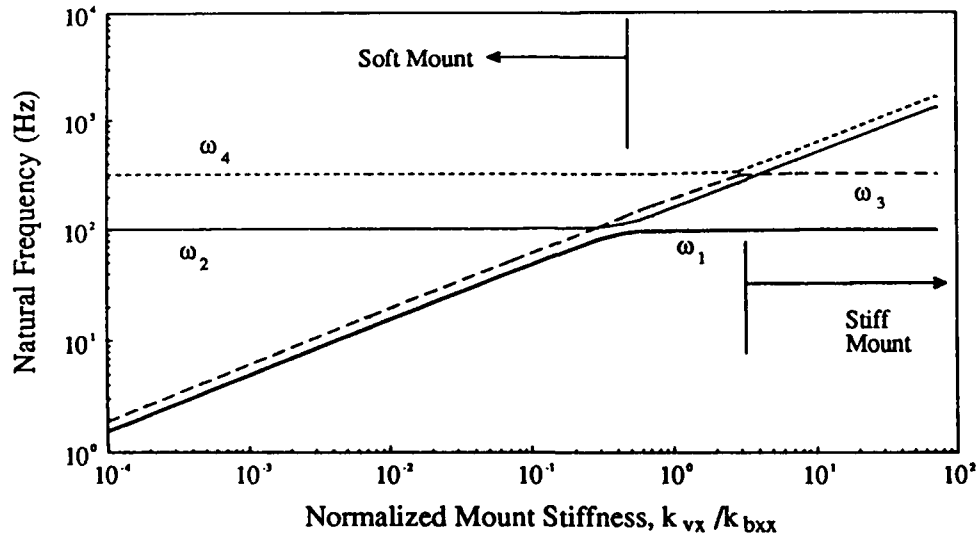
We examine the effect of casing mass m_c (and inertia $I_{yc} \propto m_c$) while retaining other parameters of Table 4.2. The fundamental frequency ω_1 (first transverse mode of the shaft-rotor system) and ω_3 (second transverse shaft-rotor mode) are quite insensitive to m_c . On the other hand, ω_5 and ω_6 are proportional to $(m_c)^{-1/2}$ for a light-weight casing given by $m_c/(m_s+m_R) < 1$, but are invariant for $m_c/(m_s+m_R) > 1$ as shown in Figure 4.6a. The converse is seen for ω_2 and ω_4 which are nearly constant for $m_c/(m_s+m_R) < 1$, but are proportional to $(m_c)^{-1/2}$ for $m_c/(m_s+m_R) > 1$. These results imply that the single degree of freedom approximation can be applied to ω_5 and ω_6 in the region where $m_c/(m_s+m_R) < 1$, and similarly to ω_2 and ω_4 in the other region.

Next, we vary mount stiffness coefficients k_{vx} (and $k_{v\theta_y} = L_s^2 k_{vx}$) to simulate the effect of mount flexibility on the system. Here ω_5 and ω_6 are found to be unaffected by k_{vx} due to the fact that the corresponding modes are predominantly shaft bending motion type as shown in Figure 4.5. Figure 4.6b indicates that ω_1 and ω_3 are proportional to $(k_{vx})^{1/2}$ for soft mounts ($k_{vx}/k_{bxx} \ll 1$) but are insensitive to k_{vx} for stiff mounts ($k_{vx}/k_{bxx} \gg 1$). Conversely, ω_2 and ω_4 are proportional to $(k_{vx})^{1/2}$ for stiff mounts but remain nearly invariant for soft mounts. Similarly, each mode in its appropriate region can be assumed to behave like a single degree of freedom system. In Figure 4.6b, unlike Figure 4.6a where only one transition point at $m_c=m_s+m_R$ exists, 2 transition points are found. These are located below and above $k_{vx}/k_{bxx} = 1$, and increase with increasing shaft and bearing stiffnesses.

Now, we examine the range of bearing preload F_{zbm} from 100 to 5000N on ω_j . It is seen that ω_j increases with increasing F_{zbm} due to an increase in the magnitudes of the



(a)



(b)

Figure 4.6 Effect of casing mass m_c normalized with respect to shaft and rotor masses, and mount stiffness k_{vx} normalized with respect to k_{bxx} on system natural frequencies ω_j for example case I.

bearing stiffness coefficients k_{bwj} as shown in Table 4.4 for the two extreme F_{zbm} values; this observation is similar to those found earlier in the bearing system studies of Chapter III. Note that ω_2 is the most insensitive to F_{zbm} , and ω_3 and ω_4 show a moderate variation. But ω_1 increases by about 45% due to larger bearing motions as compared to ω_2 , ω_3 and ω_4 modes. The remaining two modes of interest are also affected significantly as large motions across the bearings are again found in these modes. Unlike the trends associated with variations of m_c and k_{vx} , here each ω_j approaches an upper bound solution, as shown in Figure 4.7 for ω_1 , if F_{zbm} is sufficiently high to stabilize magnitudes of k_{bwj} terms.

Table 4.4 Effect of bearing preload F_{zbm} on ω_j (Hz) for example case I

Preload F_{zbm} (N)	ω_1	ω_2	ω_3	ω_4	ω_5	ω_6
100	89.4	262	305	331	1366	1706
5000	130	263	321	346	1855	1968

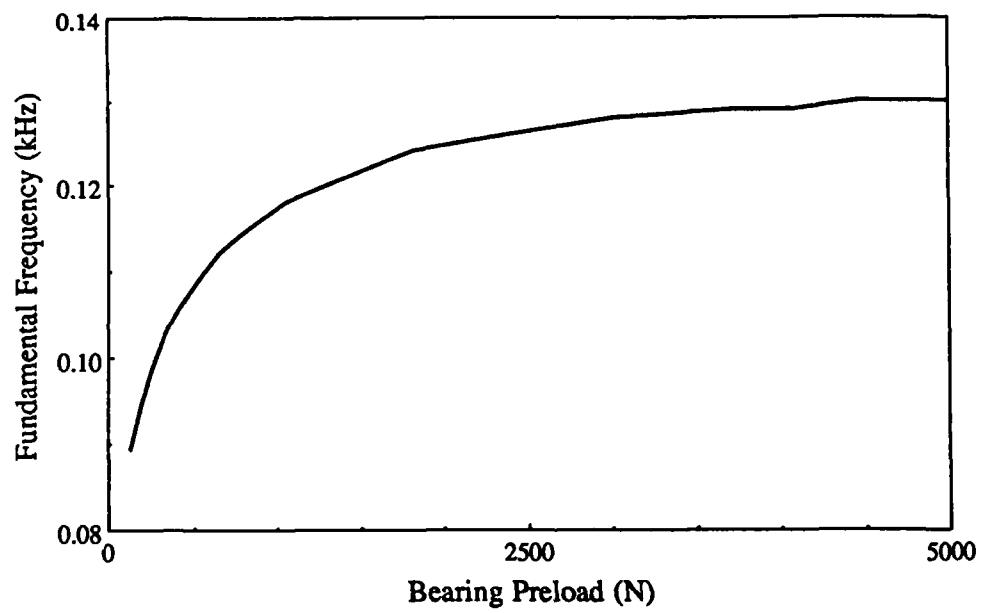
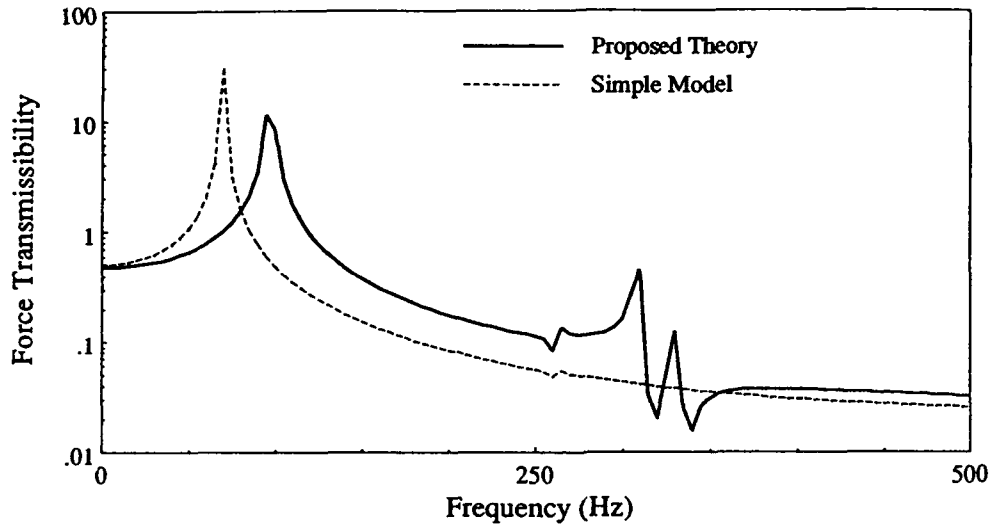


Figure 4.7 Effect of bearing preload F_{bzm} on ω_1 for example case I.

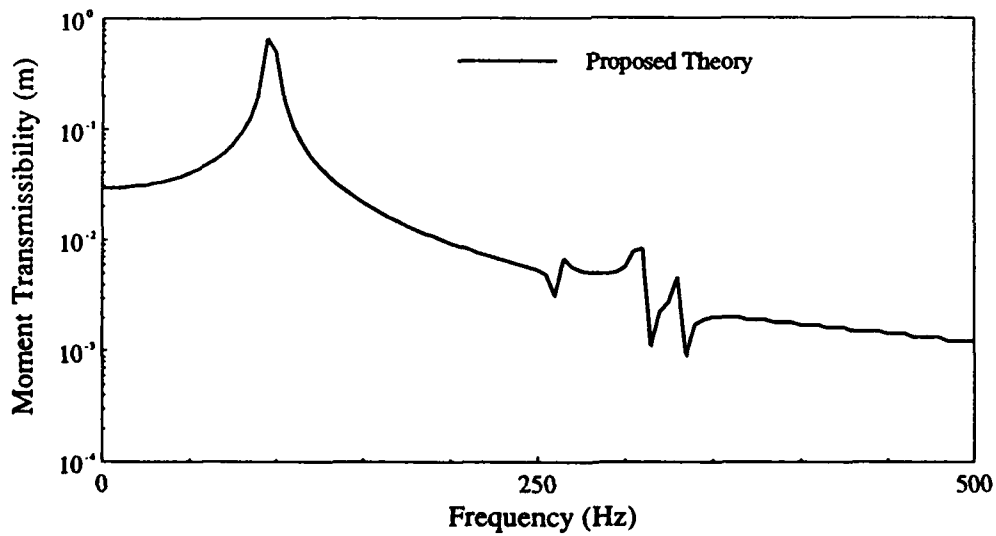
4.5.3 Transmissibility

The forced harmonic response due to the rotating rotor mass unbalance force $F_{xsa}(t) = F_{xsa1}(\Omega_z) e^{i\Omega_z t}$ is obtained using the dynamic stiffness technique given earlier in Chapter III. Also, recall from Chapter III the definition of sinusoidal load transmissibility functions $R(\Omega_z)$ between two arbitrary locations I and II with load vectors $f_{wIa}(t)$ and $f_{jIIa}(t)$ as $R(\Omega_z) = |f_{wIa}(\Omega_z)| / |f_{jIIa}(\Omega_z)|$ where in this case $f_{jIIa}(t) = F_{xsa}(t)$. The bearing force $R_{F_{xba}, F_{xsa}}(\Omega_z)$ and moment $R_{M_{yba}, F_{xsa}}(\Omega_z)$ transmissibility spectra are compared in Figure 4.8 for our formulation and simple model, given the same system of Table 4.2, both models differ only in $[K]_{bm}$ formulation. Note that the results presented are for only one bearing due to symmetry of the problem. We observe that the simple model predicts lower $R_{F_{xba}, F_{xsa}}(\Omega_z)$ than proposed model except in the vicinity of ω_1 . On the other hand, $R_{M_{yba}, F_{xsa}}(\Omega_z)$ is not predicted at all by the simple model. This component of the bearing transmissibility spectra is primarily due to coefficients $k_{bx\theta_y}$ and $k_{b\theta_y\theta_y}$ which are obviously not included in the simple model. Our predictions also show that higher modes over 250-350 Hz contribute significantly to the bearing transmissibility which are not seen in the force transmissibility spectra yielded by the simple model.

Now we compare the mount load transmissibility in Figure 4.9. We observe that the trends of mount force transmissibility $R_{F_{yva}, F_{xsa}}(\Omega_z)$ spectra predicted by both models are similar, although the simple model predicts slightly lower amplitudes above ω_1 . The simple model again can not predict the moment transmission $R_{M_{yva}, F_{xsa}}(\Omega_z)$ across the mounts. Unlike the bearing transmissibility spectra, here the effects of ϕ_3 and ϕ_4 on $R_{M_{yva}, F_{xsa}}(\Omega_z)$ are more significant than ϕ_1 and ϕ_2 . This is mainly due to the large angular motions on the casing for ϕ_3 and ϕ_4 .

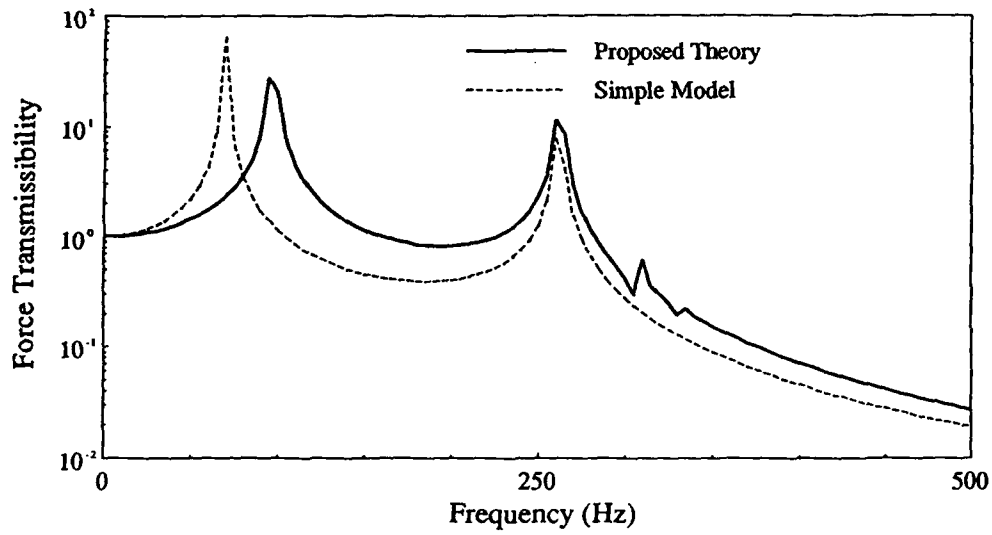


(a)

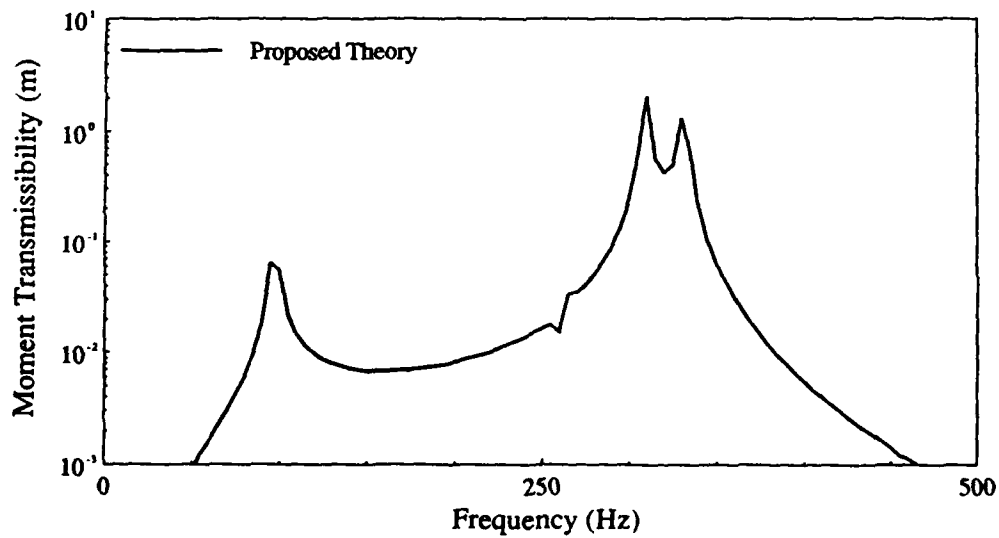


(b)

Figure 4.8 Bearing transmissibility for example case I. (a) Force transmissibility $R_{F_{x_{ba}}, F_{x_{sa}}}(\Omega_2)$. (b) Moment transmissibility $R_{M_{y_{ba}}, F_{x_{sa}}}(\Omega_2)$ which is not predicted by simple model.

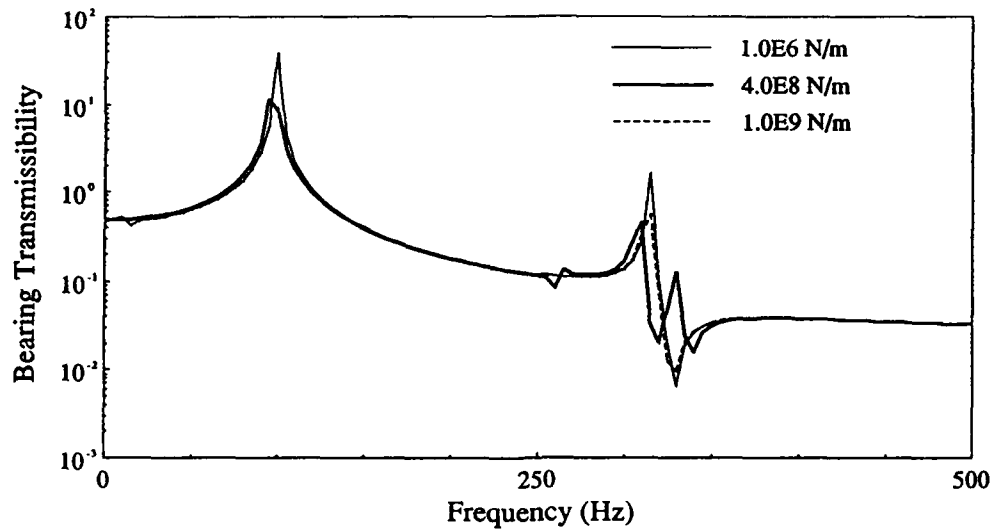


(a)

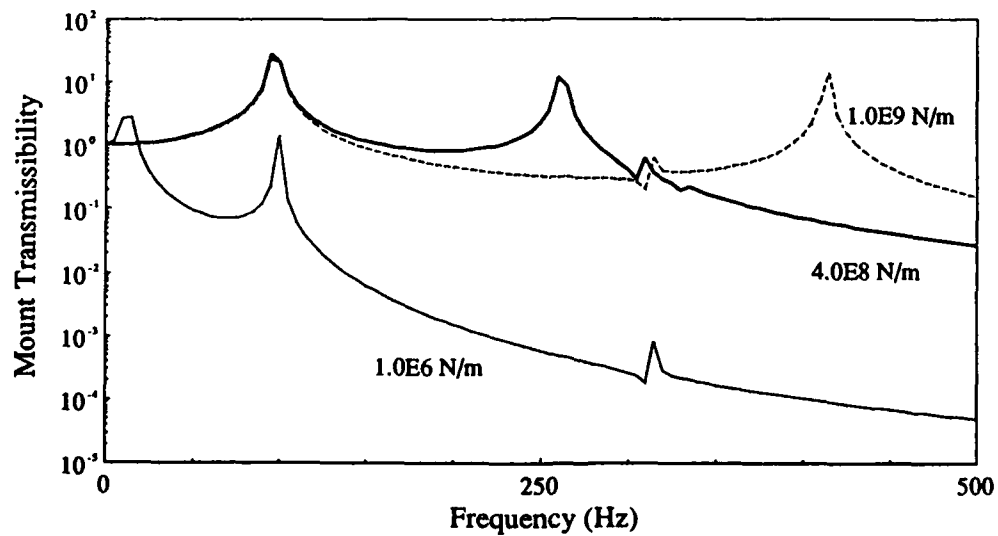


(b)

Figure 4.9 Mount transmissibility for example case I. (a) Force transmissibility $R_{F_{xva}, F_{xsa}}(\Omega_z)$. (b) Moment transmissibility $R_{M_{yva}, F_{xsa}}(\Omega_z)$.

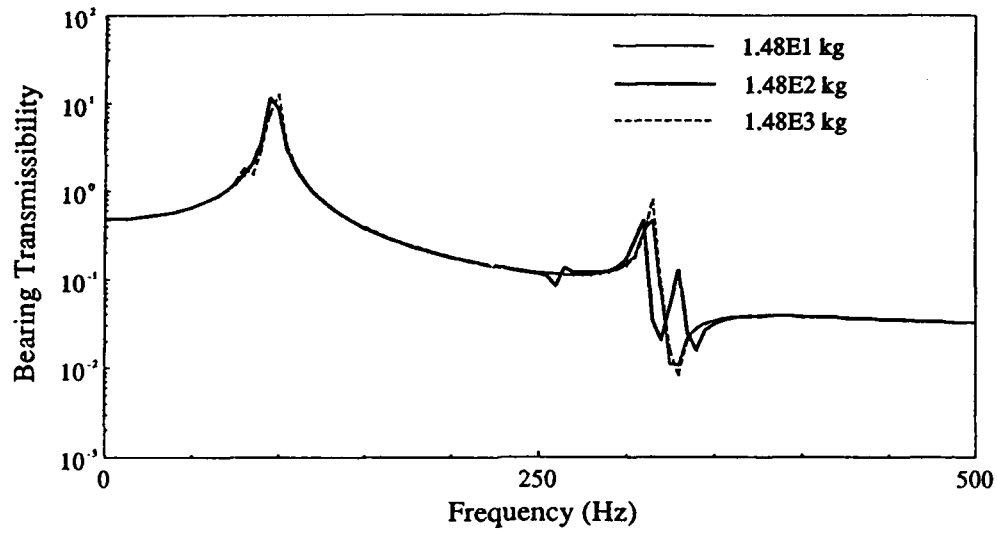


(a)

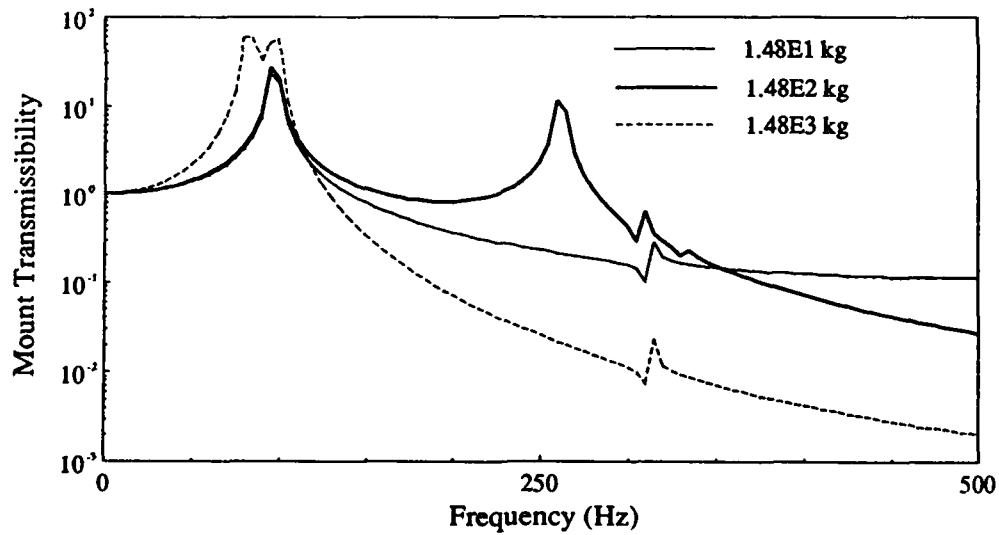


(b)

Figure 4.10 Effect of mount stiffness k_{vx} on the force transmissibilities for example case I. (a) Bearing. (b) Mount.



(a)



(b)

Figure 4.11 Effect of casing mass m_c on the force transmissibilities for example case I.
(a) Bearing. (b) Mount.

Next, we investigate the effects of m_c and k_{vx} on the bearing and mount transmissibilities. Figure 4.10a shows that essentially the same bearing transmissibilities are obtained for three k_{vx} values. In the case of the mount transmissibility as shown in Figure 4.10b, the amplitudes in general decrease with lower k_{vx} except near resonances. The casing mass m_c also does not affect the bearing transmissibility significantly as shown in Figure 4.11a. The mount transmissibility amplitudes increase with lower m_c as shown in Figure 4.11b except near resonances again. It may be noted that similar trends are observed in the bearing and mount moment transmissibility spectra.

4.6 EXAMPLE CASE II: GEARED ROTOR SYSTEM WITH RIGID CASING AND FLEXIBLE MOUNTS

4.6.1 Bearing Analysis

Now consider the geared rotor system in Figure 4.1 with flexibly mounted rigid casing whose bearing and other system parameters are given in Tables 4.1 and 4.5 respectively. Four ball bearings which support the two shafts are subjected to identical mean axial displacement δ_{zm} . The spur gear pair drive is driven by a mean torque $T_{zsm} \neq T_{zsm}(t)$ which also generates mean radial bearing force F_{ybmj} and moment M_{xbmj} . The stiffness matrix $[K]_{bm}$ for each bearing under these loads has significant coefficients k_{bxx} , k_{byy} , k_{bzz} , $k_{b\theta_x\theta_x}$, $k_{b\theta_y\theta_y}$, $k_{b\theta_x\theta_y}$, $k_{by\theta_x}$, $k_{by\theta_y}$, $k_{b\theta_z\theta_z}$ and $k_{bz\theta_x}$. A set of governing nonlinear algebraic equations, consisting of 3 bearing load-displacement relations for each bearing as given in Chapter II and from the shaft bending theory is given by

$$\begin{aligned} M_{xbmw_I} &= T_{zsm} L_s / (8 d_G) - 2EI(2\beta_{xmw_I} + \beta_{xmw_{II}} + 3(\delta_{ymw_I} - \delta_{ymw_{II}})/L_s) / L_s ; \\ M_{xbmw_{II}} &= -M_{xbmw_I} ; \text{ for } w_{II} = n_s + 1 \text{ if } w_I = 1, \text{ and } w_{II} = 2n_s + 2 \text{ if } w_I = n_s + 2. \end{aligned} \quad (4.26)$$

Table 4.5 System parameters of example case II: geared rotor system shown in Figure 4.1[†]

Gear and pinion masses $m_p = m_g$ (kg)	0.5
Gear and pinion rotary inertias $I_{yG}=I_{yP}, I_{zG}=I_{zP}$ (kgm ²)	1.5E-4, 3.0E-4
Number of gear/pinion teeth	28
Gear/Pinion Pressure Angle (degrees)	20°
Shaft mass m_s (kg) and length L_s (m)	2.8, 2.54E-1
Casing mass m_c (kg) rotary inertias I_{xc}, I_{zc} (kgm ²)	77, 1.5, 1.9
Shaft flexural rigidity EI (Nm ²)	1.25E4
Effective Torsional Stiffness k_{TM}, k_{TL} (Nm/rad)	6.05E3, 2.45E4
Motor and Load inertia I_{zM}, I_{zL}	1.00E-1, 3.35
Gear mesh stiffness k_h (N/m)	1.0E8
Mean axial bearing displacement δ_{zm} (N)	6.00E-4
Mean input torque T_{zbm} (Nm)	72
$k_{byy}, k_{by\theta_x}, k_{b\theta_x\theta_x}$ ^{††}	9.7E8, 6.0E5, 1.0E6
$k_{vy}, k_{v\theta_x}, k_{v\theta_z}$	9.0E8, 1.4E7, 2.4E7

[†] The internal rotating spur gear pair is currently being used in a NASA gear test facility [55].

^{††} Only relevant bearing stiffness coefficients are tabulated.

Due to the physical symmetry, we assume $\delta_{ymw_I} = \delta_{ymw_{II}}$ and $\beta_{xmw_I} = -\beta_{xmw_{II}}$ which simplify the nonlinear algebraic equation set for each bearing to

$$M_{x_{bm}} = T_{zsm} L_s / (8 d_G) - 2 EI \beta_{xm} / L_s ; F_{y_{bm}} = T_{zsm} / d_G \quad (4.27)$$

where $M_{x_{bm}}$ and $F_{y_{bm}}$ are expressed in terms of a constant δ_{zm} , and variables δ_{ym} and β_{xm} . Solution to these 2 equations may then be used to compute $k_{bij}(\delta_{zm}, \delta_{ym}, \beta_{xm})$ directly.

4.6.2 Vibration Models

A lumped parameter model of Figure 4.1 is developed in accordance with Section 4.4.1. Each shaft is divided into n_s number of segments as shown in Figure 4.3a. The system matrices of equation (4.4) are simplified by neglecting the longitudinal shaft motion and casing rigid body degrees of freedom $u_{zca}(t)$, $u_{xca}(t)$ and $\theta_{yca}(t)$. Both driving and driven shafts are assumed to be coupled to the motor and load respectively through flexible torsional couplings. Therefore, only the motor I_{zM} and load I_{zL} rotary inertias are considered, and the exterior portion of the shafts beyond the flexible couplings are modeled as purely torsional stiffness elements which are then combined with the flexible coupling stiffnesses. The system is excited by the static transmission error $e(t)$ at the mesh point which generates gear and pinion force $F_h(t) = k_h e(t)$, parallel to the line of action, and torque $T_{hG}(t) = 1/2 d_G k_h e(t)$ or $T_{hP}(t) = 1/2 d_P k_h e(t)$, about the axial z -axis. The mass matrix $[M]$ in equation (4.4a) in terms of $\{q(t)\} = \{u_{ysaj}(t), u_{yca}(t), \theta_{xGa}(t), \theta_{zGa}(t), \theta_{xPa}(t), \theta_{zPa}(t), \theta_{zM_a}(t), \theta_{zL_a}(t), \theta_{xca}(t), \theta_{zca}(t)\}^T$ is

$$[M] = \text{DIAG} \{ m_{sej}, m_{xc}, I_{xG}, I_{zG}, I_{xP}, I_{zP}, I_{zM}, I_{zL}, I_{xc}, I_{zc} \} \quad (4.28)$$

The matrices $[K]_{11}$, $[K]_{12}$, $[K]_{13}$, $[K]_{22}$, $[K]_{23}$ and $[K]_{33}$ define the symmetric $[K]$ of dimension $2n_s + 11$ in equation (4.4b). Nonzero elements of $[K]_{11}$ of dimension $2n_s + 3$ are

$$k_{n_s+2, n_s+2} = k_{2n_s+2, 2n_s+2} = k_{11} = k_{n_s+1, n_s+1} = 12 EI/L_e^3 + k_{byy} \quad (4.29a)$$

$$k_{w_I+1, w_I} = k_{w_I, w_I+1} = -12 EI/L_e^3 ;$$

$$k_{w_I+n_s+2, w_I+n_s+1} = k_{w_I+n_s+1, w_I+n_s+2} = -12 EI/L_e^3 ; \quad w_I = 1, 2, 3, \dots, 2n_s \quad (4.29b)$$

$$k_{w_{II}, w_{II}} = 24 EI/L_e^3 ; \quad k_{w_{II}+n_s+1, w_{II}+n_s+1} = 24 EI/L_e^3 ;$$

$$w_{II} = 2, 3, \dots, n_s/2, n_s/2+2, \dots, n_s \quad (4.29c)$$

$$k_{n_s/2+1, n_s/2+1} = 24 EI/L_e^3 + k_h ; \quad k_{3n_s/2+2, 3n_s/2+2} = 24 EI/L_e^3 + k_h ;$$

$$k_{n_s/2+1, 3n_s/2+2} = k_{3n_s/2+2, n_s/2+1} = -k_h ; \quad k_{2n_s+3, 2n_s+3} = 4k_{byy} + k_{vy} ; \quad (4.29d)$$

$$k_{w_{III}, 2n_s+3} = k_{2n_s+3, w_{III}} = -k_{byy} ; \quad w_{III} = 1, n_s+1, n_s+2, 2n_s+2 \quad (4.29e)$$

The nonzero elements of $[K]_{12}$ of $2n_s+3$ rows and 8 columns are

$$k_{3n_s/2-1, 1} = -k_{3n_s/2+3, 1} = k_{n_s/2, 3} = -k_{n_s/2+2, 3} = 6 EI/L_e^2 ; \quad k_{2n_s+3, 7} = 4k_{by\theta_x} ;$$

$$-k_{n_s/2+1, 2} = k_{3n_s/2+2, 2} = k_h/(2d_G) ; \quad k_{n_s/2+1, 4} = -k_{3n_s/2+2, 4} = k_h/(2d_P) \quad (4.30a)$$

$$k_{w_{III}, 7} = -k_{by\theta_x} + z_{w_{III}} k_{byy} ; \quad k_{w_{III}, 8} = -x_{w_{III}} k_{byy} ; \quad w_{III} = 1, n_s+1, n_s+2, 2n_s+2 \quad (4.30b)$$

The nonzero elements of $[K]_{13}$ of $2n_s+3$ rows and $2n_s$ columns are

$$\begin{aligned}
k_{11} = k_{n_s+2, n_s+1} &= 6 EI/L_e^2 + k_{by\theta_x} ; \quad k_{n_s+1, n_s} = k_{2n_s+2, 2n_s} = -6 EI/L_e^2 + k_{by\theta_x} ; \\
k_{3n_s/2+2, 3n_s/2+1} &= -k_{3n_s/2+1, 3n_s/2} = k_{n_s/2+1, n_s/2+1} = -k_{n_s/2+1, n_s/2} = 6 EI/L_e^2 ; \\
k_{2n_s+3, 1} &= k_{2n_s+3, n_s} = k_{2n_s+3, n_s+1} = k_{2n_s+3, 2n_s} = -k_{by\theta_x} \quad (4.31a)
\end{aligned}$$

$$\begin{aligned}
k_{12} &= -k_{n_s+1, n_s-1} = k_{n_s/2, n_s/2-1} = k_{n_s/2+2, n_s/2+2} = k_{n_s+2, n_s+2} = 6 EI/L_e^2 ; \\
-k_{2n_s+2, 2n_s-1} &= -k_{3n_s/2+1, 3n_s/2-1} = k_{3n_s/2+3, 3n_s/2+2} = 6 EI/L_e^2 ; \quad n_s > 2 \quad (4.31b)
\end{aligned}$$

$$\begin{aligned}
-k_{w_{IV}, w_{IV}-1} &= k_{w_{IV}, w_{IV}+1} = k_{w_{IV}+n_s/2+1, w_{IV}+n_s/2+1} = -k_{w_{IV}+n_s+1, w_{IV}-1+n_s} = 6 EI/L_e^2 ; \\
k_{w_{IV}+n_s+1, w_{IV}+1+n_s} &= -k_{w_{IV}+n_s/2+1, w_{IV}+n_s/2-1} = k_{w_{IV}+3n_s/2+2, w_{IV}+3n_s/2+1} = 6 EI/L_e^2 ; \\
-k_{w_{IV}+3n_s/2+2, w_{IV}+3n_s/2-1} &= 6 EI/L_e^2 ; \quad n_s \geq 6 ; \quad w_{IV} = 2, 3, \dots, n_s/2-1 \quad (4.31c)
\end{aligned}$$

where nonzero elements given by equations (4.31b) and (4.31c) exist only if $n_s > 2$ and $n_s \geq 6$ respectively. The nonzero elements of symmetric $[K]_{22}$ of dimension 8 are

$$\begin{aligned}
k_{11} = k_{33} &= 8 EI/L_e ; \quad k_{22} = k_{TM} + k_h d_G^2/4 ; \quad k_{25} = -k_{TM} ; \quad k_{46} = -k_{TL} ; \\
k_{44} &= k_{TL} + k_h d_P^2/4 ; \quad k_{24} = k_{42} = -k_h d_G d_P/4 ; \quad k_{55} = k_{TM} ; \quad k_{66} = k_{TL} ; \\
k_{77} &= 4k_{b\theta_x\theta_x} + \Sigma (z_j)^2 k_{byy} + k_{v\theta_x} ; \quad k_{88} = k_{v\theta_z} + \Sigma (x_j)^2 k_{byy} \quad (4.32)
\end{aligned}$$

where k_{TL} and k_{TM} are the effective torsional stiffnesses due to shaft and torsional coupling respectively at load and motor ends, and the summation Σ is over the 4 ball bearings denoted by $j = 1, n_s+1, n_s+2, 2n_s+2$. The nonzero elements of $[K]_{23}$ of 8 rows and $2n_s$ columns are

$$\begin{aligned}
k_{1, n_s/2} &= k_{1, n_s/2+1} = k_{3, 3n_s/2} = k_{3, 3n_s/2+1} = 2 EI/L_e \quad (4.33a) \\
k_{7, w_V} &= +z_{w_{III}} k_{by\theta_x} - k_{b\theta_x\theta_x} ; \quad k_{8, w_V} = -x_{w_{III}} k_{by\theta_x} ;
\end{aligned}$$

$$w_{III}=1(w_V=1), n_s+1(w_V=n_s), n_s+2(w_V=n_s+1), 2n_s+2(w_V=2n_s) \quad (4.33b)$$

Finally, the nonzero elements of symmetric $[K]_{33}$ of dimension $2n_s$ are

$$k_{11} = k_{n_s, n_s} = k_{n_s+1, n_s+1} = k_{2n_s, 2n_s} = 4 EI/L_e + k_{b\theta_y, \theta_y} \quad (4.34a)$$

$$k_{w_{VI}, w_{VI}} = k_{n_s+w_{VI}, n_s+w_{VI}} = 8 EI/L_e \quad ; \quad n_s > 2, w_{VI} = 2, 3, \dots, n_s \quad (4.34b)$$

$$k_{w_{VII}, w_{VII-1}} = k_{w_{VII-1}, w_{VII}} = k_{n_s+w_{VII}, n_s+w_{VII-1}} = 2 EI/L_e \quad ;$$

$$k_{n_s+w_{VII-1}, n_s+w_{VII}} = 2 EI/L_e \quad ; \quad n_s > 2, w_{VII} = 2, 3, \dots, n_s (w_{VII} \neq n_s/2+1) \quad (4.34c)$$

As discussed earlier, our proposed vibration model again differs from the conventional spur gear pair dynamic models essentially due to $[K]_{bm}$ formulation. The simple model with casing and mount dynamics can be obtained from our proposed model by retaining only k_{bxx} , k_{byy} and k_{bzz} in $[K]_{bm}$.

4.6.3 Eigensolution

The natural frequencies ω_j and modes ϕ_j of Figure 4.1 with system parameters given in Tables 4.1 and 4.5 are computed using the proposed theory, a dynamic finite element model, and the simple theory with and without casing and mounts. The FEM model includes casing flexibility – this will be described later in example case II. Our proposed theory differs from FEM by less than $\pm 4\%$ for the first six ω_j and is within $\pm 10\%$ for ω_7 and ω_8 as shown in Table 4.6a. The corresponding natural modes are described in Table 4.6b. Simple models in general predict lower natural frequencies and deviate substantially except for ω_1 and ω_3 . The simple model without any casing

Table 4.6 Eigensolution of example case II

a. Comparison of natural frequencies ω_j in Hz

Mode ϕ_j	Proposed Theory	FEM	$\Delta_1\%$	Simple Models		$\Delta_2\%$
				without casing	with casing	
1	0	0	0.0	0	0	0.0
2	31.0	31.0	0.0	29.8	29.1	6.1
3	480	480	0.0	not predicted	480	0.0
4	526	525	-0.2	not predicted	510	2.9
5	563	564	0.2	not predicted	560	0.7
6	790	760	-3.9	666	650	14.5
7	1147	1093	-4.9	837	809	26.0
8	1208	1100	-9.8	694	681	38.1

$$\Delta_1\% = 100 \times (\text{FEM} - \text{Proposed Theory}) / \text{FEM}$$

$$\Delta_2\% = 100 \times (\text{FEM} - \text{Simple Model}) / \text{FEM}$$

b. Summary of mode shapes

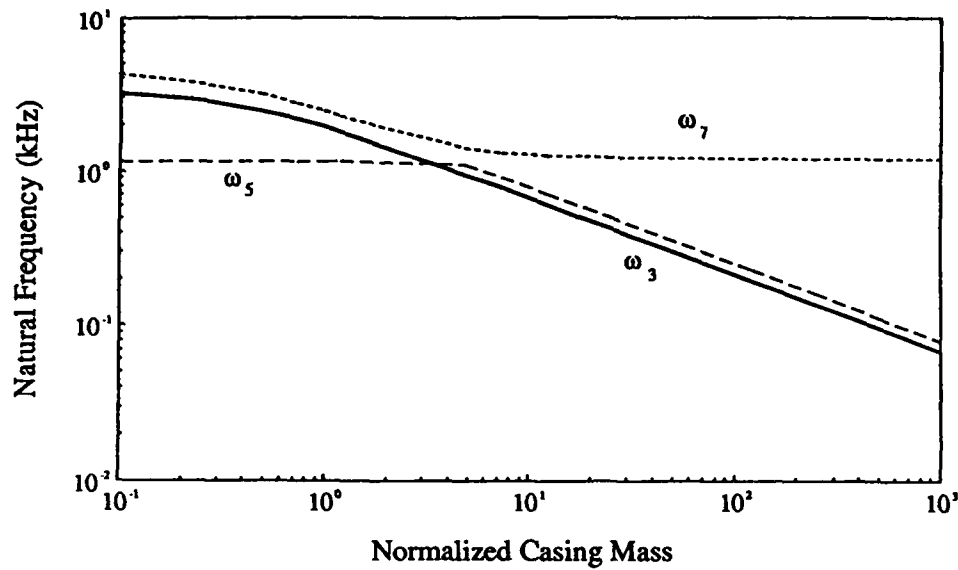
Mode ϕ_j	Description
1	Motor-gear-pinion-load system rigid body torsional motion
2	Motor-gear-pinion-load system torsional motion
3	Casing rigid body rotational motion θ_{xca}
4	Casing rigid body translational motion u_{yca}
5	Casing rigid body torsional motion θ_{zca}
6	First shaft coupled transverse-torsional motion
7	Second shaft coupled transverse-torsional motion
8	Shaft transverse motion

dynamics as outlined here is in excellent agreement with the results reported by Kahraman et al. [15]. This provides further validation for our theory.

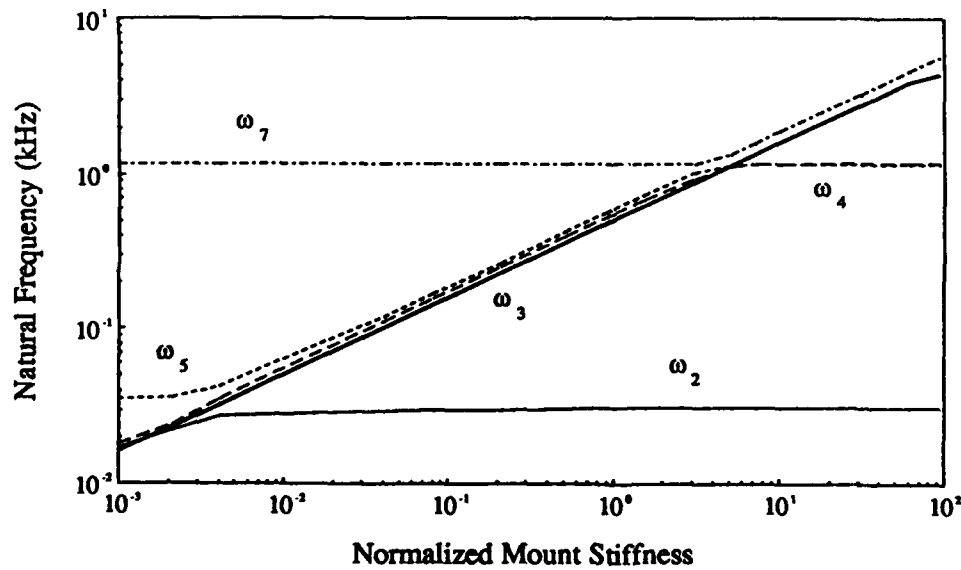
The effect of casing mass m_c (and inertias $I_{xc}, I_{zc} \propto m_c$) is shown in Figure 4.12a for ω_3, ω_5 and ω_7 . Here ω_2 and ω_6 are unaffected by m_c . On the other hand, ω_3 is always proportional to $(m_c)^{-1/2}$ except when $m_c/(m_s+m_G+m_P) \ll 1$. This proportionality feature, similar to the single degree of freedom theory, is also seen for ω_7 and ω_8 for a lightweight casing, and ω_4 and ω_5 for a massive casing. It may be noted that the trends of ω_8 and ω_4 are similar to ω_7 and ω_5 respectively although they are not included in Figure 4.12a. Unlike example case I where the transition point is at $m_c/(m_s+m_G+m_P) = 1$, two transition points are observed here due to the effects of the gear, pinion and casing rotary inertias.

The effect of mount stiffness k_{vy} (and $k_{v\theta_x}, k_{v\theta_z} \propto k_{vy}$) on ω_j is given in Figure 4.12b. We again find that ω_2 and ω_6 are not affected by a variation in k_{vy} . Also, two transition points are found which separate a region of constant ω_j from the region where $\omega_j \propto (k_{vy})^{1/2}$ for some of the natural frequencies. Here ω_8 is similar to ω_7 which is proportional to $(k_{vy})^{1/2}$ for stiff mounts but is insensitive to k_{vy} for softer mounts. The converse is seen for ω_2 with a lower transition point. On the other hand, $\omega_5 \propto (k_{vy})^{1/2}$ in the region between the two transition points, and is constant elsewhere. Finally, ω_3 is seen to be always increasing with k_{vy} .

The effect of mean bearing displacement δ_{zm} is summarized in Table 4.7 for two extreme δ_{zm} values. Only the natural frequencies associated with the shaft transverse and/or torsional motion are sensitive to δ_{zm} or preloads $F_{zbm}(\delta_{zm})$. The rate of increase for ω_j is high for low δ_{zm} , but the rate decreases with a higher δ_{zm} as observed earlier in example case I due to the stabilization of k_{bij} .



(a)



(b)

Figure 4.12 Effect of casing mass m_c (normalized with respect to shaft and gear masses) and mount stiffness k_{vx} (normalized with respect to k_{bxx}) on the system natural frequencies ω_i for example case II.

Table 4.7 Example case II: effect of mean bearing displacement δ_{zm} on ω_j (Hz)

δ_{zbm} (mm)	ω_1	ω_2	ω_3	ω_4	ω_5	ω_6	ω_7	ω_8
0.06	0	29.9	480	520	562	764	852	852
1.00	0	31.0	480	526	563	791	1180	1215

4.6.4 Transmissibility Spectra

The response due to the static transmission error excitation $e(t)$ at the mesh point is computed using the same dynamic stiffness technique used for example case I. Here, only the fundamental harmonic of $e(t)$ at mesh frequency ω_h is included. All transmissibility functions are normalized with respect to the magnitude of the gear mesh force $F_h(t) = k_h e(t)$. Figure 4.13a and 4.13b compare the bearing force $R_{F_{yba}, F_h}(\omega_h)$ and moment $R_{M_{xba}, F_h}(\omega_h)$ transmissibility spectra as predicted by our formulation and simple model. It may be noted that the transmissibility spectra for all four bearings are similar. Although simple model compares reasonably well with our proposed theory for $R_{F_{yba}, F_h}(\omega_h)$, it is not capable of predicting $R_{M_{xba}, F_h}(\omega_h)$, as also seen previously. In the case of the mount transmissibility shown in Figure 4.13c, only the net moment $M_{zva}(t)$ is transmitted. The resultant vertical force $F_{yva}(t)$ and moment $M_{xva}(t)$ are negligible due to the force and moment cancellations at the mount feet. The Fourier spectrum of the normalized dynamic transmission error $p(t) = [y_P(t) - y_G(t) + (d_P \theta_P(t)/2) - (d_G \theta_G(t)/2)]/e(t)$ is shown in Figure 4.13d. Only two modes, ϕ_2 which is predominantly torsional vibration of the shafts and ϕ_6 which is a coupled

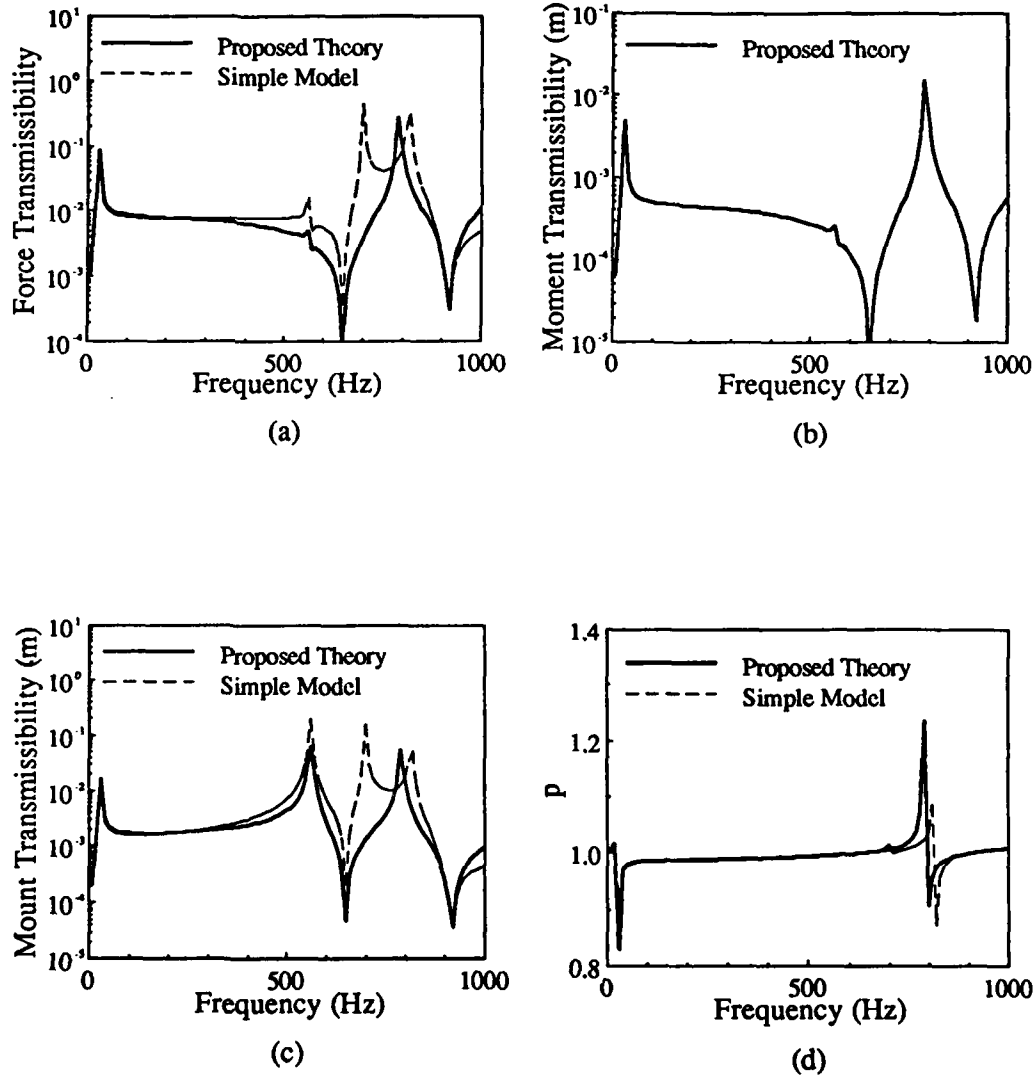


Figure 4.13 Comparison of transmissibility and normalized dynamic transmission error spectra for example case II. (a) Bearing force transmissibility $R_{F_{yba}, F_h}(\omega_h)$. (b) Bearing moment transmissibility $R_{M_{xba}, F_h}(\omega_h)$ which is not predicted by simple model. (c) Mount transmissibility $R_{M_{zba}, F_h}(\omega_h)$. (d) Normalized dynamic transmission error $p(\omega_h)$.

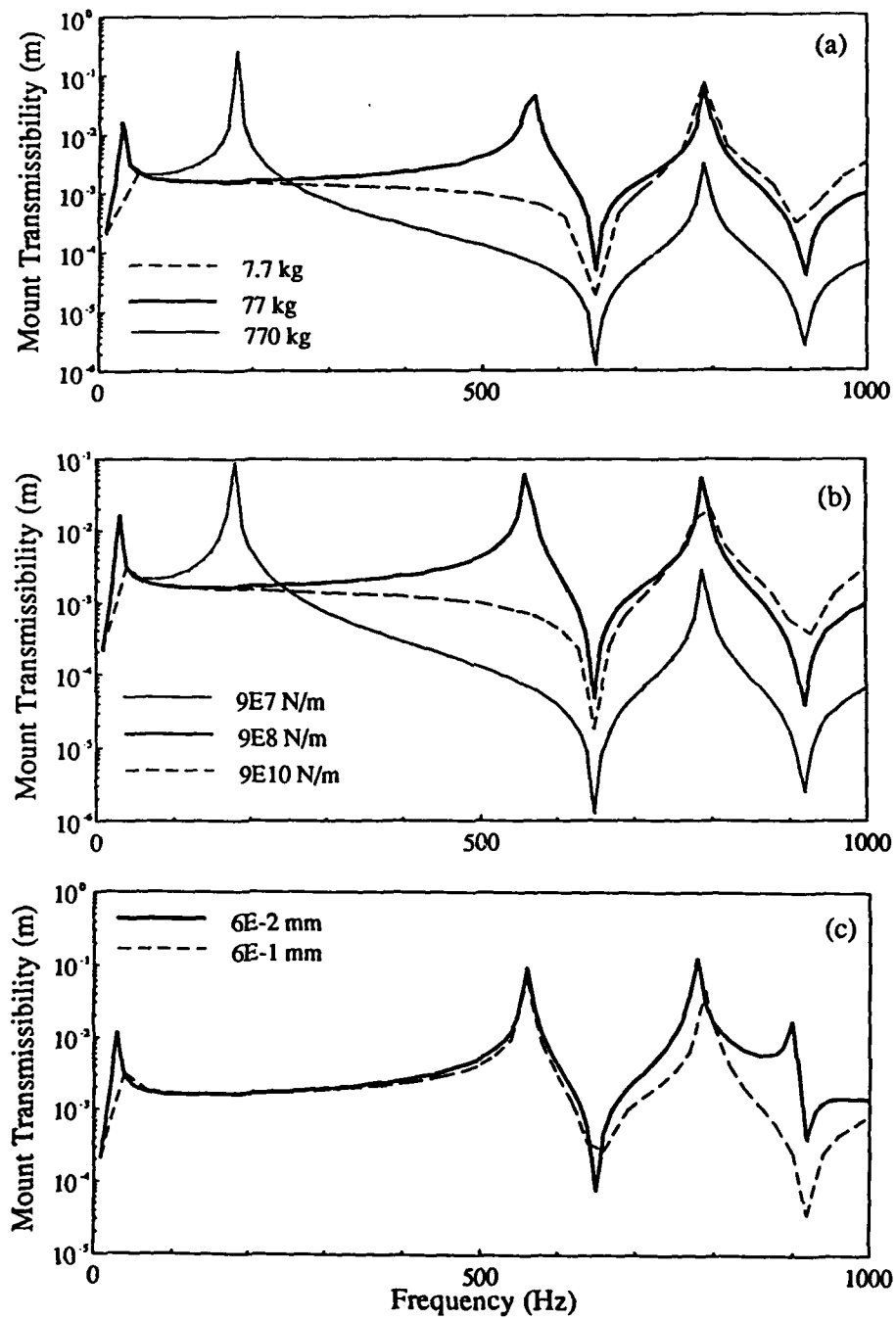


Figure 4.14 Mount transmissibility studies for example case II. Effect of (a) casing mass m_c , (b) mount stiffness k_{vx} and (c) mean bearing displacement δ_{zm} on $R_{M_{2ba}, F_h}(\omega_h)$.

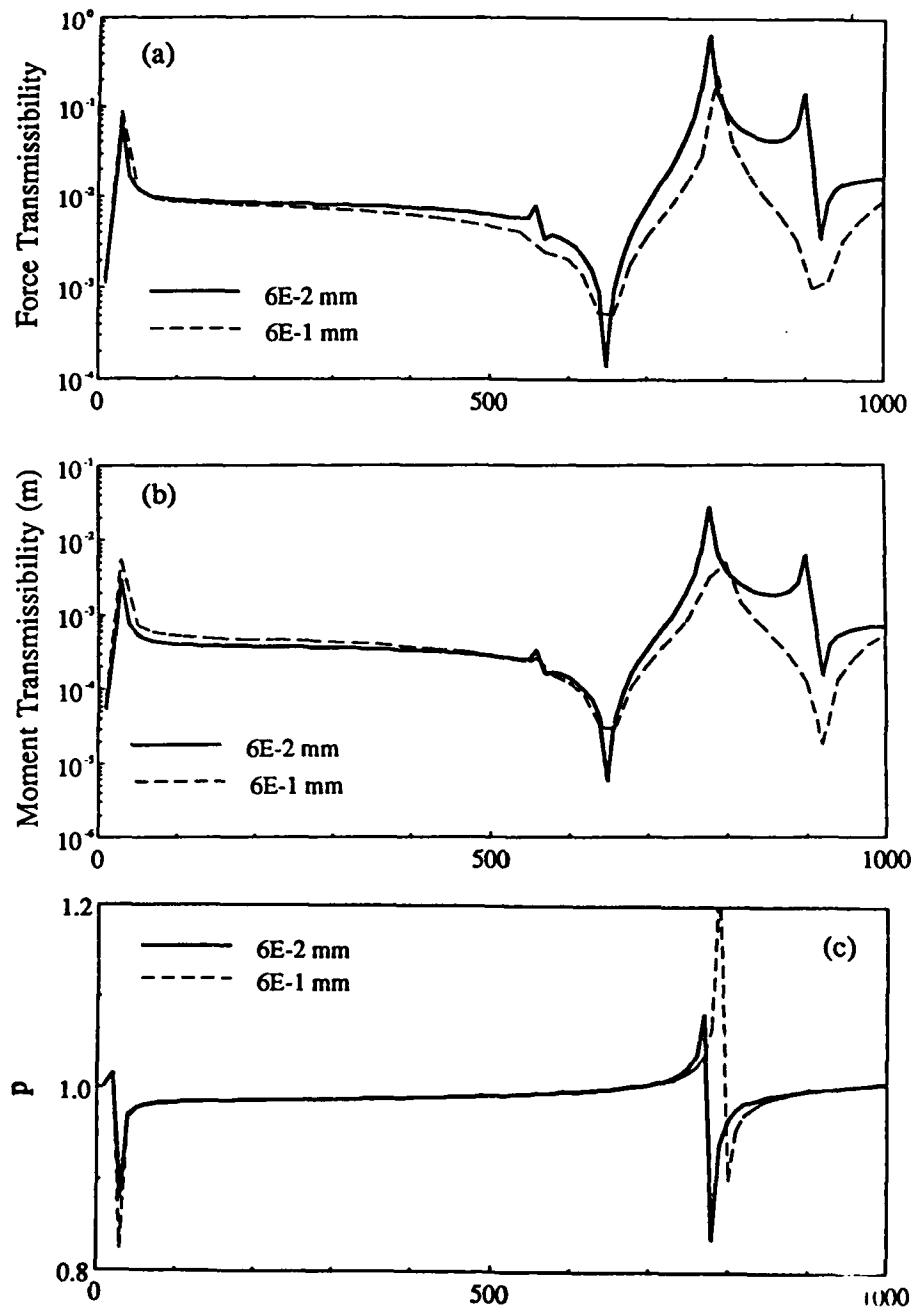


Figure 4.15 Effect of mean bearing displacement δ_{zm} on (a) bearing force transmissibility $R_{F_{yba}, F_h}(\omega_h)$, (b) bearing moment transmissibility $R_{M_{xba}, F_h}(\omega_h)$, and (c) normalized dynamic transmission error $p(\omega_h)$ for example case II.

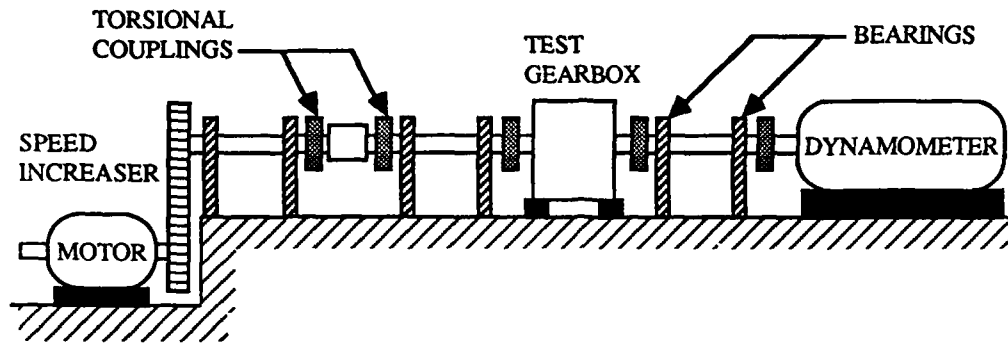
transverse-torsional mode, affect $p(\omega_h)$ significantly. The sixth mode produces a higher $p(\omega_h)$ amplitude at ω_h than ϕ_2 . Additionally, the simple theory underestimates $p(\omega_h)$ as compared to the proposed model.

The effects of m_c , k_{vx} and δ_{zm} on the transmissibility spectra and $p(\omega_h)$ are given in Figures 4.14 and 4.15. Mount transmissibility $R_{M_{zva}, F_h}(\omega_h)$ is lower for a heavier casing, more compliant mount and higher δ_{zm} as shown in Figure 4.14. In addition, the effects of m_c and k_{vx} on $R_{M_{zva}, F_h}(\omega_h)$ are more prominent than those of δ_{zm} . The bearing transmissibility spectra and $p(\omega_h)$ are affected only by δ_{zm} as shown in Figure 4.15, and are virtually insensitive to m_c and k_{vx} for the parameters given in Tables 4.1 and 4.5. Vibratory force and moment transmission through the bearing are slightly lower for a larger δ_{zm} due to the additional constraint provided by higher k_{bij} values on the rotating shafts. Conversely, normalized dynamic transmission error $p(\omega_h)$ increases if a larger bearing preload is specified.

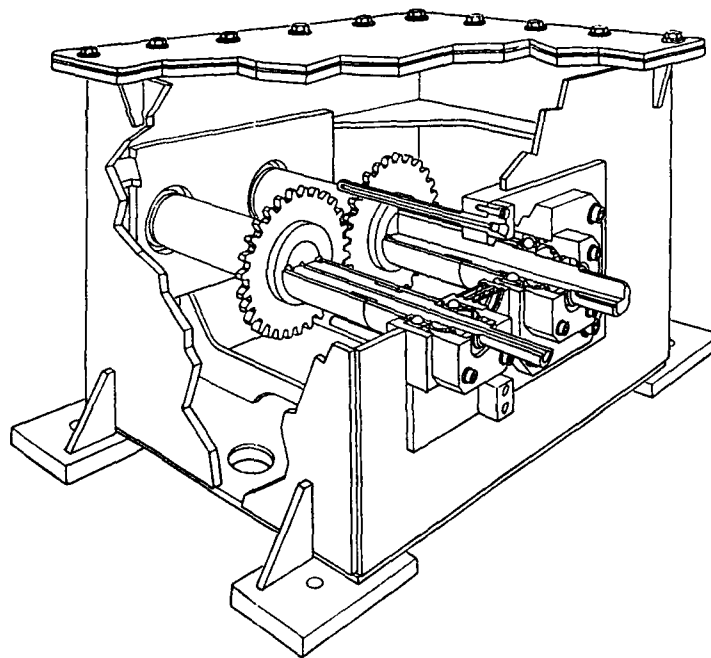
4.7 EXAMPLE CASE III: GEARED ROTOR SYSTEM WITH RIGIDLY MOUNTED FLEXIBLE CASING

4.7.1 Physical Setup

The final example case examines the NASA gear test facility as shown in Figure 4.16 [55]. The system parameters are equivalent to those in Tables 4.1 and 4.5 except for the flexible steel casing of approximate dimensions $0.33 \times 0.28 \times 0.25$ m and plate thickness of 0.006m. Rigid mount feet attach the four corners of the bottom casing plate to a massive foundation. High precision gear and pinion are used which are identical with 0.006m facewidth, 0.089m diameter and 1:1 ratio. Four axially preloaded high precision deep groove ball bearings are being used to support 0.03m diameter shafts of length 0.254m on the flexible casing. The input and output shafts are only coupled



(a)



(b)

Figure 4.16 Example case III: (a) Schematic of the NASA gear test facility. (b) NASA spur gear pair system supported on rigidly mounted flexible casing [55].

torsionally to the rest of the gear test facility through flexible couplings, and the geared system is driven by a 149kW DC motor. Vibrational level at various positions on the casing plate are measured using PCB 303A and Endevco 2271 accelerometers over the operational speed range of 2250–5750 rpm which corresponds to the gear mesh frequency ω_h range of 1050–2683 Hz.

4.7.2 Vibration Models

A dynamic finite element model of Figure 4.16b is developed using a commercial software [39] as outlined in Section 4.4.1. The magnitudes of k_{bij} , which are included in the FEM model through a 6 dimensional generalized stiffness matrix element, are computed using the two nonlinear algebraic equations (4.27) which neglect the static elastic deformation of the casing plate. The shafts are modeled using 2 noded Timonshenko beam elements with axial degrees of freedom capability. Four noded quadrilateral plate elements with shear deformation and rotary inertia effects are used to construct the flexible casing. The shafts and torsional couplings exterior of the test gearbox are modeled as torsional stiffness elements only, and the gear, pinion, motor and load are incorporated in the FEM model using generalized mass and inertia elements. Gear mesh coupling between the gear and pinion is described by a generic stiffness matrix of dimension 6, similar to $[K]_{bm}$. Free rotational $\theta_{za}(t)$ boundary condition is specified at the motor and load inertias, while ideally clamped $u_{wa}=\theta_{wa}=0$, $w=x,y,z$, boundary points at the corner of the bottom plate are assumed to simulate the rigid mount feet.

Natural frequencies and modes predicted by a similar FEM model have already been verified by comparison with experimental modal analysis in an earlier publication

by us [50]. Hence, eigensolutions will not be discussed here. But, it may be noted that the conventional geared rotor dynamic models with simple bearing models and without casing dynamics are not valid for high excitation frequencies (beyond the first casing plate elastic mode). For the forced response study, only the fundamental harmonic ω_h of the static transmission error excitation $e(t) = 3.5 \sin(\omega_h t) \mu\text{m}$ computed from the gear tooth profile and geometry [46]. About 110 dynamic degrees of freedom are selected to minimize computational effort while still maintaining sufficient accuracy. Modal damping ratio $\zeta = 0.05$ is assumed over the frequency range of interest.

4.7.3 Casing Response

Several locations on 3 different casing plate surfaces as shown in Figure 4.17 have been chosen for the experimental validation of our theory. Figure 4.18 compares predicted and measured mean square acceleration spectra at ω_h over 0 kHz to 4 kHz even though measurements have been conducted only between 1 kHz to 3 kHz. In general, good agreement is found between experiment and theory. Some discrepancy is observed above 2.4 kHz which is due to the limitation of the FEM model in the high modal density regime. It may be noted that the simple theory which utilizes only conventional bearing models cannot predict flexural vibration of the casing plate as shown in Figure 4.18. A broad band vibratory energy comparison is achieved by averaging the mean square value of the acceleration over one-third octave bands, L_A in dB per unit frequency bandwidth $\Delta\omega$, which is defined as follows

$$L_A, \text{dB} = 10 \log_{10} \left[\left(\frac{1}{2\Delta\omega} \right) \sum_{\Delta\omega} \text{Re} \left\{ \frac{(AA^*)}{\langle A^2 \rangle_{\text{ref}}} \right\} \right]; \langle A^2 \rangle_{\text{ref}} = 1.0 \text{ g}^2 \quad (4.35)$$

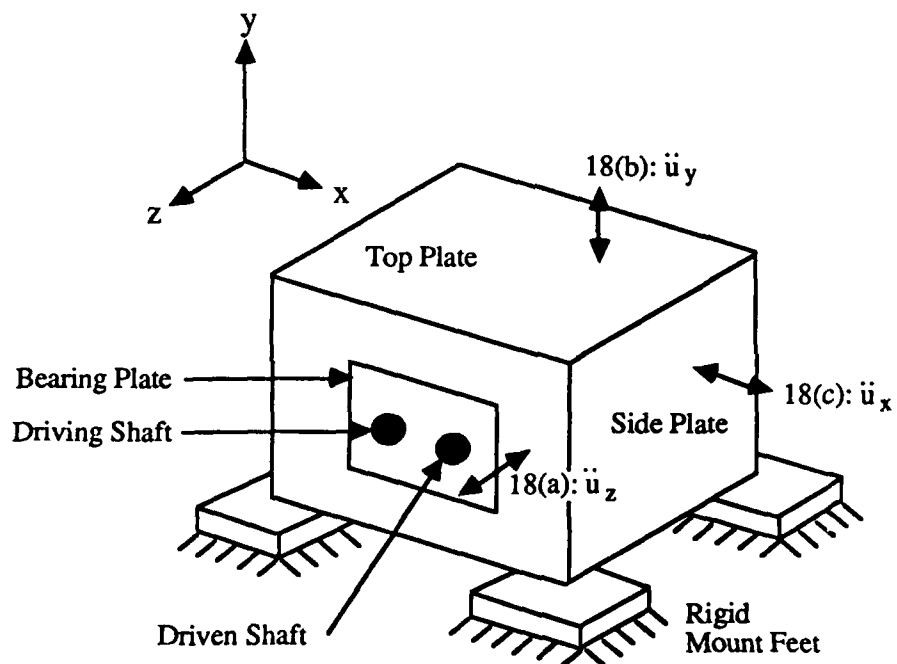


Figure 4.17 Measurement locations on the casing plate for example case III.

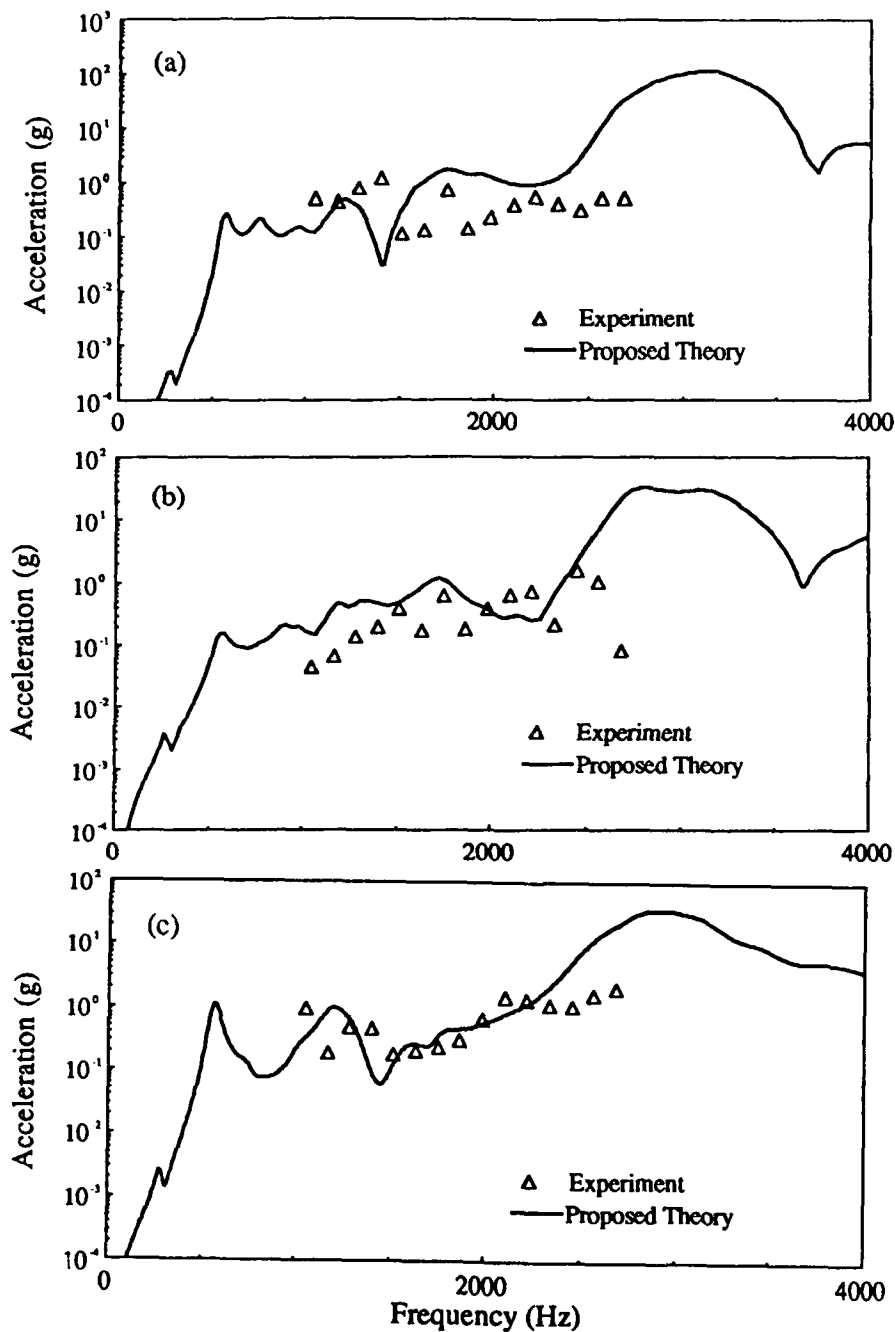


Figure 4.18 Comparison of casing flexural vibrations for example case III with $\delta_{zm} = 0.08$ mm. (a) Side plate supporting the bearings and facing the dynamometer (location 18a). (b) Top plate cover (location 18b). (c) Side plate with no bearings (location 18c).

where A^* implies the complex conjugate of the acceleration. Our predictions are within ± 5.0 dB of the measured values as shown in Table 4.8.

The sensitivity of results to $[K]_{bm}$ is evaluated next. Recall that $[K]_{bm}$ is computed based on the knowledge of the mean axial displacements δ_{zm} applied to the bearings. This parameter has been assumed to be a constant in our analysis although its exact value for the NASA experimental setup is not known. Using 2 reasonable values of δ_{zm} , we obtain a range of acceleration spectra in Figure 4.19. Almost all the experimental data are now within this range. This explains experimental scatter observed in Figure 4.18 as experimental δ_{zm} may vary slightly from one steady-state speed to another during testing.

In example case II, we found that only a few coefficients in $[K]_{bm}$ are necessary depending on the excitation. Accordingly, we had used only k_{byy} , $k_{by\theta_x}$ and $k_{b\theta_x\theta_x}$. But in the present FEM model of case III, we must include the entire symmetric $[K]_{bm}$ matrix of dimension 6 with no simplification at all. Now if we omit the off-diagonal term $k_{bx\theta_y}$ which is not directly excited by $e(t)$ in the y-direction of Figure 4.1 while still retaining other k_{bij} coefficients, no significant changes in our predictions are seen. Similarly, if the off-diagonal terms k_{bzy} and $k_{bz\theta_x}$ which are related to the shaft axial degrees of freedom are also neglected, predicted acceleration spectra vary slightly. However, if $k_{by\theta_x}$ and $k_{b\theta_x\theta_x}$ which constraint the bending motion of the shaft excited by $e(t)$ are assigned zero values per simple theory, zero out-of-plane acceleration levels are observed. This confirms that the vibration transfer through the bearings, from the shaft bending motion to the casing flexural motion, is highly dependent on these two terms.

Table 4.8 Comparison of L_A (dB) for example case III.

Center Frequency (Hz)		Location in Figure 4.17		
		18(a)	18(b)	18(c)
1250	Theory	-3.0	-13	-4.5
	Experiment	-2.0	-17	-8.4
1600	Theory	-5.5	-7.0	-11
	Experiment	-10	-8.1	-14
2000	Theory	-11	-5.4	2.1
	Experiment	-10	-7.4	0.0
2500	Theory	-3.0	0.5	5.9
	Experiment	-7.3	-1.0	4.0

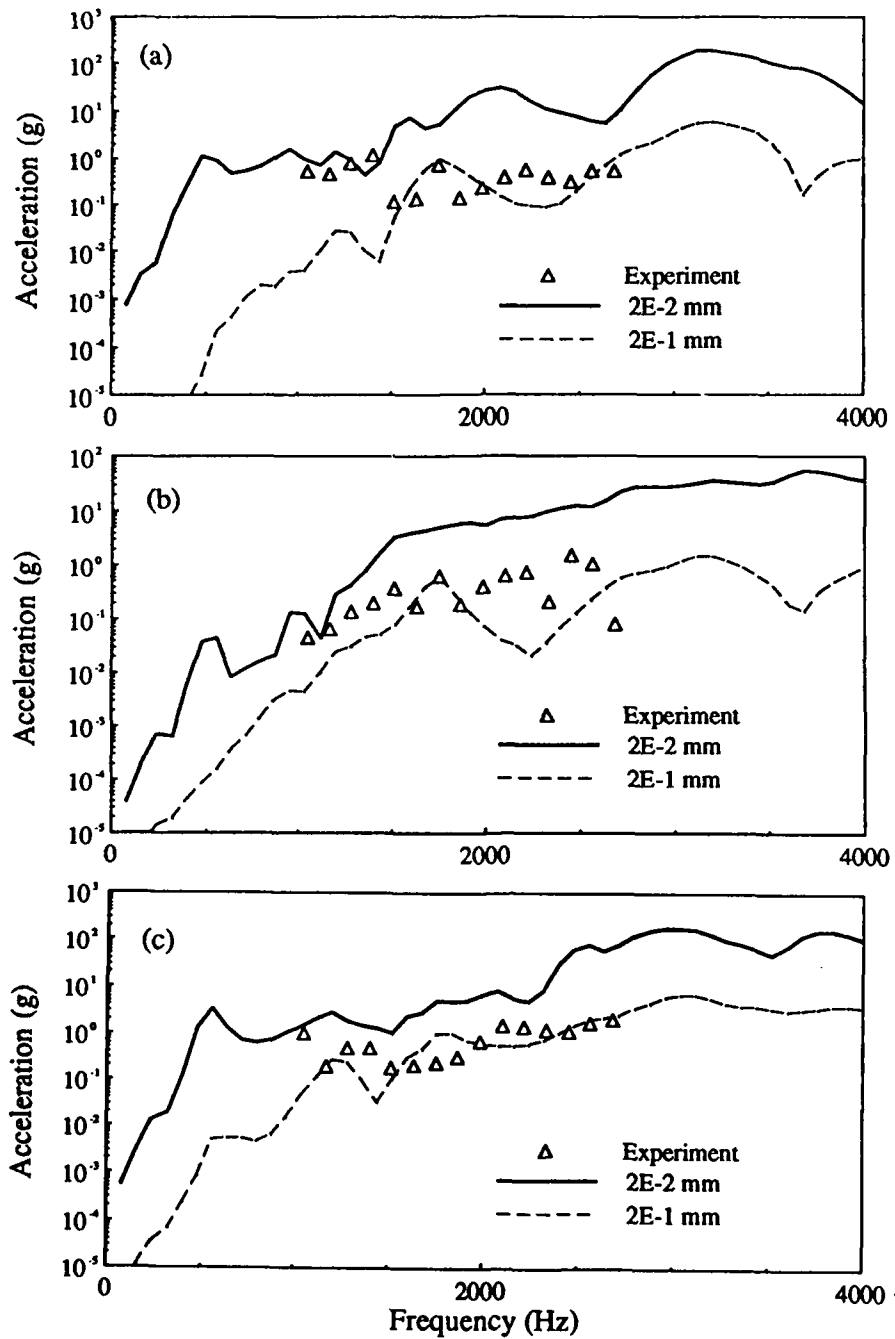


Figure 4.19 Sensitivity of predicted casing acceleration to preload δ_{zm} for example case III. (a) Side plate supporting the bearings and facing the dynamometer (location 18a). (b) Top plate cover (location 18b). (c) Side plate with no bearings (location 18c).

4.8 CONCLUDING REMARKS

A generic geared rotor system model has been developed using lumped parameter and dynamic finite element techniques which incorporates a new mathematical model for precision rolling element bearings proposed earlier in Chapter II. This system oriented model includes internal rotating system, rolling element bearings, flexible torsional couplings, motor and load, flexible or rigid casing, and compliant or massive mounts. The discrete shaft model excludes the effect of gyroscopic moment, but includes torsional, flexural and longitudinal motions. In example cases I and II, only flexural and torsional motions are predicted. The effects of mount stiffness, casing mass and bearing preload on the overall dynamic behavior have been investigated through 3 example cases of single-stage rotor and geared rotor systems excited by rotating mass unbalance at shaft frequency and kinematic transmission error excitation at mesh frequency respectively. The results indicate that our proposed model is more accurate than conventional models given in the literature. For instance, we are able to predict bearing and mount moment transmissibilities and improve casing flexural vibration prediction significantly using our theory; measurements made on case III validate our formulations partially. Conversely, the conventional models are unable to account for any bearing moment transmissibility, and consequently predict zero flexural response on the casing.

Natural frequencies of the example case III geared rotor system increase with higher mount stiffness and bearing preload, and lower casing mass. Transition mass and stiffness points which separate regimes of a natural frequency diagram are predicted. Through extensive parametric studies, we find that bearing transmissibilities may be reduced by using a higher bearing preload. However, this may result in higher

dynamic transmission error for the spur gear pair, mostly due to the coupled flexural-torsional motion. Mount transmissibility is affected by changes in casing mass, mount stiffness and mean bearing axial displacement, but bearing transmissibility is most sensitive to the mean bearing axial displacement. Similar conclusions can be drawn regarding the other two example cases.

Our theory, though restricted to the linear and time-invariant dynamic system, is comprehensive. It can be used for analysis as well as design studies of other rotating mechanical systems with multiple shafts and gear pairs or multi-staged rotors.

CHAPTER V

STATISTICAL ENERGY ANALYSIS

5.1 INTRODUCTION

It has been shown in Chapters II-IV, using classical lumped parameter and dynamic finite element techniques, that the proposed bearing model is more accurate than existing models for predicting vibration transmission through bearings in a geared rotor system. Although the proposed model has been shown to be reliable up to a moderately high frequency, it is conceivable that this model is inadequate at very high frequencies where the modal density is high. Classical vibration models do not predict modes accurately in this frequency regime, and even if it is possible to do so by employing closely spaced nodal points, such models require a significantly large computational effort. Moreover, the vast amount of predicted response spectra at many spatial points would be difficult to interpret. Accordingly, asymptotic or statistical methods must be adopted; typical techniques include the statistical energy analysis [56-60], asymptotic modal analysis [61-63] and asymptotic analysis using infinite system impedances [64].

This study concentrates on the development of a broad band vibratory energy transfer model for a geared rotor system with the proposed bearing model using the statistical energy analysis (SEA) method. This method has been applied successfully to a wide variety of structural dynamic and acoustic systems with large number of modes

[56-60,65-69]. However several unresolved research issues still exist [57,61,62,70, 71]. The specific objectives of this study are to: (i) conduct modal analysis of a geared rotor system with flexible casing and mounts, (ii) investigate the feasibility of applying SEA to this problem, (iii) analyze the following 4 example cases using SEA: I. a plate-cantilevered rectangular beam, II. case I with circular shaft-bearing system replacing the cantilevered beam, III. a circular shaft-bearing-plate-mount system, and IV. a simple geared rotor system, and (iv) perform parametric studies to examine the characteristics of vibratory energy transfer through bearings, and mean square vibroacoustic response of the casing. The first and second example cases are revised and extended versions of a study performed by Lyon and Eichler [56,58]. The later two example cases are taken from Chapters III and IV where these systems have been studied at low frequencies. Experimental validations are also included.

5.2 MODAL ANALYSIS OF GEAR CASING AND MOUNTS

Analytical and experimental modal analyses of a real gear casing and mounts have been conducted to investigate the feasibility of using SEA. Natural frequencies ω_j and modes ϕ_j are calculated using a commercial finite element method (FEM) program [39], and predictions for a rigidly mounted, stiffened gearbox are verified by the experimental modal analysis (EMA).

5.2.1 Finite Element Model

The rectangular gearbox as shown in Figure 5.1a is approximately 0.254m x 0.279m x 0.330m (10.0in x 11.0in x 13.0in), and all of its plates are 0.006m (1/4 in) thick made of 1020 steel except the regions near the bearings which are 0.025m (1.0in)

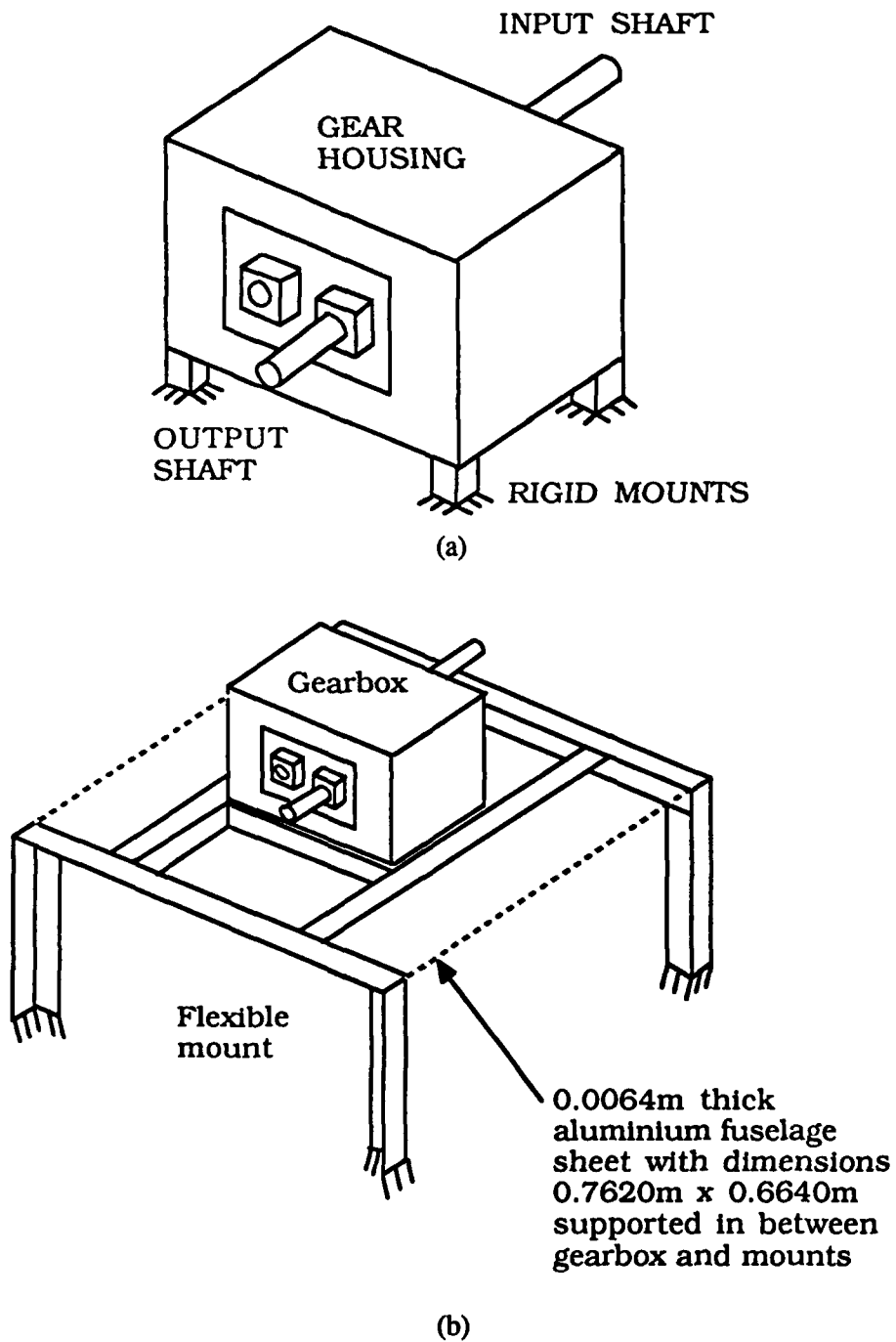


Figure 5.1 Gearbox with rigid and flexible mounts.

thick. There are four circular holes for the bearings, two at each side plate supporting the shafts. Figure 5.1b illustrates the 0.254m (10.0in) tall flexible mount frame which is constructed from eight 0.006m (1/4 in) thick, 1020 steel angle beams with three different lengths. Fuselage sheet, as shown in Figure 5.1b, is attached horizontally to the flexible mount structure. The casing is supported at each corner of the base plate for all mounting conditions, and the mounts are attached to a rigid foundation.

Two FEM models of the rectangular gearbox without its spur gears set, shafts and bearings are developed for the rigidly and flexibly mounted casings. These FEM models consist of four-noded quadrilateral plate elements with bending and membrane capabilities for the housing and attached fuselage, and two-noded shaft element with shear deformation and rotary inertia capabilities for the flexible mount skeleton and housing plate stiffeners. The boundary conditions are: (i) zero displacements and rotations at each corner of the base plate for the rigid mount, and (ii) similar conditions at each foot of the flexible mount. The interfaces between adjacent housing plates are assumed to be continuous. About 100 dynamic degrees of freedom are specified to reduce computational effort while still maintaining sufficient accuracy. Natural frequencies are computed up to at least 4 kHz to cover the gear mesh frequency regime.

5.2.2 Experiments and Model Validation

Modal experiments have been performed on a NASA high precision gearbox with the spur gear set, shafts, and ball bearings installed. An approximate configuration of the NASA gearbox is shown in Figure 5.2. The nominal dimensions of the gear housing have been given in the previous section. The variable center distance gear-shaft pair is supported by four ball bearings. Four side plates and a base plate are welded

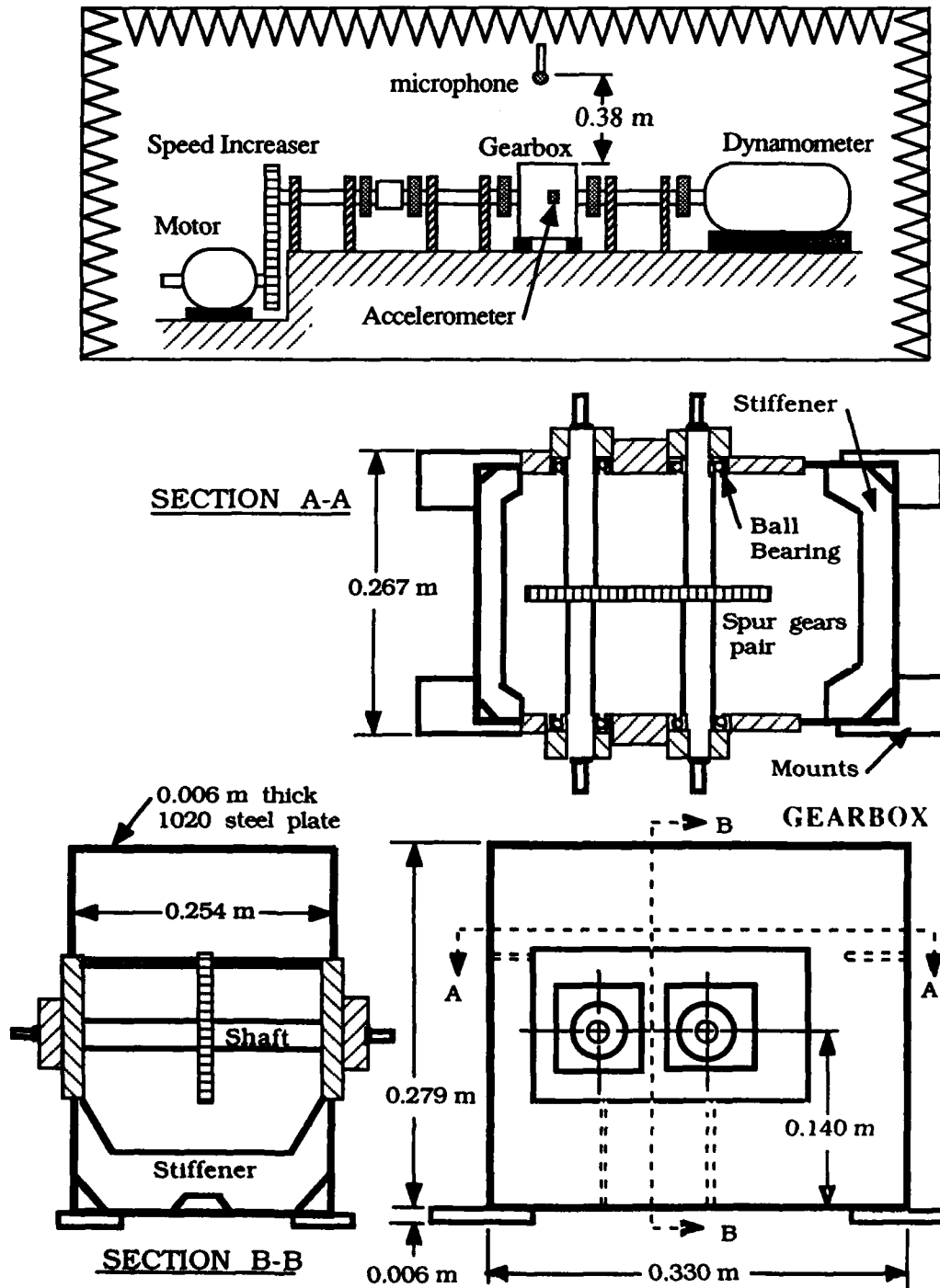


Figure 5.2 NASA gear test facility [55].

together while the top plate is bolted to the side plates. The housing plates are stiffened internally, and the gear housing system is mounted rigidly to a massive foundation. Dynamic transfer functions are obtained only on the exterior of the gear casing structure using the GENRAD 2515 system [72]. For these experiments, 154 measurement points have been selected in the direction transverse to the plane of the casing plates with the reference point being approximately near the center of the top plate to avoid nodal points of interest. Natural frequencies and modes are then estimated using the MODAL PLUS program [73]. Here, the exponential method has been used to extract modal parameters and generate analytical functions for the transfer functions, while the circle fit method has been used to construct the modal vectors.

Figure 5.3 compares predicted and measured ω_j , and FEM is found to be in good agreement with EMA. For each mode ϕ_j , two simplified illustrations are shown in Figure 5.3: (i) mode shape of the three visible plates, and (ii) mode shape of the three nonvisible plates in an approximate isometric view. The higher modes, not shown here, are also given by similar combinations of plate flexural motions. Comparison between theory and experiment for the higher modes is made on the basis of number of modes within each one-third octave bands over 500-4000 Hz in Figure 5.4a, because of the high number of participating modes observed. The results again indicate that FEM is in good agreement with EMA.

5.2.3 Parametric Studies

The rigidly mounted gear housing is observed to possess only the elastic modes of the casing plates. On the other hand, FEM model of the flexibly mounted gear casing indicates that the first six modes are translational and rotational rigid body modes of the

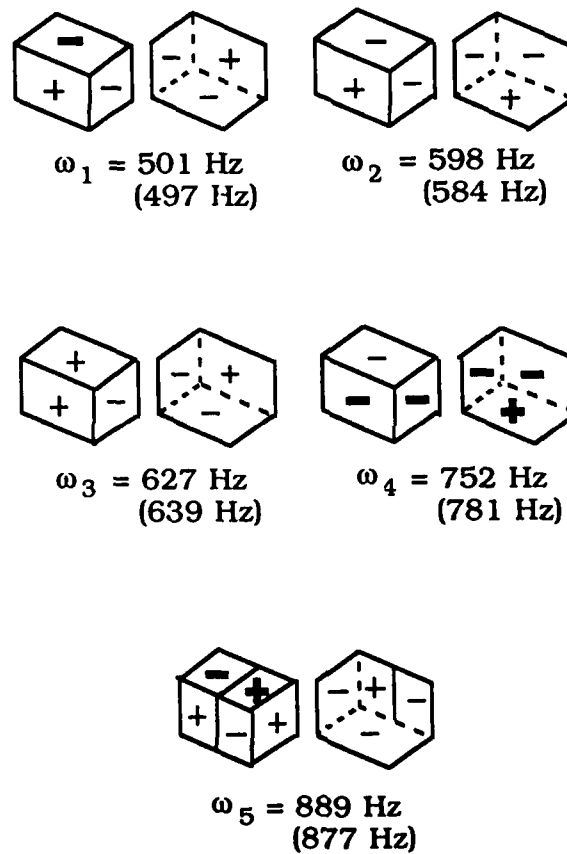
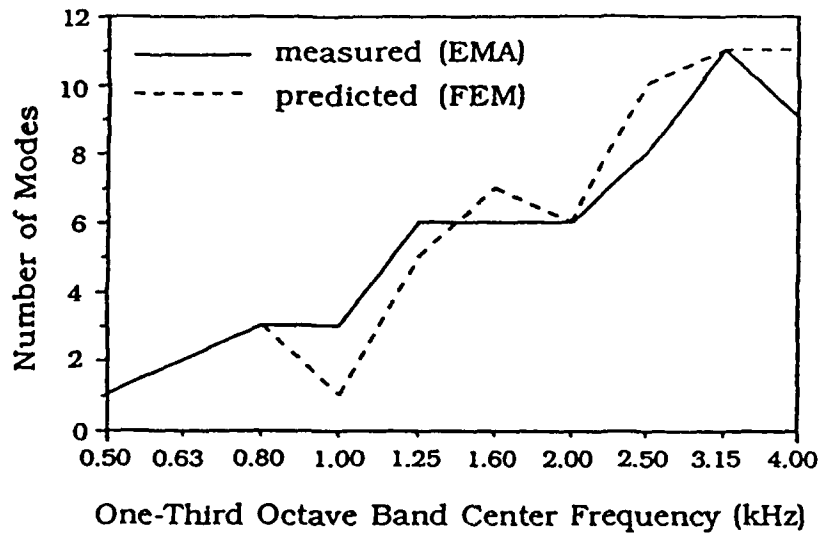
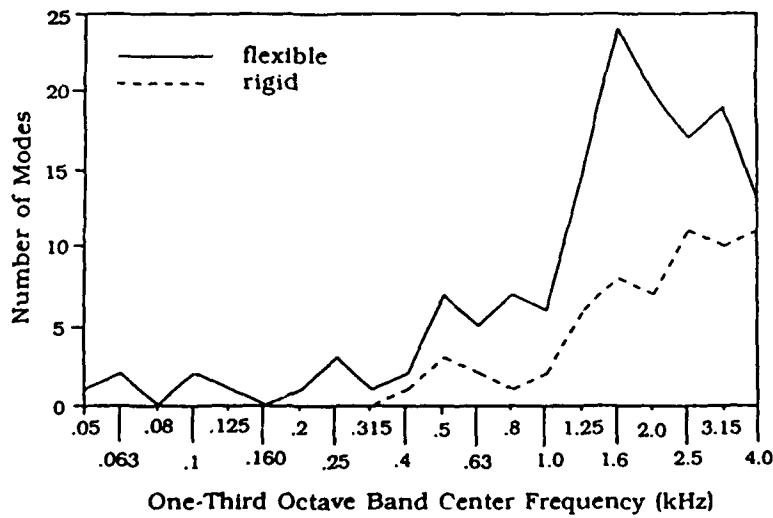


Figure 5.3 Mode shapes of the rigidly mounted, stiffened NASA gearbox as predicted by FEM (EMA results are given in parenthesis). Bold sign implies larger amplitude.



(a)



(b)

Figure 5.4 Number of modes within each one-third octave bands for the NASA gearbox. (a) Predicted and measured number of modes for rigidly mounted casing. (b) Number of modes for rigid and flexible mounting conditions.

the casing as shown in Figure 5.5; for example, $\omega_1 = 54$ Hz corresponds to the casing vibrating in the Y-direction as shown. In addition, ω_j are considerably lower, by approximately one order of magnitude as compared to those of the rigidly mounted gear casing. These rigid body vibration modes result from the complex elastic deformations of the flexible mount skeleton and fuselage sheet. The casing plate natural frequencies are also lowered, especially the first few, when the box is mounted flexibly. Figure 5.4b compares the number of modes of the flexibly mounted gear casing to that of the rigidly mounted one. High modal counts above 1 kHz are seen.

The introduction of gear casing plate stiffeners as shown in Figure 5.2 does not change the nature of the mode predictions. Also, the natural frequencies for this case only vary slightly; lower modes are affected more by the stiffeners than the higher ones. Note that the numbers of modes in each 1/3 octave band over 400-4000 Hz range remain nearly the same as evident from Table 5.1.

Table 5.1 Number of modes for the stiffened and unstiffened gearboxes mounted rigidly.

1/3 Octave Band Center Frequency (kHz)	0.4	0.5	0.63	0.8	1.0	1.25	1.6	2.0	2.5	3.15	4.0
Stiffened	0	1	2	3	1	5	7	6	10	11	11
Unstiffened	1	3	2	1	2	6	8	7	11	10	11

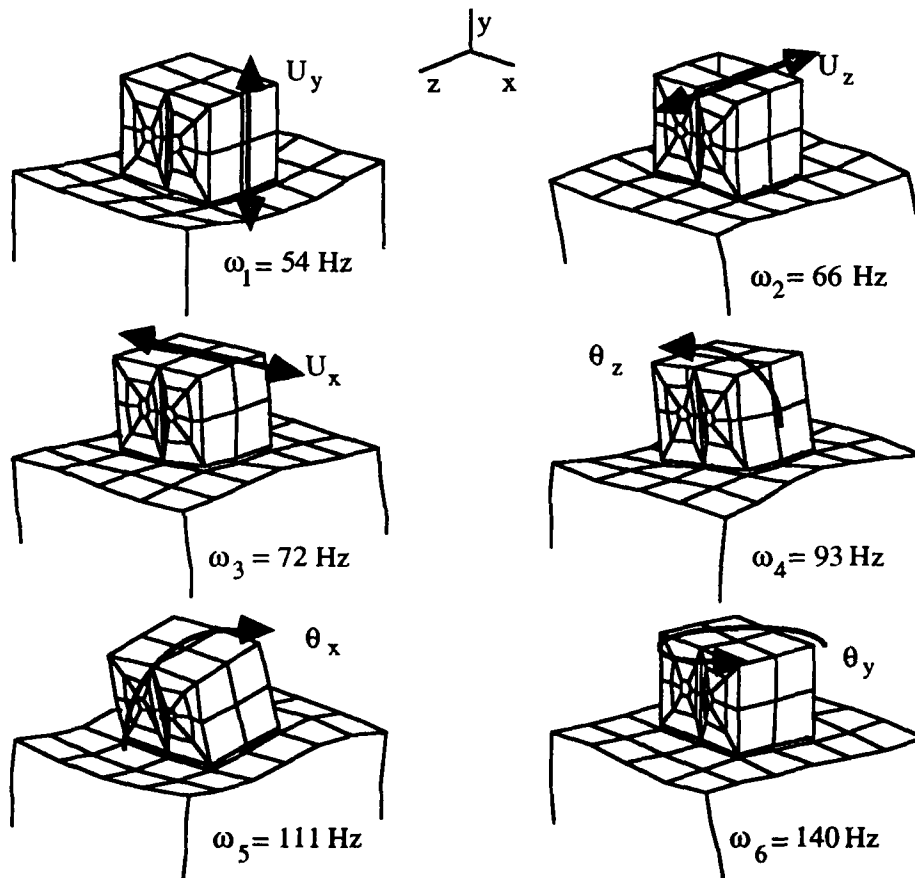


Figure 5.5 Rigid body modes of the flexibly mounted gearbox as predicted by FEM.

5.3 JUSTIFICATION FOR USING SEA

5.3.1 Modal Densities

Analytical and experimental modal analyses of the NASA gear casing clearly show that modal density tends to be high at higher frequencies. Although the analysis is restricted to a gear casing system, it is reasonable to assume that similar results are valid for other rotating mechanical system housings. Accordingly, SEA can be used justifiably.

Next, consider the modal densities of a shaft or beam n_s and rectangular plate n_c , given for bending motion with simply-supported boundary conditions [56]

$$n_s = L_s \sqrt[4]{\frac{\rho_s \pi h_s^2}{4 E I_s \omega^2}} \quad ; \quad n_c = \frac{A_c}{h_c} \sqrt{\frac{3 \rho_c (1 - \mu^2)}{E}} \quad (5.1)$$

where ρ is the material density, A_c is the plate surface area, L_s is the shaft length, E is the modulus of elasticity, I_s is the area moment of inertia of the shaft, ω is the bandwidth center frequency, h is the plate or shaft thickness, μ is the Poisson's ratio, and the subscripts s and c denote shaft and plate respectively. For typical numerical values given later in Section 5.4 we find that: (i) $n_c = 0.227$, and (ii) $n_s = 0.012$ at 100 Hz, $n_s = 0.004$ at 1000 Hz and $n_s = 0.002$ at 4000 Hz. Note that $n_c \gg n_s$ as expected. Although the shaft has a fairly low number of modes in the frequency range of interest, SEA is still valid since the plate modal density n_c is very high.

5.3.2 Literature Review

A majority of publications are on the application of the SEA procedure to dynamic systems with high n such as structural-acoustical interactions in a fuselage [56,65,74], sound transmission through panels [60], and vibratory energy transmission in mechanical equipment [56]. Of interest here are analytical or experimental estimation of SEA parameters for simple structural systems described by a flat plate, a cylinder and/or a shaft [56,58,59,66]. In these studies, structural connections are often assumed rigid such as in the ideally welded case.

Lyon and Eichler [56,58] in 1964 and Lyon and Scharton [59] in 1965 developed analytical expressions for the coupling loss factor η in several connected structures, such as a plate bonded to a cantilevered beam [56,58]. Here η was derived assuming a semi-infinite beam attached to an infinite plate and by further assuming that only a dynamic moment coupling at the joint can describe the motion/force transmission phenomenon. This problem is re-examined in this study and is then extended to a circular shaft-bearing-plate-mount system. In addition, Lyon and Eichler [56,58] also developed SEA models of two structures inter-connected through a single (scalar) stiffness element. Typical examples include two longitudinal rods connected via a linear stiffness element, two discrete masses coupled by a linear spring, and a plate attached to a single degree of freedom resonator [56]. A similar analysis on the longitudinal vibration of linearly coupled rods was performed by Keane and Price [69] in 1987. Loss factors of typical line or point connected structures such as a plate welded to a cylinder, cross beams and two perpendicular plates bolted or welded together, have been calculated assuming ideal rigid joints [56,58,59,75,76]. But a compliant bearing system problem is yet to be analyzed.

5.4 EXAMPLE CASE 1: COUPLING LOSS FACTOR OF PLATE-CANTILEVERED BEAM SYSTEM

First, we attempt to rework the plate-cantilevered beam problem of Lyon and Eichler [56,58] as shown in Figure 5.6. Only flexural motions of the plate and beam are considered in this case. Accordingly, Lyon and Eichler [56,58] developed an expression for the coupling loss factor η_{sc} which describes the vibratory energy transfer between the beam(s) and the plate(c) due to a moment coupling at the joint

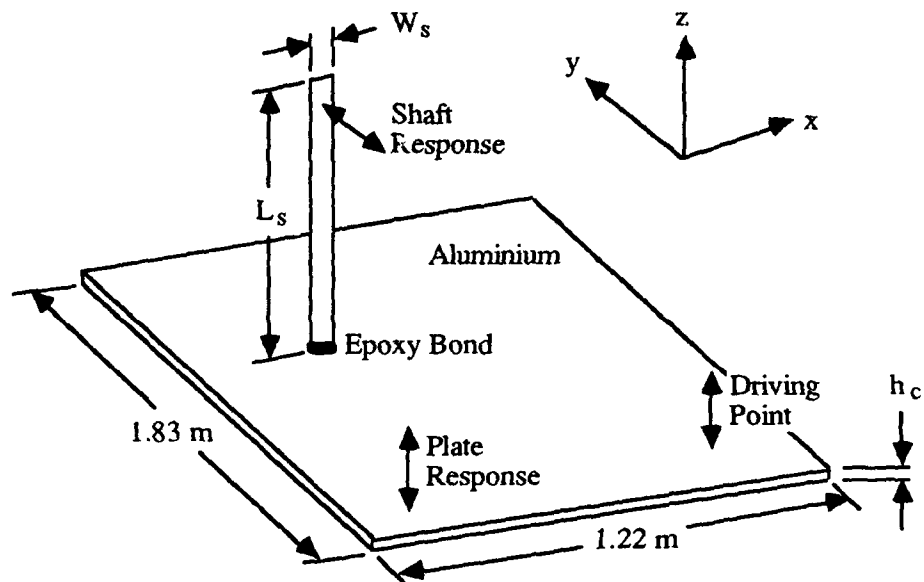
$$\eta_{sc}(\omega) = \frac{(2\rho_s A_s \kappa_s c_s)^2}{\omega m_s} \left| \frac{Z_c}{Z_c + Z_s} \right|^2 \operatorname{Re} \left(\frac{1}{Z_c} \right) \quad (5.2)$$

where $\kappa = \sqrt{I_s/A_s}$ is the radius of gyration, $c = \sqrt{E/\rho_s}$ is the wave speed, m is the mass and $\operatorname{Re}(\)$ implies the real part of a complex variable. The driving point moment impedances for the plate Z_c and beam Z_s are [58,77]

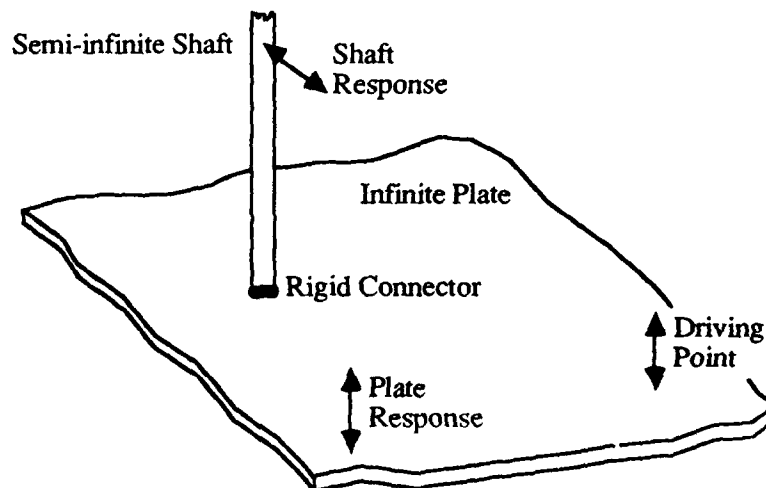
$$Z_c(\omega) = \frac{16\rho_c h_c \kappa_c^2 c_c^2}{\omega \left(1 - \frac{4i}{\pi} \ln(k_c h_s) \right)} ; Z_s(\omega) = \frac{\rho_s A_s \kappa_s^2 c_s^2 k_s}{\omega} (1 - i) \quad (5.3)$$

where k is the wavenumber and h is the plate or beam thickness. Here, note that Z_s of equation (5.3) differs from Lyon and Eichler's expression [56,58] in the sign of the imaginary part which is probably a typographical error. They assumed that $|Z_c| \gg |Z_s|$, $\kappa_s = \kappa_c$, $c_s = c_c$ and $\rho_s = \rho_c$, and simplified equation (5.2) to yield a frequency invariant expression for η_{sc} as

$$\eta_{sc} = W_s / (4L_s) \quad (5.4)$$



(a) Finite System



(b) Infinite Systems

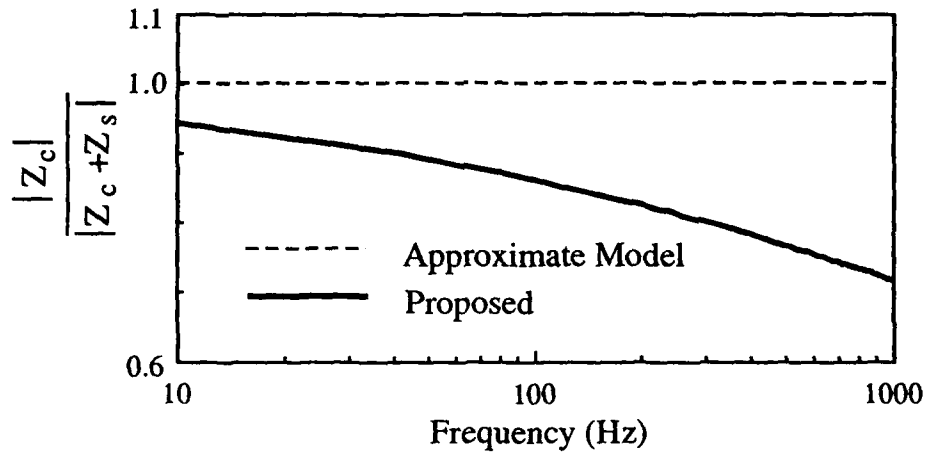
Figure 5.6 Schematic of example case I: a plate-cantilevered beam. (a) Experimental finite system. (b) Theoretical infinite system.

where W_s and L_s are the beam width and length respectively as shown in Figure 5.6. However, our calculations indicate that $|Z_c| > |Z_s|$ but not $|Z_c| \gg |Z_s|$ for the parameters used by Lyon and Eichler [58], as shown in Figure 5.7a. Using equation (5.2), η_{sc} is recomputed and compared with the approximate model given by equation (5.3) in Figure 5.7b. Experimental results given by Lyon and Eichler are also plotted in Figure 5.7b. It can be seen that our calculation is better than earlier prediction. At low frequency, a discrepancy is observed between theory and experiment which is primarily due to the low modal density in this regime. The presence of a low natural frequency may be due to the compliant epoxy bond between the beam and plate. However, above the threshold frequency where many modes participate, shown as a vertical line in Figure 5.7b, the slope of the least square straight line fit on the experimental data is nearly the same as the predicted η_{sc} .

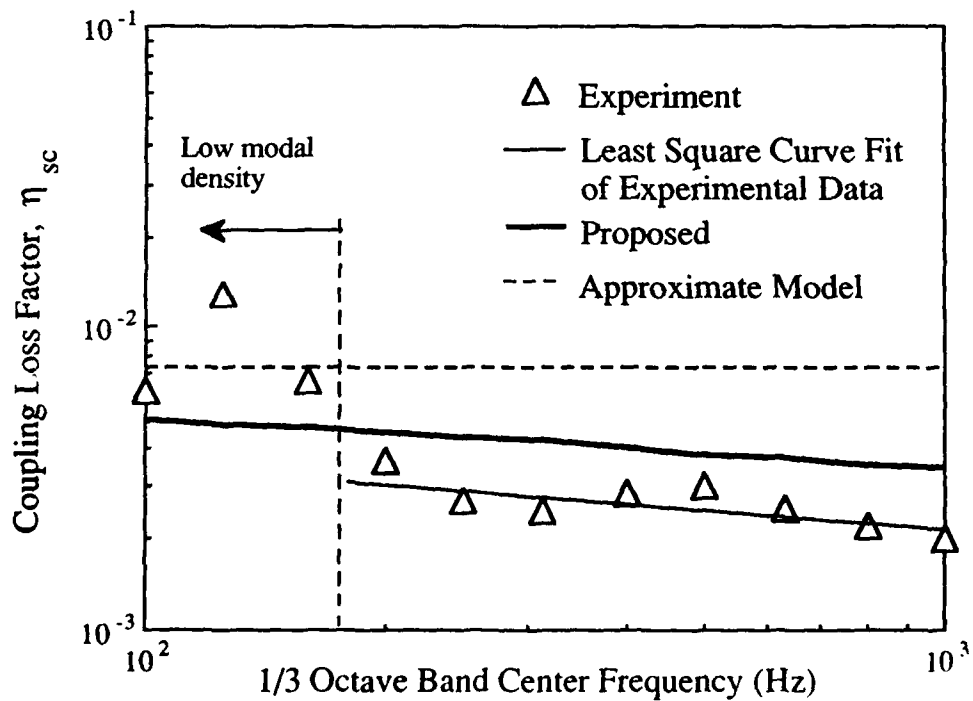
5.5 EXAMPLE CASE II: COUPLING LOSS FACTOR OF CIRCULAR SHAFT-BEARING-PLATE SYSTEM

Next, we modify Figure 5.6 by inserting a ball bearing between the circular shaft (which replaces the beam in Figure 5.6) and the rectangular plate. Again, a semi-infinite shaft and an infinite plate are assumed. For SEA, we reduce the system to a plate subsystem and a shaft-bearing subsystem. The coupling loss factor η_{sc} is still given by equation (5.2), but Z_s must be modified to account for the compliant bearing.

Consider a shaft with boundary conditions shown in Figure 5.8. The bearing end is subjected to zero transverse velocity $v_{ysa}(t, z=0^-)=0$ and a sinusoidally varying moment $M_{xsa}(t, z=0^-)=M_{xsa}e^{i\omega t}$. Here, $z=0^-$ refers to the junction point between bearing and plate, and $z=0^+$ is the junction point between the bearing and shaft. In the frequency domain, using the definition of bearing force vector



(a)



(b)

Figure 5.7 Comparison between Lyon and Eichler's approximation [56,58] and our proposed formulation for example case I. (a) Comparison of $|Z_c|/|Z_c + Z_s|$. (b) Comparison of predicted η_{sc} with experimental results given by Lyon and Eichler [56,58].

$$M_{xsa}(\omega, z=0^-) = M_{xsa}$$

$$v_{ysa}(\omega, z=0^-) = 0$$

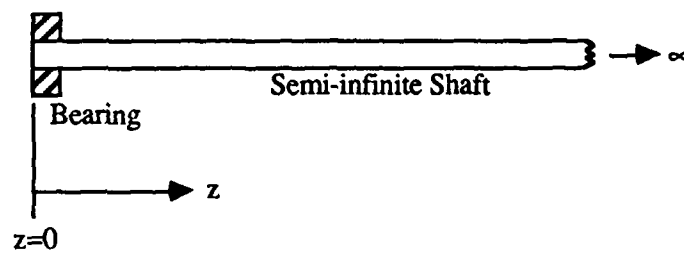


Figure 5.8 Boundary conditions for example case II: semi-infinite shaft-bearing system.

$\{f(\omega)\}_b = [K]_{bm} \{v(\omega)\}_b / i\omega$ in terms of the velocity vector $\{v(\omega)\}_b$ and the proposed bearing stiffness matrix $[K]_{bm}$. $v_{ysa}(\omega, z=0^-) = 0$ is shown to be equivalent to $F_{ysa}(\omega, 0^+) = (k_{by\theta_x} / k_{b\theta_x\theta_x}) M_{xsa} + v_{ysa}(\omega, 0^+) \{ (k_{by\theta_x} / k_{b\theta_x\theta_x})^2 k_{b\theta_x\theta_x} - k_{byy} \} / (i\omega)$.

The governing equations for $M_{xsa}(\omega, z)$ and $F_{ysa}(\omega, z)$ of the shaft in terms of $v_{ysa}(\omega, z)$ are

$$M_{xsa} = -\frac{EI_s}{i\omega} \frac{d^2 v_{ysa}}{dz^2} ; \quad F_{ysa} = \frac{EI_s}{i\omega} \frac{d^3 v_{ysa}}{dz^3} \quad (5.5)$$

In general, the bounded solution for $v_{ysa}(\omega, z)$ is

$$v_{ysa}(\omega, z) = \{ b_1 e^{-jk_s z} + b_2 e^{-k_s z} \} \quad (5.6)$$

Using equations (5.5) and (5.6), we enforce the boundary conditions for the shaft at $z=0^+$ to obtain the following closed form solution for the coefficient vector $\{b\} = \{b_1, b_2\}^T$.

$$b_1 = \frac{i\omega M_{xsa}}{EI k_s^2} + \frac{\frac{\omega k_{by\theta_x}}{k_{b\theta_x\theta_x}} - i\omega k_s - \frac{\omega}{EI k_s^2} \left(k_{byy} - \frac{k_{by\theta_x}^2}{k_{b\theta_x\theta_x}} \right)}{EI k_s^3 (1+i) - 2ik_{byy} + \frac{2ik_{by\theta_x}^2}{k_{b\theta_x\theta_x}}} M_{xsa} ;$$

$$b_2 = \frac{\frac{\omega k_{by\theta_x}}{k_{b\theta_x\theta_x}} - i\omega k_s - \frac{\omega}{EI k_s^2} \left(k_{byy} - \frac{k_{by\theta_x}^2}{k_{b\theta_x\theta_x}} \right)}{EI k_s^3 (1+i) - 2ik_{byy} + \frac{2ik_{by\theta_x}^2}{k_{b\theta_x\theta_x}}} M_{xsa} \quad (5.7)$$

Hence, the bearing-shaft impedance Z_s is then given by

$$Z_s(\omega) = \frac{M_{xsa}(\omega, 0)}{\frac{dv_{ysa}}{dz}(\omega, 0^-)} = \frac{k_{b\theta_x \theta_x}}{i\omega + \frac{k_{by\theta_x} v_{ysa}(\omega, 0^+) + k_{b\theta_x \theta_x} \frac{dv_{ysa}}{dz}(\omega, 0^+)}{M_{xsa}}} \quad (5.8)$$

Although M_{xsa} appears in equation (5.8), Z_s is independent of the magnitude of M_{xsa} since $v_{ysa}(\omega, 0^+)$ and $\frac{dv_{ysa}}{dz}(\omega, 0^+)$ are linearly proportional to M_{xsa} in equation (5.5).

Using equations (5.2), (5.7) and (5.8), η_{sc} is computed for several bearings whose stiffness coefficients are tabulated in Table 5.2. Figure 5.9 compares these where the material and geometrical properties of the shaft and plate are equivalent to those used by Lyon and Eichler [56,58] in example case I. For a very soft bearing, Z_s is dominated by the bearing parameters, and hence $|Z_c| \gg |Z_s|$ is valid. This implies that η_{sc} reduces to the frequency invariant expression given by equation (5.4) as shown by set A in Figure 5.9. On the other hand, η_{sc} for a rigid bearing (say set B or C) is typically smaller than η_{sc} for a soft bearing given by A. The extreme values of η_{sc} , as k_{bij} or bearing preload becomes very large, depend on the relative magnitudes of the bearing stiffness coefficients as shown in Figure 5.9 for sets D and E. Such deviation for a stiff bearing from set B is primarily due to the presence of off-diagonal stiffness coefficient such as $k_{by\theta_x}$. However it is found that η_{sc} for most stiff bearings will approach set E in Figure 5.9 which is obviously identical to the prediction for the example case I using equations (5.2) and (5.3).

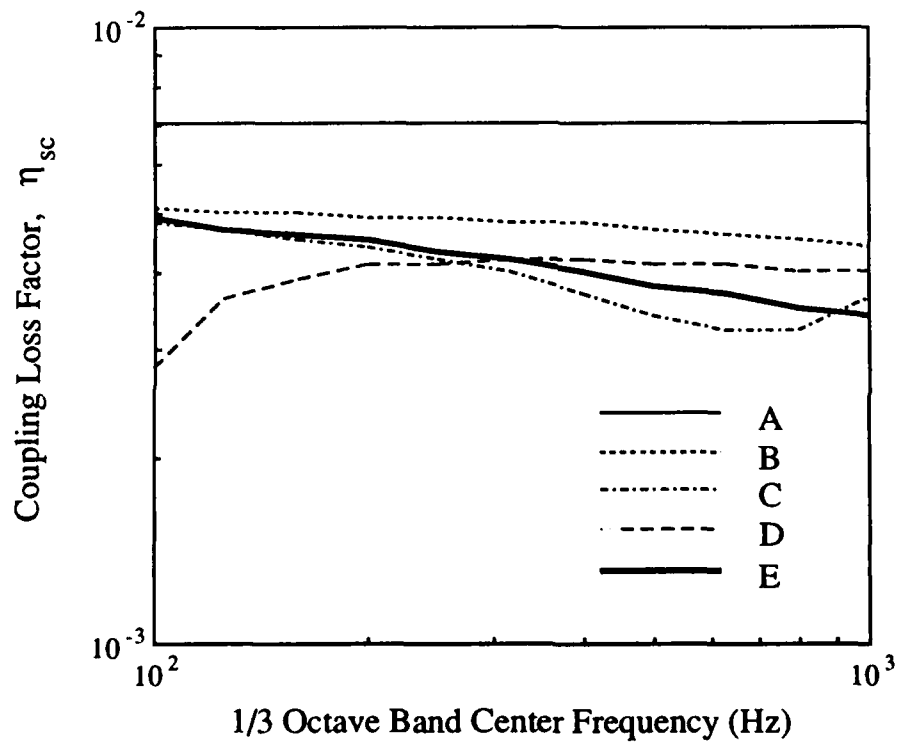


Figure 5.9 Coupling loss factor η_{sc} used in example case II for various bearing stiffness coefficients listed in Table 5.2.

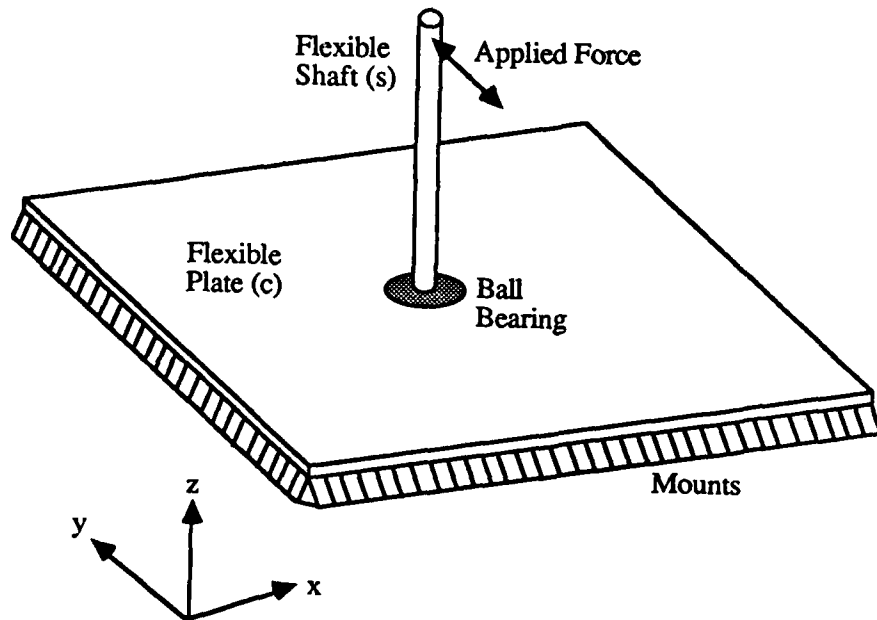
Table 5.2 Typical bearing stiffness coefficients of Figure 5.9 for example case II.

Set	k_{byy} (N/m)	$k_{by\theta_x}$ (N)	$k_{b\theta_x\theta_x}$ (Nm)
A	Very Compliant Bearings ($k_{bij} < 1E3$)		
B	1E5	5E4	2E4
C	5E5	8E4	5E4
D	1E8	1E7	1E6
E	1E8	3E7	1E7

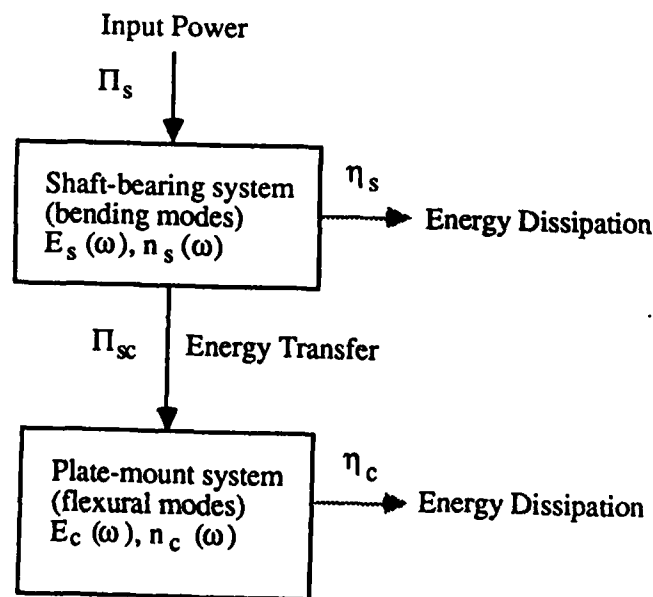
5.6 EXAMPLE CASE III: A CIRCULAR SHAFT-BEARING-PLATE SYSTEM

5.6.1 Theory

Consider a circular shaft-bearing-plate-mount system similar to example case II but with a shaft of finite length as shown in Figure 5.10a. Note that this system has been analyzed earlier using the deterministic vibration modeling technique for low frequency response. Recall the unconstrained end of the non-rotating circular shaft is subjected to a harmonically varying force $F_{ys}(t) = F_{ysa}e^{i\omega t} + F_{ysm}$, where F_{ysm} is the mean force. From Chapter III, we know that the longitudinal and torsional motions of the shaft, and the in-plane vibration of the plate can be neglected. Hence, the shaft bending vibration and plate flexural motion are of interest here. Also, the previous deterministic vibration models indicate that the coupling between these two motions is mainly due to the dynamic moment at the bearing provided the longitudinal shaft vibration is not excited. Accordingly, two subsystems which can be easily identified using SEA are the transverse modes of the shaft-bearing system and the flexural modes of the plate-mount



(a)



(b)

Figure 5.10 Example case III: (a) schematic of the circular shaft-bearing-plate-mount system and (b) A SEA model of the shaft-bearing-plate-mount system.

system as shown in Figure 5.10b. We now proceed to derive η_{sc} governing the vibratory energy flow between these two subsystems using the driving point junction impedance method suggested by Lyon [56].

Since the rectangular plate dimension is much larger than the bearing dimension, the plate is again assumed infinite. Consider the vibrational power flow Π_{sc} from the shaft-bearing subsystem (subscript s) to the plate (subscript c), due to the uniform external Gaussian random force over a frequency bandwidth $\Delta\omega$ with center frequency ω ,

$$\Pi_{sc}(\omega) = \omega \eta_{sc}(\omega) n_s(\omega) \left(\frac{E_s(\omega)}{n_s(\omega)} - \frac{E_c(\omega)}{n_c(\omega)} \right) \quad (5.9)$$

where n_j and E_j ($j = s, c$) refer to subsystem modal density and total vibratory energy respectively. Since the plate is assumed to be reasonably well damped and geometrically large, equation (5.9) is approximated assuming $n_c \gg n_s$ or $E_c/n_c \ll E_s/n_s$ to yield

$$\eta_{sc}(\omega) \approx \frac{\Pi_{sc}(\omega)}{\omega E_s(\omega)} \quad (5.10)$$

For the shaft, $E_s = m_s \langle V_s^2 \rangle$ where m_s is the shaft mass and $\langle V_s^2 \rangle$ is mean square shaft transverse velocity averaged over $\Delta\omega$ and shaft length L_s . Using the expression for Π_{sc} given by Lyon and Eichler [58] as discussed in the previous section, η_{sc} in terms of Z_s and Z_c is identical to equation (5.2) which is rewritten here for the circular shaft case as

$$\eta_{sc}(\omega) = \frac{4 EI_s}{\omega L_s} \operatorname{Re} \left(\frac{1}{Z_c} \right) \left| \frac{Z_c}{Z_c + Z_s} \right|^2 \quad (5.11)$$

For an infinite steel plate of thickness h_c , the point moment impedance Z_c is given by equation (5.3); it is rewritten as

$$Z_c(\omega) = \frac{4 E h_c^3}{3 \omega (1 - \mu^2)} \left\{ 1 - \frac{4i}{\pi} \ln \left(\frac{9}{20} k_c d_s \right) \right\}^{-1} ; \quad k_c d_s \ll 1 \quad (5.12)$$

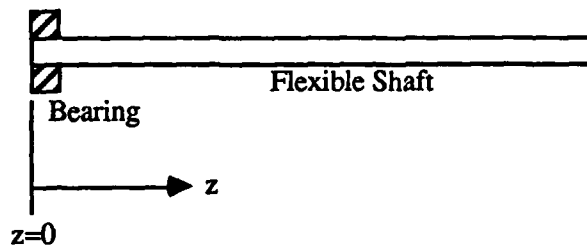
The shaft-bearing impedance Z_s in equation (5.11) is derived next by solving the boundary-value problem for the system shown in Figure 5.11a. The free end of the shaft has a vanishing dynamic shear force $F_{ysa}(\omega, z=L_s)=0$ and bending moment $M_{xsa}(\omega, z=L_s)=0$. The bearing end is similar to Figure 5.8. Following the same argument used previously for example case II will lead to the two boundary conditions described by $M_{xsa}(\omega, z=0^+) = M_{xsa}$ and $F_{xsa}(\omega, z=0^+) = (k_{bx\theta_y}/k_{b\theta_y\theta_y})M_{xsa} + v_{ysa}(\omega, 0^+) \{ (k_{bx\theta_y}/k_{b\theta_y\theta_y})^2 k_{b\theta_y\theta_y} - k_{bxx} \} / (i\omega)$. Governing equations are still given by equation (5.5), but the solution for $v_{ysa}(\omega, z)$ is assumed to be of the following form [77]

$$v_{ysa}(t, z) = \{ b_1 e^{-jk_s z} + b_2 e^{jk_s z} + b_3 e^{-k_s z} + b_4 e^{k_s z} \} \quad (5.13)$$

Using equations (5.5) and (5.13), the boundary conditions yield the following algebraic problem

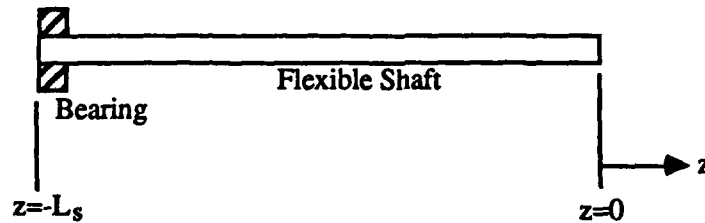
$$[B]\{b\} = M_{xsa} \left\{ k_{by\theta_x}/k_{b\theta_x\theta_x}, i\omega/(EIk_s^2), 0, 0 \right\}^T \quad (5.14)$$

$$\begin{aligned}
 M_{xsa}(\omega, z=0^-) &= M_{xsa} & M_{xsa}(\omega, z=L_s) &= 0 \\
 v_{ysa}(\omega, z=0^-) &= 0 & F_{ysa}(\omega, z=L_s) &= 0
 \end{aligned}$$



(a)

$$\begin{aligned}
 v_{ysa}(\omega, z=-L_s^-) &= 0 & M_{xsa}(\omega, z=0) &= 0 \\
 \frac{dv_{ysa}}{dz}(\omega, z=-L_s^-) &= 0 & F_{ysa}(\omega, z=0) &= F_{xsa}
 \end{aligned}$$



(b)

Figure 5.11 Boundary conditions for example case III: finite shaft-bearing system.
 (a) Moment applied at the bearing end. (b) Force applied at the free end.

The nonzero elements of coefficient matrix [B] of dimension 4 are

$$\begin{aligned}
 B_{11} &= \frac{1}{\omega} \left(EIk_s^3 - ik_{byy} + \frac{ik_{by\theta_x}^2}{k_{b\theta_x\theta_x}} \right) ; \quad B_{12} = \frac{1}{\omega} \left(-EIk_s^3 - ik_{byy} + \frac{ik_{by\theta_x}^2}{k_{b\theta_x\theta_x}} \right) ; \\
 B_{13} &= \frac{i}{\omega} \left(EIk_s^3 - k_{byy} + \frac{k_{by\theta_x}^2}{k_{b\theta_x\theta_x}} \right) ; \quad B_{14} = \frac{i}{\omega} \left(-EIk_s^3 - k_{byy} + \frac{k_{by\theta_x}^2}{k_{b\theta_x\theta_x}} \right) ; \\
 B_{21} &= B_{22} = -B_{23} = -B_{24} = 1 ; \quad B_{31} = -iB_{41} = ie^{-jk_s L_s} ; \quad B_{32} = iB_{42} = -ie^{jk_s L_s} ; \\
 B_{33} &= -B_{43} = -e^{-k_s L_s} ; \quad B_{34} = B_{44} = e^{k_s L_s}
 \end{aligned} \quad (5.15)$$

Both [B] and {b} = {b₁, b₂, b₃, b₄}^T can be easily obtained numerically. The bearing-shaft impedance Z_s is still given by equation (5.8).

The same procedure may be applied to obtain the driving point force impedance for a harmonically varying transverse force F_{ysa}(t, z=0). Note that the origin is redefined at the forcing point as shown in Figure 5.11b for convenience. The boundary conditions are F_{ysa}(ω, z=0)=F_{ysa}, M_{xsa}(ω, z=0)=0, v_{ysa}(ω, z=-L_s⁻)=0, and $\frac{dv_{ysa}}{dz}(\omega, -L_s^-) = 0$. These conditions at z=-L_s⁻ can be rewritten for z=-L_s⁺ like the previous case to obtain

$$\begin{aligned}
 M_{xsa}(\omega, z=-L_s) &= -\left(k_{b\theta_x\theta_x} \frac{dv_{ysa}}{dz}(\omega, -L_s^+) + k_{by\theta_x} v_{ysa}(\omega, -L_s^+) \right) / (i\omega) ; \\
 F_{ysa}(\omega, z=-L_s) &= -\left(k_{by\theta_x} \frac{dv_{ysa}}{dz}(\omega, -L_s^+) + k_{byy} v_{ysa}(\omega, -L_s^+) \right) / (i\omega)
 \end{aligned} \quad (5.16)$$

These prescribed boundary conditions again yield a set of algebraic problem similar to Equation (5.14). The nonzero elements of the coefficient matrix [B] of dimension 4 are

$$\begin{aligned}
B_{11} &= -B_{21} = B_{12} = B_{22} = -B_{13} = iB_{23} = -B_{14} = -iB_{24} = -1.0 ; \\
B_{31} &= (-jk_s k_{b\theta_x \theta_x} + k_{by\theta_x} + EIk_s^2) e^{ik_s L_s} ; \\
B_{32} &= (jk_s k_{b\theta_x \theta_x} + k_{by\theta_x} + EIk_s^2) e^{-ik_s L_s} ; \\
B_{33} &= (-k_s k_{b\theta_x \theta_x} + k_{by\theta_x} - EIk_s^2) e^{k_s L_s} ; \\
B_{34} &= (k_s k_{b\theta_x \theta_x} + k_{by\theta_x} - EIk_s^2) e^{-k_s L_s} ; \\
B_{41} &= (ik_s k_{by\theta_x} - k_{byy} - iEIk_s^3) e^{ik_s L_s} ; \\
B_{42} &= (-ik_s k_{by\theta_x} - k_{byy} + iEIk_s^3) e^{-ik_s L_s} ; \\
B_{43} &= (k_s k_{by\theta_x} - k_{byy} + EIk_s^3) e^{k_s L_s} ; \\
B_{44} &= (-k_s k_{by\theta_x} - k_{byy} - EIk_s^3) e^{-k_s L_s}
\end{aligned} \tag{5.17}$$

The right hand side vector $\{b\}$ of the algebraic problem is $\{0, F_{ysa}\omega/(EIk_s^3), 0, 0\}^T$. Force impedance at the driving point is then given by $Z_s(\omega, z=0) = F_{ysa}/v_{ysa}(\omega, 0)$. Accordingly, the input power is $\Pi_s = (1/2) F_{ysa}^2 \text{Re}\{(1/Z_s)^*\}$ where $\text{Re}\{\}$ is the real part of the complex variable and $()^*$ implies the complex conjugation.

We can now compute the vibratory energy transfer Π_{sc} through the bearing and steady-state subsystem energy levels E_s and E_c by applying the energy balances to both subsystems shown in Figure 5.10b; here $\eta_{cs} = \eta_{sc} n_s/n_c$.

$$\begin{bmatrix} \eta_s + \eta_{sc}(\omega) & -\eta_{cs}(\omega) \\ -\eta_{sc}(\omega) & \eta_c + \eta_{cs}(\omega) \end{bmatrix} \begin{Bmatrix} E_s(\omega) \\ E_c(\omega) \end{Bmatrix} = \begin{Bmatrix} \Pi_s / \omega \\ 0 \end{Bmatrix} \tag{5.18}$$

$$\begin{aligned}
 E_s(\omega) &= \frac{\Pi_s (\eta_c + \eta_{cs})}{\omega (\eta_s \eta_c + \eta_c \eta_{sc} + \eta_s \eta_{cs})} ; \\
 E_c(\omega) &= \frac{\Pi_s \eta_{sc}}{\omega (\eta_s \eta_c + \eta_c \eta_{sc} + \eta_s \eta_{cs})}
 \end{aligned} \tag{5.19}$$

Since $E = m \langle V^2 \rangle$, the following velocity levels may be obtained at any center frequency ω from either equation (5.18) or (5.19)

$$\frac{\langle V_c^2 \rangle}{\langle V_s^2 \rangle} = \frac{m_s}{m_c} \left(\frac{\eta_{sc}(\omega)}{\eta_c + \eta_{cs}(\omega)} \right) \tag{5.20}$$

5.6.2 Validation and Parametric Studies

In order to validate our SEA formulation, we compare the mean square mobility level of the plate with experimental data reported earlier in Chapter III. Note that although all nonzero bearing stiffness coefficients k_{bij} are computed and given in Table 3.6, only $k_{byy}=3.69E8$, $k_{by\theta_x}=3.52E5$ and $k_{b\theta_x\theta_x}=4.19E4$ are used as they appear to be the most significant ones according to the proposed theory. Using equation (5.19), $\langle V_c^2 \rangle$ is computed and compared with experimental results in Figure 5.12. Theoretical predictions for three values of dissipation loss factor $\eta_s = \eta_c \neq \eta_s(\omega)$ are given since the choice of structural damping is critical to the SEA analysis. It can be seen from Figure 5.13 that the experimental data are approximately bounded by $\eta_s=0.0003$ and $\eta_s=0.03$. Here η_s is also assumed to be frequency invariant which may not be valid in the experiment. Accordingly, comparison between theory and experiment is deemed to be excellent.

Further comparison between theory and experiment can be made for the case of a semi-infinite shaft considered in the example case II. Using equations (5.2), (5.7) and

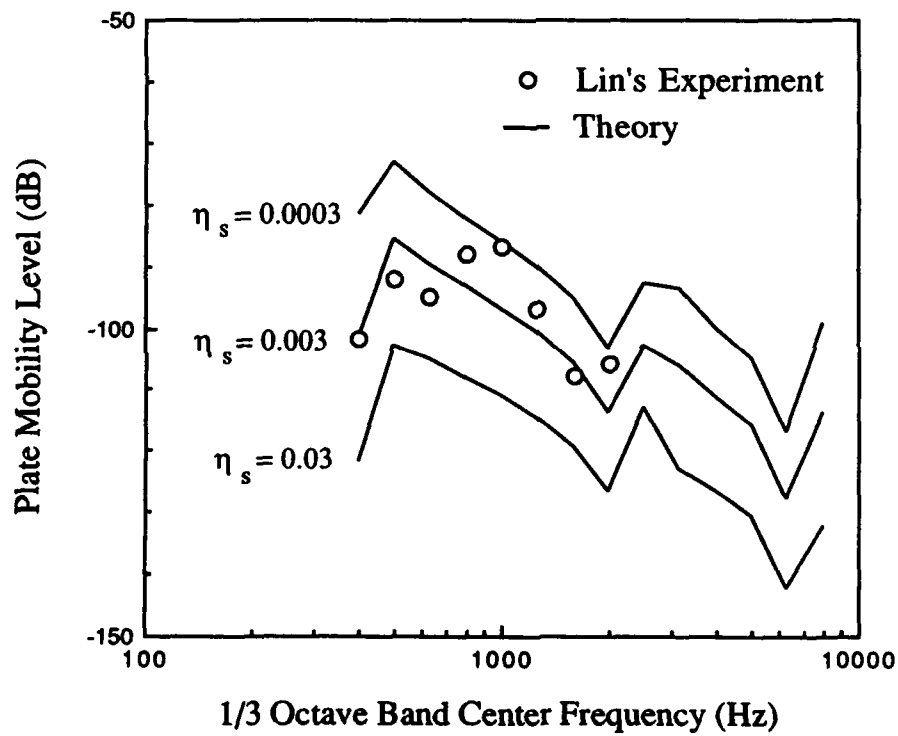


Figure 5.12 Comparison between theory and experiment [17] for example case III with a finite shaft. Here plate mobility level in dB is $10\log_{10}\langle V_c^2 \rangle$ re $\langle V_c^2 \rangle = 1.0(\text{m/s})^2$ for $F_{ysa} = 1.0\text{N}$.

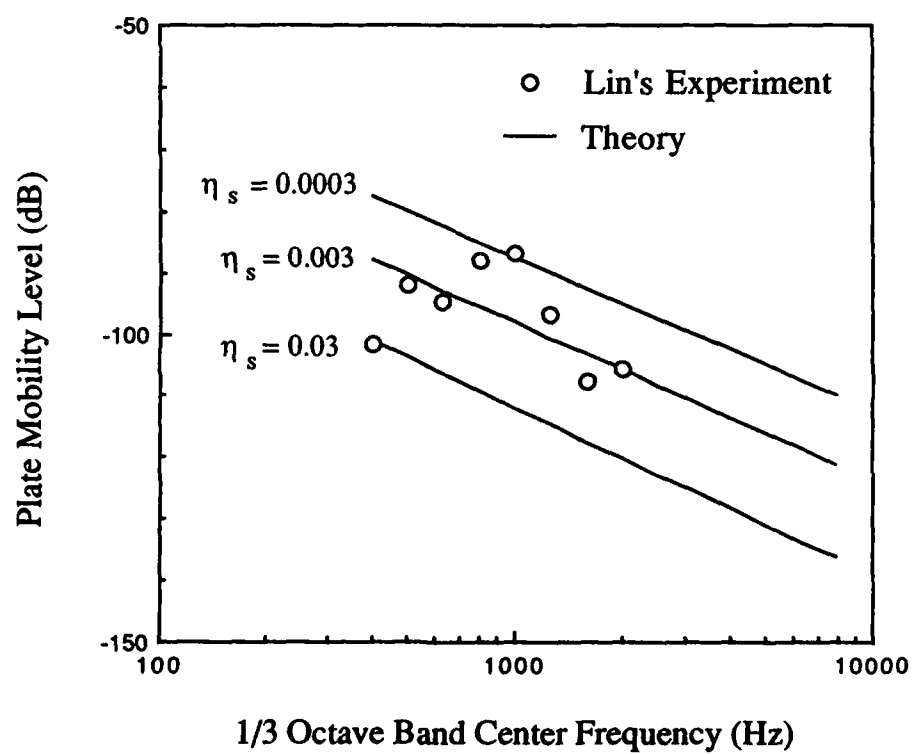


Figure 5.13 Comparison between theory and experiment [17] for example case III. Here theory considers a semi-infinite shaft.

(5.8) for η_{sc} , the mobility levels are computed and are found to be given by straight lines as shown in Figure 5.13. These lines represent the asymptotic behavior of the system when the shaft is very long i.e. $L_s \rightarrow \infty$. Also, note that Figure 5.13 is consistent with the trends reported by Lyon and Eichler [58] for the plate-cantilevered beam problem. Again, most experimental data are bounded within the range given by $\eta_s = 0.0003$ to 0.03 .

Consider the finite shaft length $L_s = 1.32$ m of high modal density n_s . In Figure 5.14 η_{sc} is compared for a finite shaft and semi-infinite shaft. It can be seen that the result for the semi-infinite shaft follows the average values of the finite shaft.

Next, the effect of bearing preload or stiffness coefficients on the mean-square velocity response of the plate-mount system is evaluated. Equation (5.20) is used to predict the curves shown in Figure 5.15 while keeping other system parameters the same. The bearing coefficients used in this analysis are from Tables 3.3 and 3.4. Three bearing preloads used here are 115N, 190N and 285N which are referred to as low, medium and high preloads. We observe minor changes with preload except in the vicinity of 4 kHz.

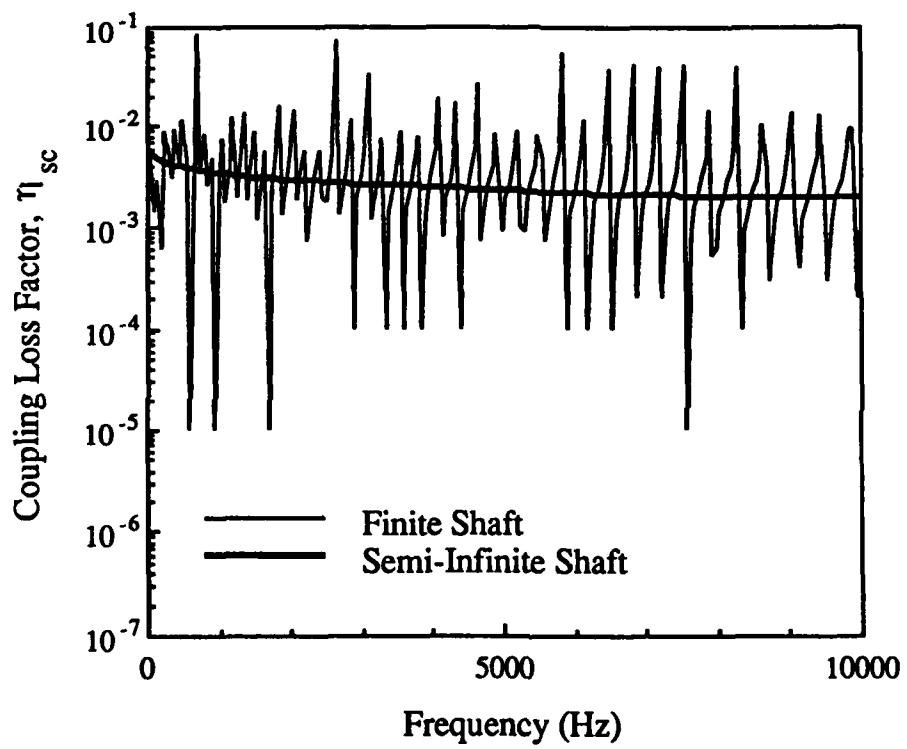


Figure 5.14 Predicted coupling loss factors η_{sc} for a semi-infinite and a finite shaft in example case III.

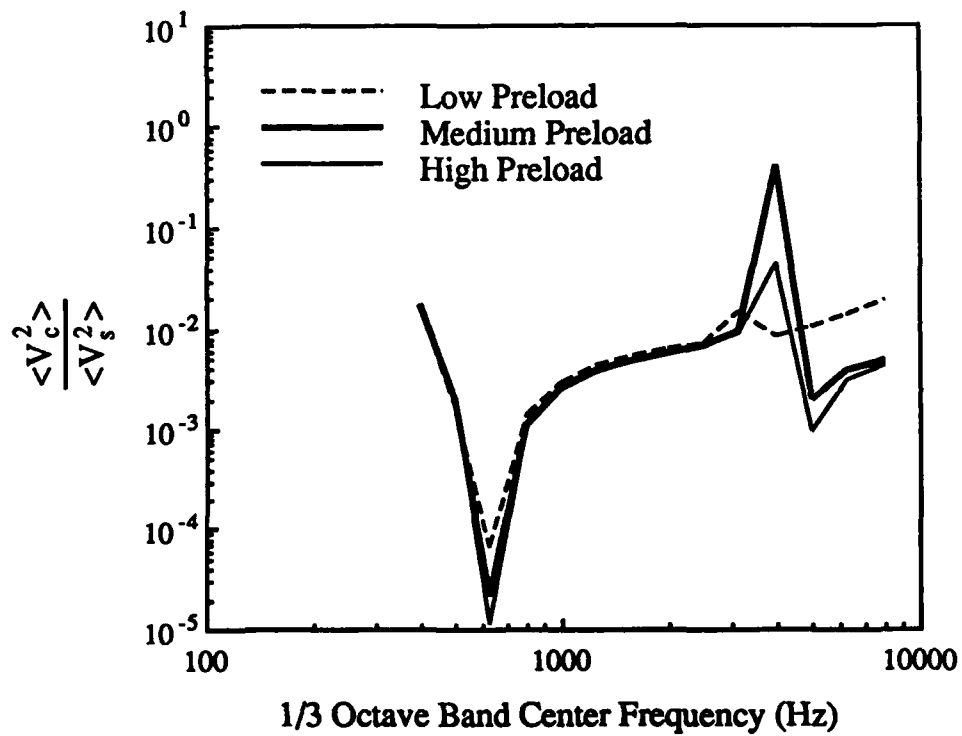


Figure 5.15 Effect of bearing preload on the normalized casing plate response (example case III).

5.7 EXAMPLE CASE IV: A GEARED ROTOR SYSTEM

5.7.1 Assumptions

As the final case, we investigate a generic geared rotor system with 4 bearings as shown in Figure 5.16a. This system is not only a natural extension to example III, it can also be treated as an approximate model of the NASA gear test facility in Figure 5.2; for gearbox details, refer to Chapter IV. The intent of the SEA analysis is to predict asymptotic casing plate response and radiated sound pressure from the gearbox, on an order of magnitude basis. Accordingly, the following assumptions are made:

1. Consider the case of 4 identical rolling element bearings and 2 identical shafts carrying gears.
2. The vibratory source associated with the static transmission error excitation is at the gear mesh. The net exchange of energy through the gear mesh coupling is neglected and the vibratory energy is assumed to flow outward from the gear mesh source to the casing through shafts and bearings. The source is assumed to be far away from the bearings.
3. Only shaft bending vibration is coupled to the casing plate flexural motion. Torsional modes are not included since they are relatively low in number compared to the shaft bending modes. In steady-state, both shafts have equal amount of vibratory energy (E_s) associated with their bending motions which are uncoupled from the external motor and load.
4. The portion of torsional vibratory energy which is transmitted to the load is incorporated in the dissipation loss factor (η_s) of the shaft-bearing subsystem. Here η_s is assumed to be given by $\eta_s = \gamma \eta_c \neq \eta_s(\omega)$ where $\eta_c \neq \eta_c(\omega)$ is the loss

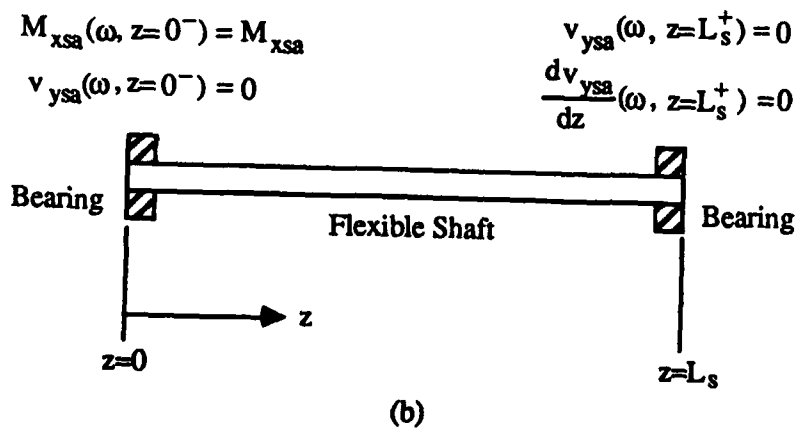
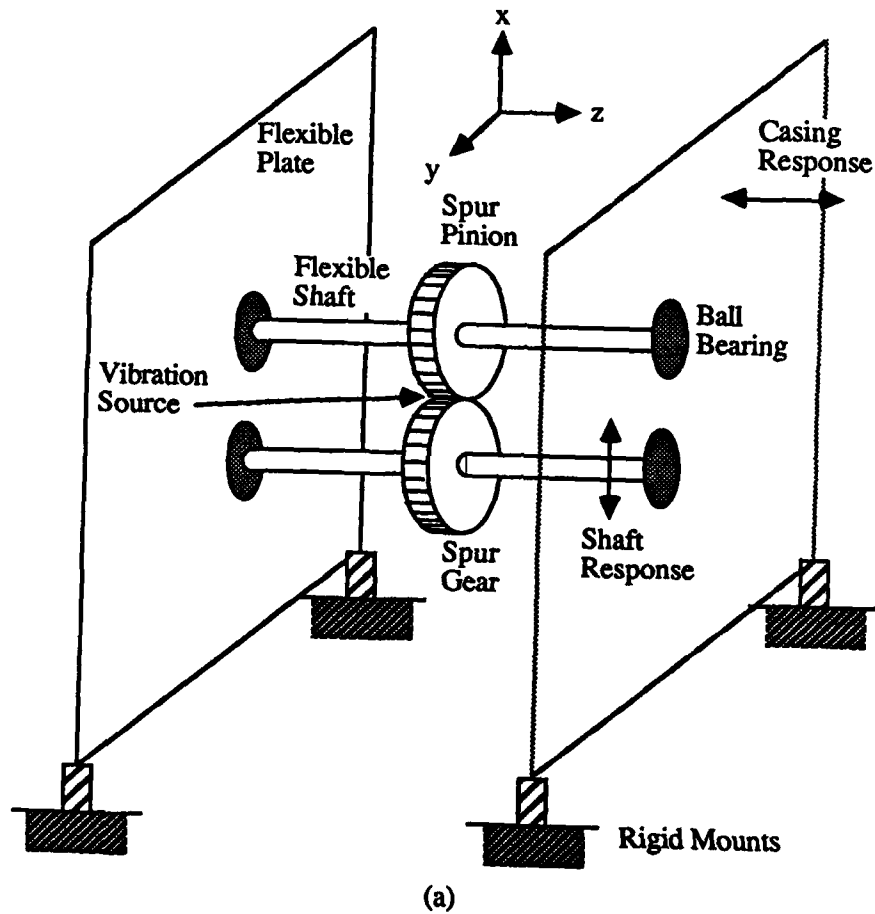


Figure 5.16 Example case IV: (a) a generic geared rotor system with casing and mounts and (b) boundary conditions for a finite shaft-bearing system.

factor of the casing; γ is expected to be higher than one due to additional losses at the bearings and load.

5. Bearing dimensions are assumed to be much smaller than the wavelength on the casing plate. Also, bearings are not expected to be exchanging vibratory energy.
6. Modal densities of shaft n_s and casing plate n_c are given by equation (5.1).
7. A diffuse vibration field is assumed for the external casing-mount system. The energy dissipation mechanism for this system includes acoustic energy radiated from the plate in addition to the structural damping.

Application of the SEA principle will result in 2 subsystems, one internal consisting of 2 shafts and 4 bearings and one external consisting of 2 casing plates and mounts similar to Figure 5.10b. The internal subsystem in this case can store the total vibratory energy of 2 shafts. Vibratory energy transfer as viewed through Figure 5.10b represents the algebraic sum of the energy transfers through 4 bearings.

5.7.2 Coupling Loss Factor

The coupling loss factor η_{sc} between the internal (shafts-bearings) and external (casing) systems is derived, based on the formulation given by equations (5.11) and (5.12). This implies that vibratory energy transfer is associated with only the dynamic moment at the bearing, and the casing plate is infinite with respect to the bearing dimensions. The driving point impedance of the shaft Z_s is derived next given the boundary conditions shown in Figure 5.16b. At the left bearing end ($z=0^-$), $v_{ysa}(\omega, z=0^-)=0$, and $M_{xsa}(\omega, z=0^-)=M_{xsa}$ which are equivalent to $M_{xsa}(\omega, z=0^+)=M_{xsa}$.

and $F_{ysa}(\omega, 0^+) = (k_{by\theta_x}/k_{b\theta_x\theta_x})M_{xsa} + v_{ysa}(\omega, 0^+) \{ (k_{by\theta_x}/k_{b\theta_x\theta_x})^2 k_{b\theta_x\theta_x} - k_{byy} \} / (i\omega)$.

The other bearing end at $z=L_s^+$ with zero translational and angular velocities is described at $z=L_s^-$ as

$$\begin{aligned} M_{xsa}(\omega, z=L_s^-) &= - \left(k_{b\theta_x\theta_x} \frac{dv_{ysa}}{dz}(\omega, L_s^-) + k_{by\theta_x} v_{ysa}(\omega, L_s^-) \right) / (i\omega) ; \\ F_{ysa}(\omega, z=L_s^-) &= - \left(k_{by\theta_x} \frac{dv_{ysa}}{dz}(\omega, L_s^-) + k_{byy} v_{ysa}(\omega, L_s^-) \right) / (i\omega) \end{aligned} \quad (5.21)$$

Using equations (5.5) and (5.13), the above boundary conditions are evaluated to formulate an algebraic problem of the type given by equation (5.14). The nonzero elements of the coefficient matrix [B] are

$$\begin{aligned} B_{11} &= \frac{1}{\omega} \left(EIk_s^3 - ik_{byy} + \frac{ik_{by\theta_x}^2}{k_{b\theta_x\theta_x}} \right) ; \quad B_{12} = \frac{1}{\omega} \left(-EIk_s^3 - ik_{byy} + \frac{ik_{by\theta_x}^2}{k_{b\theta_x\theta_x}} \right) ; \\ B_{13} &= \frac{i}{\omega} \left(EIk_s^3 - k_{byy} + \frac{k_{by\theta_x}^2}{k_{b\theta_x\theta_x}} \right) ; \quad B_{14} = \frac{i}{\omega} \left(-EIk_s^3 - k_{byy} + \frac{k_{by\theta_x}^2}{k_{b\theta_x\theta_x}} \right) ; \end{aligned}$$

$$B_{21}=B_{22}=-B_{23}=-B_{24}=1 ;$$

$$B_{31} = (-jk_s k_{b\theta_x\theta_x} + k_{by\theta_x} + EIk_s^2) e^{-ik_s L_s} ;$$

$$B_{32} = (jk_s k_{b\theta_x\theta_x} + k_{by\theta_x} + EIk_s^2) e^{ik_s L_s} ;$$

$$B_{33} = (-k_s k_{b\theta_x\theta_x} + k_{by\theta_x} - EIk_s^2) e^{-k_s L_s} ;$$

$$B_{34} = (k_s k_{b\theta_x\theta_x} + k_{by\theta_x} - EIk_s^2) e^{k_s L_s} ;$$

$$B_{41} = (ik_s k_{by\theta_x} - k_{byy} - iEIk_s^3) e^{-ik_s L_s} ;$$

$$\begin{aligned}
B_{42} &= (-ik_s k_{by\theta_x} - k_{byy} + iElk_s^3) e^{ik_s L_s} ; \\
B_{43} &= (k_s k_{by\theta_x} - k_{byy} + Elk_s^3) e^{-k_s L_s} ; \\
B_{44} &= (-k_s k_{by\theta_x} - k_{byy} - Elk_s^3) e^{k_s L_s}
\end{aligned} \tag{5.22}$$

The right hand side vector $\{b\}$ of equation (5.14) is $M_{ysa} \{k_{by\theta_x}/k_{b\theta_x\theta_x}, i\omega/(Elk_s^2), 0, 0\}^T$, and the shaft impedance Z_s is evaluated numerically using equation (5.8).

5.7.3 Vibroacoustic Response

Consider the total energy dissipation by the casing as the sum of the energy terms associated with structural damping dissipation and energy escape via sound radiation. Hence the total dissipation loss factor η_{cT} for the casing of area A_c and mass m_c is

$$\eta_{cT}(\omega) = \eta_c + \frac{z_0 A_c \sigma_c(\omega)}{\omega m_c} \tag{5.23}$$

where z_0 is the characteristic impedance of the surrounding medium, and σ_c is the radiation efficiency of the casing. In this analysis, two radiation efficiency models are used: (i) $\sigma_{c1} = 1.0$ for an ideal radiator as for many gearboxes the measured radiation efficiency has been found to be close to unity [78], and (ii) σ_{c2} for a simply-supported rectangular plate [79]. Several investigators have used σ_{c2} successfully in SEA applications [60,66,67].

Since this SEA model is very similar to the one developed for example case III, solutions given by equations (5.19) and (5.20) are still valid here provided the existence of multiple paths, as opposed to only one path in example case III, is recognized. The mean-square velocity levels of the shafts-bearings system $\langle V_s^2 \rangle$ and casing-mount system $\langle V_c^2 \rangle$ are

$$\begin{aligned} \langle V_s^2 \rangle(\omega) &= \frac{\Pi_s (\eta_{cT} + 4\eta_{cs})}{m_s \omega (\eta_s \eta_{cT} + 4\eta_{cT} \eta_{sc} + 4\eta_s \eta_{cs})} ; \\ \langle V_c^2 \rangle(\omega) &= \frac{4\Pi_s \eta_{sc}}{m_c \omega (\eta_s \eta_{cT} + 4\eta_{cT} \eta_{sc} + 4\eta_s \eta_{cs})} \end{aligned} \quad (5.24)$$

Power injected into the system is developed by examining the internal static transmission error excitation $e(t) = e_h(\omega)e^{i\omega t}$. For the spur gear pair, the gear mesh frequency $\omega(\text{rad/sec}) = N_g \Omega_{zM} \pi / 30$ where N_g is the number of gear teeth and $\Omega_{zM}(\text{rpm})$ is the driven shaft speed. By definition, the input power by the gear mesh elastic force $F_h(t) = k_h e(t) = e_h(\omega)e^{i\omega t}$ is given by $\Pi_s(\omega) = 1/2 (k_h e_h)^2 \text{Re}\{(1/Z_s(\omega))^*\}$. At a very high frequency, it is reasonable to assume that the boundaries of the shafts do not affect the gear mesh source regime. Hence the infinite shaft assumption should hold. Accordingly, Z_s can be obtained analytically using the driving point shaft impedance given in Reference [77]; however, the gear mass m_g must be included.

$$Z_s(\omega) = 2\rho_s A_s c_s (1 + i) + i\omega m_g \quad (5.25)$$

Sound power W radiated from the casing is computed using the following equation where A_c is the total casing surface area

$$W(\omega) = z_o A_c \langle V_c^2(\omega) \rangle \sigma_c(\omega) \quad (5.26)$$

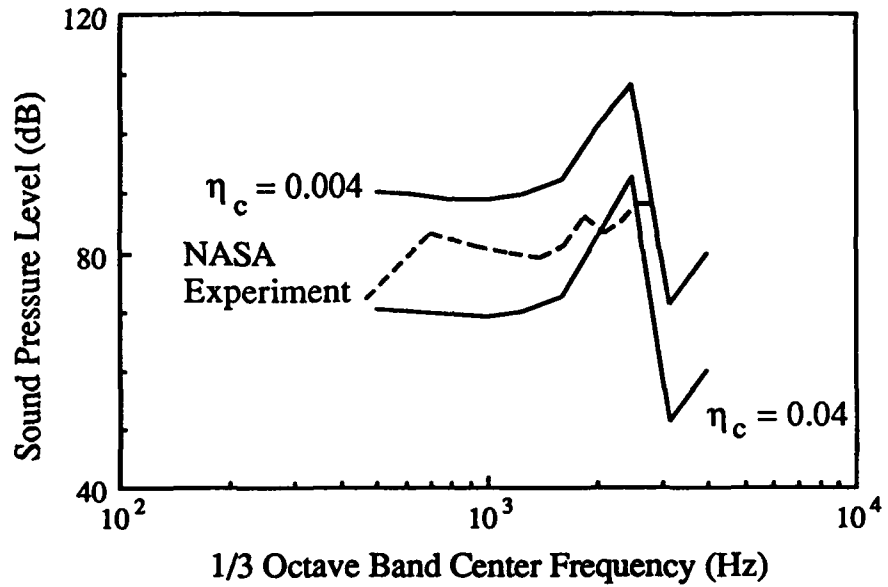
Assuming a source directivity $Q(\omega)$ associated with geared system mounting condition, the sound pressure level L_p (dB re 20 μ Pa) in the far field at distance r from the casing is

$$L_p(\omega) = L_W(\omega) + 10 \log_{10} \left(\frac{Q(\omega)}{4\pi r^2} + \frac{4}{R(\omega)} \right) \quad (5.27)$$

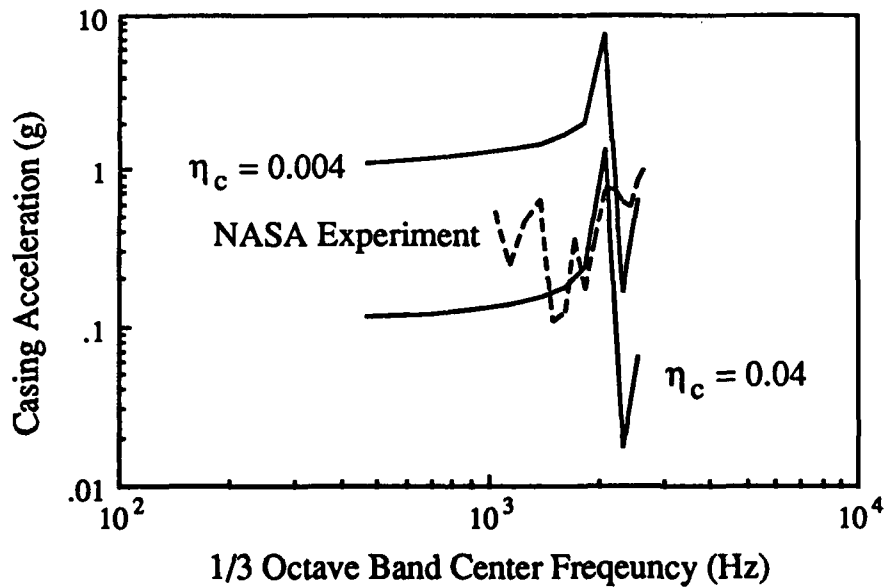
where $R(\omega) = \bar{\alpha} S / (1 - \bar{\alpha})$ is the room constant, $\bar{\alpha}(\omega)$ is the average absorption coefficient, S is the room surface area and L_W (dB re 1.0pW) is the sound power level.

5.7.4 Experimental Validation and Parametric Studies

The SEA formulation for this example case is verified by comparing results with vibroacoustic responses measured on the NASA gearbox [55]. A detail description of the experimental setup and its system parameters have been given in Chapter IV. Additionally unweighted L_p at $r \approx 0.38$ m, directly above the surface of the top cover casing plate as shown in Figure 5.2, has been measured with a B&K type 2230 sound level meter. Predicted and measured L_p are compared in Figure 5.17a for $\gamma=10$, $\sigma_c=\sigma_{c2}$ and bearing preload $\delta_{zm}=0.04$ mm. The second term in equation (5.27) is dominated by $Q/(4\pi r^2)$ since $4/R \ll Q/(4\pi r^2)$ in this case due to $\bar{\alpha} \approx 1.0$ and room surface area S being very large. Predictions are found to be within ± 10 dB of the measured values for typical structural dissipation loss factor $0.004 \leq \eta_c \leq 0.04$. Figure 5.17b shows the comparison of spatially averaged mean-square casing acceleration level ($\omega^2 \langle V_c^2 \rangle$) between theory and experiment. Experimental curve represents the averaged value of the measurements made at 3 casing plate locations (top plate, side plate with



(a)



(b)

Figure 5.17 Comparison between theory and NASA experiment [55] for example case IV ($\gamma=10$, $Q=2$, $\sigma_c=\sigma_{c2}$, $\delta_{zm}=0.04\text{mm}$). (a) Sound pressure level L_p . (b) Spatially averaged casing acceleration.

bearings and side plate without bearings). Again, predicted acceleration spectra, which are similar to that found for the sound level, are found to be in reasonable agreement with the measured spectrum given the appropriate values of η_c and γ . In general, we observe that the response level decreases with increasing η_c . Also, comparisons suggest that η_c in this system may be frequency dependent.

Next we vary γ but keep $\eta_c=0.02$ constant in Figure 5.18. Comparison between theory and measurements also indicates that $\gamma=10$ is the best fit for the experimental data especially at the higher frequencies. Here, radiation efficiency σ_{c1} and bearing axial preload $\delta_{zm}=0.04\text{mm}$ have been specified.

Now we investigate the effects of casing plate radiation efficiency σ_c and bearing preload or mean axial displacement δ_{zm} on L_p . Figure 5.19 compares σ_{c1} and σ_{c2} . Based on the comparison with experiment it seems that the radiation efficiency of the NASA gearbox is better modeled with σ_{c1} although the measured L_p curve is mostly between σ_{c1} and σ_{c2} curves. Differences between σ_{c1} and σ_{c2} are significant at lower frequencies, but the variation never exceeds 10dB over the entire frequency range of interest. It may be noted that since the acoustic energy radiated $W(\omega)$ is significantly smaller than the energy dissipated by the system, virtually no change is found in the predicted casing acceleration spectra by varying σ_c . The effect of bearing preload on L_p is shown in Figures 5.20a and 5.20b for σ_{c2} and σ_{c1} respectively. Figure 5.20 indicates that L_p is lower when the bearing preload is increased. A similar effect is seen for the casing acceleration level which is consistent with the deterministic model prediction of Chapter IV.

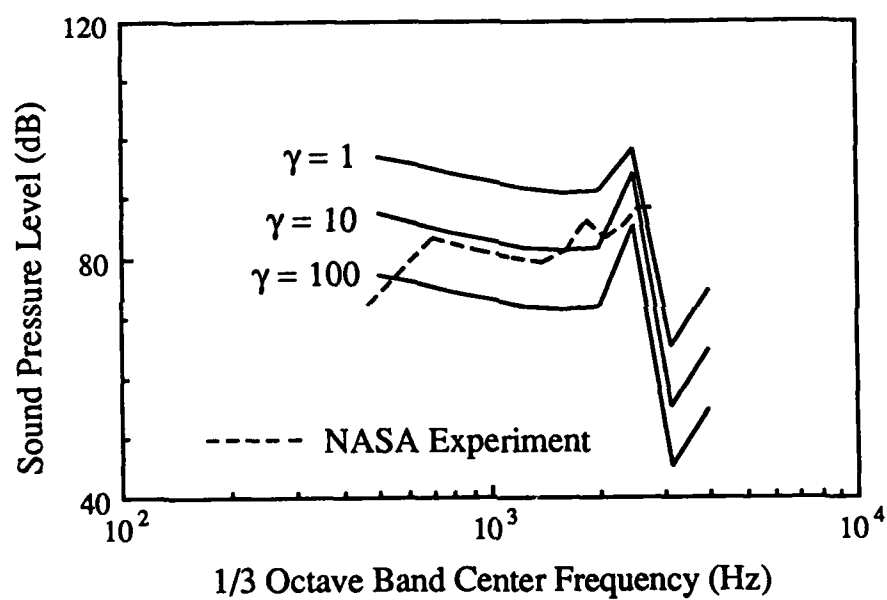


Figure 5.18 Effect of $\gamma = \eta_s / \eta_c$ on predicted L_p for example case IV ($\eta_c = 0.02$, $Q = 2$, $\sigma_c = \sigma_{c1}$, $\delta_{zm} = 0.04 \text{ mm}$).

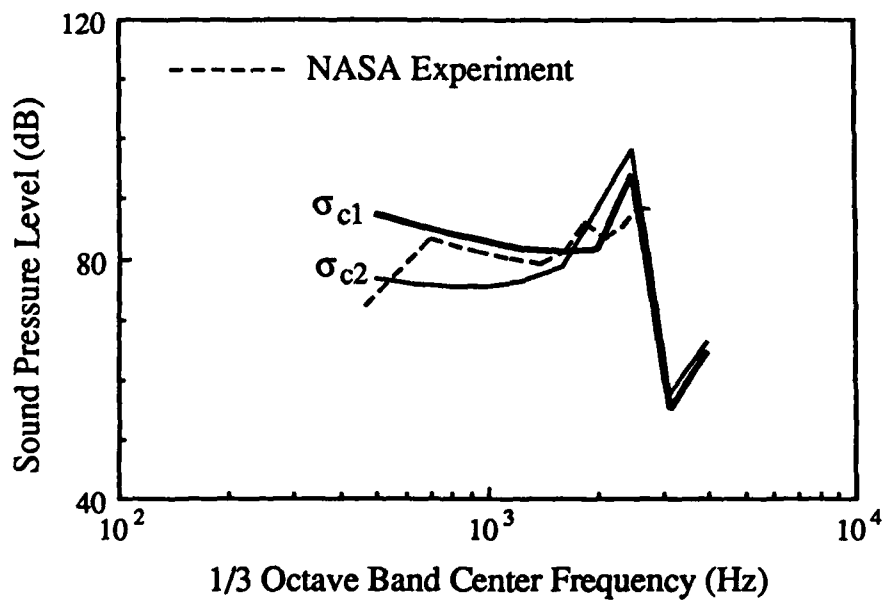


Figure 5.19 Sound pressure level prediction with two σ_c formulations for example case IV: $\sigma_{c1} = 1.0$ (ideal radiator) and σ_{c2} for simply-supported plate ($\gamma=10$, $Q=2$, $\eta_c=0.02$, $\delta_{zm}=0.04\text{mm}$).

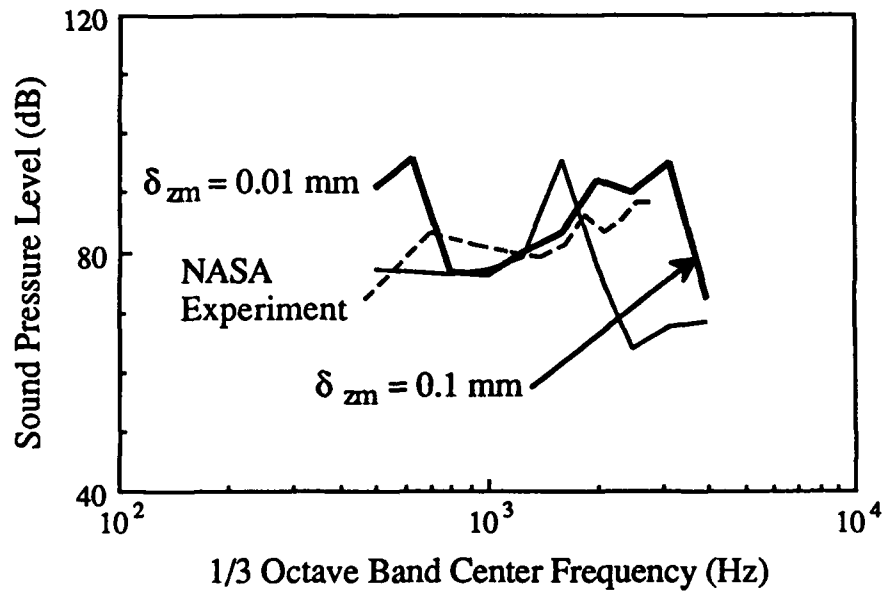
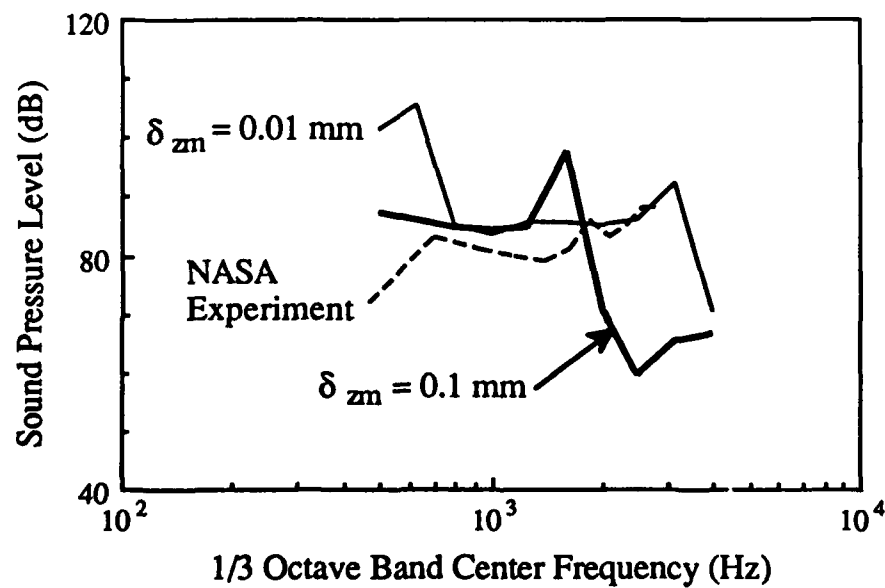
(a) $\sigma_c = \sigma_{c2}$ (b) $\sigma_c = \sigma_{c1}$

Figure 5.20 Effect of bearing axial preload δ_{zm} on L_p for example case IV ($\eta_c = 0.02$, $Q = 2$, $\gamma = 10$).

5.8 CONCLUDING REMARKS

The vibration transmission through bearing has been analyzed using the SEA technique. A new procedure has been developed to compute the coupling loss factor which relies on the solution of the boundary value problem at the bearing-casing interface. This scheme incorporates the bearing stiffness matrix developed earlier as a part of the deterministic vibration models in Chapters II-IV. Experimental validations verify the proposed theory even though a very simple model for the geared rotor system has been presented. A more detailed SEA model including energy sharing between subsystems is required to analyze this system. This is left for future research.

CHAPTER VI

CONCLUSIONS AND RECOMMENDATIONS

6.1 SUMMARY

A new precision rolling element bearing model is proposed for the analyses of the vibration transmission through bearings and overall system dynamics in rotating mechanical equipment including geared rotor systems. Current bearing models, based on either ideal boundary conditions or purely translational stiffness element description, can not explain how the vibratory motion may be transmitted from the rotating shaft to the casing and other connecting structures in rotating mechanical equipment. For example, a vibration model of a rotating system based upon the existing bearing models can only predict purely in-plane type motion on the flexible casing plate given only the bending motion on the shaft. However, experimental results have shown that the casing plate motion is primarily flexural or out-of-plane type. Chapter II clarifies this issue qualitatively and quantitatively by developing a new mathematical model for the precision rolling element bearings from basic principles. A comprehensive bearing stiffness matrix $[K]_{bm}$ of dimension 6 is proposed which clearly demonstrates a coupling between the shaft bending motion and the flexural motion on the casing plate. A numerical scheme which involves a solution to nonlinear algebraic equations is proposed for the estimation of the stiffness coefficients given the mean bearing load vector. And, a second method which requires the direct evaluation of these stiffness

coefficients given the mean bearing displacement vector is also discussed. Some of the translational stiffness coefficients of the proposed bearing matrix have been verified using available analytical and experimental data. Further validation of $[K]_{bm}$ is not possible as coupling coefficients are never measured. Also, parametric studies on the effect of unloaded contact angle, preload, or bearing type are included. These results lead to a complete characterization of the bearing stiffness matrix.

Chapter III extends the proposed bearing stiffness formulation and demonstrates its superiority over existing models in vibration transmission analyses for a generic single shaft-bearing-plate-mount system. The bearing stiffness matrix $[K]_{bm}$ is incorporated in discrete system models using lumped parameter and finite element modeling techniques. Shaft, plate and mount flexibilities are also included in such models. The stability issue associated with the proposed bearing model is addressed analytically using Liapunov's stability method and the system is found to be dynamically stable provided the preloads are sufficiently high. Eigensolution and forced harmonic response to the following rolling element bearing system example cases are obtained using our formulation and results are compared with the predictions yielded by the current vibration models: I. rigid shaft and plate system freely suspended, II. rigid shaft and plate supported on flexible mounts, and III. an experimental setup consisting of a flexible shaft, two ball bearings, a rectangular plate and the supporting structure. Analytical results indicate that our proposed model is indeed capable of predicting plate rigid body angular motion or plate flexural motion as excited by shaft motion. Such predictions are not observed in simple vibration models. Also, lower degrees of freedom models, developed by several previous investigators tend to underestimate the resonant frequencies and force or moment transmissibilities as compared with our multi-

degree of freedom models. Comparisons between our model and the available experiments have been found to be reasonably good.

The overall dynamics of a geared rotor system which includes a spur gear pair, shafts, rolling element bearings, prime mover and load (attached to the geared rotor system through flexible torsional couplings), rigid or flexible casing, and compliant or massive mounts is studied in Chapter IV. Linear time-invariant, discrete dynamic models of a generic geared rotor system with proportional viscous damping are developed using lumped parameter and dynamic finite element techniques which are then used to predict the vibration transmissibility through bearings and mounts, casing vibration motion, and dynamic response of the internal rotating system. The proposed bearing formulation is also included. Each rotating shaft is modeled as an Euler beam in the lumped parameter model and as a Timoshenko beam in the dynamic finite element model, but the gyroscopic moment is not included. Eigensolution and forced harmonic response studies due to rotating mass unbalance or kinematic transmission error excitation for the following example cases are obtained using our formulation and compared with simple models currently available in the literature and/or experiment: I. a single-stage rotor system with flexibly mounted rigid casing consisting of two bearings as a special case of the geared rotor system, II. a spur gear pair drive supported by four bearings installed in a flexibly mounted rigid casing, and III. an experimental setup consisting of high precision gear and pinion, and four identical rolling element bearings contained in a flexible casing mounted rigidly on a massive foundation. In example cases II and III of Chapter IV, the gear mesh stiffness is assumed to be linear and time-invariant. Analytical predictions show that our theory is indeed capable of predicting bearing and mount moment transmissibilities in addition to the force transmissibilities.

Also, flexural vibrations of the casing plate are predicted well as our theory is in good agreement with measurements made on case III of Chapter IV; such predictions are not seen in simple models.

In Chapters II-IV, the deterministic vibration models of geared rotor system with proposed bearing stiffness matrix incorporated have been shown to be reliable up to moderately high frequencies. But these models are inadequate at very high frequencies when the modal density is high. Classical vibration models usually do not predict modes accurately in this frequency regime, require large computational effort and produce spectra at many spatial points which are difficult to interpret. Accordingly, we have used the statistical energy analysis (SEA) method to predict the mean-square vibratory response of internal and external subsystems in a geared rotor system. The feasibility of applying SEA to this system is also investigated by performing modal analysis of a gearbox. Four example cases are analyzed using SEA: I. a plate-cantilevered rectangular beam, II. case I with circular shaft-bearing system replacing the cantilevered rectangular beam, III. a circular shaft-bearing-plate-mount system, and IV a simple geared rotor system. In the first two example cases, we have revised and extended Lyon and Eichler's plate-cantilevered rectangular beam problem [56,58] to improve the coupling loss factor prediction and to formulate the vibratory energy transfer problem through rolling element bearings. The third and final example cases compute the system response spectra and compare them with measurements. Good agreement is found between theory and experiment provided proper values of the dissipation loss factors and bearing preloads are used. The NASA gearbox radiation efficiency is found to be nearly unity at higher frequencies.

6.2 FUTURE RESEARCH

Several areas of potential research problems based on the present study of the vibration transmission through bearings, are identified as follows:

1. Analyze vibration transmission through hydrodynamic bearings, using the proposed work on rolling element bearings. Develop an experimental methodology to estimate the bearing stiffness matrix and transfer properties. Also, develop bearing diagnostic techniques using vibration transmission theory proposed in this dissertation.
2. Extend the proposed overall geared rotor system vibration model with spur gears to helical, bevel and worm gear drives. Develop vibration models using the proposed bearing model to analyze multiple transmission paths. Improve gear diagnostic procedures using analytical bearing transfer properties.
3. Refine the current statistical energy analysis formulation of a generic geared rotor system to investigate the vibratory energy transfer among smaller subsystems and to include the effects of rotating shaft torsional modes. Generate analytical and experimental schemes to predict coupling loss factors for typical shaft-bearing-plate system. Finally, establish gearbox design methodology for reduced airborne and structure-borne noise.

LIST OF REFERENCES

1. R.H. BADGLEY and R.M. HARTMAN 1974 *Journal of Engineering for Industry, Transaction of the American Society of Mechanical Engineers* 96(2), 567-577. Gearbox noise reduction: prediction and measurement of mesh-frequency vibrations within an operating helicopter rotor-drive gearbox.
2. R.H. BADGLEY and I. LASKIN 1970 *USAAVLABS Technical Report* 70-12. Program for helicopter gearbox noise prediction and reduction.
3. R.H. BADGLEY and T. CHIANG 1972 *USAAMRDL Technical Report* 72-6. Investigation of gearbox design modifications for reducing helicopter gearbox noise.
4. M.A. BOWES and A. BERMAN 1977 *Institute of Environmental Sciences*, 334-338. Prediction of vibration and noise of a transmission using a dynamic model partially derived from test data.
5. D. R. HOUSER 1989 *Gear Noise Short Course Notes, The Ohio State University*.
6. T.C. LIM and R. SINGH 1989 *NASA Contractor Report* 185148 or *AVSCOM Technical Memorandum* 89-C-009. A review of gear housing dynamics and acoustics literature.
7. R.J. DRAGO 1980 *Machine Design* 52(27), 114-115. New approach for analyzing transmission noise.
8. L. BATTEZZATO and S. TURRA 1984 AGARD Conference, Lisbon. Possible technological answers to new design requirements for power transmission systems.

9. K. ISHIDA, T. MATSUDA and M. FUKUI 1981 *Proceedings of the International Symposium on Gearing and Power Transmissions, Tokyo*, 13-18. Effect of gear box on noise reduction of geared device.
10. H. N. OZGUVEN 1984 *Journal of Vibration, Acoustics, Stress, and Reliability in Design, Transaction of the American Society of Mechanical Engineers* 106, 59-61. On the critical speed of continuous shaft-disk systems.
11. A. D. DIMAROGONAS and S. A. PAIPETIS 1983 *Analytical Methods in Rotor Dynamics*. London: Applied Science.
12. J. S. RAO 1983 *Rotor Dynamics*. New York: John Wiley.
13. E. S. ZORZI and H. D. NELSON 1977 *Journal of Engineering for Power, Transaction of the American Society of Mechanical Engineers* 99(1), 71-77. Finite element simulation of rotor-bearing systems with internal damping.
14. E. P. GARGIULO 1980 *Machine Design* 52, 107-110. A simple way to estimate bearing stiffness.
15. A. KAHRAMAN, H. N. OZGUVEN, D. R. HOUSER and J. J. ZAKRAJSEK 1989 *Proceedings of the International Power Transmission and Gearing Conference, Chicago*, 375-382. Dynamic analysis of geared rotors by finite elements.
16. A. M. MITCHELL, F. B. OSWALD and H. H. COE 1986 *NASA Technical Report* 2626. Testing of UH-60A Helicopter Transmission in NASA Lewis 2240kW(3000-hp) Facility.
17. J. S. LIN 1989 *M. S. Thesis, The Ohio State University*. Experimental analysis of dynamic force transmissibility through bearings.
18. T. A. HARRIS 1966 *Rolling Bearing Analysis*. New York: John Wiley.
19. A. PALMGREN 1959 *Ball and Roller Bearing Engineering*. Philadelphia: S. H. Burbank.

20. M.F. WHITE 1979 *Journal of Applied Mechanics* 46, 677-684. Rolling element bearing vibration transfer characteristics: effect of stiffness.
21. M. D. RAJAB 1982 *Ph.D. Dissertation, The Ohio State University*. Modeling of the transmissibility through rolling element bearing under radial and moment loads.
22. D. R. HOUSER, G. L. KINZEL, W. B. YOUNG and M. D. RAJAB 1989 *Proceedings of the Seventh International Modal Analysis Conference, Las Vegas*, 147-153. Force transmissibility through rolling contact bearings.
23. W. B. YOUNG 1988 *M.S. Thesis, The Ohio State University*. Dynamic modeling and experimental measurements of a gear shaft and housing system.
24. J. KRAUS, J. J. BLECH and S. G. BRAUN 1987 *Journal of Vibration, Acoustics, Stress, and Reliability in Design, Transaction of the American Society of Mechanical Engineers* 109, 235-240. In situ determination of rolling bearing stiffness and damping by modal analysis.
25. S.V. NERIYA and T.S. SANKAR 1984 *The Shock and Vibration Bulletin* 54(3), 67-75. Effect of coupled torsional-flexural vibration of a geared shaft system on dynamic tooth load.
26. S.V. NERIYA and T.S. SANKAR 1985 *The Shock and Vibration Bulletin* 55(3), 13-25. Coupled torsional-flexural vibration of a geared shaft system using finite element method.
27. H. IIDA, A. TAMURA and H. YAMAMOTO 1986 *Bullentin of the Japanese Society of Mechanical Engineers* 29, 1811-1916. Dynamic characteristics of a gear train system with softly supported shafts.
28. N. IWATSUBO, S. ARII and R. KAWAI 1984 *Bullentin of the Japanese Society of Mechanical Engineers* 27, 271-277. Coupled lateral-torsional vibrations of rotor system trained by gears (1. Analysis by transfer matrix method).

29. H.N. OZGUVEN and D.R. HOUSER 1988 *Journal of Sound and Vibration* 121(3), 383-411. Mathematical models used in gear dynamics - a review.
30. T. L. H. WALFORD and B. J. STONE 1980 *Journal of Mechanical Engineering Science* 22(4), 175-181. The measurement of the radial stiffness of rolling element bearings under oscillation conditions.
31. P. ESCHMANN, L. HASBARGEN and K. WEIGAND 1985 *Ball and Roller Bearings*. New York: John Wiley.
32. B. J. HAMROCK and W. J. ANDERSON 1983 *NASA Reference Publication* 1105. Rolling-element bearings.
33. P. K. GUPTA 1984 *Advanced Dynamics of Rolling Elements*. Berlin: Springer-Verlag.
34. A. B. JONES 1946 *New Departure Engineering Data, General Motors*. Analysis of stresses and deflections.
35. R. R. DAVIS 1988 *Proceedings of the Second International Symposium on Transport Phenomena, Dynamics and Design of Rotating Machinery, Honolulu*, 241-254. Incorporating general race and housing flexibility and deadband in rolling element bearing analysis.
36. W. H. PRESS, B. P. FLANNERY, S. A. TEUKOLSKY and W. T. VETTERLING 1986 *Numerical Recipes*. Cambridge: Cambridge University Press.
37. J. ORTEGA and W. RHEINBOLDT 1970 *Iterative Solution of Nonlinear Equations in Several Variables*. New York: Academic Press.
38. STRUCTURAL DYNAMICS RESEARCH CORPORATION 1986 *SYSTAN User's Guide*. Milford, Ohio: Structural Dynamics Research Corporation.
39. G. J. DESALVO AND J. A. SWANSON 1983 *ANSYS User's Manual*. Houston, Pennsylvania: Swanson Analysis System.

40. W. T. THOMPSON 1981 *Theory of Vibration with Applications*. New Jersey: Prentice-Hall.
41. W. D. PILKEY and P. Y. CHANG 1978 *Modern Formulas for Statics and Dynamics*. New York: McGraw Hill.
42. L. MEIROVITCH 1980 *Computational Methods in Structural Dynamics*. Alphen aan den Rijn: Sijthoff & Noordhoff.
43. S. TIMOSHENKO, D. H. YOUNG and W. WEAVER, Jr. 1974 *Vibration Problems in Engineering*. New York: John Wiley.
44. D. J. INMAN 1989 *Vibration with Control, Measurement, and Stability*. New Jersey: Prentice Hall.
45. L. MEIROVITCH 1970 *Methods of Analytical Dynamics*. New York: McGraw Hill.
46. A. KAHRAMAN 1989 *PhD Dissertation Research, The Ohio State University*.
47. M.S. TAVAKOLI and D.R. HOUSER 1985 *Journal of Mechanisms, Transmissions, and Automation in Design, Transaction of the American Society of Mechanical Engineers* 108, 86-95. Optimum profile modifications for minimization of static transmission errors of spur gears.
48. O. MAHREHOLTZ 1984 *Dynamics of Rotors (Stability and System Identification)*. New York: Springer-Verlag.
49. J.W. SMITH 1988 *Vibrations of Structures (Applications in Civil Engineering Design)*. London: Chapman and Hall.
50. T.C. LIM, R. SINGH and J.J. ZAKRAJSEK 1989 *Proceedings of the Seventh International Modal Analysis Conference, Las Vegas, 1072-1078*. Modal analysis of gear housing and mounts.

51. J.W. LUND and Z. WANG 1986 *Journal of Vibration, Acoustics, Stress, and Reliability in Design, Transaction of the American Society of Mechanical Engineers* 108, 177-181. Application of the Riccati method to rotor dynamic analysis of long shafts on a flexible foundation.
52. J.M. VANCE, B.T. MURPHY and H.A. TRIPP 1987 *Journal of Vibration, Acoustics, Stress, and Reliability in Design, Transaction of the American Society of Mechanical Engineers* 109, 8-14. Critical speeds of turbomachinery: computer predictions vs. experimental measurements - Part II: effect of tilt-pad bearings and foundation dynamics.
53. L.L. EARLES, A.B. PALAZZOLO, C.K. LEE and C.H. GERHOLD 1988 *Journal of Vibration, Acoustics, Stress, and Reliability in Design, Transaction of the American Society of Mechanical Engineers* 110, 300-306. Hybrid finite element - boundary element simulation of rotating machinery supported on flexible foundation and soil.
54. A. BERMAN 1984 *AGARD Conference Proceedings, Lisbon*. Transmission of gear noise to aircraft interiors prediction methods.
55. J.J. ZAKRAJSEK and F.B. OSWALD 1989 Communication on the NASA Lewis Research Center spur gear test facility.
56. R.H. LYON 1975 *Statistical Energy Analysis of Dynamical Systems*. Cambridge: The MIT Press.
57. J. WOODHOUSE 1981 *Applied Acoustics* 14, 455-469. An introduction to statistical energy analysis of structural vibration.
58. R.H. LYON and E. EICHLER 1964 *Journal of the Acoustical Society of America* 36(7), 1344-1354. Random vibration of connected structures.
59. R.H. LYON and T.D. SCHARTON 1965 *Journal of the Acoustical Society of America* 38(2), 253-261. Vibrational-energy transmission in a three-element structure.

60. M.J. CROCKER and A.J. PRICE 1969 *Journal of Sound and Vibration* 9(3), 469-486. Sound transmission using statistical energy analysis.
61. E.H. DOWELL and Y. KUBOTA 1985 *Journal of Applied Mechanics* 52, 949-957. Asymptotic modal analysis and statistical energy analysis of dynamical systems.
62. Y. KUBOTA and E.H. DOWELL 1986 *Journal of Sound and Vibration* 106(2), 203-216. Experimental investigation of asymptotic modal analysis for a rectangular plate.
63. Y. KUBOTA, H.D. DIONNE and E.H. DOWELL 1988 *Journal of Vibration, Acoustics, Stress, and Reliability in Design* 110, 371-376. Asymptotic modal analysis and statistical energy analysis of an acoustic cavity.
64. E. SKUDRZYK 1980 *Journal of the Acoustical Society of America* 67(4), 1105-1135. The mean-value method of predicting the dynamic response of complex vibrators.
65. V.R. MILLER 1980 *M.S. Thesis, The Ohio State University*. Prediction of interior noise by statistical energy analysis (SEA) method.
66. B.L. CLARKSON and K.T. BROWN 1985 *Journal of Vibration, Acoustics, Stress, and Reliability in Design* 107, 357-360. Acoustic radiation damping.
67. J.C. SUN, H.B. SUN, L.C. CHOW and E.J. RICHARDS 1986 *Journal of Sound and Vibration* 104(2), 243-257. Predictions of total loss factors of structures, Part II: Loss factors of sand-filled structure.
68. G.J. STIMPSON, J.C. SUN and E.J. RICHARDS 1986 *Journal of Sound and Vibration* 107(1), 107-120. Predicting sound power radiation from built-up structures using statistical energy analysis.
69. A.J. KEANE and W.G. PRICE 1987 *Journal of Sound and Vibration* 117(2), 363-386. Statistical energy analysis of strongly coupled systems.

70. J. WOODHOUSE 1981 *Journal of the Acoustical Society of America* 69(6), 1695-1709. An approach to the theoretical background of statistical energy analysis applied to structural vibration.
71. P.W. SMITH, Jr. 1979 *Journal of the Acoustical Society of America* 65(3), 695-698. Statistical models of coupled dynamical systems and the transition from weak to strong coupling.
72. GENRAD INC. 1988 *GenRad System Operating Manual*.
73. STRUCTURAL DYNAMICS RESEARCH CORPORATION 1985 *User Manual for Modal Analysis*.
74. G.P. MATHUR, J.E. MANNING and A.C. AUBERT 1988 *NOISE-CON* 88, Purdue University, West Lafayette. Bell 222 helicopter cabin noise: analytical modeling and flight test validation.
75. J.L. GUYADER, C. BOISSON and C. LESUEUR 1982 *Journal of Sound and Vibration* 81(1), 81-92. Energy transmission in finite coupled plates, Part I: Theory.
76. W.L. GHERING and D. RAJ 1987 *Proceedings of the Winter Annual Meeting of the American Society of Mechanical Engineers, Boston*, 81-90. Comparison of statistical energy analysis predictions with experimental results for cylinder-plate-beam structures.
77. L. CREMER, M. HECKL and E.E. UNGAR 1973 *Structure-Borne Sound*. Berlin: Springer-Verlag.
78. R. SINGH 1989 Personal communication, based on the Ohio State University Gear Noise Short Courses.
79. G. MAIDANIK 1962 *Journal of the Acoustical Society of America* 34(6), 809-826. Response of ribbed panels to reverberant acoustic fields.



National Aeronautics and
Space Administration

Report Documentation Page

1. Report No. NASA CR-4334 AVSCOM TR-90-C-019		2. Government Accession No.		3. Recipient's Catalog No.	
4. Title and Subtitle Vibration Transmission Through Rolling Element Bearings in Geared Rotor Systems				5. Report Date November 1990	
				6. Performing Organization Code	
7. Author(s) Rajendra Singh and Teik Chin Lim				8. Performing Organization Report No. None (E-5716)	
				10. Work Unit No. 505-63-51	
9. Performing Organization Name and Address Ohio State University Department of Mechanical Engineering Columbus, Ohio 43210				11. Contract or Grant No. NAG3-773	
12. Sponsoring Agency Name and Address Propulsion Directorate U.S. Army Aviation Systems Command Cleveland, Ohio 44135-3191 <i>AVSCOM</i> and NASA Lewis Research Center Cleveland, Ohio 44135-3191				13. Type of Report and Period Covered Contractor Report Final	
				14. Sponsoring Agency Code	
15. Supplementary Notes Project Manager, James J. Zakrajsek, Propulsion Systems Division, NASA Lewis Research Center. This report is based on a portion of the Ph.D. thesis of Teik Chin Lim.					
16. Abstract <p>A new mathematical model is proposed to examine the vibration transmission through rolling element bearings in geared rotor systems. Current bearing models, based on either ideal boundary conditions for the shaft or purely translational stiffness element description, cannot explain how the vibratory motion may be transmitted from the rotating shaft to the casing. For example, a vibration model based upon the simple bearing formulations can only predict purely in-plane type motion on the flexible casing plate given only bending motion on the shaft. However, experimental results have shown that the casing plate motion is primarily flexural. This study clarifies this issue qualitatively and quantitatively by developing a comprehensive bearing stiffness matrix of dimension 6 to model the precision rolling element bearings using basic principles. The proposed bearing stiffness matrix is partially verified using available analytical and experimental data, and is completely characterized. This study extends the proposed bearing formulation to analyze the overall geared rotor system dynamics including casing and mounts. The bearing stiffness matrix is included in discrete system models using lumped parameter and/or dynamic finite element techniques. Eigensolution and forced harmonic response due to rotating mass unbalance or kinematic transmission error excitation for the following examples are computed: I. single-stage rotor system with flexible shaft supported by two bearings on rigid casing and flexible mounts, II. spur gear pair system with motor and load inertias attached to two flexible shafts supported by four bearings on flexibly mounted rigid casing, and III. case II with flexible casing and rigid mounts. In several of these examples, analytical predictions compare well with measured data, validating the proposed formulation. Numerical predictions show that the proposed theory is capable of predicting bearing moment transmissibility in addition to force transmissibility. A statistical energy analysis model combined with the bearing stiffness matrix is developed to predict the high frequency asymptotic dynamic behavior. The mean-square spatially averaged vibroacoustic responses are calculated for several example cases. A physical gearbox is also analyzed to demonstrate the salient features of the proposed technique. Good agreement is found between theory and experiment.</p>					
17. Key Words (Suggested by Author(s)) Vibration transmission Bearings Geared systems			18. Distribution Statement Unclassified - Unlimited Subject Category 37		
19. Security Classif. (of this report) Unclassified		20. Security Classif. (of this page) Unclassified		21. No. of pages 232	
				22. Price* All	